Advanced Diffusion MRI of Brain Tissue and Applications in Neurological Research

Von der Fakultät für Mathematik, Informatik und Naturwissenschaften der RWTH Aachen University zur Erlangung des akademischen Grades eines Doktors der Naturwissenschaften genehmigte Dissertation vorgelegt von

Licenciado en Física
Ezequiel Alejandro Farrher
aus Maggiolo, Argentinien.

Berichter:
Universitätsprofessor Dr. N. Jon Shah
Universitätsprofessor Dr. Achim Stahl

Tag der mündlichen Prüfung: 18. Dezember 2013

Diese Dissertation ist auf den Internetseiten der Hochschulbibliothek online verfügbar.

Contents

Abstract **v**

Zusammenfassung **vii**

List of publications **ix**

Journal articles ix

Conference proceedings x

1 Introduction **1**

2 Diffusion-weighted Magnetic Resonance Imaging **5**

2.1 Introduction 5

2.2 Nuclear Magnetic Resonance 6

2.2.1 Spins in a magnetic field 6

2.2.2 Bloch equations: a semi-classical description . . . 8

2.2.3 Signal detection 11

2.2.4 Spin-echo 12

2.2.5 Stimulated-echo 13

2.3 Nuclear Magnetic Resonance Imaging 15

2.3.1 The signal equation 15

2.3.2 Slice selection 17

2.3.3 Echo Planar Imaging 18

2.4 Particle diffusion 19

2.4.1 The self-diffusion propagator 19

2.4.2 Restricted diffusion 20

2.4.3 Diffusion in the central nervous system: a brief description 22

2.5 Diffusion-weighted MRI 24

2.5.1 The Sejskal-Tanner pulse sequence 24
2.5.2 The q-space model 26
2.5.3 The Bloch-Torrey equation 27
2.5.4 Diffusion-weighted stimulated-echo 28
2.5.5 Twice-refocused diffusion-weighted spin-echo . . . 29
2.6 Conclusions 30

3 Models for the DW MRI signal in the brain 31
3.1 Introduction 31
3.2 Anisotropic Gaussian diffusion: Diffusion Tensor Imaging 32
3.2.1 The apparent diffusion coefficient 32
3.2.2 2^{nd}-rank tensor model 34
3.2.3 Tensor ellipsoid representation 35
3.2.4 Tensor scalar invariants 37
3.2.5 Limitations of DTI 39
3.3 The two-compartment model 40
3.4 The statistical approach 41
3.4.1 Gaussian-like distribution 42
3.4.2 Log-normal distribution 43
3.5 Diffusion Kurtosis Imaging 44
3.5.1 DW signal and the diffusion kurtosis 44
3.5.2 Apparent Kurtosis Tensor 46
3.5.3 Kurtosis tensor scalars 48
3.6 High angular resolution diffusion imaging 50
3.7 Spherical deconvolution 51
3.8 Orientation density function 52
3.8.1 q-ball imaging 53
3.9 Fibre tractography 54
3.10 Bias in the DWIs due to the background noise 55
3.10.1 The Rician Noise 55
3.10.2 Background standard deviation 56
3.10.3 Bias correction in the limit of high SNR 57
3.10.4 The *power images* method 57
3.11 Conclusions 58

4 Multi-section anisotropic fibre phantom for diffusion MRI 61
4.1 Introduction . . . 61
4.2 Review of existing anisotropic diffusion phantoms . . . 62
4.3 Phantom construction . . . 63
4.3.1 Characteristics of Dyneema fibres . . . 63
4.3.2 Platform and manufacturing process . . . 64
4.4 MRI experiments . . . 67
4.4.1 Proton density measurements . . . 67
4.4.2 Diffusion measurements . . . 67
4.4.3 Data analysis . . . 68
4.5 Results . . . 70
4.5.1 Fibre density and conventional DTI maps . . . 70
4.5.2 Time-dependent diffusion in the parallel-area . . . 71
4.5.3 CSD and QBI analysis of HARDI data . . . 73
4.5.4 Streamline CSD-based fibre tractography . . . 74
4.6 Discussion . . . 76

5 Non-Gaussian diffusion in the human brain tissue 83
5.1 Introduction . . . 83
5.2 Materials and methods . . . 84
5.2.1 Diffusion experiments . . . 84
5.2.2 Data analysis . . . 85
5.3 Results . . . 90
5.3.1 Diffusion attenuation patterns . . . 91
5.3.2 Mean ADC maps . . . 92
5.3.3 FA, ACPhi and colour-coded directional maps . . . 97
5.3.4 Kurtosis and alpha maps . . . 102
5.3.5 Combined biexponential tensor and kurtosis map analysis . . . 105
5.4 Discussions . . . 106
5.4.1 Limitations of the study . . . 113
5.5 Conclusions . . . 113

6 On the optimal *b*-value range in DKI 115
6.1 Introduction . . . 115
6.2 Theory . . . 117

6.3 Methods . . . 118
6.3.1 DW MRI experiments . . . 118
6.3.2 Data processing . . . 119
6.4 Results . . . 121
6.4.1 Dependence of D_{app} and K_{app} on b_n . . . 121
6.4.2 Maps of b^*_{max} . . . 126
6.4.3 An optimized voxel-based evaluation of K_{app} . . . 128
6.4.4 Clinically relevant approach . . . 130
6.5 Discussion . . . 131
6.6 Conclusions . . . 134
6.7 Appendix 6.A. Algorithm for the assessment of b^*_{max} . . . 134

7 DKI and statistical approach in stroke animal models 137
7.1 Introduction . . . 137
7.2 Materials and methods . . . 139
7.2.1 Animals . . . 139
7.2.2 MRI experiments . . . 139
7.2.3 Models and data analysis . . . 140
7.3 Results . . . 141
7.3.1 DW signal attenuation . . . 141
7.3.2 Maps and histograms . . . 142
7.3.3 Analysis over regions-of-interest . . . 142
7.4 Discussion . . . 149
7.5 Conclusions . . . 154

8 Conclusions and outlook 157

Acknowledgements 159

Acronyms 165

Abstract

This work deals with the analysis of water diffusion in model and *in vivo* brain tissues by means of the diffusion-weighted (DW) magnetic resonance imaging (MRI) technique. Biological tissues in general, and the human brain in particular, represent systems of highly complex architecture that give rise to very complex diffusion behaviour of water. The random movement of water molecules appears restricted or hindered, leading to a reduction in the measured molecular diffusivity and deviations from the Gaussian diffusion behaviour.

Due to the highly complex DW MRI signal response, different problems arise regarding the validation and modelling of the experimental data. Therefore, artificial systems, or "phantoms", that mimic the relevant tissue properties, but with reduced complexity and well-known structure and physical properties, are becoming an important tool in the field.

The original research presented in this work can be divided into two parts. The first part deals with the development of new artificial diffusion phantoms that may serve as gold standard systems in the validation of DW MRI data. A new design for anisotropic fibre phantoms made of microscopic polyethylene fibres is proposed. The novel features of this design rely on the integration of several regions with different fibre architectures in a single phantom. It includes a region of nearly parallel fibres with a spatial gradient of the fibre volume fraction, a region of parallel fibres with constant volume fraction and two regions with fibres crossing at the right angles. Water diffusion in the phantom was characterized with DW MRI. Moreover, the application of the novel phantom in the validation of *high angular resolution diffusion imaging* data was investigated.

The second part of this work, deals with the investigation of the DW MRI signal in the brain at diffusion-weightings (b-values) much higher than those used conventionally. At low b-values, the DW MRI signal appears to be nearly a mono-exponential function of the b-value, characteristic of Gaussian diffusion. However, at higher b-values, clear deviations from the mono-exponential behaviour are observed. A proper theoretical relationship between the tissue structure and DW MRI signal in this regime requires differentiation of the various contributions to the average signal response and remains rather poorly understood. However, an application of various non-Gaussian models allows one to better characterize water diffusion and tissue properties of the brain. One of the important theoretical models considered in this work is the so-called *two-compartment* model. It was found that the fractional anisotropy (FA) from the fraction of "slow" diffusing molecules is larger than the conventional FA. It is therefore, a promising biomarker for characterising diseases affecting the fibrous structure of brain white mater. Moreover, several new map parameters based on the non-Gaussian behaviour of the DW MRI signal were proposed as new biomarkers.

Other theoretical models considered here include the diffusion kurtosis imaging (DKI) and the log-normal distribution function imaging (LNDFI). These models allow one to quantify the degree of the deviations from the Gaussian model and provide useful biomarkers of the tissue condition. In particular, DKI and LNDFI have been shown to enhance the contrast between the healthy tissue and ischaemic lesions in the animal stroke model.

Zusammenfassung

Diese Arbeit befasst sich mit der Analyse der Diffusion von Wasser in Hirngewebe im Modell und in vivo bei Anwendung von diffusionsgewichteter (DW) Kernresonanz-Bildgebung (MRI). Im Allgemeinen sind biologische Gewebe, und insbesondere das menschliche Gehirn, komplexe Systeme in welchen das Verhalten der Wasser-Diffusion ein hohes Maß an Komplexität aufweist. Die Zufallsbewegungen der Wassermoleküle werden eingeschränkt oder behindert, was sich in einer Verringerung der messbaren molekularen Diffusionsfähigkeit und Abweichungen vom Gauß'schen Diffusions-Verhalten äußert.

Die Auswertung und Modellierung der tatsächlicher Messdaten birgt, bedingt durch die hohe Komplexität der DW MRI Signale, viele Schwierigkeiten. Deshalb werden künstliche Systeme, sogenannte "Phantome", welche die relevanten Eigenschaften des Gewebes imitieren sollen, genutzt. Diese Systeme sind wesentlich einfacher gestaltet. Sie weisen eine geringere Komplexität auf und zeichnen sich durch klar definierte Stukturen und physikalische Eigenschaften aus. Phantome stellen ein wichtiges Hilfsmittel in diesem Forschungsgebiet dar.

Die hier vorgestellte Forschungsarbeit kann in zwei Teile unterteilt werden. Der erste Teil betrifft die Entwicklung von neuen künstlichen Diffusions-Phantomen, welche als Standardsystem für die Auswertung von DW MRI Daten genutzt werden sollen. Ein neues Design von anisotropen Phatomen aus mikroskopischen Polyethylen-Fasern wird vorgestellt. Die Besonderheit liegt hier in der Integration von Regionen unterschiedlicher Faserarchitekturen in einem einzigen Phantom. Es beinhaltet eine Region nahezu paralleler Fasern, deren Volumenanteil sich räumlich ändert, eine Region paralleler Fasern mit konstantem Volumenanteil sowie zwei Regionen mit sich rechtwinklig kreuzenden Fasern.

Die Diffusion von Wasser innerhalb des Phantoms wurde mit DW MRI charakterisiert. Ferner wurde das neuartige Phantom für die Auswertung von Daten aus *high angular resolution diffusion imaging* genutzt.

Der zweite Teil der Arbeit befasst sich mit der Erforschung des DW MRI im Gehirn für den Fall einer ungewöhnlich hohen Diffusionsgewichtung (b-Wert). Bei niedrigen b-Werten erscheint das DW MRI Signal als nahezu mono-exponentielle Funktion des b-Werts, was charakteristisch für Gauß'sche Diffusion ist. Bei hohen b-Werten kann eine klare Abweichung von diesem Verhalten beobachtet werden. Eine genaue theoretische Beziehung zwischen der Gewebestruktur und dem DW MRI Signal in diesem Regime verlangt eine differenzierte Behandlung verschiedener Einflüsse auf die mittlere Signalanwort und konnte bislang nur unzureichend bestimmt werden. Nichtsdestotrotz erlaubt die Anwendung verschiedener nicht-Gauß'scher Modelle eine bessere Charakterisierung der Wasserdiffusion und der Gewebeeigenschaften im Gehirn. Ein wichtiges theoretisches Modell, welches hier Berücksichtigung findet, ist das sogenannte *two-compartment* Modell. Es hat sich gezeigt, dass die fraktionelle Anisotropie (FA) des "langsam" diffundierenden Anteils der Moleküle größer ist als die konventionell berechnete FA. Man erhält so einen vielversprechenden Biomarker für die Charakterisierung von Krankheiten, welche die Faserstruktur der weißen Substanz beeinflussen. Außerdem werden verschiedene neue Parameter auf Basis des nicht-Gauß'schen Verhaltens der DW MRI Singale als neue Biomarker in Betracht gezogen.

Weitere behandelte theoretische Modelle sind unter anderem die Diffusion-Kurtose-Bildgebung (DKI) und die log-normale Verteilungsfunktions-Bildgebung (LNDFI). Diese Modelle erlauben die quantitative Bestimmung des Abweichungsgrades vom Gauß'schen Modell und liefern nützliche Biomarker für den Gewebezustand. Insbesondere steigern DKI und LNDFI den Kontrast zwischen gesundem Gewebe und ischämischen Läsionen im Schlaganfall-Modell bei Tieren.

List of publications

Journal articles

1. F. Grinberg, E. Farrher, A.-M. Oros-Peusquens, and N.J. Shah. *Random Walks in Model Brain Tissue.* AIP Conf. Proc. **1330**, 31-34 (2011).

2. F. Grinberg, E. Farrher, J. Kaffanke, A.-M. Oros-Peusquens, and N.J. Shah. *Non-Gaussian diffusion in human brain tissue at high b-factors as examined by a combined diffusion kurtosis and biexponential diffusion tensor analysis.* NeuroImage. **57**, 1087-1102 (2011).

3. E. Farrher, J. Kaffanke, A.A. Celik, T. Stöcker, F. Grinberg, and N.J. Shah. *Novel multisection design of anisotropic diffusion phantoms.* Mag. Reson. Imaging. **30**, 518-526 (2012).

4. I.I. Maximov, E. Farrher, F. Grinberg, and N.J. Shah. *Spatially variable Rician noise in magnetic resonance imaging.* Med. Image Anal. **16**, 536-548 (2012).

5. F. Grinberg, L. Ciobanu, E. Farrher, and N.J. Shah. *Diffusion kurtosis imaging and log-normal distribution function imaging enhance the visualisation of lesions in animal stroke models.* NMR Biomed. **25**, 1295-1304 (2012).

6. F. Grinberg, E. Farrher, I.I. Maximov, and N.J. Shah. *Complex Patterns of Non-Gaussian Diffusion in Artificial Anisotropic Tissue Models.* Microporous Mesoporous Mat. **178**, 44-47 (2013).

Conference proceedings

1. F. Grinberg, E. Farrher, J. Kaffanke, A.-M. Oros-Peusquens, and N.J. Shah. *New Quantitative Indices for DWI of the Brain Tissue at High b-Values*. Proc. Intl. Soc. Mag. Reson. Med. **18**, 4688. Stockholm, Sweden (2010).

2. E. Farrher, E. Batta, Y. Kupriyanova, O. Posnansky, F. Grinberg, and N.J. Shah. *Artificial Phantoms for Studies of Anisotropic Diffusion in the Brain*. Proc. Intl. Soc. Mag. Reson. Med. **18**, 3314. Stockholm, Sweden (2010).

3. E. Farrher, J. Kaffanke, T. Stöcker, F. Grinberg, N. Shah. *Novel artificial phantom for studies of anisotropic diffusion*. Magn. Reson. Mater. Phys. Biol. Med. **24**, abstract 686. Leipzig, Germany (2011).

4. F. Grinberg, E. Farrher, L. Ciobanu, F. Geffroy, N. Shah. *Analysis of stroke by means of kurtosis diffusion imaging in animal studies*. Magn. Reson. Mater. Phys. Biol. Med. **24**, abstract 331. Leipzig, Germany (2011).

5. F. Grinberg, E. Farrher, J. Kaffanke, A. Oros-Peusquens, N. Shah. *Analysis of non-Gaussian diffusion in brain tissue at high b-factors*. Magn. Reson. Mater. Phys. Biol. Med. **24**, abstract 324. Leipzig, Germany (2011).

6. D. Pflugfelder, E. Farrher, T. Stöcker, F. Grinberg, N.J. Shah. *Modeling the MRI diffusion signal using dispersive fibers*. Magn. Reson. Mater. Phys. Biol. Med. **24**, abstract 227. Leipzig, Germany (2011).

7. I.I. Maximov, E.A. Farrher, F. Grinberg, and N.J. Shah. *Spatially variable Rician noise in DTI*. Proc. Intl. Soc. Mag. Reson. Med. **19**, 4549. Montréal, Canada (2011).

8. J. Lindemeyer, A.-M. Oros-Peusquens, E. Farrher, F. Grinberg, and N.J. Shah. *Orientation and Microstructure Effects on Susceptibility*

Reconstruction: a Diffusion Phantom Study. Proc. Intl. Soc. Mag. Reson. Med. **19**, 4516. Montréal, Canada (2011).

9. E. Farrher, J. Kaffanke, T. Stöcker, F. Grinberg, and N.J. Shah. *Novel Artificial Phantom for Studies of Anisotropic Diffusion in the Model Brain Tissue*. Proc. Intl. Soc. Mag. Reson. Med. **19**, 2033. Montréal, Canada (2011).

10. F. Grinberg, E. Farrher, L. Ciobanu, F. Geffroy, and N.J. Shah. *Stroke Analysis by Means of Kurtosis Diffusion Imaging in In Vivo Animal Studies*. Proc. Intl. Soc. Mag. Reson. Med. **19**, 1989. Montréal, Canada (2011).

11. F. Grinberg, E. Farrher, J. Kaffanke, A.-M. Oros-Peusquens, and N.J. Shah. *Quantifying Non-Gaussian Diffusion in Brain Tissue at High b-Factors*. Proc. Intl. Soc. Mag. Reson. Med. **19**, 1983. Montréal, Canada (2011).

12. E. André, E. Balteau, C. Phillips, E. Farrher. I. Maximov, F. Grinberg, and N.J. Shah. *Impact of noise correction on diffusion kurtosis estimation*. Proc. Intl. Soc. Mag. Reson. Med. **20**, 3558. Melbourne, Australia (2012).

13. E. Farrher, F. Grinberg, and N.J. Shah. *Optimal b-Value Range in Diffusion Kurtosis Imaging*. Proc. Intl. Soc. Mag. Reson. Med. **20**, 3560. Melbourne, Australia (2012).

14. E. Farrher, T. Stöcker, F. Grinberg, and N.J. Shah. *High angular resolution diffusion imaging methods: a diffusion phantom study*. Proc. Intl. Soc. Mag. Reson. Med. **20**, 3591. Melbourne, Australia (2012).

15. I.I. Maximov, F. Grinberg, E. Farrher, N.J. Shah. *Microstructure informed fibre tracking via slow diffusion component*. Magn. Reson. Mater. Phys. Biol. Med. **25**, abstract 421. Lisbon, Portugal (2012).

16. E. Farrher, A. Celik, F. Grinberg, N.J. Shah. *A new anisotropic multiple-fibre phantom for diffusion MRI*. Magn. Reson. Mater. Phys. Biol. Med. **25**, abstract 568. Lisbon, Portugal (2012).

17. E. Farrher, F. Grinberg, N.J. Shah. *On the optimal b-value range in diffusion kurtosis imaging.* Magn. Reson. Mater. Phys. Biol. Med. **25**, abstract 740. Lisbon, Portugal (2012).

18. E. André, C. Phillips, E. Farrher, I. Maximov, F. Grinberg, N.J. Shah, and E. Balteau. *SNR dependence of mean kurtosis and how to correct it.* Proc. Intl. Soc. Mag. Reson. Med. **21**, 3199. Salt Lake City, USA (2013).

19. E. Farrher, F. Grinberg, A.A. Celik, K. Vahedipour, and N.J. Shah. *A multiple-fibre diffusion phantom for the validation of HARDI methods.* Proc. Intl. Soc. Mag. Reson. Med. **21**, 3164. Salt Lake City, USA (2013).

20. F. Grinberg, E. Farrher, I.I. Maximov, and N.J. Shah. *Complex Patterns of Non-Gaussian Diffusion in Artificial Anisotropic Tissue Models.* Proc. Intl. Soc. Mag. Reson. Med. **21**, 3124. Salt Lake City, USA (2013).

21. F. Grinberg, I.I. Maximov, E. Farrher, and N.J. Shah. *Microstructure-Informed Slow Diffusion Tractography in Humans Enhances Visualisation of Fibre Pathways.* Proc. Intl. Soc. Mag. Reson. Med. **21**, 3159. Salt Lake City, USA (2013).

22. F. Grinberg, E. Farrher, L. Ciobanu, and N.J. Shah. *On the Application of Anomalous Diffusion Metrics in Animal Stroke Models.* Proc. Intl. Soc. Mag. Reson. Med. **21**, 3083. Salt Lake City, USA (2013).

Chapter 1

Introduction

Attenuation of the water nuclear magnetic resonance (NMR) signal by molecular diffusion in biological tissue provides valuable information regarding its microstructure and physiological condition. In particular, diffusion-weighted (DW) MRI gave rise to outstanding opportunities in brain diagnostics and has become an indispensable tool in clinical practice. Unique applications refer to the diagnostics of acute stroke, tumours and various neurological disorders [1–3]. A remarkable success is associated with the diffusion tensor imaging (DTI) model which utilizes anisotropy of the water diffusion in white matter (WM) to estimate neuronal fibre pathways and connectivity [4–6]. DTI was reported to be important in the assessment of various neurodegenerative diseases such as multiple sclerosis, epilepsy, or Alzheimer's disease [7, 8] and other cognitive disorders (schizophrenia, dementia) [9, 10]. More recently, DTI studies were applied to characterization of WM structural changes accompanying brain maturation [11, 12] and normal ageing [13–15]. Many advanced techniques have been recently suggested for the reconstruction of the diffusion orientation distribution function with an enhanced angular resolution [16–20]. DTI also offers promising perspectives in accessing brain function in combination with functional studies [21].

Neuronal tissue is highly heterogeneous on multiple length scales. Establishing a proper picture of the relationship between dynamics and structure requires differentiation of the various contributions to the average NMR response, which poses some significant challenges. The conventional DTI approach suffers from intrinsic limitations from the fact

that it is based on the assumption of Gaussian free diffusion, characteristic of non-confined isotropic liquids. Usually, DTI studies are performed for low diffusion weightings (b-values) using a mono-exponential approximation for the DW MRI signal. However, a clear departure from a mono-exponential behaviour in the range of higher diffusion weightings has been reported [22–24], including our own work [25]. The underlying mechanisms of these deviations are far from being well understood and remain controversially discussed in the literature. Potentially, the propagation of water molecules in the brain is affected by multiple factors such as compartmentalization, restrictions and anisotropy imposed by the cellular microstructure [1]. Interfacial interactions with the cell membranes ("bound water") and membrane permeability may further contribute to the measured response [2]. In addition, the orientation of axonal fibres on extended length scales gives rise to anisotropic diffusion which appears faster in the direction parallel to fibres than perpendicular to them.

More recently, increasing efforts [3, 26–30] have been devoted to the development of new models and empirical approaches exploiting the observed non-Gaussian diffusion patterns. Several methods of data analysis have been suggested, in particular, the biexponential function [22,31–35], diffusion kurtosis imaging (DKI) [36, 37], stretched exponential function [38], and the statistical model by D. Yablonskiy et al. [39]. Generally, the advantage of these methods is that they allow one to enhance the information obtained from DW MRI and they form the basis for the development of new tools in clinical diagnostics.

One approach that has gained substantial attention from researchers was developed on the basis of simplified geometrical models [40] that are already well established in the studies of confined diffusion in porous media. It is based on the concept of compartmentalization of water molecules within the extracellular space (ECS) and intracellular space (ICS). In the ICS, diffusion would be more restricted giving rise to the slow diffusion component. However, a serious drawback of this model is that the relative volumes of the ICS and ECS known from histology appear in very different, nearly inverted, proportions to the experimentally measured fractions of the fast and slow diffusion components. Attempts have been made to overcome this discrepancy by considering relaxation

effects and finite membrane permeability (i.e. exchange effects in terms of the Kärger two-site model [41]. An alternative interpretation [3] suggests the existence of two differently structured water pools in intermediate or slow exchange. None of the proposed models has gained general acceptance and the phenomena are still poorly understood. Therefore, more work is required to gain a better understanding of the non-Gaussian nature of diffusion in brain parenchyma.

This dissertation is organized as follows. Chapter 2 provides a general overview of the physical principles of the DW MRI technique and a short description of the different pulse sequences used in the experimental part. Chapter 3 summarizes the most established theoretical models proposed in the literature for the analysis of the DW MRI signal. The physical principles of each model are described along with their advantages and shortcomings.

The original contribution of this work starts in Chapter 4. There, a novel design for artificial anisotropic fibre phantoms has been developed which allows one to combine several significant features of the brain tissue, such as a distribution of fibre densities and regions with crossing fibres, in a single device. Characteristic properties of water diffusion in this phantom based on DW MRI experiments are described. Furthermore, the phantom has been demonstrated to be a valuable tool in the validation of high angular resolution diffusion imaging data analysis.

In Chapter 5, a detailed study of water diffusivity in the extended range of b-values is reported. The DW signal attenuation curves are analysed by means of a combined DKI and biexponential diffusion tensor analysis (BEDTA) approach. In particular, new quantitative indices are suggested as map parameters which improve the underlying structure contrast in comparison to conventional DTI maps.

Chapter 6 is devoted to the investigation on the dependence of DKI metrics on the chosen b-value range, and a subsequent optimisation approach. The voxel-by-voxel optimisation of the b-value fitting range is shown to substantially improve the evaluation of DKI metrics and reduce the amount of the related artefacts.

Finally, in Chapter 7, DKI and log-normal distribution function imaging (LNDFI) are applied to quantify the deviations of the DW MRI signal

attenuation from the mono-exponential function in animal stroke models. It has been shown that the metrics quantifying the non-Gaussianity of the diffusion behaviour show an enhanced contrast between the healthy and affected tissue.

In Chapter 8 the main conclusions of this dissertation are drawn and future prospects are discussed.

Chapter 2

Diffusion-weighted Magnetic Resonance Imaging

2.1 Introduction

The NMR phenomenon was first observed by I. Rabi in 1938 [42]. In those experiments, a beam of molecules (LiCl) traversing a magnetic field was used to directly measure the magnetic properties of nuclei. However, it was not until 1946 that E. Purcell [43] and F. Bloch [44,45] independently demonstrated the NMR phenomenon in condensed matter. Meanwhile, F. Bloch [44] proposed the phenomenological equations to describe the NMR signal, nowadays known as "Bloch equations". Since then, NMR has become an extremely powerful technique for the investigation of physical processes and chemical structure at the atomic level in bulk samples.

The idea of spatial localization of an NMR property was first proposed by P. Lauterbur [46] in 1973. There, the superposition of a magnetic field gradient to the static magnetic field was used to spatially encode the Larmor frequency, and subsequently a technique called "backprojection" (from X-ray tomography) was used to reconstruct the image. A few years later P. Mansfield [47] proposed the echo planar imaging (EPI) technique to spatially encode the Larmor frequency in a single excitation, reducing thus the image formation to tens of milliseconds, thus starting the field of what is known today as MRI.

The first works in which the effect of particle self-diffusion on the NMR signal was taken into account, were published during the 50's by,

among others, E. Hahn [48], H. Carr and E. Purcell [49]. Meanwhile, the Bloch equations where extended to account for the effect of the particle self-diffusion and flow by H. Torrey [50].

Diffusion NMR imaging experiments were first performed by D. Taylor and M. Bushell in 1985 in a small bore magnet [51], and shortly after that, D. Le Bihan obtained for the first time DW images in a whole-body system [52, 53].

The first part of this chapter provides a short description of the NMR basics, including some of the pulse sequences commonly used in diffusion NMR studies. The idea of spatial localization of the NMR signal for image formation is subsequently described, and the notion of k-space is introduced. Thereafter, the concept of diffusion characterized by the *diffusion propagator* is briefly described. Here, the idea of *free* and *restricted* diffusion is considered in the context of water diffusion in the central nervous system (CNS), followed by its architectural description. Having established the principles of the NMR/MRI experimental techniques and the concept of molecular diffusion, we introduce the pulsed field gradient (PFG) NMR technique for diffusion measurements. Finally, we discuss experimental issues regarding sequence design and artefacts.

To cover completely the principles of diffusion NMR and MRI requires a complete monograph, rather than a single chapter. For this, the reader is referred to other text books and reviews such as References [41, 54–58].

2.2 Nuclear Magnetic Resonance

2.2.1 Spins in a magnetic field

The NMR phenomenon is found in magnetic systems that possess magnetic moments and angular momentum. Atomic nuclei possess a total magnetic moment μ and a total angular momentum $\mathbf{J}$, which are related by

$$\boldsymbol{\mu} = \gamma \mathbf{J}, \tag{2.1}$$

where γ is the nuclear gyromagnetic ratio, which is expressed in rad/(sT) and is specific for each nucleus. For the case of the hydrogen nucleus ^{1}H,

which is the most abundant in nature, it is $\frac{\gamma}{2\pi} = 42.58$ MHz T^{-1} [55].

In quantum theory, μ and $\mathbf{J}$ are treated as operators and the angular momentum is written proportional to a dimensionless operator $\mathbf{I}$, the "spin" operator, as

$$\mathbf{J} = \hbar\mathbf{I}, \tag{2.2}$$

where $\hbar = 1.054 \times 10^{-34}$ J s is the Plank's constant divided by 2π.

Consider independent nuclei in the presence of an external magnetic field $\mathbf{B}_0$ (taken along the z-axis for simplicity), then the Hamiltonian of the interaction of the nuclei with the magnetic field takes the form

$$H = -\gamma\hbar B_0 I_z, \tag{2.3}$$

having, therefore, a quantization of the energy levels (Zeeman levels) given by the expectation value of the Hamiltonian

$$E_m = -\gamma\hbar B_0 m, \tag{2.4}$$

with $m = -I, \ldots, I$ the eigenvalues of I_z.

For the ^{1}H nucleus, $I = \frac{1}{2}$ and therefore the energy levels split into two levels, usually referred as "spin-up" and "spin-down":

$$E = \begin{cases} -\frac{1}{2}\gamma\hbar B_0 & \text{spin-up} \\ \frac{1}{2}\gamma\hbar B_0 & \text{spin-down} \end{cases}, \tag{2.5}$$

with a difference of $\gamma\hbar B_0$ between the two levels. Figure 2.1(a) schematically depicts the splitting of the energy levels.

In order to be able to detect the presence of such energy levels, one needs an interaction that can induce transitions between the two energy levels, i.e. a resonance. These transitions can be induced by the spectral absorption or emission of a photon (Figure 2.1(b)) whose frequency has to be given by

$$\Delta E = \hbar\omega_0 = \gamma\hbar B_0. \tag{2.6}$$

In other words, in order to observe a resonance, the system has to be irradiated with photons of frequency

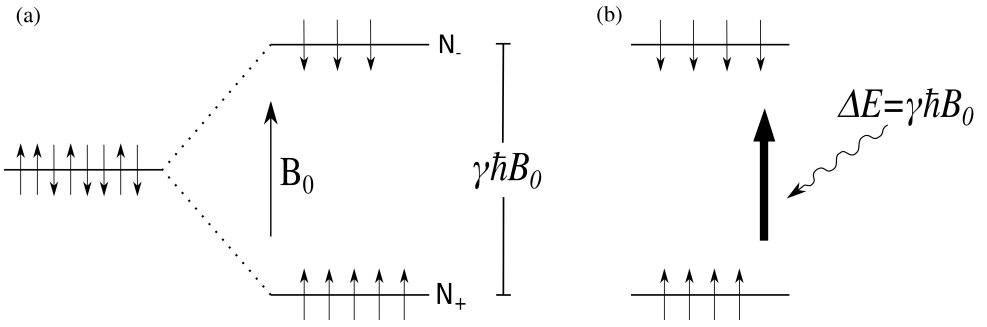


Figure 2.1: *(a) The split of the energy levels in a system of spins* $I = {}^1/_2$*, by applying a magnetic field* $\mathbf{B}_0$*. (b) Absorption of a photon of energy* $\Delta E = \gamma\hbar B_0$ *induces a transition between the energy levels.*

$$\omega_0 = \gamma B_0, \tag{2.7}$$

known as the Larmor frequency.

At thermal equilibrium, the population of each energy level is determined by the Boltzmann distribution [54], which can be written as

$$\frac{N_-}{N_+} = e^{-\frac{\Delta E}{k_B T}}, \tag{2.8}$$

where N_- and N_+ are the population of the *spin-down* and *spin-up* energy levels, respectively, $k_B = 1.38 \times 10^{-23}$ J K^{-1} is the Boltzmann's constant and T is the absolute temperature. This difference in energy populations gives rise to a net magnetisation $\mathbf{M}$, whose magnitude under the high temperature assumption is given by

$$M = \frac{N\gamma^2\hbar^2}{4k_B T} B_0 = \chi_0 B_0, \tag{2.9}$$

where N is the total number of spins and χ_0 is the nuclear susceptibility. The dependence of χ_0 on T is the well-known Curie law [54].

2.2.2 Bloch equations: a semi-classical description

Excitation

In this section the classical description of the motion of a net magnetisation $\mathbf{M}$ in an external magnetic field $\mathbf{B}$ is considered [44]. The field

$\mathbf{B}$ will produce a torque on $\mathbf{M}$ proportional to the rate of change of the angular momentum $\mathbf{M}/\gamma$:

$$\frac{\mathrm{d}\mathbf{M}}{\mathrm{d}t} = \gamma \mathbf{M} \times \mathbf{B}. \tag{2.10}$$

Equation 2.10 holds regardless of whether or not $\mathbf{B}$ is time-dependent. In the case of a constant field $\mathbf{B}_0$, which for convenience we consider along the z-axis, it predicts the precession of $\mathbf{M}$ about $\mathbf{B}_0$ with the Larmor frequency $\omega_0 = \gamma B_0$ (Equation 2.7).

The resonant phenomenon is reached when a time-dependent, oscillatory linearly polarized field, $\mathbf{B}_1$, with frequency ω_0, is applied perpendicular to the constant field. This frequency lies usually in the radio-frequency (RF) range. Expressing the linearly polarized field as the sum of two circularly polarized fields with opposite frequencies, and neglecting the field rotating in the direction opposite to the magnetisation, $\mathbf{B}_1$ can be approximated by $\mathbf{B}_1(t) = B_1 \cos(\omega_0 t)\,\mathbf{e}_x - B_1 \sin(\omega_0 t)\,\mathbf{e}_y$, with $\mathbf{e}_i$ $(i = x, y, z)$ representing the unit vectors along the x, y and z axis in the laboratory frame of reference. The solution of Equation 2.10 with $\mathbf{B} = B_0\mathbf{e}_z + \mathbf{B}_1$ under the initial condition $\mathbf{M}(0) = M_0\mathbf{e}_z$, is given by [55]

$$\begin{aligned} M_+(t) &= M_0 \sin(\omega_1 t)\, e^{-i\omega_0 t} \\ M_z(t) &= M_0 \cos(\omega_1 t), \end{aligned} \tag{2.11}$$

with $\omega_1 = \gamma B_1$ and $M_+ = M_x + iM_y$. In other words, the application of the $\mathbf{B}_1$ field produces a magnetisation $\mathbf{M}$ processing simultaneously about $\mathbf{B}_0$ with frequency ω_0 and about $\mathbf{B}_1$ with frequency ω_1 (Figure 2.2(a)). In a frame of reference rotating about $\mathbf{B}_0$ with frequency ω_0, the magnetisation simply rotates about $\mathbf{B}_1$ with frequency ω_1 (Figure 2.2(b)). This frame is known as the "rotating frame of reference". If the duration of the RF pulse is t, then $\mathbf{M}$ will rotate an angle $\varphi = \gamma B_1 t$ around $\mathbf{B}_1$. An RF pulse that flips $\mathbf{M}$ to the transverse plane, in which case $\varphi = \pi/2$ and $t = \pi/(2\gamma B_1)$, is known as the "90° pulse".

Relaxation

The effect of an RF pulse is the excitation of the spin system from its thermal equilibrium given by Equation 2.9. In terms of the magnetisation

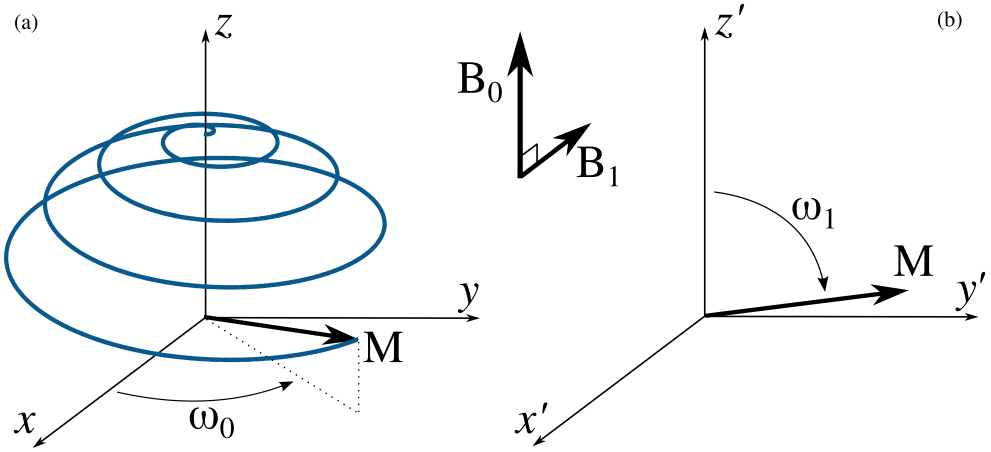


Figure 2.2: *(a) The evolution of the magnetisation* $\mathbf{M}$ *in the presence of a static magnetic field* $\mathbf{B}_0$ *and an oscillating magnetic field* $\mathbf{B}_1$ *perpendicular to* $\mathbf{M}$ *at the frequency* ω_0*, as predicted by Equations. 2.11. (b) The behaviour of the magnetisation* $\mathbf{M}$ *as seen from a rotating frame of reference (x'y'z') at the frequency* ω_0*, given by Equation 2.7.*

$\mathbf{M}$, after the RF pulse it will start precessing about the field $\mathbf{B}_0$. However, it will not precess indefinitely but gradually return to it its equilibrium state, M_0, in a characteristic time T_1, termed the "spin-lattice" relaxation time [44, 55]. This process involves an exchange of energy between the spin system and the reservoir, known as the "lattice", with which it is in thermal equilibrium. The phenomenological description of this process was given first by F. Bloch [44] and can be written as

$$\frac{\mathrm{d}M_z}{\mathrm{d}t} = -\frac{(M_z - M_0)}{T_1}. \tag{2.12}$$

This process is also known as "longitudinal relaxation" since it involves only the longitudinal magnetisation M_z.

The relaxation of the magnetisation M_+ in the transverse plane to the field $\mathbf{B}_0$ involves an exchange of energy among spins themselves and it is therefore known as the "spin-spin" relaxation. The exchange of energy among spins produces a loss of phase coherence that turns out in a relaxation of M_+ characterized by a time T_2, known as the transverse or spin-spin relaxation time. This process is therefore irreversible.

When the interactions among spins are weak compared to the main magnetic field [59], i.e. normally spins in the liquid state, the following

phenomenological equation can be used to described the process [44]:

$$\frac{\mathrm{d}M_+}{\mathrm{d}t} = -\frac{M_+}{T_2}. \tag{2.13}$$

Combining Equations 2.10, 2.12 and 2.13, the evolution of the total magnetisation in the laboratory frame of reference can be written as

$$\frac{\mathrm{d}\mathbf{M}}{\mathrm{d}t} = \gamma\mathbf{M}\times\mathbf{B} - \frac{(M_x\mathbf{e}_x + M_y\mathbf{e}_y)}{T_2} - \frac{(M_z - M_0)}{T_1}\mathbf{e}_z. \tag{2.14}$$

Equations 2.14 are known as Bloch equations.

However, the energy exchange among spins (T_2) is not the only process responsible of phase coherence loss. Static field inhomogeneities, due to magnet design imperfections, will produce also phase differences among the spins experiencing different field strengths, according to Equation 2.7. This coherence loss process is usually characterized by a time T_2' and is a reversible process by its nature, since no energy exchange is involved. The reversion of the effect of T_2' is called spin-echo (SE) and will be discussed in the following sections.

The total transverse relaxation time is commonly expressed in the literature as

$$\frac{1}{T_2^*} = \frac{1}{T_2} + \frac{1}{T_2'}, \tag{2.15}$$

which involves both the irreversible T_2 and the reversible T_2'.

Therefore, the solution of Equations 2.14 after a 90° pulse and with the initial condition $\mathbf{M}(0) = M_0\mathbf{e}_z$, can be written as [55]

$$\begin{aligned} M_+(t) &= M_0 e^{-i\omega_0 t} e^{-\frac{t}{T_2^*}} \\ M_z(t) &= M_0\left(1 - e^{-\frac{t}{T_1}}\right). \end{aligned} \tag{2.16}$$

2.2.3 Signal detection

The diagram shown in Figure 2.1 is only partially complete, since it cannot take into account the phase differences between spins. Furthermore, it is important to note that the energy of a single excitation is too small

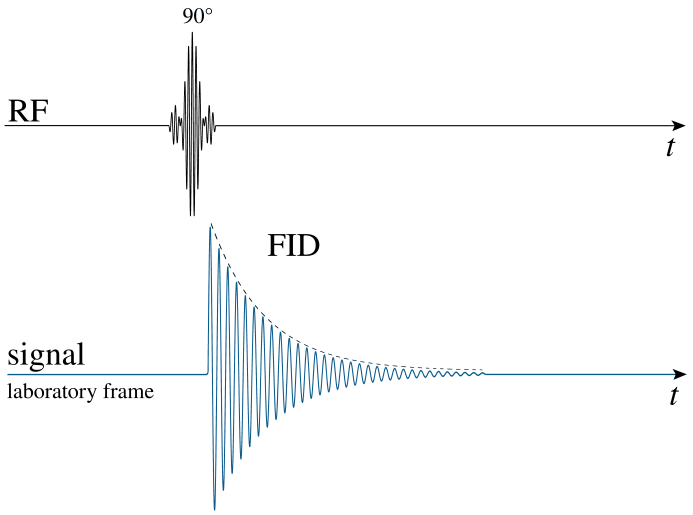


Figure 2.3: *Schematic representation of the FID. After the 90° pulse (top) the transverse magnetisation evolves towards the equilibrium state according to Equations 2.16. The solid and dashed curves (bottom) represent the signal measured in the laboratory and the rotating frame of reference, respectively.*

and therefore this effect needs to be considered in the context of an ensemble of spins.

From the Faraday's law of induction, the rotating magnetisation $\mathbf{M}$ in the transverse plane at the frequency ω_0 will induce an electromotive force (EMF) in an RF receive coil placed with its longitudinal axis perpendicular to the field $\mathbf{B}_0$. It is important to note that one needs the transverse magnetisation in order to induce the EMF in the coil, while the longitudinal magnetisation will not induce a signal. The NMR signal is collected in the time domain as an oscillating, decaying EMF induced by the magnetisation in free precession. This is known as the free induction decay (FID) and is schematically shown in Figure 2.3.

2.2.4 Spin-echo

Following the excitation of the spin system by a 90° pulse, the longitudinal magnetisation will be recovered (by 63 %) after a time T_1 and the transverse magnetisation will decay exponentially with a time constant T_2^*. In 1950 E.L. Hahn [48] showed that the effect of T_2' relaxation could be reversed by applying a 180°-pulse a time τ after the 90° pulse.

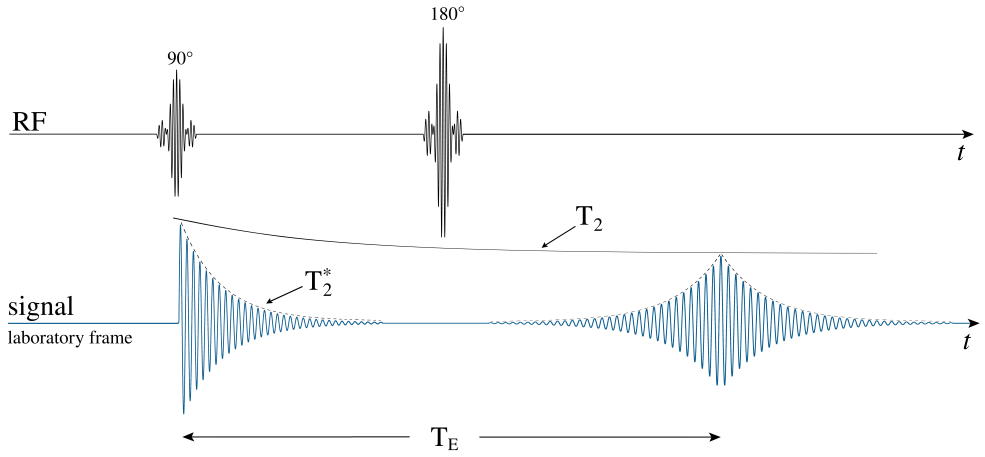


Figure 2.4: *The schematic diagram of the SE pulse sequence (top) and the signal as measured in the laboratory frame of reference (bottom). After the 90° pulse, the FID is governed by T_2^*. The dashed curve represents the signal as measured in the rotating frame of reference. After a time $T_E/2$ a 180°-pulse is applied in order to rephase the spins, producing an echo of the initial signal at the time T_E (bottom) whose amplitude is determined by Equation 2.17, schematically shown by the solid curve (bottom).*

A schematic representation of the SE sequence is depicted in Figure 2.4. After the 90° pulse, the transverse magnetisation will show an FID with a time constant T_2^*. The application of the 180°-pulse after a time $t = T_E/2$ will produce a rephasing of the spins inducing an echo of the initial signal at a time $t = T_E$. The amplitude of the echo is given by

$$M_+ (T_E) = M_0 e^{-\frac{T_E}{T_2}}, \tag{2.17}$$

where T_E is the "echo time" [48]. Therefore, T_2 can be estimated by measuring the echo amplitude for multiple echo times. It is important to mention that the field inhomogeneities responsible of the T_2' decay should be constant in the time course of a SE experiment.

2.2.5 Stimulated-echo

Some particular experiments, such as diffusion experiments (explained in the following sections), require long echo times. However, if the system has a short T_2, only a small fraction of the initial transverse magnetisation

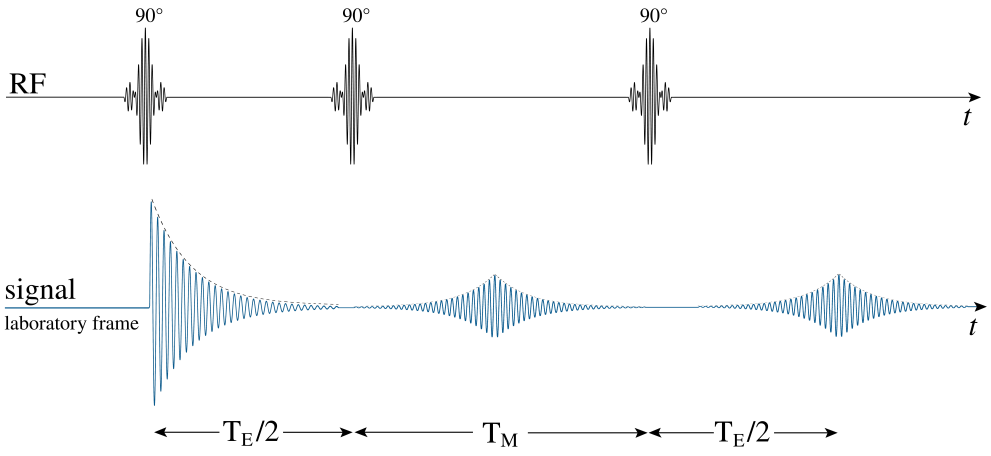


Figure 2.5: *The schematic diagram of the STE pulse sequence (top) and the signal as measured in the laboratory frame of reference (bottom). After the 90° pulse the FID is governed by T_2. The dashed curve represents the signal as measured in the rotating frame of reference. After a time $T_E/2$ the second 90° pulse is applied in order to store half of the magnetisation in the longitudinal axis. During a time T_M the signal relaxation is governed by T_1. Finally, the third 90° pulse is applied in order to flip the magnetisation back to the transverse plane and the stimulated echo is induced after a time $T_E/2$ from the third 90° pulse.*

will be recovered.

The stimulated-echo (STE) experiment [60] involves three 90° pulses, as shown in Figure 2.5. After the excitation, the spin system evolves for a time $t = T_E/2$, when the second 90° pulse is applied. The effect of the second pulse is to "store" half of the magnetisation in the longitudinal axis, and to form a primary echo with half of the initial amplitude in the transverse plane. The stored longitudinal magnetisation evolves under T_1 relaxation. Finally, after a time T_M (mixing time), the third 90° pulse is applied which gives rise to the stimulated echo [60]. The fact that in the interval between the second and the third 90° pulses the relaxation is governed only by T_1, allows one to induce the echo at much longer times compared to the SE case.

The amplitude of the simulated echo in the STE sequence is given by [41, 60]

$$M_+ (T_E + T_M) = \frac{M_0}{2} e^{-\left(\frac{T_E}{T_2} + \frac{T_M}{T_1}\right)}. \tag{2.18}$$

2.3 Nuclear Magnetic Resonance Imaging

In this section, the principles of the spatial localization of a given NMR property are briefly discussed. For a deeper description of the basic principles of this technique, the reader is referred to References [55, 56]. The image formation implies two main steps. The first part relates to the selective excitation of the spin system. The second step is related to the manner in which the signal is spatially encoded to be recorded. Both steps rely on the application of magnetic field gradients that produce a spatial variation of the Larmor frequency across the sample.

2.3.1 The signal equation

As discussed before, excitation RF pulses are used to flip the magnetisation, initially parallel to $\mathbf{B}_0$, into the transverse plane. In the case of a homogeneous object and homogeneous field $\mathbf{B}_0$, all spins in the object will be excited, and they all will have the same frequency after the excitation pulse. However, if the field has a spatial variation, i.e. $\mathbf{B}_0(\mathbf{r})$, then, according to Equation 2.7, the frequency will show a spatial variation as well. The field gradients commonly used in MRI are applied independently of the main static field $\mathbf{B}_0$ using specially designed coils. Since the magnitude of the varying fields is usually much less than that of the main static field, the Larmor frequency is only affected by the component along $\mathbf{B}_0$. In other words, the total magnetic field can be approximated by $\mathbf{B} = (B_0 + \mathbf{G} \cdot \mathbf{r})\, \mathbf{e}_z$. Therefore, the spatially dependent Larmor frequency can be written as

$$\omega (\mathbf{r}) = \gamma B_0 + \gamma \mathbf{G} \cdot \mathbf{r}, \tag{2.19}$$

where $\mathbf{r} \equiv (x, y, z)$ and $\mathbf{G}$ is the field gradient component parallel to $\mathbf{B}_0$ which may, in principle, be time-dependent. As discussed before, the signal detected in an NMR experiment is determined by the transverse magnetisation M_+ which for an inhomogeneous object in the presence of

a magnetic field gradient becomes $M_+ = M_+(\mathbf{r}, t)$. The same holds for the transverse relaxation time T_2 which becomes $T_2 = T_2(\mathbf{r})$.

Using Equation 2.19 in the Bloch equation (Equation 2.14), it can be shown that in the presence of a time dependent magnetic field gradient, the transverse magnetisation is given by [56]

$$M_+(\mathbf{r}, t) = M_0(\mathbf{r})\, e^{-\frac{t}{T_2(\mathbf{r})}} e^{-i\omega_0 t} e^{-i\gamma \int_0^t \mathbf{G}(\tau)\cdot\mathbf{r} d\tau}, \tag{2.20}$$

with the initial condition $M_0 = M_{0,x} + iM_{0,y}$.

Assuming that the receive coil is uniformly sensitive to the volume-of-interest (V), the total signal acquired is determined by

$$S(t) = \int_V M(\mathbf{r}, t)\, d\mathbf{r}. \tag{2.21}$$

In the following, it is assumed that the effects of T_2 relaxation are negligible. Furthermore, since $S(t)$ is typically demodulated in frequency by ω_0 using phase sensitive detection, the term $\exp(-i\omega_0 t)$ in Equation 2.20 can be skipped. Thus, the total measured signal results in the well-known *signal equation* [55, 56]:

$$S(t) = \int_V \rho(\mathbf{r})\, e^{-i2\pi\mathbf{k}\cdot\mathbf{r}} d\mathbf{r}, \tag{2.22}$$

where $\rho(\mathbf{r})$ represents the spin density in the object, proportional to the initial magnetisation according to Equation 2.9 (the proportionality factor has been dropped), and

$$\mathbf{k}(t) = \frac{\gamma}{2\pi} \int_0^t \mathbf{G}(\tau)\, d\tau, \tag{2.23}$$

is the reciprocal "k-space" vector [47, 55, 56].

Equation 2.22 is a fundamental relationship in MRI since it describes the relationship between the spin density and the measured MR signal through the Fourier transform. When the signal is acquired at certain positions in the k-space, the spin density $\rho(\mathbf{r})$ can be recovered using a discrete Fourier transform.

2.3.2 Slice selection

As discussed before, the applied RF field $\mathbf{B}_1$ at the Larmor frequency produces a rotation of the magnetisation around the axis $\mathbf{B}_1$. If the magnetic field is constant along the object, then all spins will be flipped. On the other hand, in order to restrict the excitation to a plane, say perpendicular to the z axis, a field gradient needs to be applied along this direction, according to Equation 2.19.

The selective excitation of a slice in the object will occur provided that the RF pulse contains the necessary range of frequencies in the slice of interest, i.e. the RF pulse in the frequency domain will be a rectangular-shaped function (Figure 2.6). Therefore, the RF pulse in the time domain, given by the Fourier transform of the RF pulse in the frequency domain, will be a sinc-shaped function [55, 56], as schematically depicted in Figure 2.6. Although a complete envelope of the RF pulse

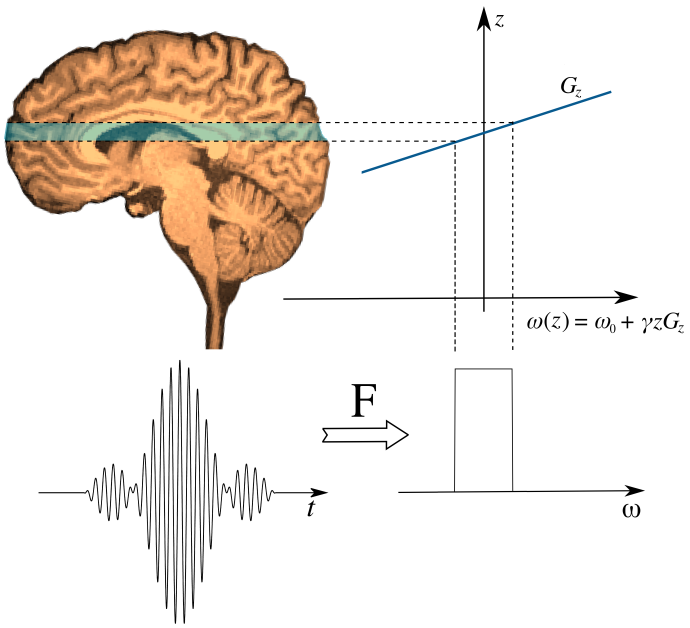


Figure 2.6: *The magnetic field gradient G_z, here applied along the z direction produces a variation of the Larmor frequency with z. The application of an RF pulse with a given frequency bandwidth will produce an excitation of the spin system lying only in the desired slice. In order to have a rectangular shaped RF pulse in the frequency domain, it must be sinc shaped in the time domain.*

is in practice never reached (the sinc function stretches into infinity), a good approximation of the rectangular pulse in the frequency domain is achieved by taking the central lobes of the sinc function [55].

2.3.3 Echo Planar Imaging

In conventional MRI, each line in the k-space is acquired after a separate excitation pulse, which is time consuming. In the case of diffusion MRI (described in the following sections), fast sequences covering the whole k-space in a short time are required in order to avoid motion artefacts.

The standard fast imaging technique is the echo planar imaging (EPI) introduced first by P. Mansfield [47], in which the k-space is sampled after a single excitation, during the echo formation. Here, alternating positive and negative readout field gradients (G_{read}) are applied to move along the k_{x}-direction in k-space. Between these gradients, small gradient (G_{phase}) are played out in order to change the position in the k_{y}-direction (Figure 2.7).

Moreover, since diffusion MRI relies on the application of extra field gradients between the excitation and the readout, the sampling of the k-space is done during the echo formation as schematically shown in Figure 2.7(a). In this case, the central part of the spin-echo (SE) must be located at the origin of the k-space in order to maximize the signal intensity of the low frequency part of the image ($k = 0$) (Figure 2.7(b)) [56].

Whereas EPI is less sensitive to motion artefacts, it suffers from eddy current and susceptibility artefacts [61]. Eddy currents arise in the coils as a consequence of the EPI readout in which strong field gradients are switched on and off in short periods of time. These eddy currents produce unwanted field gradients, introducing errors in the k-space encoding [61]. Several sequence modification and post-processing approaches have been proposed showing significant improvements [62–64]. Susceptibility artefacts arise when the magnetic susceptibility of the object and the surrounding medium are different, producing additional field gradients that distort the k-space trajectory.

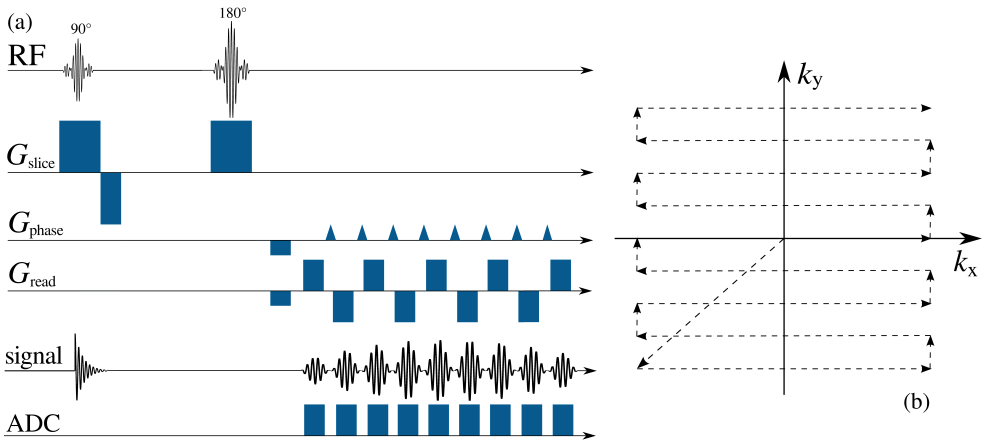


Figure 2.7: *(a) A schematic representation of the SE EPI sequence. The sequence starts with the excitation pulse applied in the presence of a slice-selection field gradient,* G_{slice}*. The EPI readout starts with the application of two field gradients,* G_{read} *and* G_{phase}*, in order to move to a corner of the k-space. During the echo formation, a train of alternating field gradients,* G_{read}*, shifting the position in k-space along the* k_{x} *direction, and small field gradients* G_{phase} *changing the position along* k_{y} *is applied. ADC is an abbreviation for analog-to-digital converter. (b) A representation of the k-space trajectory. Normally, between 64 and 256 lines are sampled in k-space.*

2.4 Particle diffusion

2.4.1 The self-diffusion propagator

Molecular propagation is conventionally described with the help of the self-diffusion propagator $P(\mathbf{r}_0|\mathbf{r},t)$, which is a probability density [41, 55, 57]. In this formalism, the probability that a particle will have moved from $\mathbf{r}_0$ into the volume element $d\mathbf{r}$ centred at $\mathbf{r}$ in the time interval t, is given by $P(\mathbf{r}_0|\mathbf{r},t)\,d\mathbf{r}$. Here, the molecular propagation is considered to be a stationary process and therefore the time t represents any time interval of duration t.

Assuming the *a priori* initial condition $P(\mathbf{r}|\mathbf{r}_0,0) = \delta(\mathbf{r}-\mathbf{r}_0)$, the analytical form of the diffusion propagator can be found by solving the second Fick's law with the appropriate boundary conditions [55, 65]:

$$\frac{\partial P(\mathbf{r}_0|\mathbf{r},t)}{\partial t} = \nabla^{\mathrm{T}}\mathbf{D}\nabla P(\mathbf{r}_0|\mathbf{r},t)\,, \tag{2.24}$$

where $\nabla^{\mathrm{T}} \equiv \left(\frac{\partial}{\partial x}, \frac{\partial}{\partial y}, \frac{\partial}{\partial z}\right)$ and $\mathbf{D}$ is a matrix representing the 2^{nd}-rank diffusion tensor, which is expressed as follows

$$\mathbf{D} = \begin{pmatrix} D_{xx} & D_{xy} & D_{xz} \\ D_{yx} & D_{yy} & D_{yz} \\ D_{zx} & D_{zy} & D_{zz} \end{pmatrix}. \tag{2.25}$$

The diffusion tensor is positive definite and symmetric, which means that its eigenvalues are positive.

For unrestricted diffusion, i.e. $P(\mathbf{r}_0|\mathbf{r}, t) \to 0$ for $\mathbf{r} \to \infty$, the solution of Equation 2.24 is the Gaussian propagator

$$P(\mathbf{r}_0|\mathbf{r}, t) = \frac{1}{(4\pi t|\,\mathbf{D}|)^{d/2}} \exp\left(-\frac{(\mathbf{r}-\mathbf{r}_0)^{\mathrm{T}}\,\mathbf{D}^{-1}\,(\mathbf{r}-\mathbf{r}_0)}{4t}\right), \tag{2.26}$$

where d (= 1, 2, 3) is the Euclidean dimension and $|\ldots|$ is the determinant [41, 55, 57]. The second moment of this function is the well-known Einstein relation

$$\langle \mathbf{r}\mathbf{r}^{\mathrm{T}} \rangle = 2dt\mathbf{D}, \tag{2.27}$$

and denotes the mean square displacement (MSD) of particles in the *observation time* t and in the direction $\mathbf{r}^{\mathrm{T}} \equiv (x, y, z)$.

2.4.2 Restricted diffusion

The diffusion process of water molecules in heterogeneous media such as biological tissue is restricted, hindered and, in some cases, anisotropic [2, 66, 67]. The underlying cellular microstructure of biological tissue influences the mobility of water molecules due to the presence of different types of cells, organelles, axons, neurons, etc. Therefore, the particle displacement (Equation 2.27) will be a function of the bulk diffusion coefficient of the diffusing molecules, the diffusion time t and the size and shape of the restricting geometry [2, 66]. Thus, the diffusion coefficient measured in MRI experiments and evaluated with the help of Equation 2.27 is not equal to the bulk diffusion coefficient D_0. In the literature, it is therefore referred as the ADC, as first introduced by D. Le Bihan et al. in 1986 [2, 53].

The ADC in heterogeneous environments, in contrast to D_0, may become dependent on the observation time. This time-dependence of the ADC provides useful information about the microstructure and microdynamics of the surrounding medium [2,40,67,68]. This is schematically demonstrated by the following example (see Figure 2.8), comparing unrestricted diffusion (a) and diffusion in a closed cavity (b) with a characteristic linear size l. For observation times $t \ll l^2/D_0$ the particle displacement will appear to be unrestricted in both cases (compare Figure 2.8(a) and 2.8(b)), whereas for $t \gg l^2/D_0$, the molecular propagation in the cavity will be restricted by the boundaries. All molecules, irrespective of the initial position, will traverse the whole space, and the MSD will appear to be time-independent, of the order of l^2 [58]. The measured ADC, in turn, will be inversely proportional to t. In the intermediate time-scale, $t \sim l^2/D_0$, the behaviour is more complicated and depends on the detailed geometry of the system [40,67].

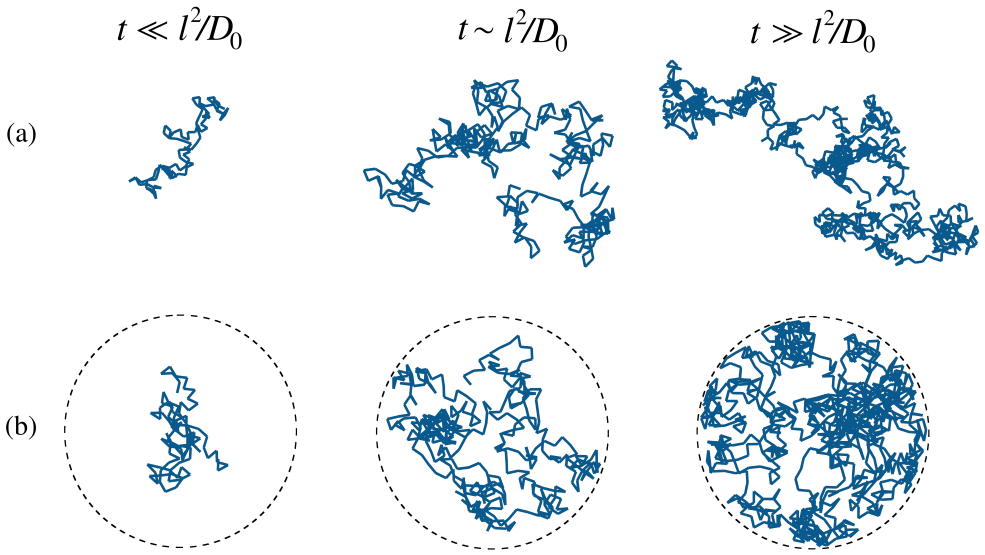


Figure 2.8: *Qualitative comparison of diffusion process in a free (a) and confined (b) environment.*

2.4.3 Diffusion in the central nervous system: a brief description

A brief description of the architectural environment relevant for water diffusion in the CNS is presented in Figure 2.9. Many different factors affect the molecular diffusivity. Figure 2.9(a) shows a coronal T_1-weighted MR image of the human brain. There, the grey matter (GM) and the white matter (WM), the two main tissue components of the CNS can be visualized. The cortical GM appears as the grey cortex surrounding WM, that is, the bright tissue in the central part. The sub-cortical GM, on the other hand, appears as nuclei in the central part of the brain. Besides GM and WM, there are cavities filled with cerebrospinal fluid (CSF) called *ventricles*. The water molecules in CSF show an isotropic diffusion behaviour.

WM is composed of bundles (Figure 2.9(b)) of myelinated nerve cells connecting various GM areas (the locations of nerve cell bodies) of the brain to each other, and carry nerve impulses between neurons. The nerve fibres (Figure 2.9(c)) are made up of groups of fasciculi (also known as tracts) and blood vessels surrounded by the epineurium [70, 71].

A single fasciculus is composed of a group of myelinated axons enclosed by a connective tissue called the perineurium. The diameter of the fasciculi lie in the range of 0.1-10 mm. The axon (Figure 2.9(d)) is the cylindrical projection that transmits the electrical impulses away from the cell body of the neuron. It is composed of the microtubuli (~ 25 nm in diameter) and neurofilaments (~ 5 nm in diameter) arranged in parallel and wrapped by the axonal membrane [70]. An axon is uniform in diameter usually showing a smooth surface. Axons are normally wrapped by a myelin sheath (Figure 2.9(d)), necessary for the insulation of electrical impulses. When myelin degrades, the conduction of signals can be disturbed or even lost. The presence of these myelin sheaths gives rise to the typical white colour observed in normal WM. The permeability of myelin sheaths is very low and they are arranged in concentric layers (Figure 2.9(d)) [2].

The axons in WM show a high packing density. Data from histology indicates volume fractions for the intra- and extra-axonal water of about 0.8 and 0.2, respectively [72]. Diffusion inside axons is highly anisotropic,

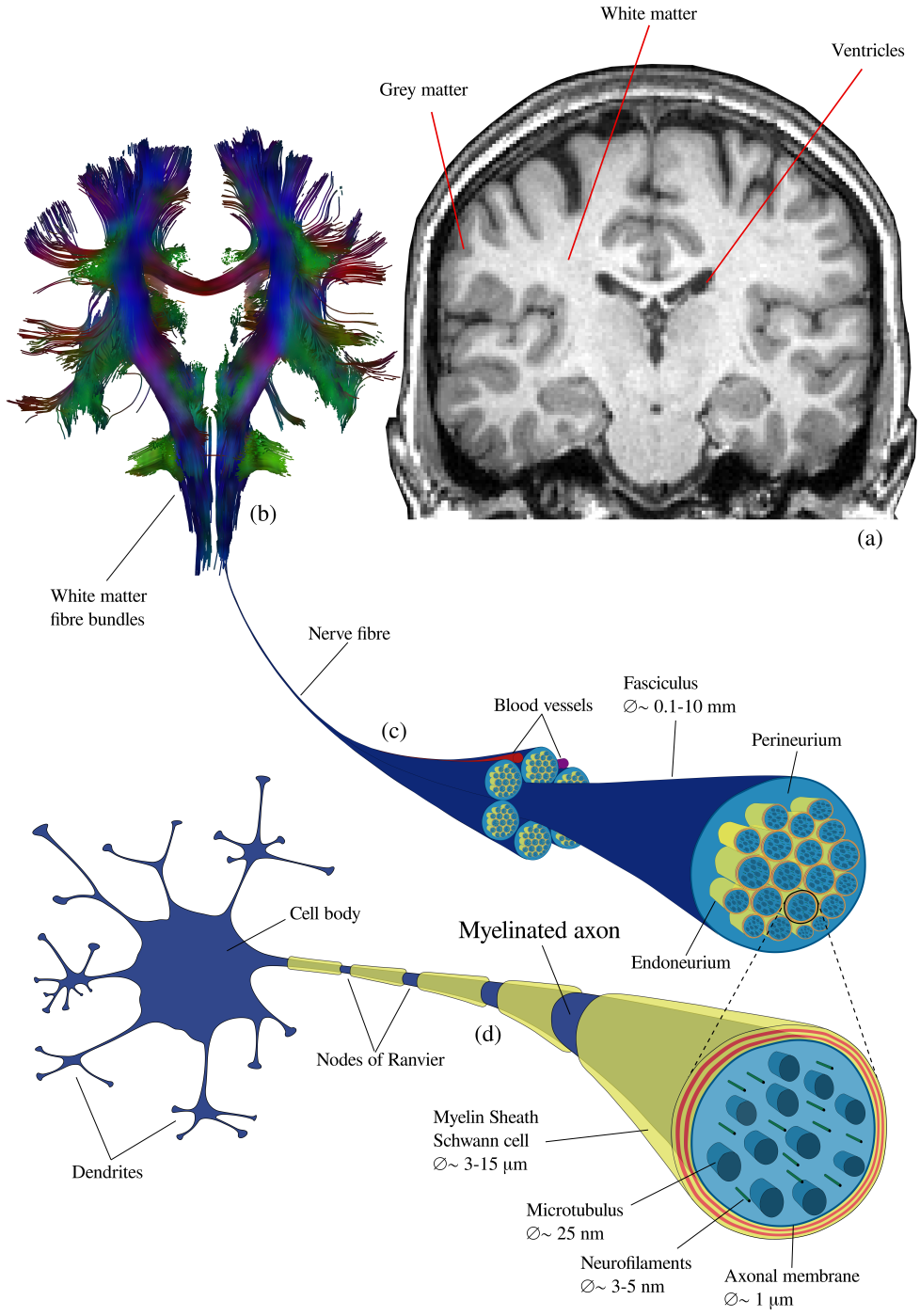


Figure 2.9: *A schematic representation of the CNS from the macroscopic to the microscopic point of view: (a) a coronal T_1-weighted image showing the GM, WM and CSF regions. (b) White matter fibre tracts (generated with the help of the ExploreDTI toolkit [69]). (c) Geometrical description of a nerve fibre bundle and the fasciculus. (d) Description of a neuron and its components.*

showing longitudinal diffusivity (along the axons) 2 to 5 time larger than the transverse diffusivity (across the axon) [2]. The exact microstructural features leading to this degree of anisotropy are still under debate. The hypothesized sources are the axonal membranes, myelin sheaths and microtubules, among others [2, 65].

Diffusion in the extra-axonal space, on the other hand, is considered to be hindered. For long diffusion times, the water displacement profile will become Gaussian and can be characterized by the tortuosity factor [40, 67].

GM consists mainly of neuronal cell bodies, dendrites and unmyelinated axons, glial cells and capillaries [70]. The distribution of dendrites and unmyelinated axons are randomly oriented in GM. Therefore, in spite of restrictions and local anisotropies, the diffusion behaviour in the macroscopic scale tends to be isotropic.

In general, diffusion of water molecules takes place in complicated multiple intracellular and extracellular compartments, leading to a highly restricted molecular movement. The Gaussian diffusion, on the other hand, occurs in systems where there is no restriction at all (Equation 2.26). Therefore, the concept of "Gaussian diffusion" in the brain tissue is to be considered only as an approximation of the underlying diffusion propagator.

2.5 Diffusion-weighted MRI

2.5.1 The Sejskal-Tanner pulse sequence

The standard pulsed field gradient (PFG) NMR sequence [73] is based on the use of the SE sequence (Section 2.2.4) with two additional PFGs, $\mathbf{g}(t)$, as schematically shown in Figure 2.10. This sequence was first proposed by O.E. Stejskal and J.E. Tanner [73], and is known as the Stejskal-Tanner sequence. The two PFGs are placed before and after the refocusing RF 180°-pulse in the conventional SE sequence (Figure 2.4).

Let us consider two rectangular pulses of the magnetic field gradient along the z-direction, with duration δ and strength g. The separation between the two field gradient pulses is denoted by Δ. Relaxation effects

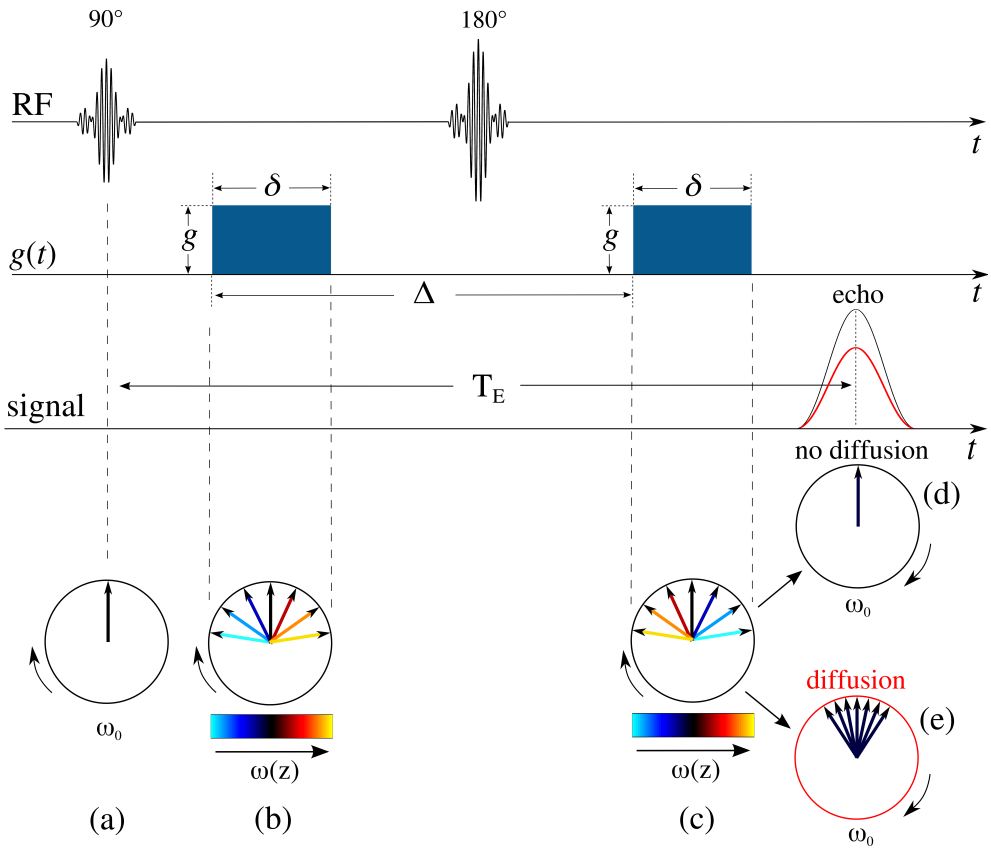


Figure 2.10: *A schematic representation of the PFG SE sequence. After the excitation all spins have ideally the same frequency (a). The effect of the first field gradient pulse is to spread the Larmor frequencies $\omega(z)$ (b). The colour bar represents the spatial dependence of Larmor frequencies. Following the refocusing 180°-pulse, the second field gradient pulse is applied with the same polarity (c), restoring the spin phases. If the spin positions are constant, then the complete magnetisation is recovered (d). If spin positions at the echo-time differ from the initial ones, then an attenuation of the magnetisation is observed (e).*

are skipped in the following discussion. After the excitation pulse, all spins have ideally the same phase. This is schematically depicted by the arrows in the bottom line in Figure 2.10(a). The effect of the first field gradient pulse (Figure 2.10(b)), conveniently set at $t = 0$, is to shift the spin phase according to

$$\phi_0 = \gamma \int_0^{\delta} g(t)\, z(t)\, dt = \gamma g \delta z_0. \tag{2.28}$$

The phase shift produced by the second field gradient pulse (Figure 2.10(c)) is

$$\phi_1 = -\gamma \int_{\Delta}^{\Delta+\delta} g(t)\, z(t)\, dt = \gamma g \delta z_1, \tag{2.29}$$

where the change of sign in Equation 2.29 is due to the refocusing 180°-pulse.

In Equations 2.28 and 2.29, the spin positions z_0 and z_1 are assumed to be approximately constant during the application of the field gradient pulses, i.e. $\sqrt{2D\delta}$ is negligible. This is known as the short gradient pulse (SGP) approximation [41, 65].

Therefore, the phase shift during the time Δ is simply

$$\phi = \phi_0 + \phi_1 = \gamma g \delta (z_0 - z_1). \tag{2.30}$$

If the spin position is the same at $t = 0$ and $t = \Delta$, then the phase shift is zero (Figure 2.10(d)). However, if the positions differ, there will be a net phase shift (Figure 2.10(e)), resulting in an attenuation of the transverse magnetisation.

The net NMR signal after the second gradient pulse in the SGP approximation can be written as [41, 74]

$$S = S_0 \iint_V \rho(\mathbf{r}_0)\, P(\mathbf{r}_0|\mathbf{r}, \Delta)\, e^{-i\gamma \mathbf{g}\cdot(\mathbf{r}-\mathbf{r}_0)\delta} d\mathbf{r}_0 d\mathbf{r}, \tag{2.31}$$

where $\rho(\mathbf{r}_0)$ is the initial spin density, $P(\mathbf{r}_0|\mathbf{r}, \Delta)$ is the diffusion propagator defined in Section 2.4.1 and the field gradient $\mathbf{g}$ is generalized to an arbitrary direction. In Equation 2.31 the echo intensity is normalized to the initial signal.

2.5.2 The q-space model

The phase shift term in Equation 2.31 depends on the displacement $\mathbf{R} \equiv \mathbf{r} - \mathbf{r}_0$. In order to remove the dependence on the initial spin distribution $\rho(\mathbf{r}_0)$, the *average propagator* $\overline{P}(\mathbf{R}, t)$ is defined as [41]

$$\overline{P}(\mathbf{R}, t) = \int_V \rho(\mathbf{r}_0)\, P(\mathbf{r}_0|\mathbf{r}_0 + \mathbf{R}, t)\, d\mathbf{r}_0, \tag{2.32}$$

and the echo attenuation due to diffusion is

$$S(\mathbf{q},t) = \int \overline{P}(\mathbf{R},t)\, e^{-i2\pi\mathbf{q}\cdot\mathbf{R}} d\mathbf{R}, \tag{2.33}$$

where $\mathbf{q} \equiv \gamma\delta\mathbf{g}(2\pi)^{-1}$. This means that in the SGP approximation, the echo attenuation due to particle diffusion is the Fourier transform of the average propagator defined in Equation 2.32 with the reciprocal space given by $\mathbf{q}$ [55, 58]. Therefore, the diffusion propagator can be obtained by the inverse Fourier transform of the DW signal:

$$\overline{P}(\mathbf{R},t) = \int S(\mathbf{q},t)\, e^{i2\pi\mathbf{q}\cdot\mathbf{R}} d\mathbf{q}. \tag{2.34}$$

In the following, the averaged diffusion propagator will be denoted simply as $P(\mathbf{r},t)$.

2.5.3 The Bloch-Torrey equation

In 1956 H.C. Torrey [50] extended the Bloch equation (Equation 2.14) to account for the effect of the particle self-diffusion and flow by adding two additional terms. In the rest of this work the flow term is skipped and only the diffusion term is considered. Combining the Bloch equation (Equation 2.14) with the Fick's second law (Equation 2.24), the evolution of the spatial distribution of magnetisation $\mathbf{M}(\mathbf{r},t)$ after the excitation RF pulse can be written as

$$\frac{\mathrm{d}\mathbf{M}}{\mathrm{d}t} = \gamma\mathbf{M}\times\mathbf{B} - \frac{(M_x\mathbf{e}_x + M_y\mathbf{e}_y)}{T_2} - \frac{(M_z - M_0)\mathbf{e}_z}{T_1} + \sum_{i=x,y,z} \nabla^{\mathrm{T}}(\mathbf{D}\nabla M_i)\,\mathbf{e}_i, \tag{2.35}$$

where $\mathbf{B}(\mathbf{r},t) = B_0\mathbf{e}_3$ is the static magnetic field [41, 65].

When a PFG NMR sequence is applied, the total magnetic field can be written as $\mathbf{B}(\mathbf{r},t) = (B_0 + \mathbf{g}(t)\cdot\mathbf{r})\,\mathbf{e}_3$. The analytical expression for the echo intensity is given by [41, 65]

$$S(T_E) = S_0 e^{-\frac{T_E}{T_2}} e^{-b\mathbf{u}^{\mathrm{T}}\mathbf{D}\mathbf{u}}, \tag{2.36}$$

where the term S_0 is the echo intensity without the effect of diffusion and relaxation, $\mathbf{u}$ is the unit vector pointing in the direction of $\mathbf{g}$, and b, given by

$$b = \gamma^2 \int_0^{T_E} dt \left[\int_0^t \mathbf{g}^{\mathrm{T}}(t')\, dt' \right] \left[\int_0^t \mathbf{g}(t')\, dt' \right], \tag{2.37}$$

is known as the *b-value*, in units ms μm^{-2}. For the time diagram of the Stejskal-Tanner sequence (Figure 2.10), b is given by [41, 65]

$$b = \gamma^2 \delta^2 g^2 \left(\Delta - \frac{\delta}{3} \right). \tag{2.38}$$

Equation 2.36 is known as the Stejskal-Tanner equation [65, 73]. In the case of Gaussian diffusion, it holds regardless of the validity of the SPG condition [74]. In conventional DW MRI, the dephasing induced by the imaging field gradients (such as those in the EPI readout) is assumed to be negligible.

Thus, assuming a Gaussian diffusion, Equations 2.36 and 2.38 allow one to estimate the diffusion tensor $\mathbf{D}$ (or the diffusion coefficient D in the case of isotropic diffusion) by measuring the SE amplitude for different b-values [65].

2.5.4 Diffusion-weighted stimulated-echo

The longest separation time between two diffusion-sensitizing field gradient pulses in the Stejskal-Tanner sequence, Δ, is limited by the T_2 of the system under investigation [41, 57]. Thus, the echo attenuation at the largest possible Δ in systems showing very slow diffusivity may not be sufficient for a reliable estimation of the diffusion coefficient. Since the longitudinal relaxation governed by T_1 is usually longer than the transverse one, the use of the STE sequence (Figure 2.5), combined with diffusion-sensitizing gradients, has been proposed to measure the diffusivity in such systems [60]. Figure 2.11 shows the time diagram of the DW STE sequence.

For this sequence, the attenuation of the stimulated echo is given by [57, 60]

$$S(T_E + T_M) = \frac{S_0}{2} e^{-\left(\frac{T_E}{T_2} + \frac{T_M}{T_1}\right)} e^{-b\mathbf{u}^{\mathrm{T}}\mathbf{D}\mathbf{u}}, \tag{2.39}$$

with b given by Equation 2.38.

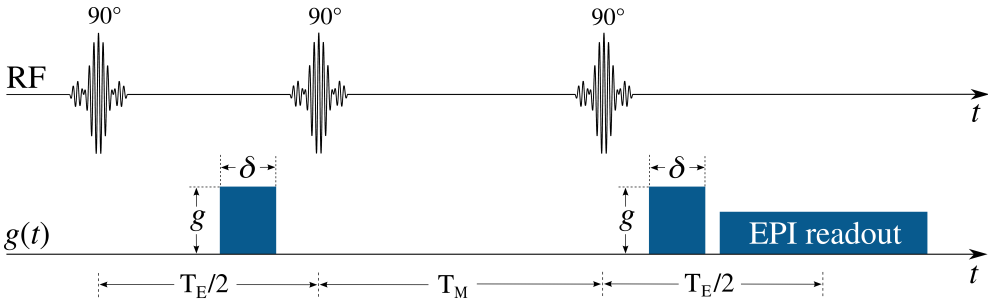


Figure 2.11: *The time diagram of the DW STE sequence. Two diffusion-sensitizing field gradients g are placed after the first and the third RF 90°-pulses. The DW stimulated echo occurs at the time $T_E + T_M$.*

2.5.5 Twice-refocused diffusion-weighted spin-echo

The application of high intensity diffusion-weighting field gradients in PFG NMR sequences produces persistent eddy currents with a dependence on the applied field gradient direction. If the induced eddy current is sufficiently long so that residual field gradients persist during the EPI readout, this additional field gradient will produce an image distortion [62]. The twice-refocused spin-echo (TRSE) sequence was proposed by T.G. Reese et al. [62] in order to reduce the eddy current distortions in DW images. The TRSE is based on the Stejskal-Tanner sequence with an additional 180° refocusing pulse and two bipolar field gradients with equal duration, $\delta_1 + \delta_2 = \delta_3 + \delta_4$, as shown in Figure 2.12.

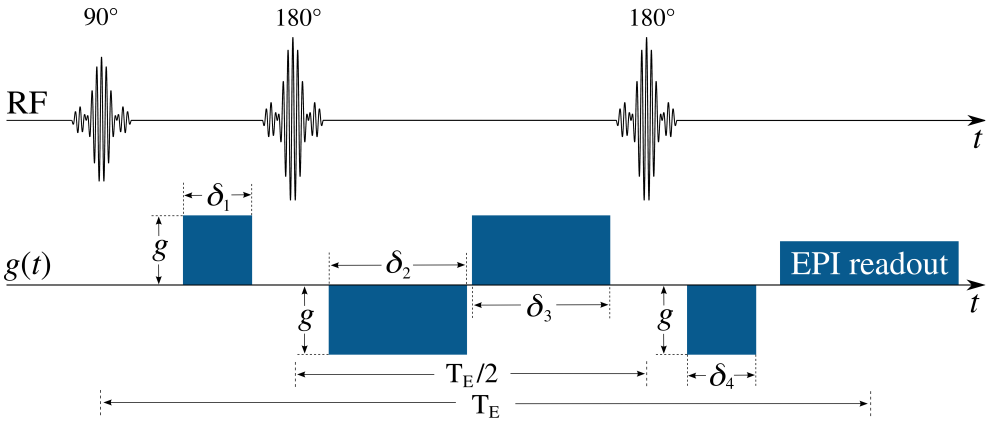


Figure 2.12: *The time diagram of the DW TRSE sequence. The two refocusing pulses have a separation $T_E/2$. The bipolar diffusion weighting field gradients have equal duration $\delta_1 + \delta_2 = \delta_3 + \delta_4$.*

By adjusting the timing of the diffusion field gradient pulses, the effect of remaining eddy currents with single exponential decay during the EPI readout can be reduced without loss of scanning efficiency [62].

2.6 Conclusions

In this chapter, a general overview of the physical principles of the NMR technique was carried out. Some the basic NMR pulse sequences for diffusion measurements, such as the SE and the STE, were introduced. Afterwards, the idea of spatial localization of the NMR signal to reconstruct an image was discussed, together with a short description of the basic approach for the image readout commonly used in diffusion MRI, namely the EPI.

Following the introduction of NMR and MRI techniques, the concept of particle diffusion and its characterization through the *diffusion propagator* has been introduced. The influence of the surrounding media on molecular diffusion was discussed. Since the ultimate goal of this dissertation is the study of water diffusion in the CNS, a short anatomical description has been provided, and its influence on the molecular diffusion has been discussed.

In the last part of this chapter, the use of NMR and MRI techniques to measure molecular diffusion was shortly summarized. Finally, some of the most important pulse sequences were introduced.

Chapter 3

Models for the DW MRI signal in the brain

3.1 Introduction

A proper interpretation of DW MRI experiments relies on the development of theoretical models that relate the features of the tissue microstructure and microdynamics to the DW MRI signal. In this chapter, a summary of various theoretical models used to describe the DW signal in the human brain is presented. Due to the high complexity of the CNS (Discussed in Chapter 2, Section 2.4.3) these models are not completely perfect since they cannot capture all tissue properties affecting diffusion. However, they represent a useful framework that allows one to quantify important tissue properties such as tissue anisotropy, fibre directionality, cell integrity and permeability, among others. This Chapter also describes some selected models used in the experimental chapters of this work.

3.2 Anisotropic Gaussian diffusion: Diffusion Tensor Imaging

3.2.1 The apparent diffusion coefficient

The conventional approach to describe the DW signal attenuation in biological tissue is to use Equation 2.36 and the ADC, D_{app}. In the case of isotropic diffusion,

$$\ln \frac{S(b)}{S(0)} = -bD_{app}, \tag{3.1}$$

with the b-value given by Equation 2.38. In this context, D_{app} should be considered as a phenomenological parameter that incorporates integrative information on the tissue microstructure [53, 74].

Usually, D_{app} is determined by measuring the DW signal for at least two b-values in a single gradient direction. Figure 3.1 schematically shows the approach for evaluating D_{app}. The DW signal is shown for a healthy human brain measured with the DW TRSE sequence, using b-values between 0.0 ms μm^{-2} and 4.0 ms μm^{-2} and two non-collinear gradient directions. In this graphic, $S(b)$ is shown for a small region-of-interest (ROI) located in WM.

One can see that Equation 3.1 represents a good approximation within the range 0.0 ms μm^{-2} to 1.0 ms μm^{-2}. Moreover, due to the anisotropy of WM (discussed in Section 2.4.3), the slope of the signal attenuation depends on the gradient encoding direction. However, it has been demonstrated in several works [24, 25, 35, 75–77] that the DW signal attenuation in the human brain beyond $b = 1.0$ ms μm^{-2} deviates from the mono-exponential behaviour. This means that at high b-values the Gaussian approximation is not valid, as schematically shown in Figure 3.1. In the following sections several models accounting for the anisotropy and non-Gaussianity of the DW signal are briefly discussed.

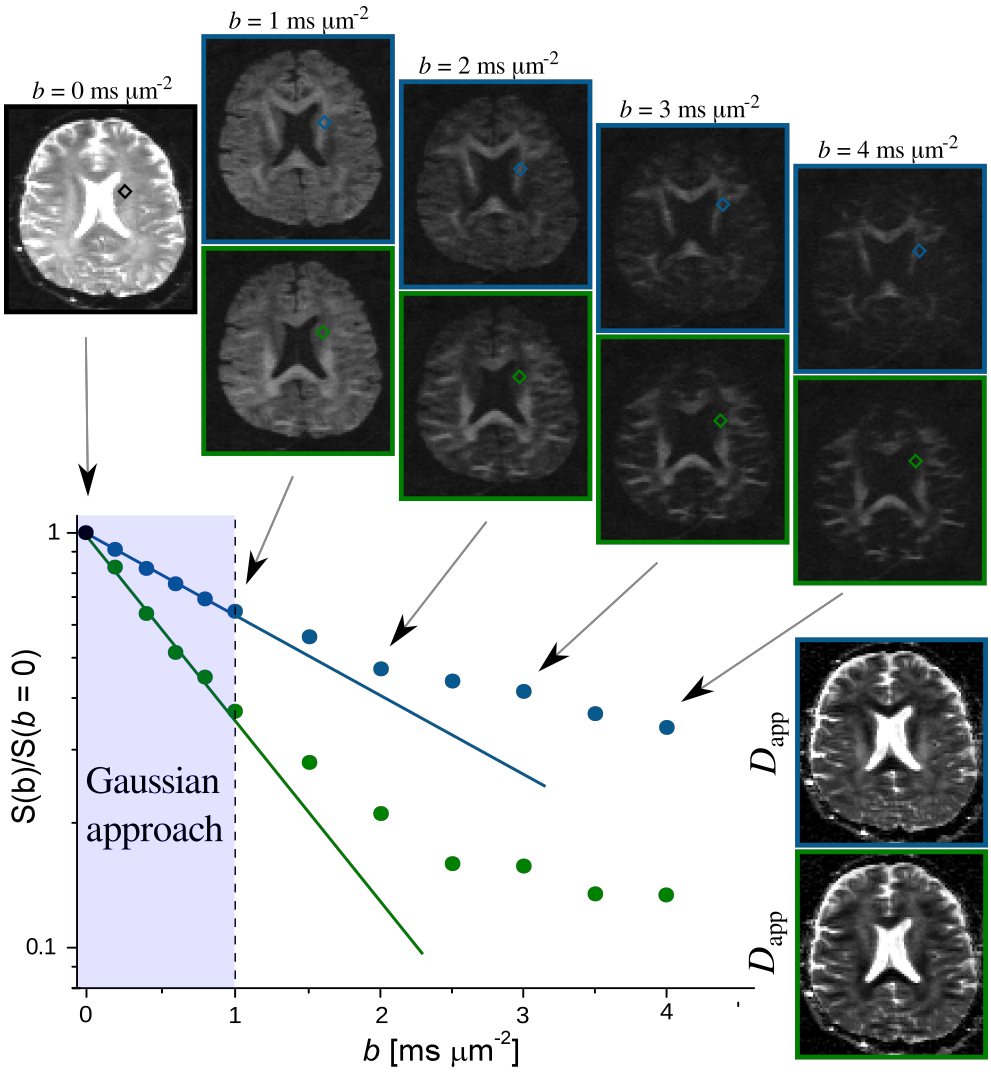


Figure 3.1: *A schematic representation of the approach for the evaluation of the ADC from the DW MRI signal attenuation. The DW images are shown for an axial slice in the human brain, two gradient encoding directions and b-values between 0.0* ms μm^{-2} *and 4.0* ms μm^{-2}*. The signal averaged for a small ROI in WM is shown in the graphic. Due to the anisotropy of WM, the attenuation slopes in different gradient directions are different. Moreover, the mono-exponential approach is shown to be valid approximately in the range* $b \leq 1.0$ ms μm^{-2}*.*

3.2.2 2nd-rank tensor model

The anisotropic behaviour of water diffusion observed in WM cannot be described by a single scalar parameter such as D_{app}. One of the most successful techniques describing the anisotropic diffusion is the so-called diffusion tensor imaging (DTI) proposed by P.J. Basser et al. [78, 79] in 1994. In this theory, a rigorous framework of the anisotropic Gaussian diffusion is established, providing not only a quantitative measure for the diffusion anisotropy, but also the main directions of water diffusion.

DTI is based on the extension of Equation 3.1 to the anisotropic case. For a single gradient direction $\mathbf{g}$, Equation 2.36 can be written as

$$\begin{aligned} \ln \frac{S(b)}{S(0)} &= -\gamma^2 \delta^2 \left(\Delta - \frac{\delta}{3} \right) g^2 \mathbf{u}^{\mathrm{T}} \mathbf{D}_{\text{app}} \mathbf{u} \\ &= -b \sum_{i=1}^{3} \sum_{j=1}^{3} u_i u_j D_{ij}^{\text{app}}, \end{aligned} \tag{3.2}$$

where $S(0)$ includes the relaxation factor in Equation 2.36. Therefore, the ADC for a single gradient direction is given by

$$D_{\text{app}} = \mathbf{u}^{\mathrm{T}} \mathbf{D}_{\text{app}} \mathbf{u} = \sum_{i=1}^{3} \sum_{j=1}^{3} u_i u_j D_{ij}^{\text{app}}. \tag{3.3}$$

Since $\mathbf{D}_{\text{app}}$ is a 2nd-rank symmetric tensor and positive definite, the number of degrees of freedom is 6 [58]. To evaluate the apparent diffusion tensor $\mathbf{D}_{\text{app}}$, the DW images must be acquired for N non-coplanar gradient directions $\mathbf{g}_i$ $(i = 1...N)$ plus a non-DW image $(b = 0)$ [58, 80]. For a set of $N = 6$ non-coplanar gradient directions, Equation 3.2 has a unique solution. However, due to the effect of noise, it is convenient to acquire the DW images for $N > 6$ directions, in which case the system of Equations 3.3 is overdetermined and must be solved using fitting approaches [81, 82]. As discussed in the previous section, in conventional DTI the b-value is usually set to $b = 1.0$ ms μm^{-2} [5]. This prevents one of having systematic bias the estimation of the tensor elements [83].

3.2.3 Tensor ellipsoid representation

By diagonalizing the tensor $\mathbf{D}_{\text{app}}$, one finds the tensor eigenvalues (principal diffusivities) and eigenvectors [58, 79]. Due to the fact that $\mathbf{D}_{\text{app}}$ is symmetric and positive definite, its three eigenvectors $\boldsymbol{v}_i$ $(i = 1, 2, 3)$ are orthogonal and the eigenvalues λ_i (by convention $\lambda_1 \geq \lambda_2 \geq \lambda_3$) are positive

$$\mathbf{D}_{\text{app}}\mathbf{V} = \mathbf{V}\boldsymbol{\Lambda}, \tag{3.4}$$

with

$$\mathbf{V} = \begin{pmatrix} v_{1,x} & v_{2,x} & v_{3,x} \\ v_{1,y} & v_{2,y} & v_{3,y} \\ v_{1,z} & v_{2,z} & v_{3,z} \end{pmatrix} \quad \text{and} \quad \boldsymbol{\Lambda} = \begin{pmatrix} \lambda_1 & 0 & 0 \\ 0 & \lambda_2 & 0 \\ 0 & 0 & \lambda_3 \end{pmatrix}, \tag{3.5}$$

where $\boldsymbol{\Lambda}$ is the diagonal matrix of eigenvalues and $\mathbf{V}$ is the matrix of orthonormal eigenvectors, arranged in columns.

As discussed before, the basis of DTI is the assumption of a Gaussian propagator $P(\mathbf{r}_0|\mathbf{r}', t)$ (Equation 2.26) describing molecular diffusion. An ellipsoidal shape representing the iso-probability surface of molecular diffusion can be associated to the tensor $\mathbf{D}_{\text{app}}$ by fixing the quadratic form in the exponent of $P(\mathbf{r}_0|\mathbf{r}', t)$:

$$\frac{(\mathbf{r}' - \mathbf{r}_0)^{\mathrm{T}} \mathbf{D}_{\text{app}}^{-1} (\mathbf{r}' - \mathbf{r}_0)}{4t} = 1, \tag{3.6}$$

which defines a surface of constant mean translational displacement of an ensemble of tagged particles diffusing from the centre of the voxel (at $\mathbf{r}_0$), at time t [79]. Changing to the principal frame of reference, the iso-probability surface can be written as

$$\left(\frac{x}{\sqrt{2\lambda_1 t}}\right)^2 + \left(\frac{y}{\sqrt{2\lambda_2 t}}\right)^2 + \left(\frac{z}{\sqrt{2\lambda_3 t}}\right)^2 = 1, \tag{3.7}$$

where $\mathbf{r} = \mathbf{V}^{\mathrm{T}}(\mathbf{r}' - \mathbf{r}_0)$. The main axes of the ellipsoid, are the root mean square displacements, $\sqrt{\langle x_i^2 \rangle} = \sqrt{2\lambda_i t}$, along the three principal directions in a time t [79] (Figure 3.2).

Examples of diffusion tensor ellipsoids are shown for an *in vivo* data set in Figure 3.2. In case of prolate diffusion, the tensor appears to be

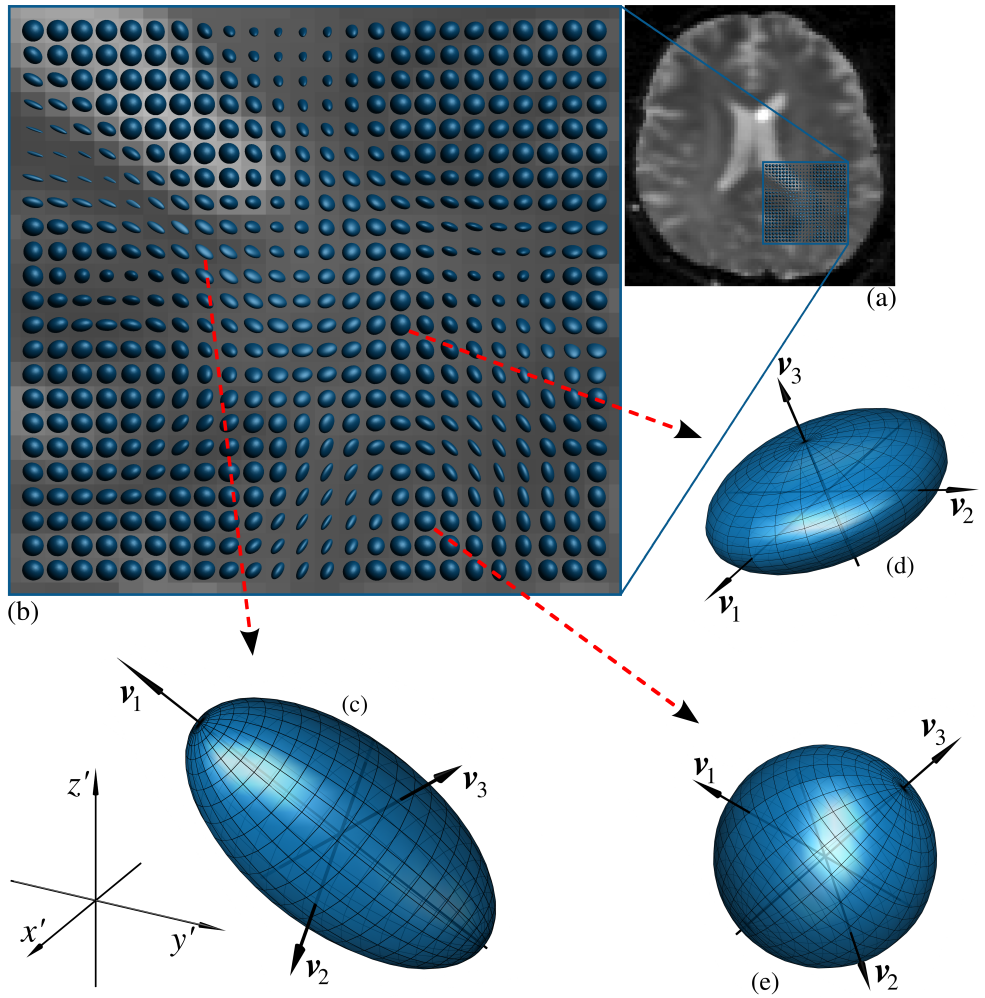


Figure 3.2: *(a) A non-DW image where the diffusion tensor field is plotted for a selected ROI, zoomed in (b). The cases of prolate (c), oblate (d) and isotropic (e) diffusion are shown for three selected voxels. The tensor field was produced with the help of the ExploreDTI toolkit [69].*

cigar-shaped (Figure 3.2(c)), where $\lambda_1 > \lambda_2 \approx \lambda_3$. It corresponds to the case of single ordered fibre bundles, such as the *corpus callosum* in WM (see Figure 2.9). The oblate diffusion tensor is represented by a disc-shaped surface (Figure 3.2(d)), where $\lambda_1 \approx \lambda_2 > \lambda_3$. This occurs in complex arrangements of fibre bundles in WM, such as crossing or merging fibres (see following discussion). Finally, the case of anisotropic diffusion is represented by a sphere (Figure 3.2(e)), where $\lambda_1 \approx \lambda_2 \approx \lambda_3$, corresponding to CSF and GM [58].

It is important to note that in the brain WM, the anisotropic behaviour of water diffusion in the macroscopic voxel length-scale is due to the microscopic arrangement of the tissue (Figure 2.9) [58, 79]. In particular, the eigenvector $\boldsymbol{v}_1$ associated to the largest eigenvalue (λ_1) can be related to the axis of the tissue fibre track in the voxel [79]. The local orientation provided by $\boldsymbol{v}_1$ has been used to connect coherently ordered fibre tracts trajectories along adjacent voxels. The mathematical procedures to accomplish this connection are known as *fibre tractography* or *fibre tracking*, which are used in the investigation of WM connectivity in the brain [1, 58, 71, 84]. A brief description of this technique will be given in Section 3.9.

3.2.4 Tensor scalar invariants

Besides the directional information, the diffusion tensor $\mathbf{D}_{\text{app}}$ provides rotationally invariant scalars related to different tissue proprieties [58,80].

One of the most important invariant scalars is the so-called mean diffusivity (MD), defined as the trace of the diffusion tensor divided by three

$$\text{MD} \equiv \frac{1}{3}\text{Tr}\left(\mathbf{D}_{\text{app}}\right) = \frac{1}{3}\left(\lambda_1 + \lambda_2 + \lambda_3\right) = \langle\lambda\rangle, \tag{3.8}$$

where $\text{Tr}\left(\dots\right)$ denotes the *trace* of the tensor. According to Equation 2.27, MD is a measure of the directionally averaged square displacement of diffusing molecules in the voxel [58]. MD appears to be fairly uniform in the healthy human brain and does not give a marked contrast between GM and WM [58, 85]. An example of MD in a healthy human brain in the axial plane is demonstrated in Figure 3.3(a).

In the case of prolate diffusion, one may also define the *axial* and *radial* diffusivities [2] (also known as *longitudinal* and *transversal*), as follows

$$\lambda_{\parallel} \equiv \lambda_1 \quad \text{and} \quad \lambda_{\perp} \equiv \frac{\lambda_2 + \lambda_3}{2}. \tag{3.9}$$

The most popular scalars characterizing the tensor anisotropy are the relative anisotropy (RA) and the fractional anisotropy (FA), defined as follows [80, 86]

$$\mathrm{RA} \equiv \frac{1}{\sqrt{3}} \frac{\sqrt{\left(\lambda_1 - \langle\lambda\rangle\right)^2 + \left(\lambda_2 - \langle\lambda\rangle\right)^2 + \left(\lambda_3 - \langle\lambda\rangle\right)^2}}{\langle\lambda\rangle} \tag{3.10}$$

and

$$\mathrm{FA} \equiv \sqrt{\frac{3}{2}} \frac{\sqrt{\left(\lambda_1 - \langle\lambda\rangle\right)^2 + \left(\lambda_2 - \langle\lambda\rangle\right)^2 + \left(\lambda_3 - \langle\lambda\rangle\right)^2}}{\sqrt{\lambda_1^2 + \lambda_2^2 + \lambda_3^2}}, \tag{3.11}$$

which are dimensionless parameters. In the case of isotropic diffusion ($\lambda_1 \approx \lambda_2 \approx \lambda_3$), both FA and RA equal zero. For a cylindrically symmetric system ($\lambda_1 \gg \lambda_2 \approx \lambda_3$), RA $\approx \sqrt{2/3}$ and FA ≈ 1 [80]. Among these two parameters, FA is more frequently used since it is less sensitive to the eigenvalue noise [87]. Examples of the RA and FA maps in the healthy human brain are depicted in Figures 3.3(b) and 3.3(c).

Apart from drawing a vector field, S. Pajevic et al. [88] have proposed to assign each video channel (**R**ed, **G**reen, **B**lue) to a component of the main eigenvector $\boldsymbol{v}_1$. Furthermore, in order to distinguish between the regions of high and low anisotropy, the FA has been used to modulate the brightness, according to

$$\mathrm{R} = |v_{1,x}|\,\mathrm{FA}, \quad \mathrm{G} = |v_{1,y}|\,\mathrm{FA}, \quad \mathrm{B} = |v_{1,z}|\,\mathrm{FA}, \tag{3.12}$$

where conventionally R, G and B are assigned to the directions perpendicular to the sagittal, coronal and axial 2D planes, respectively. An example of the colour-coded FA (CFA) is shown in Figure 3.3(d). Note that GM has low brightness indicating low FA. Therefore, orientations of $\boldsymbol{v}_1$ in GM become random and do not have a significant meaning.

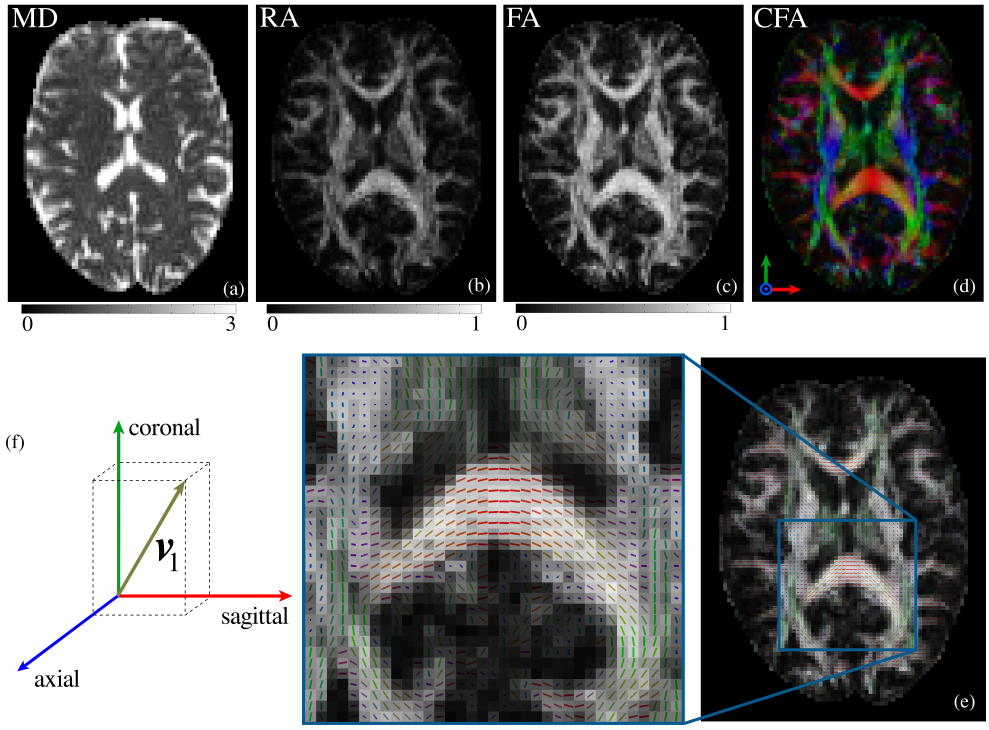


Figure 3.3: *Maps of MD (a), RA (b), FA (c), CFA (d) for a healthy human brain in a slice perpendicular to the axial direction. (e) The field of vectors* $\boldsymbol{v}_1$ *for the same slice overlaid to the FA map. Each line represents a vector whose colour is determined by the RGB combination defined in Equations 3.12, related to the directions perpendicular to the sagittal, coronal and axial 2D planes, respectively (f).*

3.2.5 Limitations of DTI

Although DTI has established itself as a valuable tool in brain research, it has some limitations. One limitation relates to the fact that it is valid only at low b-values, where the Gaussian assumption holds. However, as one increases the strength of the b-value, the Gaussian assumption is not valid any longer. In that case, the DW signal attenuation curve becomes non-mono-exponential [24, 25, 35, 75, 77] and cannot be adequately described by DTI, as schematically shown in Figure 3.1. As demonstrated by E.S. Hui et al. [83], the use of DTI to describe the DW signal at high b-values leads to a systematic bias in the DTI metrics.

Another limitation of DTI is related to its inability to differentiate complex patterns of fibre arrangements. While DTI can accurately

characterize the fibre direction and anisotropy in bundles of coherently aligned fibres, it fails in regions with complex fibre architecture such as "crossing fibres" and "merging fibres" [16, 89]. This is because DTI provides only one main diffusion direction ($\boldsymbol{v}_1$), since it is based on a 2$^{\text{nd}}$-rank tensor. Therefore, the main directions of two or more non-parallel fibre bundles remain undetermined, and the estimated FA values appear artificially reduced [65, 89].

3.3 The two-compartment model

The *biexponential* diffusion model has been proposed to describe the non-mono-exponential behaviour of the DW signal in the brain [25, 31, 32, 34, 75, 90]. In this model, the DW signal is assumed to originate from two non-exchanging water pools and represents the superposition of two mono-exponential functions [75]

$$\frac{S(b)}{S(0)} = f_{\text{f}} e^{-bD_{\text{f}}} + (1 - f_{\text{f}})\, e^{-bD_{\text{s}}}, \tag{3.13}$$

where D_{f} and D_{s} are the "fast" and "slow" diffusivities and f_{f} is the fraction of fast diffusing molecules. For the case of anisotropic diffusion, one needs to define the fast and slow diffusion tensors, $\mathbf{D}_{\text{f}}$ and $\mathbf{D}_{\text{s}}$. Consequently, the DW signal for a given gradient-encoding direction $\mathbf{u}$ is modelled as [25, 65]

$$\frac{S(\mathbf{u}, b)}{S(0)} = f_{\text{f}} e^{-b\mathbf{u}^{\text{T}}\mathbf{D}_{\text{f}}\mathbf{u}} + (1 - f_{\text{f}})\, e^{-b\mathbf{u}^{\text{T}}\mathbf{D}_{\text{s}}\mathbf{u}}. \tag{3.14}$$

Equations 3.13 and 3.14 have been shown to fit the DW signal in the brain tissue in the extended range of b-values (up to 7.0 ms μm^{-2}) with high accuracy. The most common interpretation of two water pools refers them to water in the intracellular space (ICS) and the extracellular space (ECS) [24, 32, 75]. In the ICS, diffusion would be more restricted, giving rise to the slow diffusion component, whereas the fast diffusion component would be dominated by water in the ECS. However, it should be noted that the relative volumes of the ICS and ECS known from histology appear in different proportions to the experimentally measured fractions of the fast and slow diffusion components. Nevertheless, the

model provides an instructive tool for the analysis of the DW MRI signal in the extended range of b-values. Other approaches consider, instead, bound and free water as the origin of the biexponential behaviour [3]. In Chapter 5, a comprehensive analysis on the use of the biexponential model to describe the DW signal in the human brain tissue is carried out.

3.4 The statistical approach

The ADC, as computed from the mono-exponential model, integrates the global properties of the tissue in a single parameter, D_{app}. Since biological tissues are complex in various microscopic length scales, a distribution of ADCs is expected in the macroscopic length scale. The *statistical model* introduced by D.A. Yablonskiy [39, 74] is a phenomenological model that takes into account the presence of variable length-scales for the restrictions and hindrances to the random displacement of water molecules and integrates them in a single expression for the DW signal.

In this model, the DW MRI signal is considered to be described by the sum of signals from a large number of individual spin packets from different positions in the voxel. The signal for a given gradient direction is written as [39]

$$\frac{S(b)}{S(0)} = \int_0^\infty p(D)\, e^{-bD} dD \tag{3.15}$$

where $p(D)$ is the distribution of diffusivities. The ADC, which is also related to the initial slope of the DW signal attenuation curve, is given by the *mean* of the distribution, i.e.

$$D_{\text{app}} = -\lim_{b\to 0} \frac{\partial S(b)}{\partial b} = \int_0^\infty D p(D)\, dD = \langle D \rangle. \tag{3.16}$$

The simplest realisation of such a distribution is given by a discrete sum of two exponentials. In this case, the signal behaves according to Equation 3.13.

3.4.1 Gaussian-like distribution

In complex biological tissue, the distribution $p(D)$ is expected to be a continuous function of D. Moreover, assuming a large number of "similar" ADCs in the voxel, the distribution $p(D)$ should have a peak and the tail should decay rather rapidly. In [39], the proposed distribution is a Gaussian function with a cut-off for the negative tail

$$p(D) = \begin{cases} A \exp\left(-\frac{(D-D_{\mathrm{G}})^2}{2\sigma^2}\right) & \text{for} \quad D > 0 \\ 0 & \text{for} \quad D < 0 \end{cases}, \tag{3.17}$$

where D_{G} and σ are the peak and the width of the distribution. In this case, the DW signal attenuation can be written as

$$\frac{S(b)}{S(0)} = \frac{1 + \mathrm{erf}\left(\frac{D_{\mathrm{G}}}{\sqrt{2}\sigma} - \frac{b^2\sigma^2}{2}\right)}{1 + \mathrm{erf}\left(\frac{D_{\mathrm{G}}}{\sqrt{2}\sigma}\right)} \exp\left(-bD_{\mathrm{G}} + \frac{b^2\sigma^2}{2}\right), \tag{3.18}$$

where $\mathrm{erf}(\dots)$ is the error function. In general, the ADC given by Equation 3.16 differs from the peak diffusivity D_{G}.

As an example, the Gaussian-type distribution defined in Equation 3.17 and the corresponding DW signal attenuations (Equation 3.18), for $D_{\mathrm{G}} = 1.0\ \mu\mathrm{m}^2\ \mathrm{ms}^{-1}$ and $\sigma = 0.1,\ 0.5$ and $1.0\ \mu\mathrm{m}^2\ \mathrm{ms}^{-1}$, are depicted in Figures 3.4(a) and 3.4(b), respectively. One can see that for a narrow distribution ($\sigma = 0.1$), the DW signal is close to the mono-exponential function. However, when the value of σ increases, the DW signal deviates from the mono-exponential behaviour.

It is important to note that in systems where the existence of spin packets with zero diffusivities is excluded, the condition $p(D) \to 0$ when $D \to 0$ must be true. In the case of defined distributions with a cut-off at $D = 0$, such as the one defined in Equation 3.17, this is obviously not satisfied. However, for narrow distributions ($\sigma \ll D_{\mathrm{G}}$), the approximation is valid. Alternatively, other functions such as the log-normal distribution can be used (See Chapter 7) [91].

3.4.2 Log-normal distribution

In order to avoid artificial truncations, the use of the log-normal distribution function [92–94], defined only for positive arguments, was proposed in Reference [91]. In this section the basics of this approach are discussed.

The log-normal distribution function is given by

$$p(D) = \frac{1}{D\sigma\sqrt{2\pi}} \exp\left(-\frac{[\ln D - \ln D_{\mathrm{LD}}]^2}{2\sigma^2}\right), \tag{3.19}$$

where $\ln D_{\mathrm{LD}}$ and σ are the *location* and *scale* parameters, respectively, related to the mean and the standard deviation of the distribution.

There is no analytical solution for Equation 3.15 for the log-normal distribution. However, a numerical approach can be used to estimate D_{LD} and σ from the experimental data.

As an example, the log-normal distribution and the corresponding DW signal attenuations (evaluated numerically using Equation 3.15), for $D_{\mathrm{LD}} = 1.0\ \mu\mathrm{m}^2\ \mathrm{ms}^{-1}$ and $\sigma = 0.1,\ 0.5$ and 1.0, are depicted in Figures 3.4(c) and 3.4(d), respectively. Again, as in the case of the Gaussian distribution, the DW signal is close to mono-exponential if the distribution is narrow ($\sigma = 0.1$). For larger σ, the DW signal becomes non-mono-exponential.

An application of the statistical model of diffusion based on the log-normal distribution in animal models of stroke [91] is discussed in detail in Chapter 7.

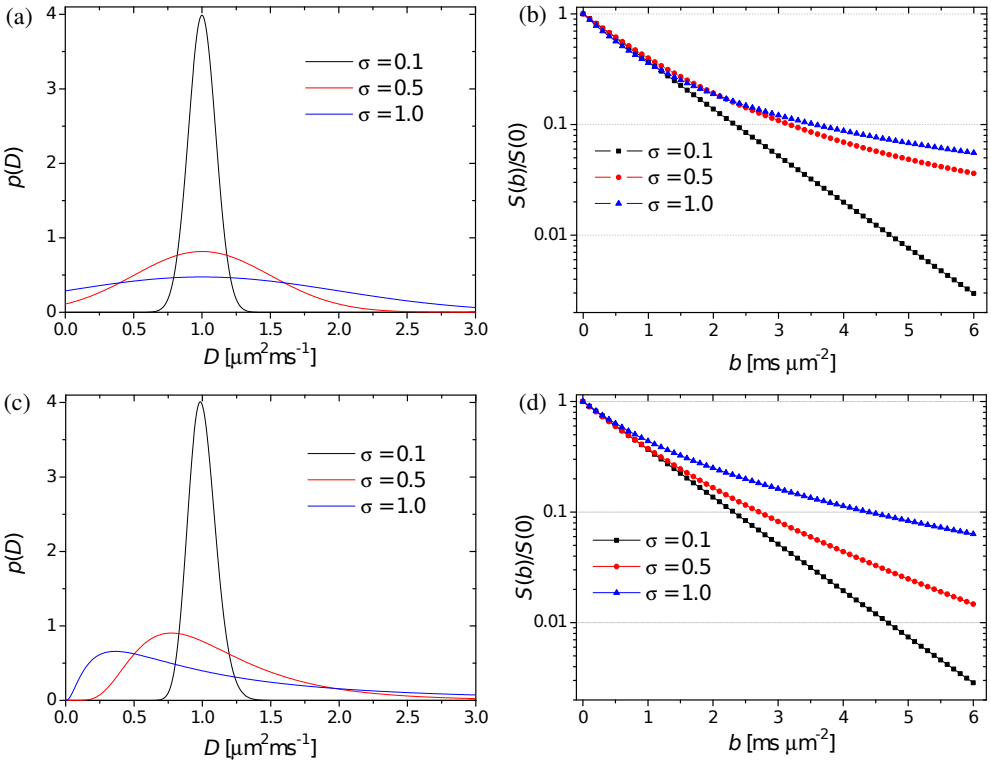


Figure 3.4: *The Gaussian-like distribution defined in Equation 3.17 (a) and the corresponding DW signal attenuations (Equation 3.18) for* $D_{\mathrm{G}} = 1.0$ $\mu\mathrm{m}^2$ ms^{-1} *and* $\sigma = 0.1$*, 0.5 and 1.0* $\mu\mathrm{m}^2$ ms^{-1} *(b). The log-normal distribution (Equation 3.19) (c) and the DW signal, calculated numerically according to Equation 3.15 for* $D_{\mathrm{LD}} = 1.0$ $\mu\mathrm{m}^2$ ms^{-1} *and* $\sigma = 0.1$*, 0.5 and 1.0 (d).*

3.5 Diffusion Kurtosis Imaging

The diffusion kurtosis imaging (DKI) approach was introduced by J.H. Jensen et al. in 2005 [36] as the simplest model-free extension of DTI allowing to quantify the deviations from the Gaussian diffusion profile. DKI is based on the cumulant expansion of the DW signal.

3.5.1 DW signal and the diffusion kurtosis

As explained in Section 2.5.2, the DW signal in the SPG approximation is the Fourier transform of the averaged diffusion propagator (Equation 2.33). The cumulant expansion of Equation 2.33 up to fourth order in q (in fact, the Taylor expansion of its natural logarithm around $q = 0$)

can be written, in the one-dimensional case, as [36]

$$\ln S(b) = \ln S(0) - bD_{\text{app}} + \frac{1}{6}b^2 D_{\text{app}}^2 K_{\text{app}} + \vartheta\left(b^3\right), \tag{3.20}$$

where b is given by Equation 2.38, D_{app} and K_{app} are, respectively, the ADC and the apparent diffusion kurtosis (ADK). D_{app} and K_{app} depend, in general, on the timing sequence parameters such as δ and Δ. In Equation 3.20, it is assumed that b is changed by varying the gradient strength, with the timing parameters being kept constant. In the SPG approximation ($\delta \to 0$), D_{app} and K_{app} are given by [36, 95]

$$\lim_{\delta\to 0} D_{\text{app}} = \frac{1}{2t_d}\langle\left(\mathbf{r}^{\mathrm{T}}\mathbf{u}\right)^2\rangle \tag{3.21}$$

and

$$\lim_{\delta\to 0} K_{\text{app}} = \frac{\langle\left(\mathbf{r}^{\mathrm{T}}\mathbf{u}\right)^4\rangle}{\langle\left(\mathbf{r}^{\mathrm{T}}\mathbf{u}\right)^2\rangle^2} - 3, \tag{3.22}$$

where $\mathbf{r}$ is the net displacement vector and $\mathbf{u}$ the unit vector along the gradient direction. In Equations 3.21 and 3.22, $\mathbf{r}^{\mathrm{T}}\mathbf{u}$ represents the particle displacement in the direction of the applied gradient $\mathbf{g}$. The averaged propagator, P, is given by Equation 2.32 and its moments are given by

$$\langle\left(\mathbf{r}^{\mathrm{T}}\mathbf{u}\right)^n\rangle = \int_V \left(\mathbf{r}^{\mathrm{T}}\mathbf{u}\right)^n P(\mathbf{r})\, d\mathbf{r}. \tag{3.23}$$

The diffusion kurtosis, also known as *excess kurtosis* or simply *kurtosis* [96] is a measure of the "sharpness" of the distribution [95]. When P is Gaussian, the kurtosis equals zero. If P has less weight on its centre and tails compared to a Gaussian with the same variance, then K_{app} is negative. If P has more weight on its centre and tails, then K_{app} is positive. The general lower bound is -2 [95, 96].

It is worth noting that a truncation of the expansion in Equation 3.20 up to first order in b (second order in q) reduces to the well-known mono-exponential approach (Equation 3.1) for the case of the Gaussian diffusion propagator. As proposed by Jensen et al. neglecting the third and higher order terms in Equation 3.20, the DW signal attenuation can be approximated by

$$\ln S(b) \approx \ln S(0) - bD_{\text{app}} + \frac{1}{6}b^2 D_{\text{app}}^2 K_{\text{app}}, \tag{3.24}$$

and both D_{app} and K_{app} can be estimated in a given gradient direction by measuring $S(b)$ using at least three b-values. Thus, the cumulant expansion allows one to approximate the DW signal when it deviates from the mono-exponential behaviour. The parameter K_{app} quantifies the degree of such deviations.

Figure 3.5(a) shows three examples of distributions with identical second moment but different kurtosis values. The corresponding DW signal attenuations are demonstrated in Figure 3.5(b). Clearly, for the Gaussian distribution the corresponding DW signal attenuation is mono-exponential (black curves). The cases of positive and negative kurtosis, lead to convex and concave DW signal attenuations, respectively. However, the DW signal attenuation is expected to be concave for biological tissue, which means that the lower bound is zero.

In order to obtain an accurate estimation of D_{app} and K_{app}, it is necessary to carefully choose the range of b-values. Due to the truncation of the term $\vartheta(b^3)$, Equation 3.24 predicts an increase of the signal for b-values larger than b_{max}, given by [95]

$$b_{\text{max}} = \frac{3}{D_{\text{app}} K_{\text{app}}}. \tag{3.25}$$

Since the signal attenuation in the brain and other biological tissues is expected to be monotonically decreasing [95], the upper boundary for fitting the DW signal using Equation 3.24 is given by b_{max}. As a rough estimation, typical reported average values in the brain are $D_{\text{app}} \approx 1.0\ \mu\text{m}^2\ \text{ms}^{-1}$and $K_{\text{app}} \approx 1.0$ [95], which leads to $b_{\text{max}} \approx 3.0\ \text{ms}\ \mu\text{m}^{-2}$. However, a more exact approach must take into account the dependence of such metrics on the gradient direction. A comprehensive investigation of this issue is carried out in Chapter 6.

3.5.2 Apparent Kurtosis Tensor

In general, D_{app} and K_{app} will depend on the gradient-sensitizing direction $\mathbf{g} = g\mathbf{u}$. Just as the directional dependence of D_{app} is taken into account by the 2^{n}-rank apparent diffusion tensor $\mathbf{D}_{\text{app}}$, the anisotropy

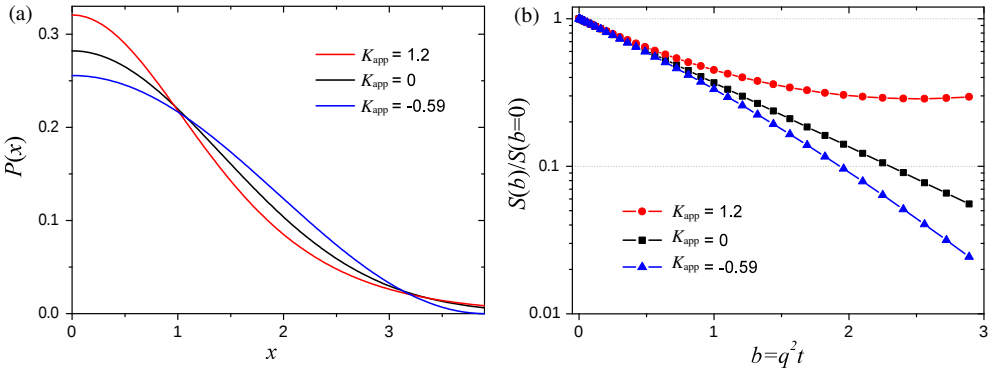


Figure 3.5: *(a) Example of three propagators in the one-dimensional case, with excess kurtosis equal 1.5 (red), i.e. having more weight on its centre and tails; 0 (black), i.e. Gaussian; and -0.59 (blue), i.e. having less weight on its centre and tails. The second moment of all three distributions (Equation 2.27), was taken to be equal 2. (b) The corresponding DW signal attenuation curves estimated according to Equation 3.24.*

of K_{app} is taken into account by the 4$^{\text{th}}$-rank apparent kurtosis tensor $\mathbf{K}_{\text{app}}$ [95]. In this case, the DW signal attenuation is approximated by

$$\ln S(\mathbf{u}, b) \approx \ln S(0) - b \sum_{i=1}^{3}\sum_{j=1}^{3} u_i u_j D_{ij}^{\text{app}} + \frac{b^2}{6}\left(\frac{1}{3}\sum_{i=1}^{3} D_{ii}^{\text{app}}\right)^2 \sum_{i=1}^{3}\sum_{j=1}^{3}\sum_{k=1}^{3}\sum_{l=1}^{3} u_i u_j u_k u_l K_{ijkl}^{\text{app}}, \tag{3.26}$$

where u_i are the components of the unit vector $\mathbf{u}$ and D_{ij}^{app} and K_{ijkl}^{app} are the elements of the apparent diffusion and kurtosis tensors, respectively. The components of the kurtosis tensor are given by [36]

$$\lim_{\delta \to 0} K_{ijkl}^{\text{app}} = \frac{9}{\langle \mathbf{r}^{\text{T}}\mathbf{r}\rangle^2}\left(\langle r_i r_j r_k r_l\rangle - \langle r_i r_j\rangle\langle r_k r_l\rangle - \langle r_i r_k\rangle\langle r_j r_l\rangle - \langle r_i r_l\rangle\langle r_j r_k\rangle\right), \tag{3.27}$$

where r_i $(i = 1, 2, 3)$ indicate the components of the net particle displacement vector $\mathbf{r}$. The diffusion kurtosis tensor has a rank of 4 and therefore 81 elements. However, because it is fully symmetric with respect to the indices permutation, only 15 are independent.

The apparent kurtosis for a given gradient direction can be written as follows

$$K_{\text{app}} = \frac{(MD)^2}{D_{\text{app}}^2} \sum_{i=1}^{3}\sum_{j=1}^{3}\sum_{k=1}^{3}\sum_{l=1}^{3} u_i u_j u_k u_l K_{ijkl}^{\text{app}}, \tag{3.28}$$

where MD is the mean diffusivity (Equation 3.8). Therefore, the elements of the apparent kurtosis tensor can be evaluated by measuring the apparent diffusivity, D_{app}, and kurtosis, K_{app}, using Equation 3.24 for $N \geq 15$ gradient directions and solving the set of N equations, each one defined by Equation 3.28. Due to the presence of background noise, it is desirable to estimate D_{app} and K_{app} for more than 15 gradient directions.

3.5.3 Kurtosis tensor scalars

Due to the mathematical complexity of the 4^{th}-rank kurtosis tensor, eigenvalues and eigenvectors are yet to be explored in terms of their physical relevance to the diffusion processes [97, 98]. However, it is intuitive to transform the kurtosis tensor from the laboratory frame of reference to the frame where the diffusion tensor is diagonal [37], as following

$$\hat{K}_{ijkl}^{\text{app}} = \sum_{i'=1}^{3}\sum_{j'=1}^{3}\sum_{k'=1}^{3}\sum_{l'=1}^{3} v_{i'i} v_{j'j} v_{k'k} v_{l'l} K_{i'j'k'l'}^{\text{app}}, \tag{3.29}$$

where $\boldsymbol{v}_i$ $(i = 1, 2, 3)$ are the eigenvectors of the diffusion tensor (See Equation 3.5).

Thus, the *axial kurtosis*, i.e. the ADK along the eigenvector associated to the main eigenvalue of the diffusion tensor, $\boldsymbol{v}_1$, is given by [37, 95]

$$K_{\parallel} \equiv K_{\text{app}}(\boldsymbol{v}_1) = \frac{MD^2}{\lambda_1^2} \hat{K}_{1111}^{\text{app}}. \tag{3.30}$$

The *transversal kurtosis*, by analogy with Equations 3.9, is defined as the average of the ADK in the plane perpendicular to $\boldsymbol{v}_1$, i.e.

$$K_{\perp} = \frac{1}{2\pi} \int_{\Omega} K_{\text{app}}(\mathbf{u})\, \delta\left(\mathbf{u}^{\text{T}} \boldsymbol{v}_1\right) d\Omega, \tag{3.31}$$

where the integral is done over the sphere Ω and $\mathbf{u} = \mathbf{u}(\theta, \phi)$ represents a unit vector. Similarly, the *mean kurtosis* is defined as the average of the ADK over the unit sphere, i.e.

$$MK = \frac{1}{4\pi} \int_{\Omega} K_{\text{app}}(\mathbf{u})\, d\Omega. \tag{3.32}$$

However, a good approximation for MK is simply given by the arithmetic average of the individual K_{app} for all gradient directions [37], i.e. $MK \approx \sum_{i=1}^{N} (K_{\text{app}})_i$.

A general definition for the anisotropy of the kurtosis tensor was proposed by D.H.J. Poot et al. in [99]. It is called *kurtosis anisotropy* (KA) and is defined as follows

$$KA = \sqrt{\frac{1}{4\pi} \int_{\Omega} \left(K_{\text{app}}(\mathbf{u}) - MK\right)^2 d\Omega}. \tag{3.33}$$

A comparison of the rotationally invariant parameters from DTI and DKI is demonstrated in Figure 3.6 for an axial slice in the human brain. In the first row the mean (a), axial (b) and radial (c) diffusivities and fractional anisotropy (d) from DTI are shown. In the second row the mean (a), axial (b) and radial (c) kurtoses and kurtosis anisotropy (d) from DKI are depicted. Parameters from GM are clearly isotropic. On the other hand, WM shows higher anisotropy. In the directions parallel to the fibre bundles, the restrictions are lower, leading to high diffusivity and low kurtosis values (Figures 3.6(b) and 3.6(f), respectively). In the directions perpendicular to the fibres, where the restrictions are higher, the diffusivity is reduced while the kurtosis is drastically increased (Figures 3.6(c) and 3.6(g), respectively).

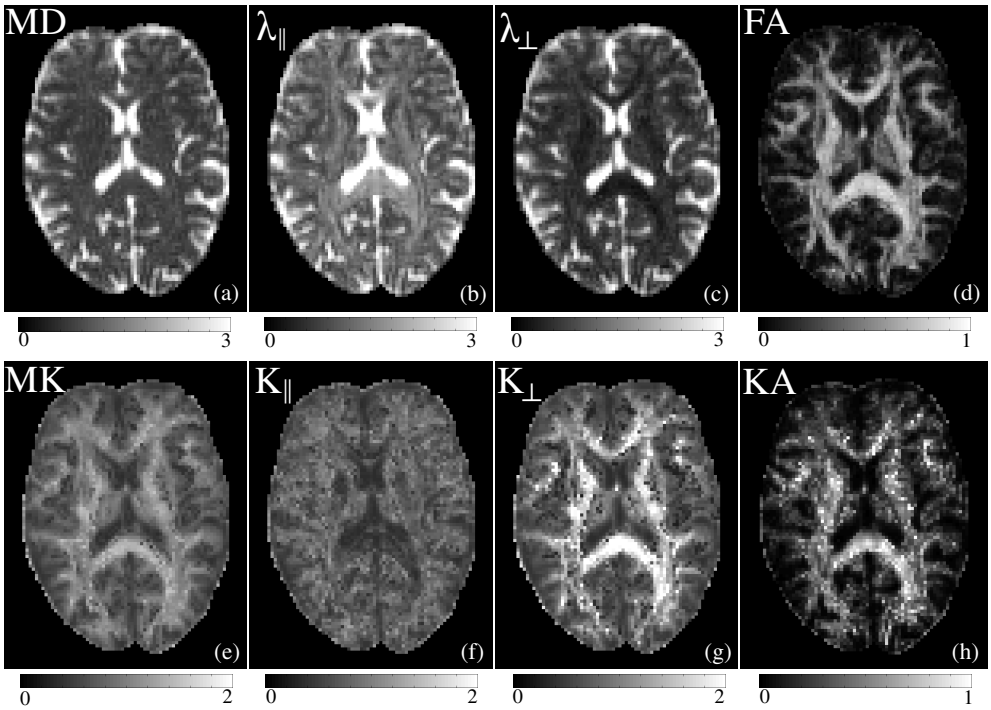


Figure 3.6: *Comparison of DTI (first row) and DKI (second row) tensors invariants from a single axial slice. First row: mean (a), axial (b) and radial (c) diffusivities, and FA (d). Second row: mean (e), axial (f) and radial (g) kurtoses, and kurtosis anisotropy (h). The data was acquired at 3T using 30 gradient encoding directions and b-values 0, 1.0 and 2.8* ms μm^{-2}*. The maps were produced using the toolkit ExploreDTI [69].*

3.6 High angular resolution diffusion imaging

In Section 3.2, the direction of preferred diffusion in single fibre bundles was identified with the eigenvector linked to the largest eigenvalue of the diffusion tensor. However, the DTI method is not capable of resolving multiple fibre orientations since the 2$^{\text{nd}}$-rank diffusion tensor possesses only a single orientational maximum. The use of high angular resolution for the diffusion gradient directions was proposed in several works [16, 100–102]. This experimental setup enables one to detect diffusion signals with multiple discrete maxima, associated to the presence of multiple underlying fibre populations. The use of large amount of gradient directions with high angular resolution is known as high angular

resolution diffusion imaging (HARDI).

The main idea is to sample the sphere in a discrete manner with a set of gradient directions $\mathbf{g}(\theta, \phi)$. Without an *a priori* knowledge of the heterogeneity of the angular signal distribution, one must sample the unit sphere uniformly. One of the most successful approaches to generate a set of N homogeneously distributed gradient directions was developed by D.K. Jones et al. [103]. It is based on the minimization of the electrostatic repulsive forces between every possible pair of charges, i.e. points in the sphere representing a gradient direction.

Another interesting geometrical approach for gradient direction generation called DISCOBALL (DIrection Scheme Obtained By ALigning points on Latitudes) was proposed by R. Stirnberg [104]. This approach provides a similar homogeneity while drastically reducing the computation time compared to the approach by Jones.

Several methods/models for HARDI data analysis have been proposed [16–18, 20, 105, 106]. In the following sections, two methods for HARDI data analysis are described, namely, the spherical deconvolution (SD) [18] and q-ball imaging (QBI) [17].

3.7 Spherical deconvolution

The SD [18], and, later the constrained spherical deconvolution (CSD) [105] methods, were proposed to directly estimate the distribution of fibre orientations in a single voxel from HARDI data by J.-D. Tournier.

The main assumptions of the SD method are [18]

- The DW signal from different fibre bundles is assumed to add independently in the total DW signal;
- for curved fibres, the radius of curvature is less than the typical distance travelled by the molecules in the time-course of a DW experiment (typically a few tens of micrometers);
- the DW signal attenuation from a single coherently aligned fibre population can be represented by an axially symmetric response function $S(\theta)$, θ being the elevation angle from the actual fibre direction.

Under these assumptions, the total DW signal $S(\theta, \phi)$ from a voxel containing N fibres, is given by the sum of the response function from each fibre bundle, weighted by the corresponding volume fraction f_i and rotated such that they are aligned along their respective orientations. It can therefore be written as follows

$$S(\theta, \phi) = \sum_{i=1}^{N} f_i \hat{A}(\theta_i, \phi_i) R(\theta), \tag{3.34}$$

where $\hat{A}(\theta_i, \phi_i)$ represents the rotation operator onto the direction (θ_i, ϕ_i). In the SD method, the signal $S(\theta, \phi)$ is expressed as the convolution over the unit sphere of the response function $R(\theta)$ with the so-called fibre orientation distribution (FOD) function, as follows

$$S(\theta, \phi) = F(\theta, \phi) \otimes R(\theta). \tag{3.35}$$

The FOD, $F(\theta, \phi)$, contains information about the fraction of fibres aligned with a given direction. In a HARDI experiment, the DW signal attenuation, $S(\theta, \phi)$, is sampled along a large number of directions. If the response function, $R(\theta)$, is known, then the FOD can be evaluated by performing a spherical deconvolution.

For further details regarding the numerical implementation of the SD method, the reader is referred to References [18, 105].

3.8 Orientation density function

In the context of the q-space formalism, the DW MRI signal $S(\mathbf{q})$ (the time dependence is omitted in this section) from a Stejskal-Tanner sequence in the SPG approximation, is the Fourier transform of the averaged diffusion propagator $P(\mathbf{r})$ with respect to the diffusion wave vector $\mathbf{q}$ (Equation 2.34). In the q-space imaging (QSI) technique, a direct reconstruction of $P(\mathbf{r})$ is achieved by applying an inverse Fourier transformation of the 3-dimensional Cartesian lattice in q-space [55]. However, reconstruction of the diffusion propagator *in vivo* is not always possible since it demands high field gradient strengths and on the other hand the phase of the signal is often corrupted by biological motion.

While $P(\mathbf{r})$ provides all information about tissue micro-architecture, information about the orientational structure of the tissue is well described by the so-called diffusion orientation density function (ODF) [17, 58, 65], which is defined as follows [17]

$$\Psi(\hat{\mathbf{r}}) = \frac{1}{Z}\int_0^\infty P(r\hat{\mathbf{r}})\,dr \tag{3.36}$$

where Z is a normalization constant.

In principle, the ODF can be directly derived from the diffusion propagator evaluated using the QSI technique. However, it requires an explicit calculation of the radial projection, Equation 3.36, and the mapping between Cartesian and spherical coordinates systems introduces artefacts in the ODFs [16]. Instead, it is more efficient to measure the DW signal in a spherical shell in the reciprocal q-space.

3.8.1 q-ball imaging

D.S. Tuch et al. [107] showed that, when the DW signal $S(q,\hat{\mathbf{q}})$ is acquired in a shell of radius q', then the ODF in a direction $\hat{\mathbf{r}}$ can be approximated by

$$\Psi(\hat{\mathbf{r}}) \approx \frac{1}{Z}\int S(q,\hat{\mathbf{q}})\,\delta\left(\mathbf{q}^{\mathrm{T}}\hat{\mathbf{r}}\right)\delta(q-q')\,d\mathbf{q} \equiv \frac{1}{Z}\Phi_{q'}\left[S(q,\hat{\mathbf{q}})\right], \tag{3.37}$$

where $d\mathbf{q} = q\;dq\;d\hat{\mathbf{q}}$ is the differential volume element and $\hat{\mathbf{q}}$ is the unit vector in the direction of $\mathbf{q}$. In Equation 3.37, $\Phi_{q'}[\dots]$ stands for the Funk-Radon transform (FRT) extended to the three-dimensional space [17] evaluated at the radius q'. Equation 3.37 tells in particular that the integration of the DW signal over an equator is related to the diffusion probability in a direction normal to the plane of the equator [17].

The exact FRT of the DW signal, shown later by D.S. Tuch et al. [17], gives the radial projection of the diffusion propagator along a Bessel beam with the width defined by the zeroth-order Bessel function J_0 [17]. In that case, the FRT is given by

$$\Phi_{q'}\left[S(q,\hat{\mathbf{q}})\right] = 2\pi q'\int P(\rho,\theta,\phi)J_0(2\pi q'\rho)\,\rho d\rho\;d\theta\;dz, \tag{3.38}$$

where (ρ, θ, ϕ) denote the cylindrical coordinates with the z-axis taken along the direction of interest, $\hat{\mathbf{r}}$. Note that in the case of $J_0(\rho) \to \delta(\rho)$, Equation 3.36 is recovered [17].

Since the maxima of the ODFs are usually overlaid to a large baseline, a rescaling of $\Psi(\hat{\mathbf{r}})$ is usually performed for visualization purposes [17,65], according to

$$\Psi'(\hat{\mathbf{r}}) \equiv \frac{\Psi(\hat{\mathbf{r}}) - \min \Psi(\hat{\mathbf{r}})}{\max \Psi(\hat{\mathbf{r}}) - \min \Psi(\hat{\mathbf{r}})}. \tag{3.39}$$

This re-scaling is known as *min - max* normalization.

For a detailed discussion on the accuracy of the QBI method the reader is referred to Reference [108]. A detailed description of the algorithm for QBI reconstruction can be found in Reference [17].

3.9 Fibre tractography

As discussed in Section 3.2, the measured diffusion anisotropy reflects the presence of spatially oriented microstructures as schematically depicted in Figure 2.9. Taking advantage of the spatial and orientational information provided by this anisotropic behaviour of water diffusion, the fibre pathways and consequently the anatomical brain connectivity can be reconstructed [71,109]. Such *in vivo* reconstruction of the brain architecture based on the DW MRI technique is known as *fibre tractography* or *fibre tracking* [71,84,110,111].

All methods for fibre tracking involve two main steps: a) biophysical interpretation of DW MRI data in terms of local fibre orientation and b) solution to a mathematical problem of combining the fibre direction between voxels in a representation of long-ranged fibre bundles.

In the so-called *diffusion tensor tractography* [71], the eigenvector associated to the largest eigenvalue $\boldsymbol{v}_1$ of the diffusion tensor is assumed to be aligned with the fibre bundle. Moreover, only the orientation and not the direction of $\boldsymbol{v}_1$ is relevant since diffusion is symmetric. The process of connecting consecutive voxels showing coherent alignment of $\boldsymbol{v}_1$ is repeated until certain stopping criteria are met. For instance, the tracking process stops when the anisotropy is less than a fixed threshold (usually

$FA \leq 0.15$). Other termination criteria are related to the maximum fibre curvature, and fibre length [71].

Due to the inability of the 2^{nd}-rank diffusion tensor to predict more than one fibre population in a single voxel (see Section 3.2.5), several approaches have been proposed to overcome this drawback, including multi-tensor and high-order tensor approaches [58]. Also, the CSD [18, 105] and QBI [17] methods have been largely used.

Regarding the second step in the process of fibre tracking, i.e. the problem of combining consecutive voxels, the first mathematical framework was proposed by P. Basser et al. [84]. In that work, a fibre tract is proposed to be represented by a 3D space curve parametrized by the arc length s of the trajectory. Under this approach the tract pathway $\mathbf{r}(s)$ is characterized by

$$\frac{d\mathbf{r}(s)}{ds} = \boldsymbol{v}_1(\mathbf{r}(s)). \tag{3.40}$$

This method is known as the *stream line* method.

For a detailed overview of different tracking algorithms the reader is referred to the following texts [69, 112–114].

3.10 Bias in the DWIs due to the background noise

3.10.1 The Rician Noise

After quadrature detection, the raw data in an MRI experiment are complex. The application of the inverse Fourier transform to obtain the voxel signal produces also a complex quantity. The voxel signal in the absence of noise is given by $S_0 = x_0 + iy_0 = m_0 \exp(i\varphi_0)$, where $\varphi_0 = \arctan(y_0/x_0)$ is the phase, $m_0 = \sqrt{x_0^2 + y_0^2}$ is the magnitude and x_0 and y_0 are the signals from the "real" and "imaginary" channels.

In practise, the real and imaginary signal are corrupted each one by an additive Gaussian noise. Assuming the noise distributions from each channel to be independent and identically distributed, the real and imaginary parts of the signal can be represented by the stochastic variables $X \sim N(x_0, \sigma)$ and $Y \sim N(y_0, \sigma)$ [115, 116], where $N(a, b)$ stands for a

Gaussian (normal) distribution with mean a and standard deviation b. Then, the joint distribution of these random variables remains Gaussian.

However, after the magnitude transformation described above, the distribution of the magnitude of the signal is not longer Gaussian, but Rician [115,117,118], described by the following probability density function

$$p\left(m; m_0, \sigma\right) = \frac{m}{\sigma^2} \exp\left(-\frac{m^2 + m_0^2}{2\sigma^2}\right) I_0\left(\frac{m m_0}{\sigma^2}\right), \tag{3.41}$$

where $I_0\left(\dots\right)$ is the zeroth order modified Bessel function and m_0 is the true magnitude signal. Note that Equation 3.41 is valid when signal is measured with a single receiver [116]. R.M. Henkelman [117] was the first to discuss this problem for a single receiver system in the context of MRI. The case of n receivers (e.g. n phased arrays) has been discussed by C.D. Constantinides [119], and the magnitude distribution is this case is given by the non-central chi distribution.

3.10.2 Background standard deviation

A special case of the Rician distribution is obtained in voxels where only noise is present, i.e. $m_0 = 0$. In this case, the magnitude distribution results in a Rayleigh distribution [118], described by the following probability density function

$$p\left(m; 0, \sigma\right) = \frac{m}{\sigma^2} \exp\left(-\frac{m^2}{2\sigma^2}\right). \tag{3.42}$$

This can be used to estimate the noise standard deviation σ from voxels where no true MRI signal is expected. The mean and the standard deviation of the Rayleigh distribution are given by $\sigma\sqrt{\pi/2}$ and $\left(2 - \pi/2\right)\sigma^2$, respectively [118], and can therefore be used to estimate σ. Another approach is based on the maximum likelihood (ML) estimator, proposed by J. Sijbers [120]. In this case, the noise standard deviation is estimated according to the following equation

$$\sigma^2 = \frac{1}{2N} \sum_{i=1}^{N} m_i^2, \tag{3.43}$$

where N and m_i are the number and magnitude of considered samples (voxels) in the background region.

Another approach for the estimation of the noise standard deviation is based on the histogram of the MR image. It is known that the MR image is characteristic of two strongly pronounced peaks one of which is related to the background voxels and the other to the voxels with the true MRI signal [121]. In the so-called *Brummer's histogram* approach [121, 122], the distribution of background voxels is fitted to the Rayleigh distribution (Equation 3.42).

3.10.3 Bias correction in the limit of high SNR

In the limit of high signal-to-noise ratio (SNR), i.e. $m_0 \gg \sigma$, Equation 3.41 can be approximated by the following distribution [118]

$$p\left(m; m_0, \sigma\right) \approx \frac{1}{\sigma\sqrt{2\pi}} \exp\left(-\frac{\left(m - \sqrt{m_0^2 + \sigma^2}\right)^2}{2\sigma^2}\right). \tag{3.44}$$

This means that for regions in the image where the signal intensity is large compared to the noise, the distribution is approximately Gaussian with mean $\sqrt{m_0^2 + \sigma^2}$ and variance σ [118]. Based on this approximation, H. Gudbjartsson and S. Patz [118] proposed the following post-processing correction scheme to reduce the bias in the magnitude image

$$m_c \equiv \sqrt{|m^2 - \sigma^2|}, \tag{3.45}$$

where m and m_c are the measured and corrected magnitudes, respectively.

3.10.4 The *power images* method

Another correction scheme has been proposed independently by A.J. Miller and P.M. Joseph [123] and G. McGibney and M.R. Smith [124], to perform quantitative analysis on low SNR images. This approach, known as the power images (PI) method, is based on the simple expression for the second moment of the Rician distribution [116]

$$\langle m^2 \rangle = m_0^2 + 2\sigma^2. \tag{3.46}$$

Thus, in the PI correction scheme [123, 124], the corrected magnitude is simply given by

$$m_c^2 = \langle m^2 \rangle - 2\sigma^2. \tag{3.47}$$

Other advanced correction schemes for noise estimation and bias reduction were proposed based on the assumption of spatially variable noise [122,125,126]. These approaches become useful when *parallel imaging* techniques are used, because in these cases the noise is known to be spatially dependent. Nonetheless, for simplicity, the PI method with ML estimation for the background noise standard deviation is used in the rest of this work.

3.11 Conclusions

In this chapter, the theoretical models for describing the DW signal in the brain tissue, used in the experimental part of this dissertation, were introduced. We have started with the DTI model, which is the most frequently used method in basic research and clinical applications. The physical assumptions of DTI were described and, based on that, the range of validity was discussed. It has been shown that DTI can accurately describe the DW signal in the low range of b-values. However it fails when the diffusion-weightings are strong, and a non-mono-exponential behaviour of the DW signal is observed.

Several approaches proposed in the literature to overcome the limitations of DTI were shortly described. The difference between models relies in that each one is intended to emphasize a given feature of interest. For instance, while the two-compartment model is intended to describe de DW signal at very high diffusion-weightings, the HARDI methods are developed to provide mostly directional information in anisotropic ordered structures.

Afterwards, the *fibre tractography* technique was shortly described and its basic principles were discussed.

Finally, some aspects related to the influence of the background noise in the analysis of the DW signal have been discussed. It was shown how the background noise leads to a bias in the DW signal. Consequently, some of the basic approaches for signal correction were introduced.

Chapter 4

Multi-section anisotropic fibre phantom for diffusion MRI

Parts of the work presented in this chapter have been published in:
E. Farrher, J. Kaffanke, A.A. Celik, T. Stöcker, F. Grinberg, and N.J. Shah. "Novel multisection design of anisotropic diffusion phantoms", Magnetic Resonance Imaging, Vol. 30, Nr. 4, p. 518–526, 2012.

4.1 Introduction

In order to enable better access to the sensitivity of the diffusion indices to the underlying microstructure in biological tissues, it is important to develop artificial model systems ("phantoms") that exhibit a well-known structure, on the one hand, but benefit from a reduced complexity on the other hand. Artificial phantoms have become an indispensable tool for the validation of DW MRI techniques as they show well defined microstructural properties and geometrical configurations.

In the first part of this chapter, the different materials and construction approaches used for hardware diffusion phantoms published in the literature are reviewed. Subsequently, a novel multi-section design for anisotropic diffusion phantoms made of polyethylene fibres is proposed. This novel design exhibits different geometrical configurations with various packing properties giving rise to various degrees of anisotropy, including rather high values, such as the typically observed in the WM tissue. In the experimental part of this chapter, the maps of fibre density (FD)

and conventional DTI parameters are discussed in correlation with the packing geometry. Thereafter, the application of the phantom to the investigation of the time-dependent diffusion behaviour for a wide range of FDs and observation times using a DW STE pulse sequence is shown. Finally, we demonstrate the performance of the QBI and CSD approaches for the analysis of HARDI data, applied to the different regions of our phantom for different values of SNR.

In the next Section, a comprehensive review of the phantoms published in the literature is presented. This review was done in order to select the optimal material for the construction of the phantom.

4.2 Review of existing anisotropic diffusion phantoms

Diffusion phantoms find a broad range of applications, including calibration of DW pulse sequences and gradient directions schemes [127], optimisation of tractography algorithms and models for HARDI data analysis [128–130], validation of theoretical diffusion models and numerical simulations [131] and data comparison in multi-centre studies [132–134]. In particular, justification of theoretical diffusion models requires phantoms with different fibre densities, since fibre packing density has a strong influence on the ADC [131,135,136]. Large homogeneous ROIs with well-defined diffusion parameters such as MD, FA, and principal fibre orientations are required for calibration purposes. Validation and optimisation of tractography algorithms rely on the existence of extended regions with different fibre configurations such as parallel, diverging, crossing at different angles, etc.

Anisotropic diffusion phantoms investigated in the literature can be classified into two groups according to the material used for the construction: biological phantoms, such as plants or excised tissue, and those made of artificial materials such as fibre glass, capillaries, polyethylene, among others.

Several plant tissues have been used as biological anisotropic test objects. To name some of them, asparagus stems have been used in the validation of pulse sequences and diffusion acquisition schemes [137–139];

celery petioles have been used to study the influence of susceptibility gradients [140, 141]; carrots were used for the study of cell permeability [142]; among others. The main disadvantages of plants in general relate to the low degree of anisotropy (for instance, FA ≈ 0.15 for asparagus [143]), biological degradation and the presence of air bubbles which are responsible of susceptibility artefacts.

Among the biological phantoms, excised nerve tissue such as spinal cord [144–147] and optic tracts [148] have been used as test objects for the validation of pulse sequences and fibre tracking algorithms. The main advantage of excised tissue phantoms is their similarity to the *in vivo* case. However biological phantoms suffer from degradation, lack of reproducibility and incomplete knowledge of structural details making them inappropriate for calibration purposes. For a more complete discussion, the reader is referred to Reference [143].

On the side of artificial anisotropic phantoms, several materials have been used, such as glass capillaries [148–151], hollow plastic fibres [152], polyamide fibres [153, 154], hemp [154], linen [154], rayon [130, 154, 155], polyester fibres [129, 155, 156] and polyethylene [127, 128].

We have tested two types of artificial fibres, namely, rayon and Dyneema®. However, rayon was shown to have much shorter echo-time compared to Dyneema®, which leads to lower SNR values. Therefore, the material used for the construction of the phantom described in this chapter was Dyneema® (Dyneema® SK75 dtex1760, DSM, Geleen, The Netherlands) which consist of microscopic fibre strands of polyethylene [127, 131].

4.3 Phantom construction

4.3.1 Characteristics of Dyneema fibres

The phantom was constructed using Dyneema® fibres (fibres strands of polyethylene with approximately 8 μm in radius according to specifications provided by the manufacturer). The fibre is chemically inert, hydrophobic and impermeable to water [143]. It has low surface relaxivity, that results in overall longer relaxation times [143] enabling diffusion

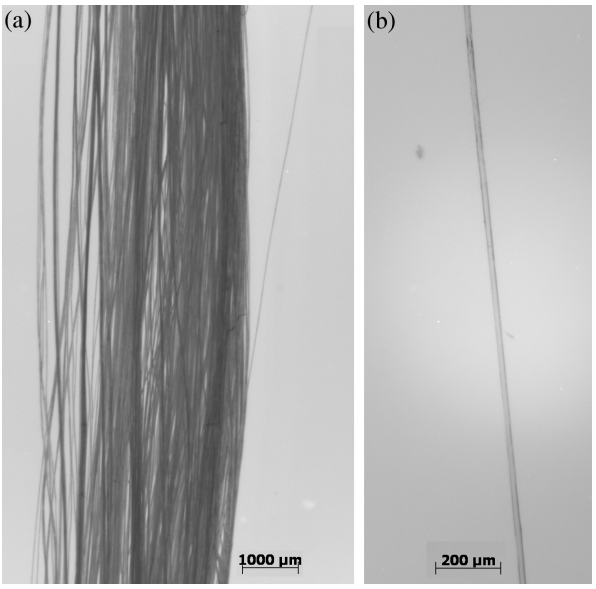


Figure 4.1: *Micrograph of a bundle of Dyneema® fibres (a) and a single fibre (b).*

measurements with higher SNR or longer echo times, which is especially important in the case of strong diffusion weightings and time-dependent studies. Flexibility is also an advantage compared to, for instance, rigid capillaries since it facilitates manufacturing of phantoms with a wide range of geometrical configurations. Another advantage of Dyneema® fibres is that they are available with fibre radii below 10 microns which makes them well suited for producing phantoms with sufficiently dense barriers to water diffusion, comparable to that of cellular structures. It is available in format of fibres bundles, each bundle containing approximately 700 fibres. Figure 4.1 shows a micrograph of a bundle of fibres (a) and a single fibre (b).

4.3.2 Platform and manufacturing process

The fibres were tightly wound around a Perspex support (Plexiglas®) in order to retain the geometrical shape of the different regions. A schematic representation of the Perspex platforms is shown in Figure 4.2.

Several layers of approximately the same amount of fibres were stacked in perpendicularly alternating directions in such a way that the resulting thickness of the cross-area was approximately 10 millimetres. Conse-

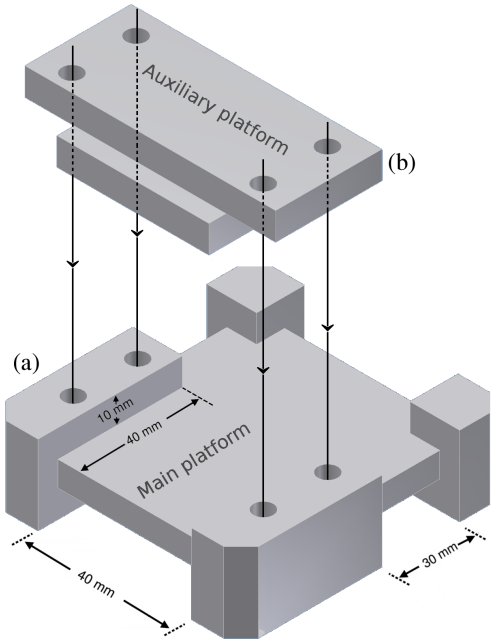


Figure 4.2: *The acrylic "main platform" where the fibres are wound (a), and the acrylic "auxiliary platform" needed to press the fibres in one of the phantom sides, in order to achieve the constant FD across this area (b).*

quently, after winding the fibres on the Plexiglas® support, the phantom contains two sides with one parallel- and one cross-fibre area each.

Figure 4.3(b) shows a schematic side-view representation of the phantom and its dimensions. The parallel-area on side 2 exhibits a gradient of FD, which is an intrinsic feature of the design of the phantom. On side 1, the FD gradient was intentionally suppressed by using an additional flat acrylic glass support (Figure 4.2(b)). The latter was screwed with the help of four plastic screws onto the main acrylic plate in such a way that a tight extended parallel-fibre region with a spatially homogeneous FD was obtained. The whole set-up was immersed in a cylindrical container made of acrylic glass (75 mm radius, 150 mm height). It was tightly fixed to the container in order to reduce unwanted vibrations caused by the application of magnetic field gradients during the measurements. The container was filled with distilled water which has a diffusivity of 2.2 μm^2 ms^{-1} at 23 °C [157].

Finally, the phantom was placed in a vacuum pump for four hours to remove remaining air bubbles and reduce undesirable effects due to

susceptibility differences. Since Dyneema® fibres are not hollow, water occupies the interstitial space between the fibres.

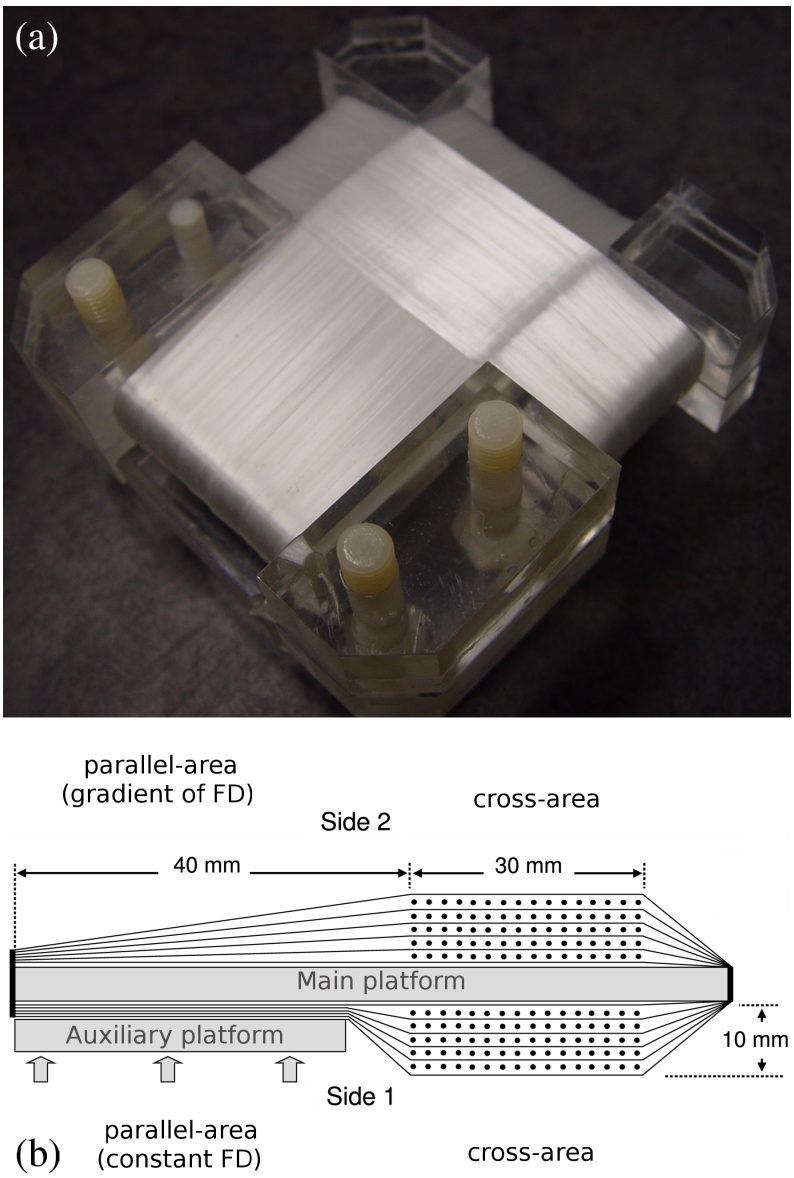


Figure 4.3: *Photograph of the multi-section fibre phantom (a) and a schematic side-view representation depicting the three geometrical characteristics: the parallel area with homogeneous FD, the parallel area with a gradient of FD and the crossing areas.*

4.4 MRI experiments

All MRI experiments were carried out in a whole-body 3T Siemens MAGNETOM Trio scanner (Siemens Medical Systems, Erlangen, Germany). The body coil was used for transmit in conjunction with a 12-channel phased-array receive head coil. Experiments were performed at approximately 23 °C. The gradient system provided a maximal gradient strength of 40 mT/m.

4.4.1 Proton density measurements

The phantom was positioned in such a way that the fibres in the parallel-areas were aligned along the main magnetic field. Proton density was evaluated using a spin-echo multi-contrast (SEMC) pulse sequence, provided by the manufacturer. Imaging parameters were: 32 contrasts with an inter-echo time spacing (ΔTE) of 6.8 ms; repetition time (TR), 2500 ms; number of averages, 2; bandwidth, 781 Hz/pixel; voxel size, 1.6×1.6×3 mm^3. The signal intensity, $S(\Delta TE)$, was assumed to attenuate exponentially (Equation 2.17). The relative proton density, S_r, was then evaluated with respect to a ROI in the bulk, and FD was calculated as $FD = 1 - S_r$.

4.4.2 Diffusion measurements

Time-dependent diffusion measurements

All time-dependent diffusion measurements were performed using a STE EPI pulse sequence programmed in-house and a SE EPI pulse sequence provided by the manufacturer. The STE sequence was developed in our laboratory in order to enable diffusion measurements in a wide range of observation times. Time-dependent diffusion behaviour was analysed for the parallel-area which exhibits a gradient of FD. Imaging parameters were: repetition and echo times, TR/TE = 3000/100 ms; number of averages, 24; receive bandwidth, 1410 Hz/pixel; voxel size, 2.2×2.2×3 mm^3; duration of the diffusion weighting gradient pulse, δ = 19.5 ms; time interval between the two gradient pulses, Δ, varied from 48 ms up to 1030 ms; number of gradient directions, 6; b-values, b = 0.05,

0.5, 1.0, 1.5, 2.0, 2.5, 3.0 ms μm^{-2}. The slice positioning was the same as used in the SEMC experiment with the purpose to correlate both results. In order to avoid unwanted background gradients [158, 159] due to susceptibility differences between the fibres and water, the phantom position was such that fibres in the parallel-areas were aligned with the main magnetic field.

Conventional DTI and HARDI measurements

The SE EPI pulse sequence was applied in order to demonstrate the applicability of the phantom for HARDI data analysis both in the parallel- as well as in the crossing-areas. Imaging parameters were: TR/TE = 2300/109 ms; receive bandwidth, 1445 Hz/pixel; voxel size, 2×2×2 mm^3; 14 slices; number of averages, 16; matrix size, 128×88; 64 gradient directions; b-values, 0 and 1.0 ms μm^{-2}. In these experiments, the phantom was positioned in such a way that all fibre strands formed an angle of 45° with respect to the main magnetic field. This was necessary in order to reduce the problem of the background gradients due to susceptibility differences in the cross-fibre areas [158, 159]. In contrast to the parallel-areas, the cross-fibre areas cannot be positioned with the predominant orientation of all fibres along the main magnetic field, since about one half of them would have a parallel and another half a perpendicular orientation to the field.

4.4.3 Data analysis

Signal diffusion attenuations were analysed for the parallel-area with the FD gradient. The curves exhibited deviations from the mono-exponential function for $b > 1.0$ms μm^{-2}. To quantify these deviations, the DKI model [36] was used to describe the measured signal attenuation, $S(b)$, according to the Equation 3.24. The fits of S_0, D_{app} and K_{app}, were applied to the attenuations in the whole range of b, for each of the six gradient directions. In the parallel-areas, only two gradient directions correspond to diffusion across the fibres, that is, lying in the plane perpendicular to the main fibre orientation. In the following, the average values of D_{app} and K_{app} in these directions will be denoted by $D_\perp$ and

$K_\perp$, respectively. Conventional DTI analysis (Chapter 3, Section 3.2) was also performed with the set of D_{app} from the six gradient directions, and the values of FA (Equation 3.11) were evaluated in dependence on the observation time, $t_{\text{d}} = (\Delta - \delta/3)$, and FD.

Analysis of the data from the SEMC was performed with the help of the in-house developed tool-kit QuanTooM. Diffusion experimental data were processed using in-house Matlab scripts (Matlab, The MathWorks, Natick, MA, USA). Bias in the DW images (DWIs) due to the background noise was corrected using the PI method [123, 124] while the ML estimator was used to assess the standard deviation of the background noise [120] (See Chapter 3, Section 3.10). Equation 3.24 was fitted to the diffusion signal attenuation for the whole range of b using the Nelder-Mead algorithm on a voxel-by-voxel basis and maps of FD, MD and FA were evaluated.

The normalized FOD in the case of CSD and the ODF in the case of QBI analysis were obtained using the toolkit ExploreDTI [69] according to Equations 3.35 and 3.37, respectively. Results from the both methods were generated using spherical harmonic order up to $l_{\max} = 8$. SNR estimation in the HARDI data analysis was carried out by taking the ratio of the signal from different ROIs in the non-DW image to the standard deviation of the background noise. Uncertainties in the estimated fibre orientation in the cross-area were characterized by the mean deviation angle, $\langle\alpha\rangle$, evaluated according to the following equation

$$\langle\alpha\rangle = \frac{1}{2\text{card}\{\text{ROI}_\perp\}} \sum_{k=1}^{2} \sum_{i \in ROI_\perp} |\cos^{-1}(\mathbf{m}_{k,i} \cdot \mathbf{x}_k)|, \tag{4.1}$$

where card$\{\text{ROI}_\perp\}$ stands for the number of voxels in $\text{ROI}_\perp$ (ROI in the cross-area containing 198 voxels), $\mathbf{m}_{k,i}$ is the unit vector pointing in the direction of the k-th maximum of the i-th FOD in the case of CSD or the ODF in the case of QBI and $\mathbf{x}_k$ is the unit vector pointing in the direction of the fibre population (Figure 4.7(b)).

Similarly, the mean deviation angles in the parallel-area, $\langle\beta\rangle$, were evaluated in three ROIs with different FDs, according to the following equation

$$\langle\beta\rangle = \frac{1}{\mathrm{card}\{\mathrm{ROI}_{\parallel}\}} \sum_{i \in ROI_{\perp}} |\cos^{-1}(\mathbf{m}_i \cdot \mathbf{x}_2)|, \tag{4.2}$$

where $\mathrm{ROI}_{\parallel}$ denotes the regions of interest selected in the parallel-area, each one containing 19 voxels, and $\mathbf{x}_2$ is the unit vector pointing in the direction of the fibre population (Figures 4.8(b) and 4.9(b)). The maxima of each FOD or ODF were evaluated with the help of the ExploreDTI toolkit [69].

4.5 Results

4.5.1 Fibre density and conventional DTI maps

Figure 4.4(a) shows the maps of FD from both sides of the phantom. Side 1 exhibits two areas of nearly homogeneous FD: the cross-area with FD $= 0.76 \pm 0.01$ and the parallel-area with FD $= 0.76 \pm 0.02$ (as averaged over the large homogeneous ROI of 198 voxels). Side 2 illustrates the crossing region with FD $= 0.77 \pm 0.01$, and the area with the gradient of FD along the x-axis. In this area, FD varies approximately in the range between 0.44 ± 0.01 and 0.65 ± 0.02 as demonstrated by the profile of FD along the x-direction in Figure 4.4(d) (depicted by the x-y frame). Each point in the profile was obtained by averaging over a strip of all voxels along the y-direction for given x (with the exception of 2 voxels at each edge of the strip to avoid partial volume affects, that is, over 19 voxels in total); the error bars correspond to the standard deviation. In particular, Figure 4.4(d) shows that FD is close to constant in the crossing region ($x < 28$ mm) but it tends to linearly increase with the distance in the parallel area ($x > 30$ mm). The part of the profile between 28 and 30 mm represents the transition region and might be affected by partial volume effects.

Figures 4.4(b) and 4.4(c) show the maps of MD and FA, respectively, for both sides of the phantom. The dependence of these two parameters on the distance x on side 2 is shown in Figures 4.4(e) and 4.4(f). One can see that both parameters remain approximately constant in the cross-areas of both phantom sides as well as in the parallel-area on side 1

(Figures 4.4(b) and 4.4(c)), but show a spatial dependence in the parallel-area of side 2 (see the profiles for $x > 30$).

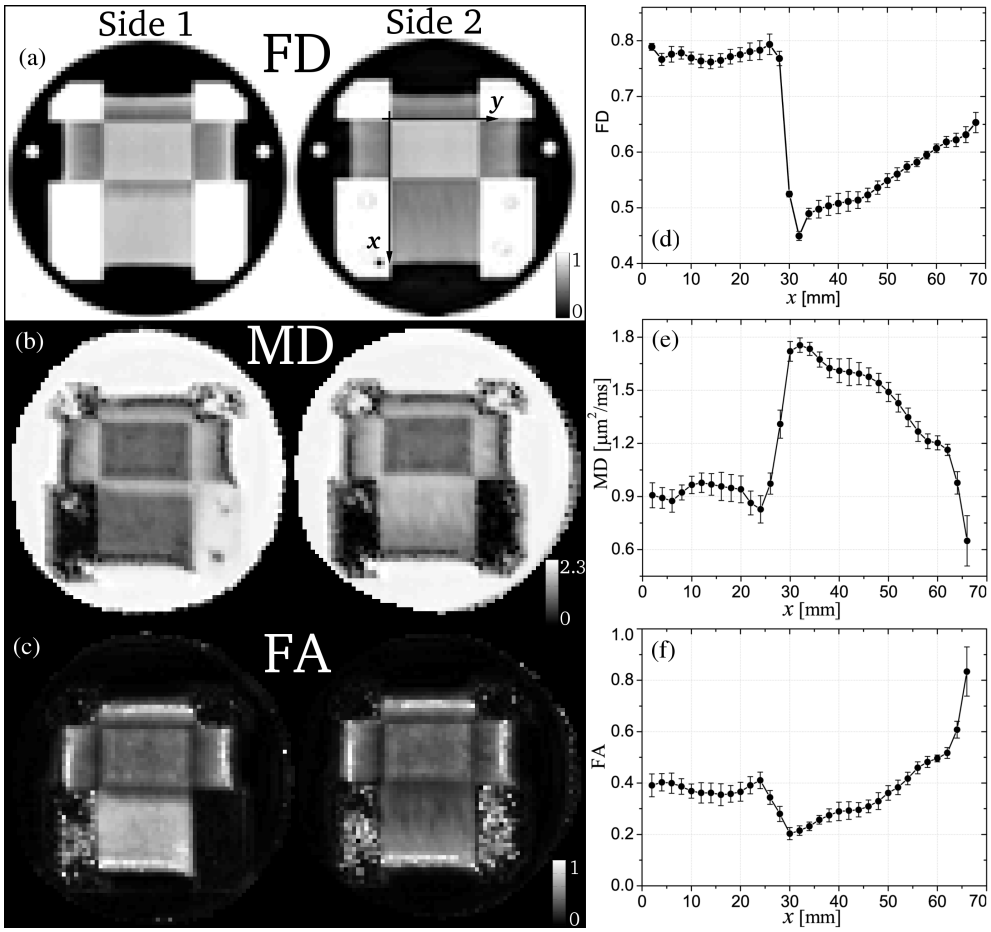


Figure 4.4: *Maps of (a) FD, (b) MD (in units of* μm^2 ms^{-1}*) and (c) FA. The maps on the left correspond to Side 1, the maps on the right to Side 2. The spatial profiles of (d) FD, (e) MD and (f).*

4.5.2 Time-dependent diffusion in the parallel-area

Figure 4.5 shows the DW signal attenuations for a gradient direction perpendicular to the fibres for two selected ROIs with FD ≈ 0.43 (black) and FD ≈ 0.59 (red). Diffusion times are $t_d = 42.3$ ms (a) and 1024 ms (b). The fits of the mono-exponential function (Equation 3.1) and the kurtosis function (Equation 3.24) are shown by the dotted and solid lines, respectively. The corresponding fitting parameters are provided in

Table 4.1.

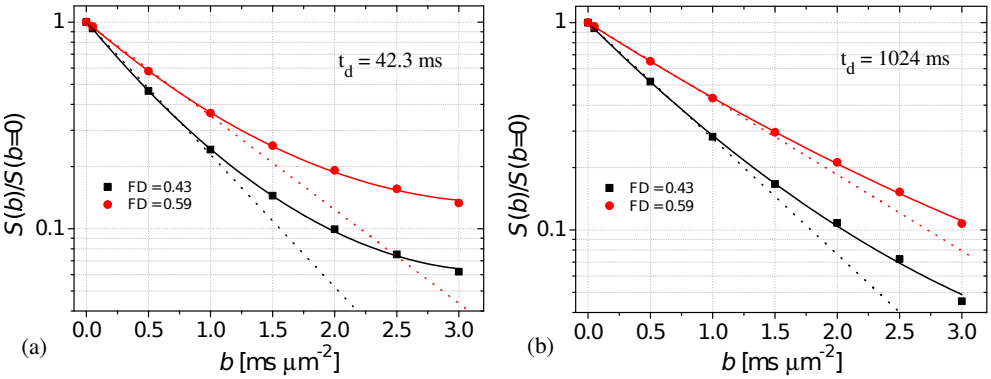


Figure 4.5: *DW signal attenuation in the parallel-area for a gradient direction perpendicular to the fibres, for* $t_{\mathrm{d}} = 42.3$ *ms (a) and* 1024 *ms (b) and* FD ≈ 0.43 *(black) and* 0.59 *(red). The fits of the mono-exponential and kurtosis functions are shown by the dotted and solid lines, respectively. The corresponding fitting parameters are provided in Table 4.1.*

	$t_{\mathrm{d}} = 42.3$ ms		$t_{\mathrm{d}} = 1024$ ms	
	FD ≈ 0.43	FD ≈ 0.59	FD ≈ 0.43	FD ≈ 0.59
$D_{\perp,\mathrm{m}}$ μm^2 ms^{-1}	1.48 ± 0.03	1.04 ± 0.02	1.25 ± 0.01	0.84 ± 0.01
$D_{\perp,\mathrm{k}}$ μm^2 ms^{-1}	1.67 ± 0.02	1.17 ± 0.01	1.37 ± 0.01	0.88 ± 0.01
$K_{\perp}$	0.53 ± 0.01	0.73 ± 0.01	0.39 ± 0.02	0.38 ± 0.02

Table 4.1: *The fitted parameters to the DW signal attenuations in Figure 4.5.* $D_{\perp,\mathrm{m}}$ *and* $D_{\perp,\mathrm{k}}$ *refer to the diffusivity from the mono-exponential (Equation 3.1) and kurtosis (Equation 3.24) methods, respectively, for a gradient direction perpendicular to the fibres.*

The 3D plot in Figure 4.6(a) shows the dependence of $D_{\perp}$ on t_{d} and FD. One can see that, for any value of t_{d}, $D_{\perp}$ decreases with increasing FD. In the short t_{d} regime, $D_{\perp}$ decreases rapidly with increasing t_{d}, but tends towards a plateau in the long time limit. On the other hand, the longitudinal eigenvalue of the diffusion tensor, $\lambda_{\parallel}$, shows practically no dependence on FD and t_{d} (Figure 4.6(c)). This is the expected behaviour since molecular diffusion along the fibres is free.

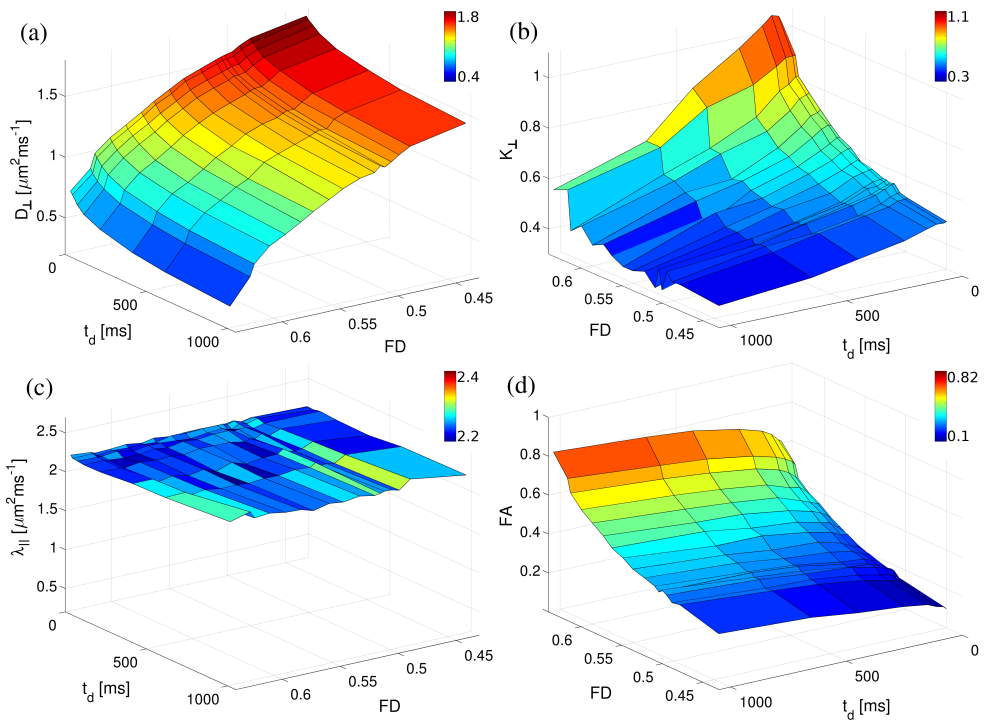


Figure 4.6: *Three-dimensional plots representing: a) $D_\perp$, b) $K_\perp$, c) $\lambda_\parallel$ and d) FA as a function of FD and the observation time. The investigated range of FD varied approximately between 0.44 ± 0.01 and 0.65 ± 0.01. The experimental values of t_d varied in the range of 42-1024 ms.*

Figure 4.6(b) shows the dependence of $K_\perp$ on both FD and t_d. Large values are observed for short observation times and high FDs. With increasing t_d and decreasing FD, $K_\perp$ strongly decreases. The dependence of FA on t_d and FD is depicted in Figure 4.6(d). FA appears to be strongly correlated with the packing density and increases by a factor of about 4 when FD increases from the lowest to the largest value studied. For any fixed FD values, the largest values of FA are observed for the long observation times.

4.5.3 CSD and QBI analysis of HARDI data

Figure 4.7(a) demonstrate the FOD from CSD (left column) and ODF from QBI (right column) for increasing values of SNR (from top to bottom), taken from a selected ROI in the cross-area (red rectangle in Figure 4.7(b)). In all cases, the surfaces are RGB colour-coded (left/right,

anterior/posterior, bottom/top). Different values of SNR were obtained by increasing the number of averages (1, 2, 4, 8 and 16), as indicated in the bottom-left corner. One can see that uncertainties in the evaluation of perpendicularly crossing fibres by both CSD and QBI are rather high for low SNR values (first three rows), but improve as SNR increases (last two rows). Figure 4.7(b) (bottom) shows a schematic representation of the deviation angles, α_k (k = 1,2), defined as the angle between the vectors, $\mathbf{m}_k$ ($k = 1, 2$), pointing the direction of the maxima of the FOD or ODF, and the vector in the direction of the actual fibre populations, $\mathbf{x}_k$. In Figure 4.7(c) the mean deviation angle, $\langle\alpha\rangle$, evaluated according to Equation 4.1, is shown as a function of the SNR. One can see that the fibre direction determined by the CSD method shows a lower mean deviation angle compared to the QBI method.

Figure 4.8(a) shows the FODs for increasing values of SNR (from top to bottom) in the parallel-area in side 2, for three ROIs (highlighted in 4.8(b)) with fibre densities FD ≈ 0.45 (left column), ≈ 0.57 (middle column) and ≈ 0.65 (right column). Again, one can see that uncertainties in estimated fibre directions reduce with increasing SNR. A schematic representation of the deviation angle, β, defined as the angle between the vector, $\mathbf{m}$, pointing the direction of the maxima of the FOD, and the vector in the direction of the actual fibre population $\mathbf{x}_2$ is shown in Figure 4.8(b) (bottom). The mean deviation angle, $\langle\beta\rangle$, evaluated according to Equation 4.2, is shown in Figure 4.8(c) for the three values of FD as a function of the SNR. One can see that $\langle\beta\rangle$ decreases with increasing SNR and increasing FD values.

An equivalent analysis for the performance of the QBI method in the parallel-area in side 2 is shown in Figure 4.9. Again, the mean deviation angle reduces for increasing values of SNR and FD. On the other hand, by comparing Figures 4.8(c) and 4.9(c), one can see that CSD performs better than QBI in the determination of fibre directions.

4.5.4 Streamline CSD-based fibre tractography

An example of a streamline fibre tractography of the phantom based on the CSD method is shown in Figure 4.10. It clearly demonstrates that CSD-based fibre tractography can resolve the single- and multi-fibre pop-

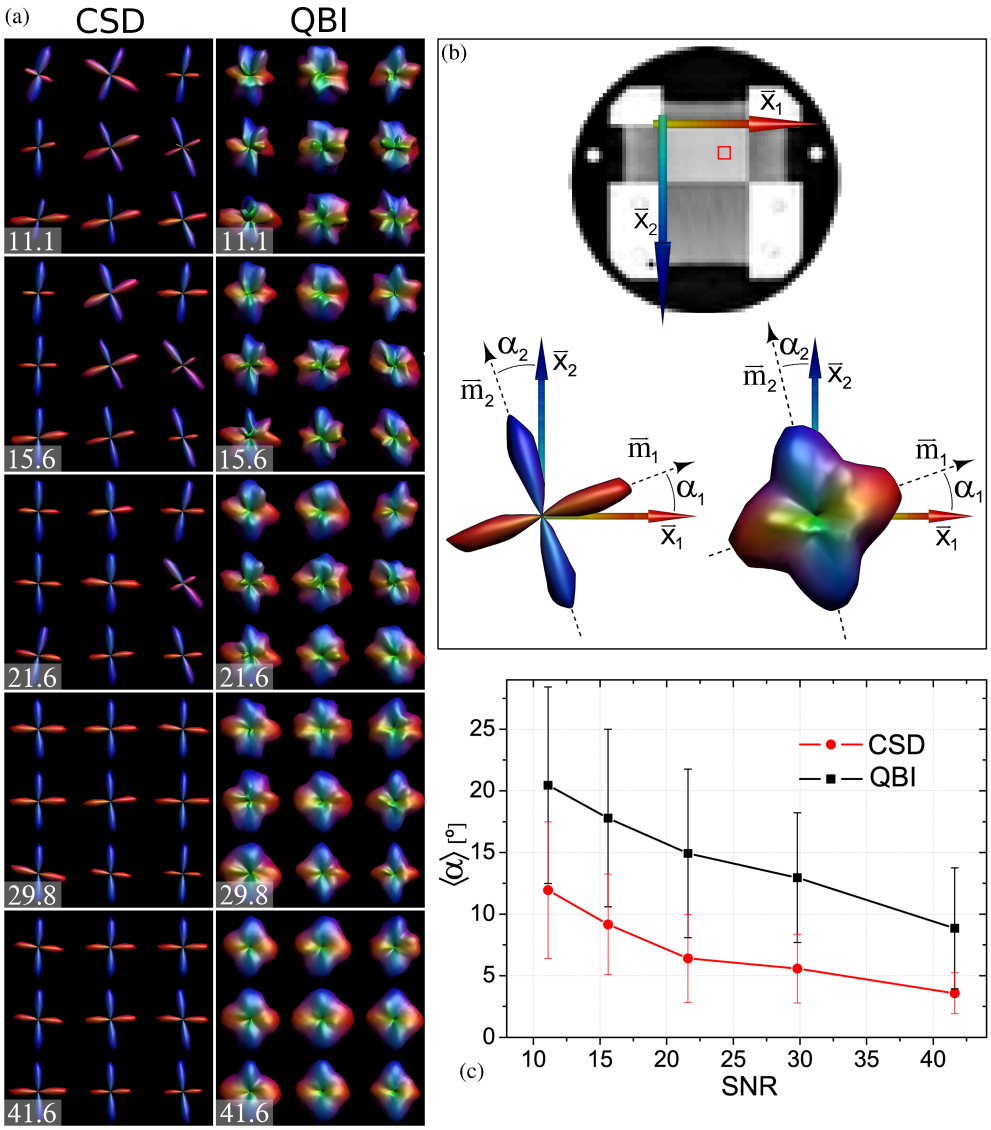


Figure 4.7: *(a) Performance of the CSD (left column) and QBI (right column) methods for increasing values of SNR (from top to bottom) demonstrated for a selected ROI in the cross-area (highlighted in (b) by the red rectangle in the cross-area). The SNRs are indicated on the bottom-left corner of the plots. (b) A schematic representation of the deviation angles, α_k ($k = 1, 2$). (c) The mean deviation angle, $\langle\alpha\rangle$, defined in Equation 4.1, as a function of the SNR.*

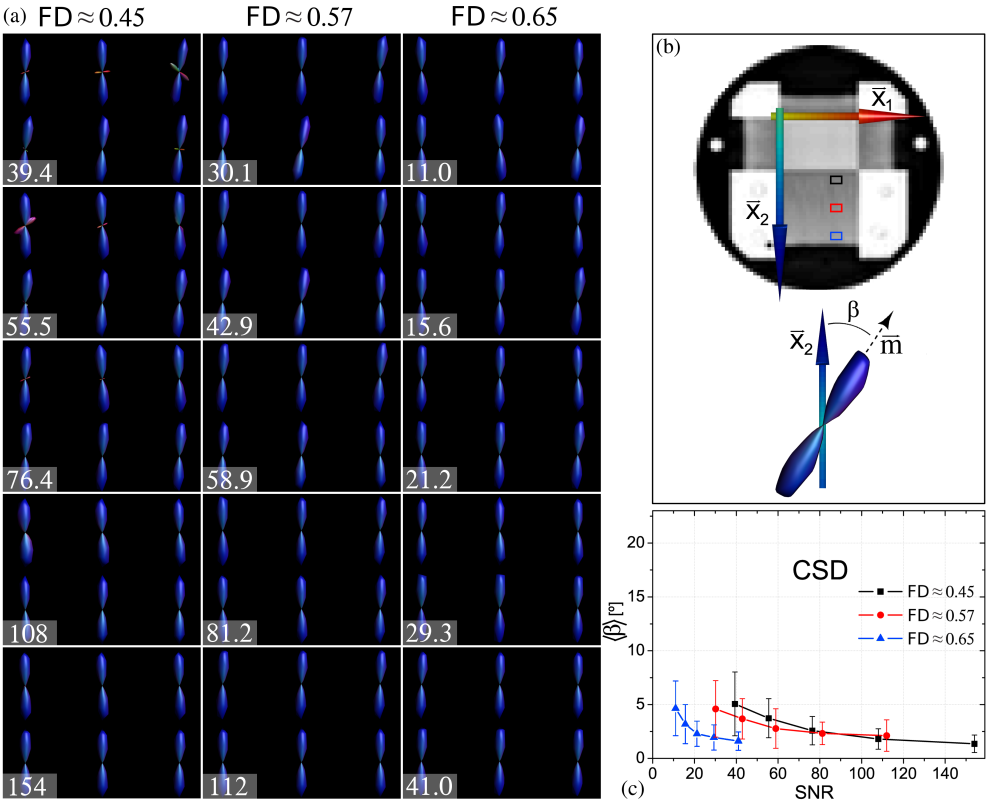


Figure 4.8: *(a) Performance of the CSD method for increasing values of SNR (from top to bottom) demonstrated for three selected ROIs (highlighted in (b)) with fibre densities* FD ≈ 0.45 *(left column),* ≈ 0.57 *(middle column) and* ≈ 0.65 *(right column). The SNRs are indicated on the bottom-left corner of the plots. (b) A schematic representation of the deviation angle,* β*. (c) The mean deviation angle* $\langle\beta\rangle$ *(Equation 4.2) as a function of the SNR for the three values of FD.*

ulations (see zoomed area of the crossing-fibres). The fibre discontinuities in the edges of the phantom are due to very low SNR and susceptibility artefacts.

4.6 Discussion

In this chapter, we have presented a novel multi-section design for diffusion phantoms which is useful for a broad range of applications. An important characteristic of the design of the phantom is the existence of three geometrical configurations with various properties, i.e. one area of

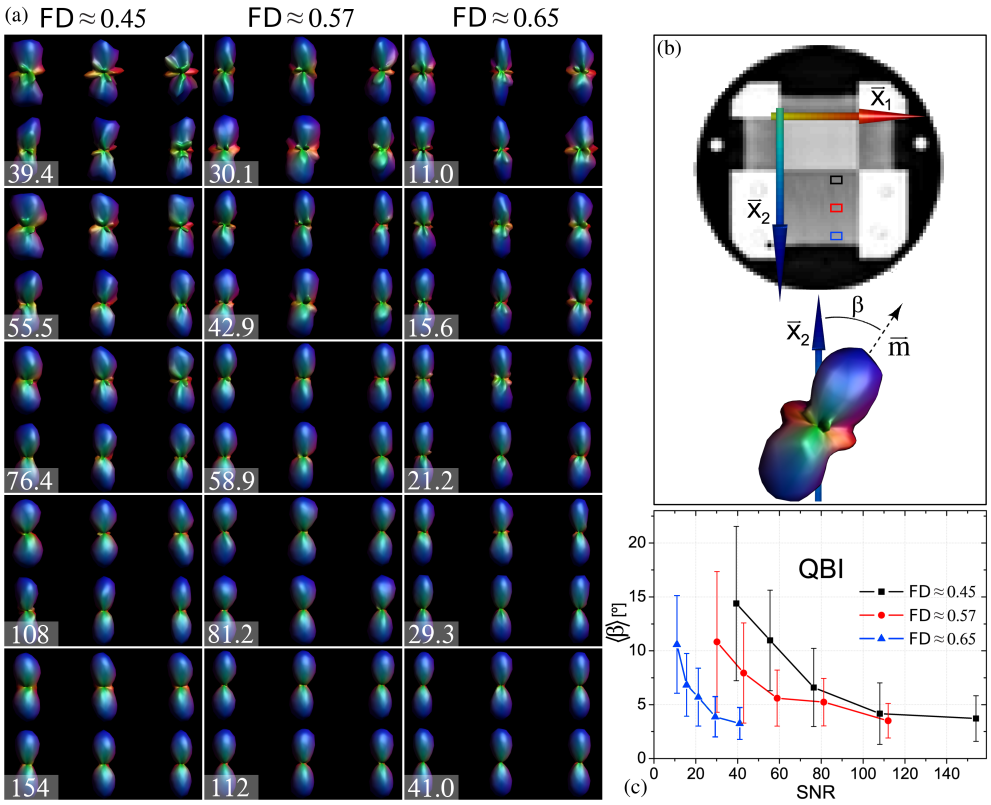


Figure 4.9: *(a) Performance of the QBI method for increasing values of SNR (from top to bottom) demonstrated for three selected ROIs (highlighted in (b)) with fibre densities* FD ≈ 0.45 *(left column),* ≈ 0.57 *(middle column) and* ≈ 0.65 *(right column). The SNRs are indicated on the bottom-left corner of the plots. (b) A schematic representation of the deviation angle,* β*. (c) The mean deviation angle* $\langle\beta\rangle$ *(Equation 4.2) as a function of the SNR for the three values of FD.*

fibres crossing at 90 degrees, one area of parallel fibres with homogeneous packing density, and finally, an area of parallel fibres with a fibre-density gradient. The fact that each of these areas is relatively large compared to the typical voxel size of $2\times2\times2$ mm^3 makes the phantom well-suited for investigations on clinical scanners since the features of interest can be reliably visualised. As an important characteristic of the phantom, we emphasize the homogeneity of fibre packing observed in the cross- and the parallel-areas of side 1 (Figure 4.4(a)). We demonstrated that homogeneous packing and rather high FA values (≈ 0.76) can be achieved by applying mechanical pressure. This scheme is more robust than some

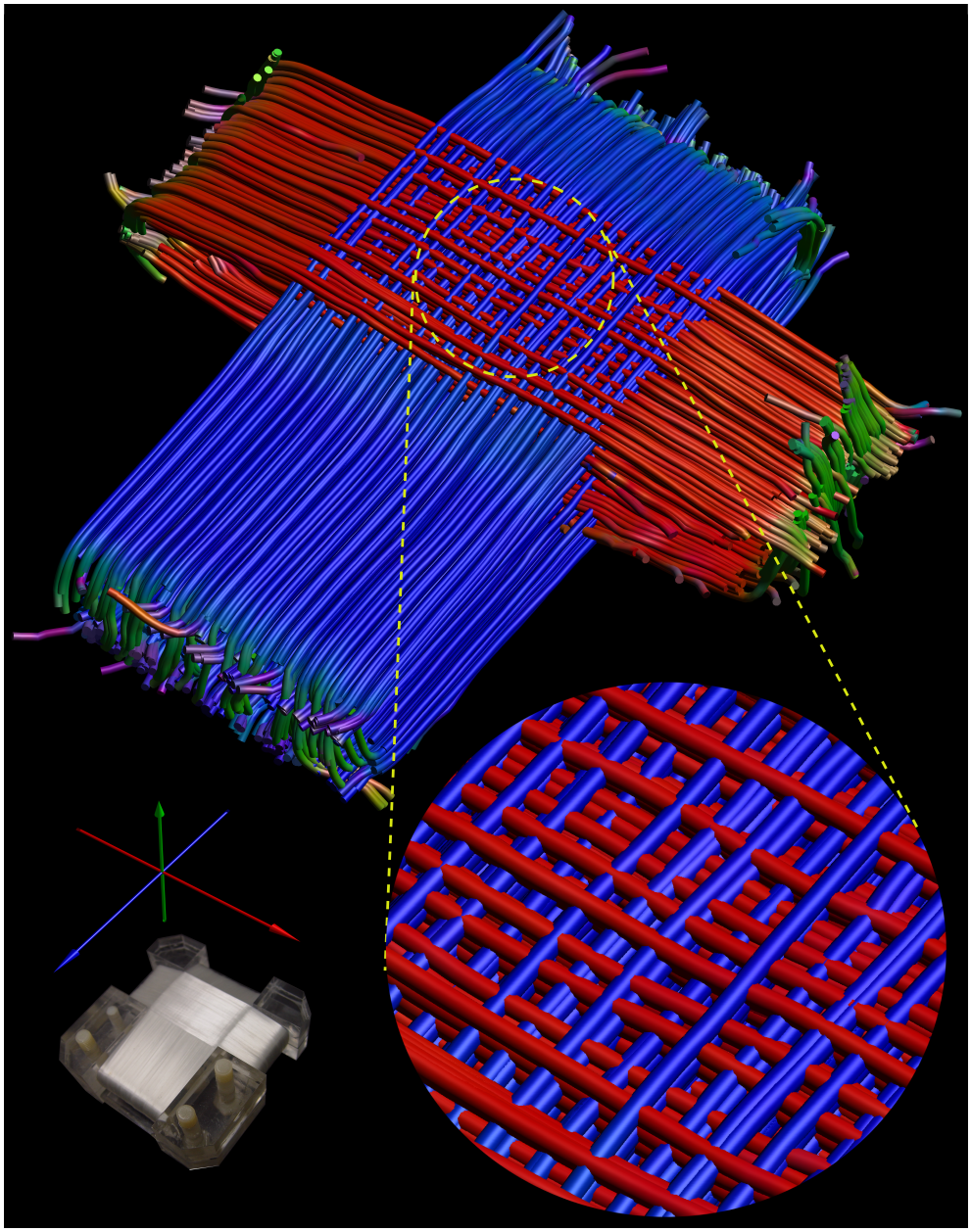


Figure 4.10: *Streamline fibre tractography of the diffusion phantom based on the CSD method. Fibre colour refer to the orientation. CSD-based tractography can clearly resolve multi-fibre populations as shown in the zoomed area of the crossing-fibres. Fibre tracks were processed with the ExploreDTI toolkit [69].*

procedures proposed in the literature in which fibre strands were wrapped with another set of fibres [127] giving rise to homogeneity problems, or with shrinking tubes [131] which do not enable easy control of the packing density. In our procedure, conversely, one can easily regulate the applied pressure. The fact that the measured values of $\lambda_{\|}$ were close to that of free water ($\approx 2.2\ \mu m^2\ ms^{-1}$) over the whole range of FDs and observation times, is an indication for the good quality of fibre alignment Figure 4.6(c).

Our results are to be compared with the results of other groups [131, 154–156, 160]. In References [154, 155], for instance, the influence of packing density on the diffusion parameters was not at all taken into account. In other works [131,156,160], the authors assessed the influence of FD on diffusion by building different phantoms with different fibre densities. One of the extremely beneficial features of the design proposed in this work is that regions with varying FDs are naturally produced within the same phantom just by the way the fibres are wound. Moreover, a nearly linear variation of FDs is achieved in a reasonably large range of values. This allowed us to carry out FD-dependent studies at the same time and under the same experimental conditions. Our experiments have shown that the density of fibre packing has a dramatic impact on the parameters such as D_{app}, K_{app} and FA. These parameters represent important metrics characterizing molecular diffusion and microstructure in diffusion MRI of the human brain.

The application of the STE sequence allowed us to perform time-dependent diffusion studies in a broad range of the observation times under clinical conditions. Monte Carlo simulations of random walks [136] in the idealized system of impermeable cylinders immersed in a liquid medium have shown that diffusion in the interstitial space between cylinders, in general, leads to non-mono-exponential attenuations for the range of observation times typically exploited in diffusion MRI experiments. The dependence of various parameters such as D_{app}, K_{app} and FA, on t_{d} and/or FD in such systems was explored in more detail by E. Fieremans et al. [131] with the help of Monte Carlo simulations. The experimental dependence of D_{app} and K_{app} on t_{d} was, however, demonstrated by the authors only for one individual phantom (FD = 0.55). In contrast, our

phantom allowed us to obtain experimental results, Figure 4.6, for various values of FDs simultaneously. In particular, our results suggest that, in frame of a simple model applied, differentiation of various FDs based on kurtosis studies would be more beneficial at shorter observation times. For instance, the difference of MK values for regions with the lowest ($\approx$ 0.44) and the highest ($\approx$ 0.65) FDs has increased from 0.18 at $t_{\mathrm{d}} = 1024$ ms to 0.51 at $t_{\mathrm{d}} = 42$ ms, that is, by approximately a factor of 3. The difference in apparent FA values for the same regions was equal to 0.55 at long $t_{\mathrm{d}} = 1024$ ms and only slightly smaller, equal to 0.48, at short $t_{\mathrm{d}} = 42$ ms.

It is worth noting that the short time limit of virtually free diffusion in which the MSD are much smaller than the mean distances between the barriers is not reached in our experiments. The root MSD during the shortest observation time of 42 ms were 12 μm and 8 μm for the lowest and the highest fibre densities, respectively. These values are larger than the mean free-path distances between the fibres in the interstitial space (about 7 μm and 3 μm for the lowest and the highest FDs, respectively, assuming, just for calculations, a hexagonal arrangement of the lattice as an example). At long observation times, the initial decrease of $D_{\perp}$with increasing t_{d} slowed down significantly and showed a tendency to slowly approach the long-time plateau (the tortuosity limit [67]) although an extended plateau regime was not reached even for the longest diffusion time of 1024 ms used in our experiments.

The applicability of the phantom for the HARDI data analysis under clinical conditions was also investigated here. The performance of the CSD and QBI approaches in estimation of the fibre directions was demonstrated for increasing values of SNR and FD. Both approaches clearly show multi-modal diffusion profiles in the cross-area (Figure 4.7(a)) and a single-modal profile in the parallel area (Figures 4.8(a) and 4.9(a)). Visual inspection shows that, for low SNRs, the uncertainties in the assessed fibre directions might be relatively large but rapidly diminish with increasing SNR. For the highest SNR these uncertainties become rather small for both methods and both fibre configurations. This feature is clearly demonstrated by the plots of the mean deviation angles ($\langle\alpha\rangle$ and $\langle\beta\rangle$) shown in Figures 4.7(c), 4.8(c) and 4.9(c). For the lowest SNR, the

uncertainties in assessment of crossing fibres are significantly larger than in the parallel areas (compare Figures 4.7(c), 4.8(c) and 4.9(c)). A comparison of uncertainties of both methods suggests that the performance of CSD is better than that of QBI in the range of low SNRs. Our results show also that the performance of both methods depends not only on the SNR but also on FD, that is, the accuracy of fibre estimation is higher for larger FDs due to larger FA values. This is illustrated by a better estimation of fibre orientations in the right column in Figures 4.8(a) and 4.9(a) in comparison to the left column of the same figures (especially clear for the first row with the lowest SNR after only one scan). This is in spite of the fact that in the case of the higher FD (right columns in Figures 4.8(a) and 4.9(a)) we obtain lower SNRs in comparison to the corresponding profiles for the areas with the lower FD (left columns in Figures 4.8(a) and 4.9(a)).

In this work we developed a novel diffusion phantom using only one kind of fibres (Dyneema® fibres) but with three distinct regions suited for the investigation of different aspects of diffusion imaging and data analysis. Quite generally, the same platform can be used for producing the phantoms with various fibre materials. Moreover, several such platforms wound with different sorts of fibres can be placed within the same container, and fibre properties can be analysed in the same experiment with respect of their impact on diffusion metrics and fibre tracking algorithms. This is planned for future work. The novel phantom can also be used to investigate the effects of background gradients and susceptibility differences [158,159] which start to be increasingly important for scanners operating at high magnetic fields. In conclusion, we introduced a novel multi-section phantom design advantageous for calibration and characterization of diffusion processes and validation of theoretical approaches and fibre tracking algorithms.

Chapter 5

Non-Gaussian diffusion in the human brain tissue

The work presented in this chapter has been published in:
F. Grinberg, E. Farrher, J. Kaffanke, A.-M. Oros-Peusquens, and N.J. Shah. "Non-Gaussian diffusion in human brain tissue at high b-factors as examined by a combined diffusion kurtosis and biexponential diffusion tensor analysis", Neuroimage, Vol. 57, Nr. 3, p. 1087–1102, 2011.

5.1 Introduction

The aim of this chapter is to examine approaches capable of capturing more detailed information on the propagation mechanisms of water molecules in the brain tissue and underlying tissue microstructure at high diffusion-weightings, in comparison to the conventional methods. It is reported a detailed *in vivo* diffusion study of the human brain in an extended range of the b-values (up to 7.0 ms μm^{-2}) performed on a group of 14 healthy volunteers at 3 T. Combined DKI and biexponential diffusion tensor analysis (BEDTA) were applied to quantify the attenuation curves. New quantitative indices are suggested as map parameters and are shown to improve the underlying structure contrast in comparison to conventional DTI. In particular, fractional anisotropy maps related to the slow diffusion tensor are shown to attain significantly higher values and to substantially improve WM mapping. This is demonstrated for the specified regions of the frontal and occipital lobes and for the anterior

cingulate. The findings of this work are substantiated by the statistical analysis of the whole slice histograms averaged over 14 subjects. Colour-coded directional maps related to the fast and slow diffusion tensors in human brain tissue are constructed for the first time and these demonstrate a high degree of axial co-alignment of the two tensors in the WM regions. It is concluded that a combined DKI and BEDTA offers a promising framework for monitoring tissue alteration during development and degeneration or as a consequence of a neurological disease.

5.2 Materials and methods

5.2.1 Diffusion experiments

In vivo experiments were carried out with a whole-body 3T Siemens MAGNETOM Tim-Trio scanner (Siemens Medical Systems, Erlangen, Germany). A body coil was used for RF transmit and the manufacturer's 12-element phased array coil for signal receive. Parallel imaging was not used. The gradient system provided a maximal gradient strength of 40 mT/m. DW images were acquired using the manufacturer's TRSE pulse sequence for 15 b-values in the range between 0 and 7.0 ms μm^{-2} and for 6 directions of the diffusion encoding gradients. The components of the gradient directional vectors were: a) $\mathbf{g}_1 = (1, 0, 1)$; b) $\mathbf{g}_2 = (-1, 0, 1)$; c) $\mathbf{g}_3 = (0, 1, 1)$; d) $\mathbf{g}_4 = (0, 1, -1)$; e) $\mathbf{g}_5 = (1, 1, 0)$; f) $\mathbf{g}_6 = (-1, 1, 0)$. Two slices 2 mm thick and with a gap of 10 mm were selected parallel to the anterior–posterior commissure, at the level of the corpus callosum. Slice 1 was positioned in such a way that an inclusion of the adjacent ventricle of CSF was largely avoided; slice 2 included a CSF region. The Siemens AutoAlign tool was used, which facilitates the positioning of slices in the same anatomical position across volunteers. The voxel size in the measured DW images was 2×2×2 mm^3. The echo and the repetition times were 113 ms and 1000 ms, respectively. Between 16 and 32 averages were acquired. The time necessary for one single acquisition was about 1.4 minute. The field-of-view in the read direction was 256 mm, and the partial Fourier sampling was 5/8. Fourteen subjects (3 female and 11 male) in the age range 22 to 56 took part in the study after providing

written, informed consent. The study was performed in accordance with ethical approval from the local ethics committee. Where not explicitly indicated, all images and histograms related to a single subject are shown for the same representative subject. All mean histograms represent the averages of the individual histograms over 14 subjects.

5.2.2 Data analysis

The bias in the DW images due to the background noise was corrected using the PI method [123,124] (See Chapter 3, Section 3.10). Computation of DTI parameter maps was performed with the help of in-house Matlab scripts (Matlab, The MathWorks, Natick, MA, USA). To increase the SNR (which was especially important at high diffusion weightings), and to facilitate the fitting procedure, the signal of each voxel was averaged with five adjacent voxels within the same slice: one on the left, one on the right, one above and one below the given voxel. The details of the fitting procedure and construction of the parameter maps are described below and are represented schematically in Figure 5.1.

The functions listed below were fitted to the normalised DW signal intensities $S(b)$ in a voxel-by-voxel basis using a non-linear least-squares Nelder-Mead algorithm. Each voxel was associated with six attenuation curves $S_i(b)$, $(i = 1...6)$, corresponding to the i-th diffusion encoding gradient direction indicated above. The fitted functions are listed below.

Mono-exponential function

Equation 3.1 was fitted to each individual gradient encoding direction in the range $0 \leq b \leq 1.0$ ms μm^{-2}. The upper boundary constraint, $D_{\text{app},i} \leq 3.0$ μm^2 ms^{-1}, was set regarding the diffusivity of free water, 3.0 μm^2 ms^{-1} at 37°C [157]. We noted that the upper constraint was encountered predominantly in the voxels of the CSF ventricles (second slice) and in the small fraction of voxels along the outermost contour of the cerebral cortex (both slices). All these voxels formed the "CSF-mask" used for a segmentation of the CSF. Diffusion tensors were evaluated using the procedure described in Chapter 3, Section 3.2.2. The MD and FA corresponding to this model and evaluated according to Equations 3.8

and 3.11 are denoted as MD_m and FA_m, respectively. Colour-coded directional maps denoted as CFA_m were evaluated as described in Chapter 3, Section 3.2.4.

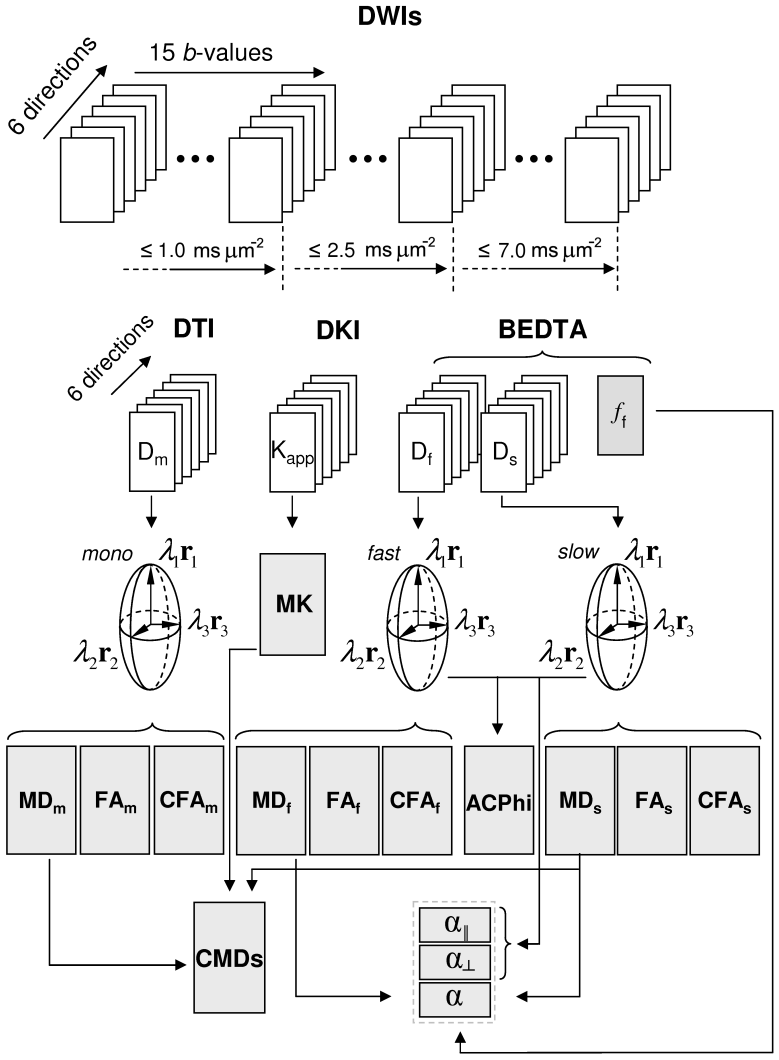


Figure 5.1: *Schematic representation of the map reconstruction workflow.*

Diffusion kurtosis model

Equation 3.24 was fitted to each gradient direction separately in the limited b-value range of $b \leq 2.5$ ms μm^{-2}. MK values were evaluated as the average over the six gradient directions.

Biexponential diffusion tensor model

In the fitting procedure of Equation 3.13, the component fractions of each exponential were taken to be independent of the gradient orientation and all six curves were fitted simultaneously with the fast fraction (f_f) as a shared parameter. This model implies a slow-exchange limit for two water pools associated with the fast and slow attenuation components. Thus, we had a total of 13 free parameters for six curves. The fitted values of $D_{\mathrm{f},i}$ and $D_{\mathrm{s},i}$ were used to calculate the elements of the fast and slow diffusion tensors. In the CSF voxels (that is, the voxels belonging to the "CSF-mask", see above) the fitted values of $D_{\mathrm{s},i}$ were replaced by the values of $D_{\mathrm{f},i}$. In this way we avoided erroneous fitting of the residual noise contribution as a slow component of the CSF attenuations which were typically close to mono-exponential ($D_{\mathrm{f},i} = D_{\mathrm{s},i}$). In the following, the MD, FA and colour-coded FA related to the fast and slow diffusion tensors are distinguished using the subscripts "f" and "s", respectively. Maps were produced for the parameters $\mathrm{MD_f}$, $\mathrm{MD_s}$, f_f, $\mathrm{FA_f}$, $\mathrm{FA_s}$, $\mathrm{CFA_f}$, $\mathrm{CFA_s}$ and ACPhi $\equiv \mathrm{abs}(\cos(\phi))$, where ϕ is the angle between the major eigenvectors of the fast and slow diffusion tensors.

The following constraints were set for the upper and lower boundaries of the diffusivities: $0.01 \leq D_{\mathrm{s},i} \leq D_{\mathrm{f},i} \leq 3.0$ $\mu\mathrm{m}^2$ ms^{-1}. The same constraints were set for the eigenvalues of the fast and slow tensors. The lower boundary of the diffusivities was set in order to suppress deriving diffusivities so low that the attenuation slopes could not be resolved in the range of the b-value used in this study. In our fits, the low-boundary constraints were encountered only for a minor fraction of the voxels and not more than in one gradient direction per voxel.

Distribution of the fast diffusion fraction

A Gaussian distribution function was fitted to the histogram of f_f

$$F(f_\mathrm{f}) = \frac{A_\mathrm{f}}{\sqrt{2\pi\sigma^2}} \exp\left(-\frac{(f_\mathrm{f} - \langle f_\mathrm{f}\rangle)^2}{2\sigma^2}\right), \tag{5.1}$$

where $\langle f_\mathrm{f}\rangle$ and σ are the mean and the standard deviation, respectively. The parameter A_f is a normalisation factor.

Distribution of the mean kurtosis

A sum of two Gaussian distribution functions was fitted to the histogram of MK

$$F\left(MK\right) = A_{MK} \sum_{i=1}^{2} \frac{p_i}{\sqrt{2\pi\sigma_i^2}} \exp\left(-\frac{\left(MK - \langle MK_i\rangle\right)^2}{2\sigma_i^2}\right), \qquad (5.2)$$

where $\langle MK_i\rangle$ and σ_i are the means and the standard deviations, respectively. p_i are the weights of the individual terms ($p_1 + p_2 = 1$); A_{MK} is a normalisation factor.

Combined biexponential and kurtosis model

A combined biexponential and kurtosis analysis was performed in which the application of the biexponential model (Equation 3.13) was restricted to only those regions of the brain in which the deviations from the mono-exponential function were sufficiently strong. This is to avoid erroneous parametrization of minor deviations (for instance, due to the noise) in terms of the slow component. Deviations from the mono-exponential function were considered "strong" if MK (note that kurtosis provides a direct quantitative measure of such deviations) exceeded a certain threshold value denoted MK^*. The values of MK^* were found empirically by analysing the corresponding histograms of the MK maps as specified below in Section 5.3. In other regions the attenuation curves were characterized by only one parameter, that is, global mean ADC per voxel, $\overline{\langle D\rangle}$. Here, the brackets stand for the average as determined by Equation 3.16 and the bar denotes the average over the gradient directions. Specifically, the values of $\overline{\langle D\rangle}$ were calculated as follows: first, the mean diffusivities, $\langle D\rangle_i$, related to the i-th curve were evaluated from the initial slopes according to Equation 3.16 by performing the mono-exponential fits up to $b \leq 0.6$ ms $\mu\mathrm{m}^{-2}$. After that, the values of $\langle D\rangle_i$ were averaged over six gradient directions providing the value of $\overline{\langle D\rangle}$ in each voxel. (Note that in the limit of the mono-exponential diffusion behaviour, $\overline{\langle D\rangle}$ merely coincides with $\mathrm{MD_m}$).

The approach described above was exploited in the construction of composite maps in which the regions characterized by strong non-

exponentiality are visualised with their $\mathrm{MD_s}$ (or $\mathrm{MD_f}$) value whereas the remaining regions are represented by their $\overline{\langle D \rangle}$. In particular, a new map parameter $\mathrm{CMD_s}$ (*composite mean diffusivity*) for slow diffusion component was obtained by setting $\mathrm{CMD_s} = \mathrm{MD_s}$ in any voxels where $\mathrm{MK} > \mathrm{MK}^*$ and $\mathrm{CMD_s} = \overline{\langle D \rangle}$ otherwise.

Alpha maps

In addition to excess kurtosis, deviations from Gaussian diffusion were assessed using new *alpha maps* constructed for three parameters, α_M, $\alpha_\parallel$ and $\alpha_\perp$. They were based on the biexponential tensor decomposition as defined below. Parameter α_M is given as

$$\alpha_\mathrm{M} = \frac{\sqrt{f_\mathrm{f} \left(MD_\mathrm{f} - \langle D \rangle\right)^2 + \left(1 - f_\mathrm{f}\right) \left(MD_\mathrm{s} - \langle D \rangle\right)^2}}{\langle D \rangle}, \tag{5.3}$$

where $\langle D \rangle \equiv f_\mathrm{f} MD_\mathrm{f} + \left(1 - f_\mathrm{f}\right) MD_\mathrm{s}$. α_M varies between 0 and 1 and quantifies the degree of non-exponentiality of the signal attenuation curves. The mono-exponential decay corresponds to $\alpha_\mathrm{M} = 0$ which implies that either $\mathrm{MD_f} = \mathrm{MD_s} = \mathrm{MD_m}$ or one of the component fractions is equal to 0 or to 1. In the opposite limit (strongest non-exponentiality), $\alpha_\mathrm{M} = 1$. This is the case if both fractions are equal to each other ($f_\mathrm{f} = 0.5$) and one of the diffusivities is negligibly small (for instance, $\mathrm{MD_s} = 0$ $\mu\mathrm{m}^2$ ms^{-1}).

Similarly, the parameters $\alpha_\parallel$ and $\alpha_\perp$ are defined for the largest eigenvalues (*axial*) and the average of the other two eigenvalues (*radial*) of the fast and slow diffusion tensors according to

$$\alpha_\parallel = \frac{\sqrt{f_\mathrm{f} \left(\lambda_\mathrm{f}^\mathrm{axial} - \langle \lambda^\mathrm{axial} \rangle\right)^2 + \left(1 - f_\mathrm{f}\right) \left(\lambda_\mathrm{s}^\mathrm{axial} - \langle \lambda^\mathrm{axial} \rangle\right)^2}}{\langle \lambda^\mathrm{axial} \rangle} \tag{5.4}$$

and

$$\alpha_\perp = \frac{\sqrt{f_\mathrm{f} \left(\lambda_\mathrm{f}^\mathrm{radial} - \langle \lambda^\mathrm{radial} \rangle\right)^2 + \left(1 - f_\mathrm{f}\right) \left(\lambda_\mathrm{s}^\mathrm{radial} - \langle \lambda^\mathrm{radial} \rangle\right)^2}}{\langle \lambda^\mathrm{radial} \rangle}, \tag{5.5}$$

where $\langle \lambda^\mathrm{axial} \rangle = f_\mathrm{f} \lambda_\mathrm{f}^\mathrm{axial} + \left(1 - f_\mathrm{f}\right) \lambda_\mathrm{s}^\mathrm{axial}$, $\langle \lambda^\mathrm{radial} \rangle = f_\mathrm{f} \lambda_\mathrm{f}^\mathrm{radial} + \left(1 - f_\mathrm{f}\right) \lambda_\mathrm{s}^\mathrm{radial}$. In Equations 5.4 and 5.5, $\lambda_\mathrm{f}^\mathrm{axial}$ and $\lambda_\mathrm{f}^\mathrm{radial}$ are, respectively, the largest

eigenvalue and the average of the other two minor eigenvalues of the fast diffusion tensor; $\lambda_{\mathrm{s}}^{\mathrm{axial}}$ and $\lambda_{\mathrm{s}}^{\mathrm{radial}}$ are, respectively, the largest eigenvalue and the average of the other two minor eigenvalues of the slow diffusion tensor.

Segmentation: WM and non-WM regions

Generally, the results of differentiation between the main tissue types, WM and GM, may vary with the applied criteria [161,162]. In this study, a high precision of segmentation was not required. The quantitative metrics obtained in frame of the BEDTA and DKI were compared for two different tissue types with relatively high and relatively low fractional anisotropies as evaluated from the mono-exponential fits. The threshold value for segmentation in the $\mathrm{FA_m}$ maps was tentatively set to 0.25. The regions in which $\mathrm{FA_m}$ exceeded this value were referred to as WM and, vice versa, the regions in which $\mathrm{FA_m}$ was equal to or smaller 0.25 were referred to as non-WM or GM.

5.3 Results

Figure 5.2 demonstrates the attenuation of the signal in the DW images for four increasing values of b ranging from the "normal" to very strong diffusion weightings, and in two directions of the magnetic field gradients as shown in rows (a) and (b) for the first slice and in rows (c) and (d) for the second slice, respectively. In different regions of brain tissue, the signal attenuates at a different rate and produces a stronger anatomical contrast between GM and WM at larger diffusion weightings. Some parts of WM remain clearly hyperintense even at the highest experimental value of $b = 7.0$ ms $\mu\mathrm{m}^{-2}$. At the same time, CSF and GM appear dark already at much lower diffusion weightings as can be seen in the images with $b = 3.0$ ms $\mu\mathrm{m}^{-2}$. Marked diffusion anisotropy is easily recognised in the WM regions.

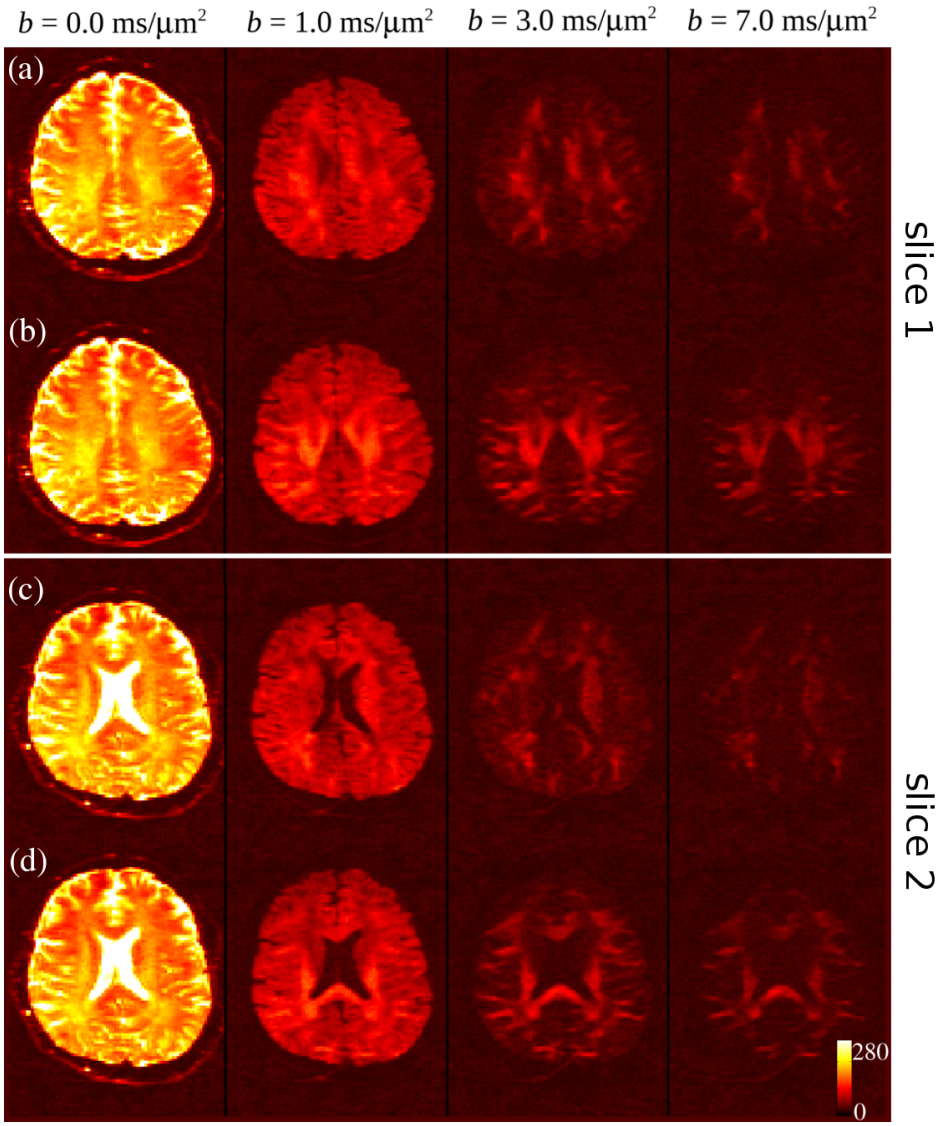


Figure 5.2: *DW images for four values of b as specified for each column and two gradient directions with vector components* $(1, 0, 1)$ *for the rows (a) and (c), and* $(0, 1, -1)$ *for the rows (b) and (d). The two upper and two bottom rows refer to the first and the second slice, respectively.*

5.3.1 Diffusion attenuation patterns

Typical diffusion attenuation curves are shown in Figures 5.3(a) and 5.3(b) for two representative averaged voxels located in GM and WM. A pronounced departure from the mono-exponential function (dashed line) accompanied by strong anisotropy can be observed in WM (Fig-

ure 5.3(b)). In contrast, the signal in GM (Figure 5.3(a)) exhibits a practically negligible dependence on the gradient orientation and rather moderate deviations from the mono-exponential function. The solid curves in Figures 5.3(a) and 5.3(b) represent the biexponential fits according to Equation 3.13. The fitted values of the free parameters and their fit errors are listed in Table 5.1. The maps of chi-squared error, χ^2, for the first and second slices are shown in Figures 5.3(c) and 5.3(d), respectively. They demonstrate a satisfactory homogeneity across the most part of the image excluding a small number of voxels along the contour line and a few localised areas in the middle including the CSF (second slice).

	Gradient direction	f_f	$D_{\mathrm{f},i}$ [μm^2 ms^{-1}]	$D_{\mathrm{s},i}$ [μm^2 ms^{-1}]
Voxel 1	$\mathbf{g}_1$	0.74 ± 0.06	1.12 ± 0.08	0.27 ± 0.05
(GM)	$\mathbf{g}_2$		1.10 ± 0.09	0.22 ± 0.05
	$\mathbf{g}_3$		1.03 ± 0.07	0.24 ± 0.05
	$\mathbf{g}_4$		0.94 ± 0.07	0.23 ± 0.05
	$\mathbf{g}_5$		0.95 ± 0.06	0.33 ± 0.06
	$\mathbf{g}_6$		0.93 ± 0.06	0.31 ± 0.05
Voxel 2	$\mathbf{g}_1$	0.69 ± 0.07	1.41 ± 0.06	0.13 ± 0.02
(WM)	$\mathbf{g}_2$		1.32 ± 0.05	0.15 ± 0.02
	$\mathbf{g}_3$		1.68 ± 0.07	0.21 ± 0.02
	$\mathbf{g}_4$		0.66 ± 0.03	0.02 ± 0.01
	$\mathbf{g}_5$		0.91 ± 0.03	0.08 ± 0.01
	$\mathbf{g}_6$		1.07 ± 0.04	0.10 ± 0.01

Table 5.1: *The values of free parameters obtained from the fits of Equation 3.13 to the experimental curves in Figures 5.3(a) (voxel 1) and 5.3(b) (voxel 2) for various gradient directions i.*

5.3.2 Mean ADC maps

Figure 5.4 shows the maps of $\mathrm{MD_m}$, $\mathrm{MD_f}$, $\mathrm{MD_s}$ and f_f for the two measured slices. In the three MD maps, the GM-WM contrast is reduced in comparison to the corresponding DW images shown in Figure 5.2. This is typical for orientationally averaged ADC maps also in conventional

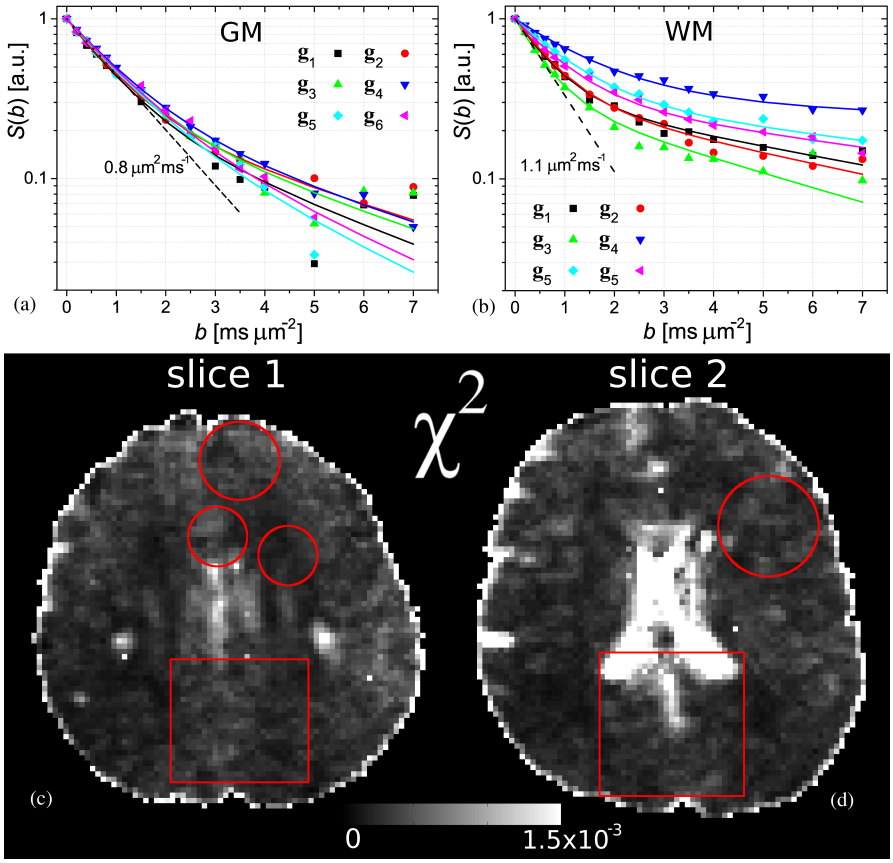


Figure 5.3: *Diffusion attenuation curves for two representative voxels located in GM (a) and WM (b); (c,d) maps of χ^2 of the biexponential fits for the first (c) and the second (d) slice. The curve parameter is the direction of the diffusion-encoding gradients. Solid curves are the fits of Equation 3.13 to the data points. Fitted parameters are listed in Table 5.1. Dashed lines represent mono-exponential functions, Equation 3.1, with the indicated slopes and serve as a guide for the eye. The squares and circles in (c,d) highlight the ROIs indicated in Figures 5.7 and 5.8.*

DTI. Note, however, that among the three ADC maps the contrast is the best in the MD_s map and is most reduced in the MD_m map.

The histograms of MD_f and MD_s are shown in Figure 5.5(a) for the first slice as an example. They are centred at 1.16 μm^2 ms^{-1} (fast) and 0.14 μm^2 ms^{-1} (slow) and exhibit only a small overlap. The ratio MD_f/MD_s corresponding to the peak values is about 8.5. Figures 5.5(b) and 5.5(c) show the histogram of the quantity MD_f/MD_s of the single subject and averaged over all subjects, respectively. The histograms

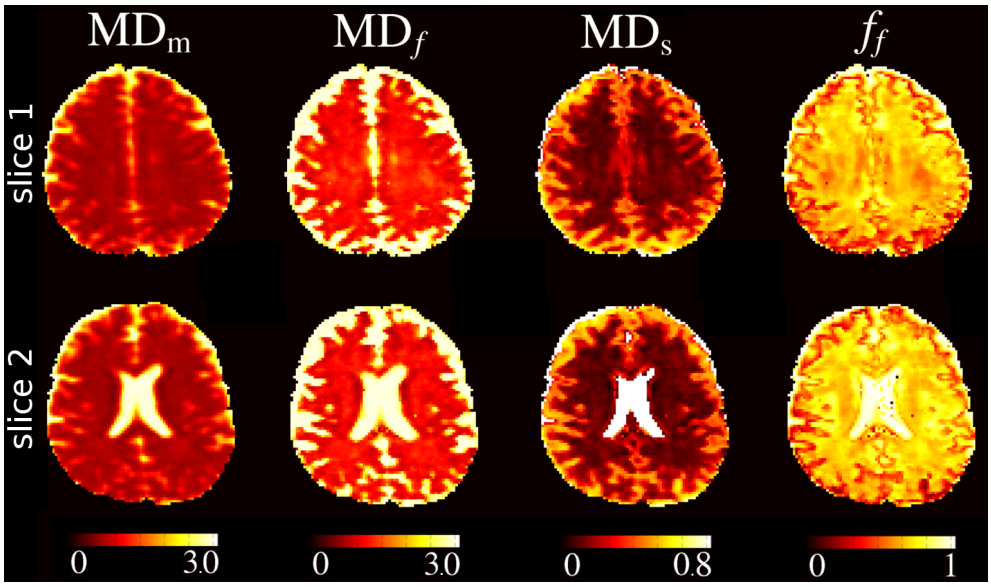


Figure 5.4: *Maps of* $\mathrm{MD_m}$, $\mathrm{MD_f}$, $\mathrm{MD_s}$ *and* f_f *for the two measured slices. The first slice is shown in the upper row. The scales of diffusivities are given in* $\mu\mathrm{m}^2\ \mathrm{ms}^{-1}$.

were evaluated for the whole slice and, additionally, for two subsets of all voxels with $\mathrm{FA_m} \leq 0.25$ and $\mathrm{FA_m} > 0.25$. The major part of the whole-slice histogram is located in the range of values between 2 and 12. The peak values corresponding to the voxel subsets with $\mathrm{FA_m} > 0.25$ (WM) and $\mathrm{FA_m} \leq 0.25$ (non-WM) in Figure 5.5(b) are about 9 and 5, respectively. This means that the difference between the slow and fast diffusion components is considerably larger in WM than in GM. This finding is confirmed by the averaged histograms in Figure 5.5(c) which shows that the partial histogram related to the voxel subset with $\mathrm{FA_m} > 0.25$ (WM) is considerably shifted towards the larger values of $\mathrm{MD_f}/\mathrm{MD_s}$ in comparison to that with $\mathrm{FA_m} \leq 0.25$.

The maps of f_f shown in Figure 5.4 exhibit characteristic patterns which tend to partially correlate with the patterns in the corresponding DW images (Figure 5.2) although the appearance of the fibre structure is less distinct. At the same time, it is worth noting that f_f tends to be somewhat lower in the large WM tracts, such as corpus callosum and centrum semiovale, than in the other WM regions. The histograms of f_f for the whole slice and two voxel subsets are shown in Figure 5.6(a)

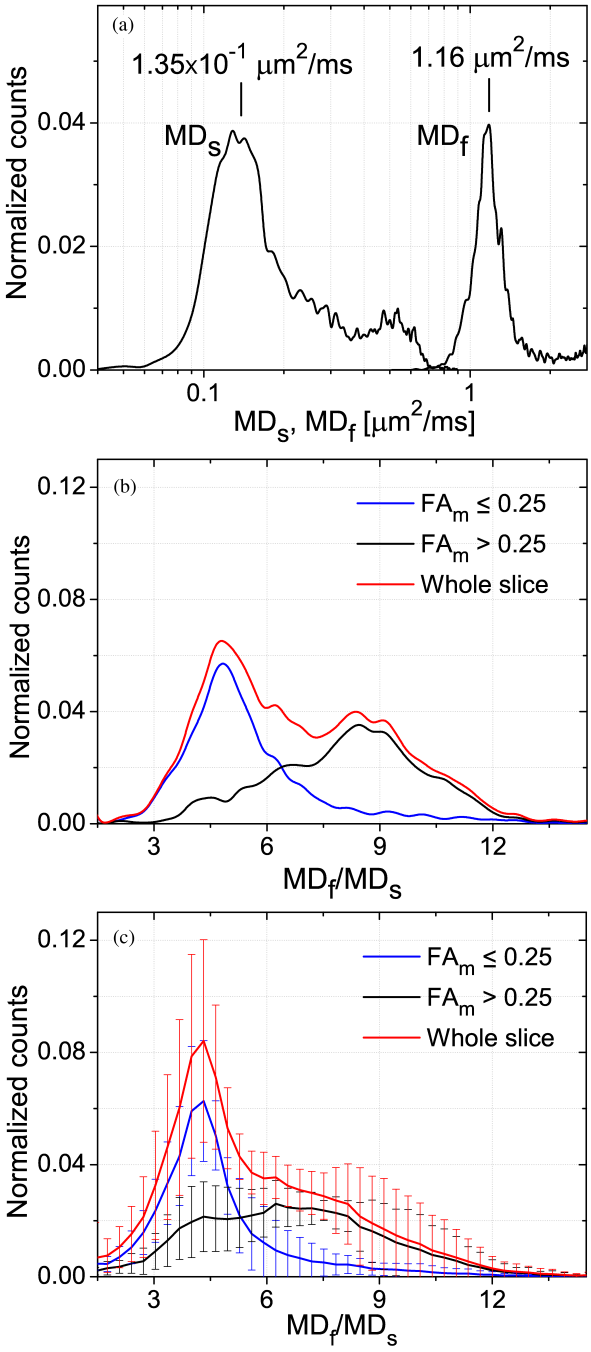


Figure 5.5: *(a) Histograms of* $\mathrm{MD_f}$ *and* $\mathrm{MD_s}$ *for the entire first slice; (b,c) histograms of the ratio* $\mathrm{MD_f}/\mathrm{MD_s}$ *for the whole slice and for two subsets of all voxels with* $\mathrm{FA_m} \leq 0.25$ *(non-WM) and* $\mathrm{FA_m} > 0.25$ *(WM) related to (b) a single subject, (c) the average over 14 subjects. The error bars in (c) indicate standard deviations from the mean value.*

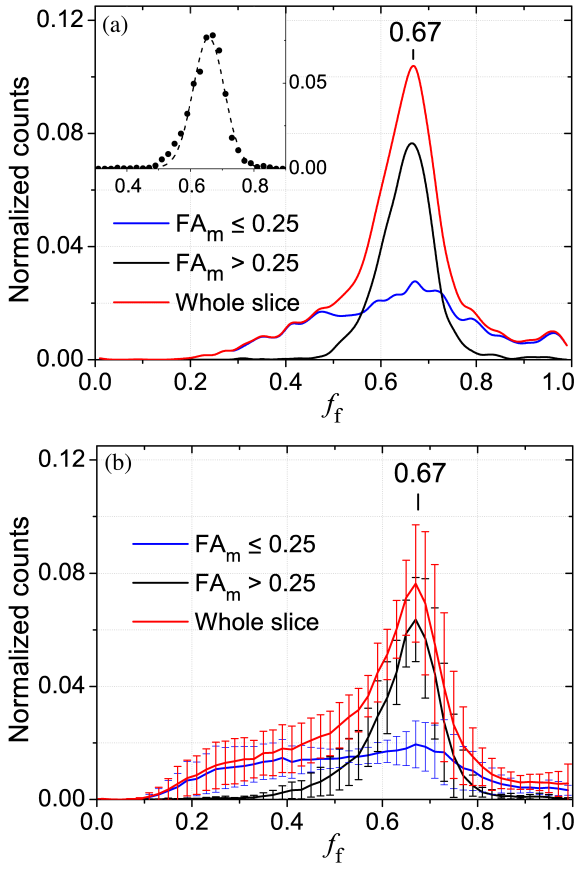


Figure 5.6: *Histograms of f_f for the whole slice and two subsets of all voxels with* $FA_m \leq 0.25$ *(non-WM) and* $FA_m > 0.25$ *(WM) related to (a) a single subject, (b) the average over 14 subjects; the error bars indicate standard deviations from the mean value. All data refer to the first slice. The data points in the inset correspond to the black curve in the main plot, i.e. refer to the subset of all voxels with* $FA_m > 0.25$*. The dashed curve in the inset represents the Gaussian function, Equation 5.1, fitted to the data points. The fitted value of the mean was 0.657 ± 0.001 and the standard deviation was 0.050 ± 0.001.*

for the first slice as an example. The histogram of f_f averaged over all subjects is shown in Figure 5.6(b). The whole-slice histograms of both the individual subject and averaged over all subjects are centred around the peak value of 0.67, in good agreement with the values reported earlier [3, 22]. Figures 5.6(a) and 5.6(b) demonstrate that the distribution of f_f in WM ($FA_m > 0.25$) occurs in the relatively narrow range around

the central peak (black curves) whereas the distribution in the remaining voxels (non-WM, $FA_m \leq 0.25$) is, in contrast, fairly broad (blue curves). The inset in Figure 5.6(a) shows that the WM component of the histogram can be satisfactorily approximated by the Gaussian function, Equation 5.1, ignoring some asymmetry of the left branch, with a mean value of about 0.66 and standard deviation of 0.05.

The contour line along the cortical GM separating it from CSF exhibits reduced values of f_f, see Figure 5.4. This is to be attributed to partial volume effect (PVE) in the CSF containing voxels. In the latter, water is located in at least two compartments, CSF and brain tissue, giving rise to biexponential diffusion attenuations. The fraction of the fast component in these voxels, however, merely reflects the content of CSF relative to tissue and thus is of a different nature than that in WM or GM voxels that are not contaminated by CSF.

5.3.3 FA, ACPhi and colour-coded directional maps

The maps of the fractional anisotropy, FA_m, FA_f, FA_s, and the corresponding colour-coded directional maps are shown in Figures 5.7 (slice 1) and 5.8 (slice 2). The maps of FA_m/CFA_m and FA_f/CFA_f referring to the same slice are, as expected, very similar to each other. In contrast, the maps of FA_s/CFA_s exhibit considerably higher values and reveal more structural peculiarities than the maps of FA_m/CFA_m or FA_f/CFA_f; consider for instance the marked regions at the level of the frontal gyrus in the frontal lobe, the anterior cingulate (Figure 5.7, circles, upper row), and the cuneus in the occipital lobe (Figure 5.7, squares, middle and bottom rows); also note an improved visualisation of tiny microstructures in the zoomed areas in Figure 5.8 (squares, middle and bottom rows). "Brighter" FA_s maps (that is, higher FA_s values in comparison to FA_m and FA_f) were observed in all subjects studied, see examples of the zoomed map regions for various volunteers in Figure 5.9.

A comparison of the colour patterns in the CFA_f and CFA_s maps in Figures 5.7 and 5.8 shows that fibre tract orientations derived from the fast and slow diffusion components appear largely correlated in most parts of WM; they also correlate with the directions constituted by CFA_m. However, in a few regions the fibre tract orientations as depicted

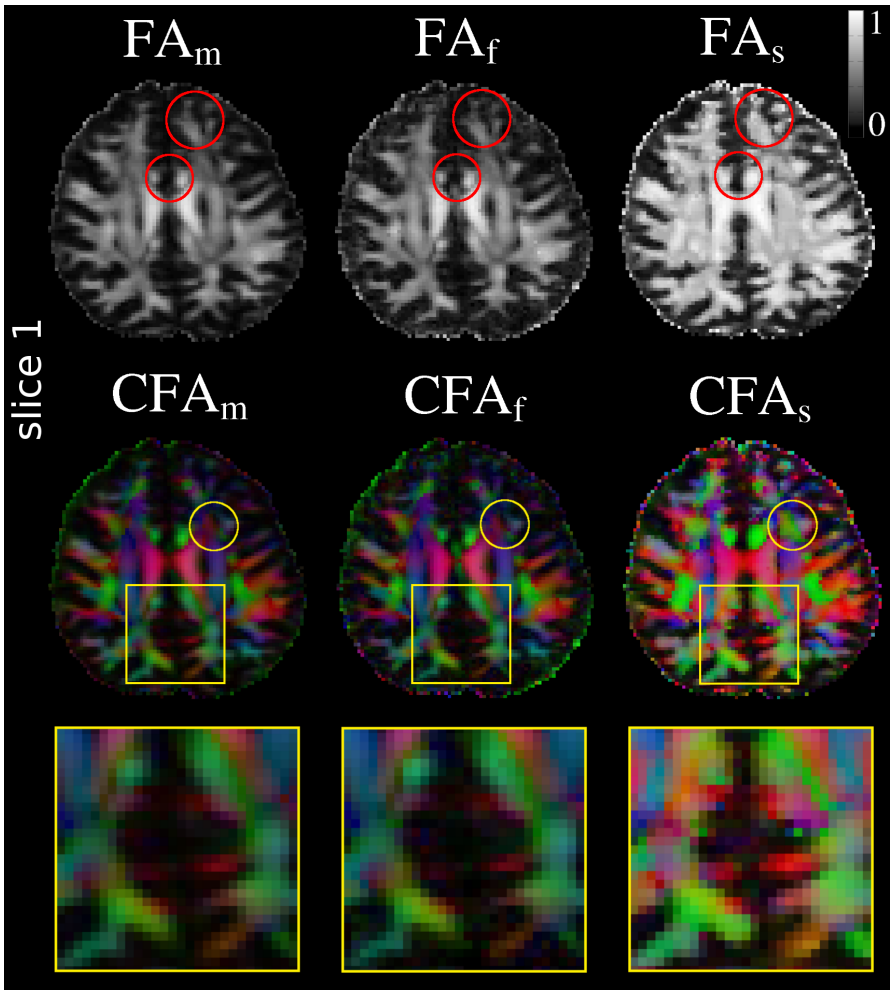


Figure 5.7: *Maps of* FA_m, FA_f, FA_s *(upper row) and the corresponding colour-coded directional maps (middle row) of the first slice. The circles and squares overlaid on the images indicate the regions in which the differences in the* FA_s/CFA_s *maps with respect to the* FA_f/CFA_f *and* FA_m/CFA_m *maps are clearly visible. The bottom row shows zoomed regions depicted by the squares in the colour-coded directional maps.*

by the CFA_m/CFA_f and CFA_m maps were different, see for instance the marked regions (Figure 5.7, circles, middle row; Figure 5.8, circles, middle row).

Figure 5.10(a) shows the histograms of FA_m, FA_f and FA_s related to the maps in Figure 5.7 (slice 1). Characteristic of all three histograms is the presence of a relatively narrow peak in the range of values below 0.25 attributed to non-WM. The histogram of FA_f closely resembles

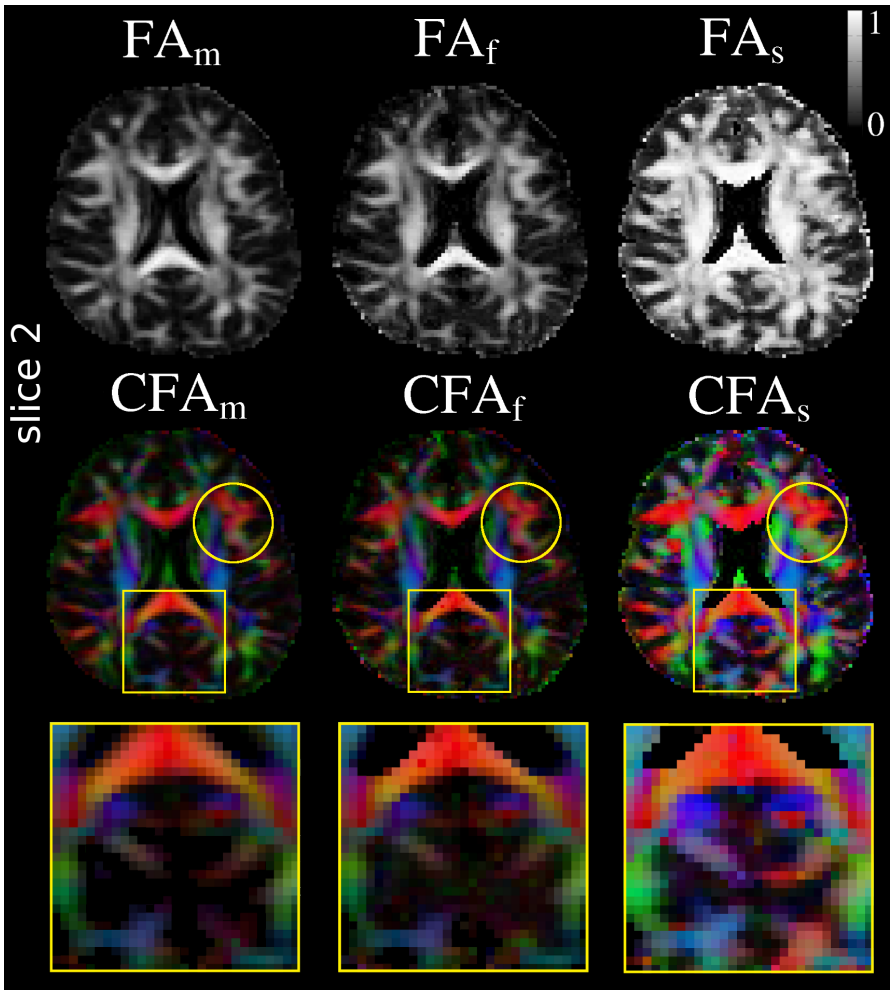


Figure 5.8: *Maps of* FA_m, FA_f, FA_s *(upper row) and the corresponding colour-coded directional maps (bottom row) of the second slice. The circles and squares overlaid on the images indicate the regions in which the differences in the* CFA_s *maps with respect to the* CFA_f *and* CFA_m *maps are clearly visible. The bottom row shows zoomed regions depicted by the squares in the colour-coded directional maps.*

the shape of the histogram of FA_m. In contrast, the histogram of FA_s appears considerably shifted towards the larger values. Besides, it exhibits an additional peak in the range of values between 0.7 and 0.75. These features also appear to be retained in the average histograms of 14 subjects related to the same slice, Figure 5.10(b).

Figure 5.11 shows the maps of ACPhi. Dark red visualises the regions with parallel (ϕ equal to 0 or π) or close to parallel orientations between

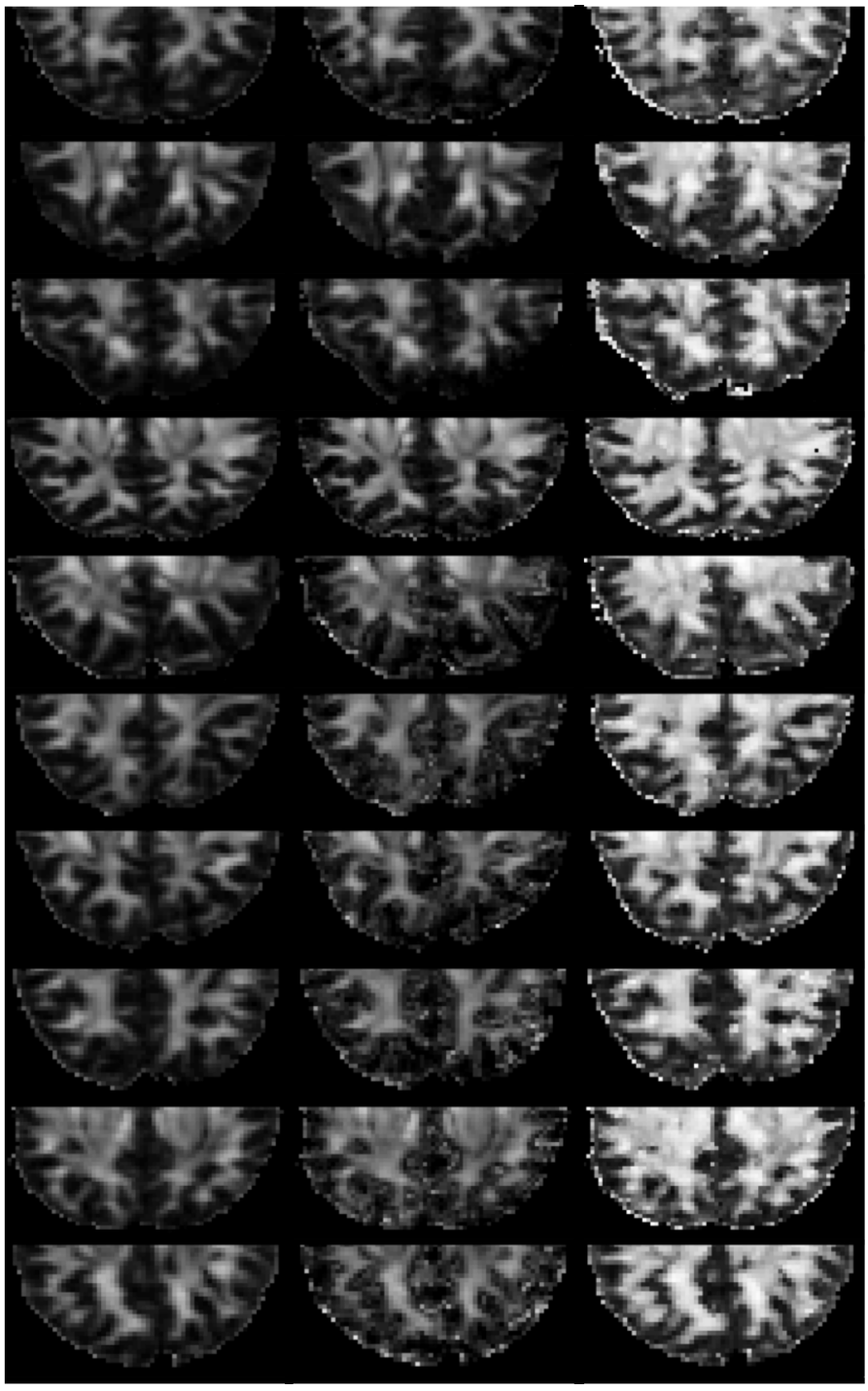


Figure 5.9: *Zoomed regions of the maps of* $\mathrm{FA_m}$ *(left)* $\mathrm{FA_f}$ *(middle) and* $\mathrm{FA_s}$ *(right) for various subjects (first slice); each row refers to one individual subject.*

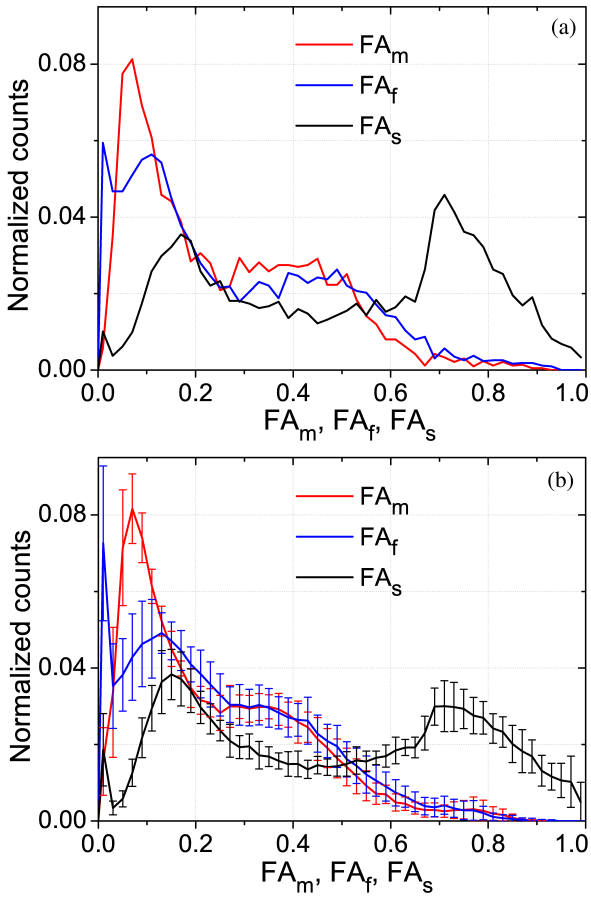


Figure 5.10: *Histograms of* $\mathrm{FA_m}$, $\mathrm{FA_f}$ *and* $\mathrm{FA_s}$ *of the entire first slice related to (a) a single subject, see maps in Figure 5.7, (b) the average over 14 subjects; the error bars indicate standard deviations from the mean value.*

the major eigenvectors of the fast and slow diffusion tensors. The dark red pattern in Figure 5.11 correlates well with regions of high anisotropy as compared with the patterns in Figures 5.7 and 5.8. Thus, the major eigenvectors tend to be strongly co-aligned in WM in contrast to GM in which orientations of the major eigenvectors are random (consider the variation of the different colours in the GM regions, Figure 5.11).

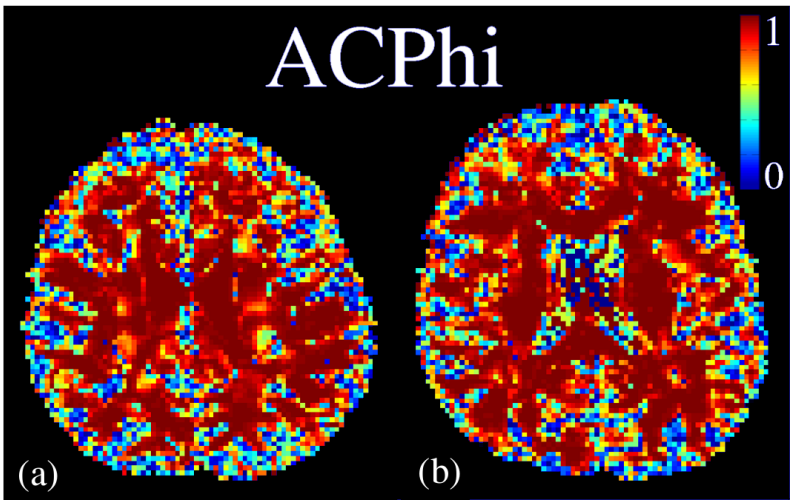


Figure 5.11: *Maps of ACPhi. A value of ACPhi equal to 1 means that the major eigenvectors of the fast and slow diffusion tensors are oriented parallel to each other (ϕ equal to 0 or π); a value equal to 0 corresponds to the perpendicular orientations of the major eigenvectors. The major eigenvectors tend to be strongly co-aligned in the regions of high anisotropy.*

5.3.4 Kurtosis and alpha maps

Figures 5.12(a) and 5.12(b) show the maps of MK for the two measured slices and the corresponding histograms. Both maps demonstrate two distinct regions with relatively high and low kurtosis values. The second slice, in addition, visualises the CSF ventricle in which excess kurtosis vanishes. The histograms exhibit two peaks centred approximately at 0.78 and 1.16 (first slice) and 0.78 and 1.11 (second slice) as shown in Figures 5.12(c) and 5.12(d). Each of the two histograms was reasonably fitted by a sum of two Gaussian distributions, Equation 5.2, shown by solid curves. The individual Gaussian terms are shown by solid curves in the insets. The fitted values of the corresponding means and standard deviations are indicated in Table 5.2. The insets in Figs 5.12(c) and 5.12(d) show in addition the histogram components for two subsets of all voxels related to non-WM ($FA_m \leq 0.25$, closed circles) and WM ($FA_m > 0.25$, open circles). These data agree rather well with the Gaussian distributions (take into account that the solid curves are not the fits of the data points in the insets). On this basis, the two components of the kurtosis histograms can be attributed to WM and non-WM.

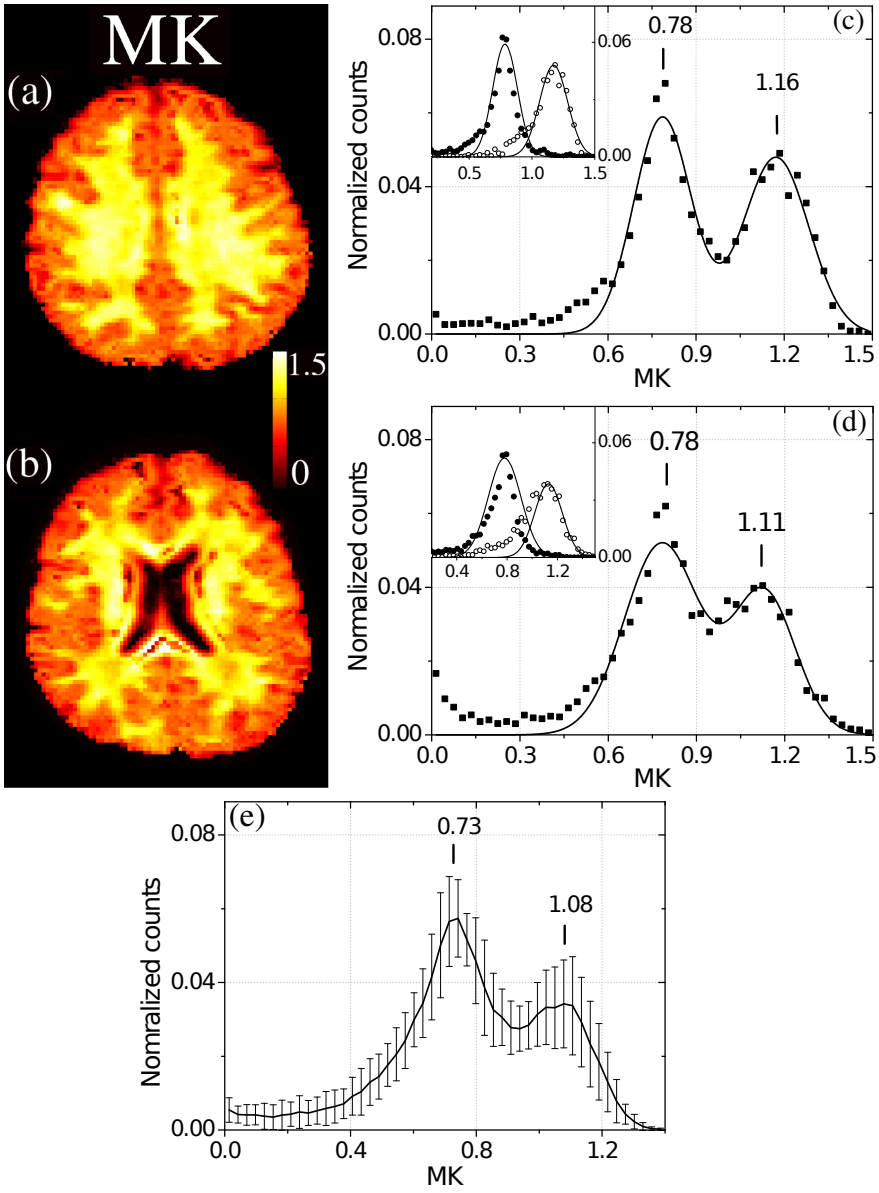


Figure 5.12: *(a,b) Maps of MK and (c,d) the corresponding histograms of the entire first (a,c) and second (b,d) slice; (e) the histogram of MK (first slice) averaged over 14 subjects; the error bars in (e) indicate standard deviations from the mean value. The solid curves in (c,d) are the fits of the sum of two Gaussian distributions, Equation 5.2, to the data points. The fitted values are listed in Table 5.2. The insets in (c,d) show the individual components of the sum (solid curves) and the histograms of two voxel subsets with* $\mathrm{FA_m} \leq 0.25$ *(closed circles, non-WM) and* $\mathrm{FA_m} > 0.25$ *(open circles, WM).*

	Gaussian terms, i	$\langle \mathrm{MK}_i \rangle$	δ_i
Slice 1	a	0.785 ± 0.005	0.098 ± 0.005
	b	1.172 ± 0.006	0.112 ± 0.007
Slice 2	a	0.780 ± 0.010	0.130 ± 0.010
	b	1.130 ± 0.010	0.110 ± 0.010

Table 5.2: *The fitted values of the means, $\langle \mathrm{MK}_i \rangle$, and standard deviations, δ_i , related to the fits of the histograms in Figures 5.12(c) and 5.12(d) using Equation 5.2.*

Figure 5.12(e) shows the histogram of MK of the first slice averaged over 14 subjects. Two peaks observed retain approximately the same positions, at 0.73 and 1.08, as in Figures 5.12(c) and 5.12(d).

The maps of α_{M}, $\alpha_{\parallel}$ and $\alpha_{\perp}$ are shown in Figure 5.13. These maps quantify the deviations from the Gaussian model and are to be compared with the kurtosis maps shown in Figures 5.12(a) and 5.12(b). In comparison to the latter, all alpha maps produce a poorer contrast between the WM and non-WM regions. At the same time, however, they

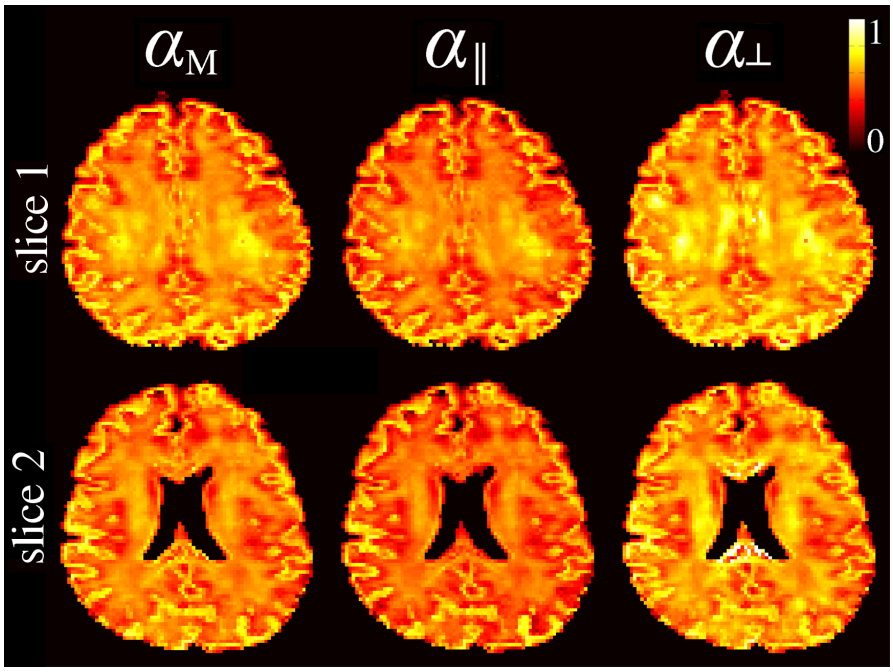


Figure 5.13: *Maps of α_{M}, $\alpha_{\parallel}$ and $\alpha_{\perp}$ of the first (upper row) and second (bottom) slice.*

tend to show more structural details than the kurtosis maps (note less homogeneous appearance both in WM and non-WM regions; note also the enhanced appearance of the internal capsule and genu and splenium of corpus callosum in the second slice). Among the three alpha maps, the best contrast is to be seen in the $\alpha_\perp$ maps.

The enhancement of the voxels along the contour line of the cortical GM in all alpha maps is due to the PVE of the same origin as discussed above with respect to the f_f maps. Here, again, the biexponential nature of the curves and the cause of the enhanced alpha values are different from that in the WM and GM tissues.

5.3.5 Combined biexponential tensor and kurtosis map analysis

Figures 5.14(a) and 5.14(b) show the maps of $\mathrm{CMD_s}$ which were produced as specified in Section 5.2. The darkest regions, predominantly in WM, visualise the values of $\mathrm{MD_s}$, whereas the brighter regions are represented by the mean diffusivity $\overline{\langle D \rangle}$ of the voxel. The values of MK^* used in the map construction as criterion of the curve non-exponentiality were chosen at the positions of the minima in the kurtosis histograms, see Figures 5.12(c) and 5.12(d). They were equal to 0.97 for both slices. One observes that in the $\mathrm{CMD_s}$ maps WM has a rather homogeneous appearance and reveals good contrast with respect to non-WM. The corresponding histograms are shown in Figures 5.14(c) and 5.14(d). Note the change of the shape of the histogram in comparison to that of $\mathrm{MD_s}$ in Figure 5.5(a) (slice 1). The histogram of $\mathrm{CMD_s}$ in Figure 5.14(c) contains two well-resolved components centred around 1.35×10^{-1} and 8.03×10^{-1} $\mu\mathrm{m}^2$ ms^{-1}. The smaller component with the higher peak-value on the right side refers to the regions with small kurtosis (predominantly GM) and depicts the distribution of the mean ADCs in these regions. A comparison with Figure 5.5(a) shows that the counterpart of this peak in the histogram of $\mathrm{MD_s}$ is a broad feature in the range of approximately $(2-8) \times 10^{-1}$ $\mu\mathrm{m}^2$ ms^{-1}. The larger peak at lower values in Figure 5.14(c) refers to the regions with large kurtosis ($\mathrm{MK} > 0.97$), predominantly WM. It now exhibits a more symmetric shape than the

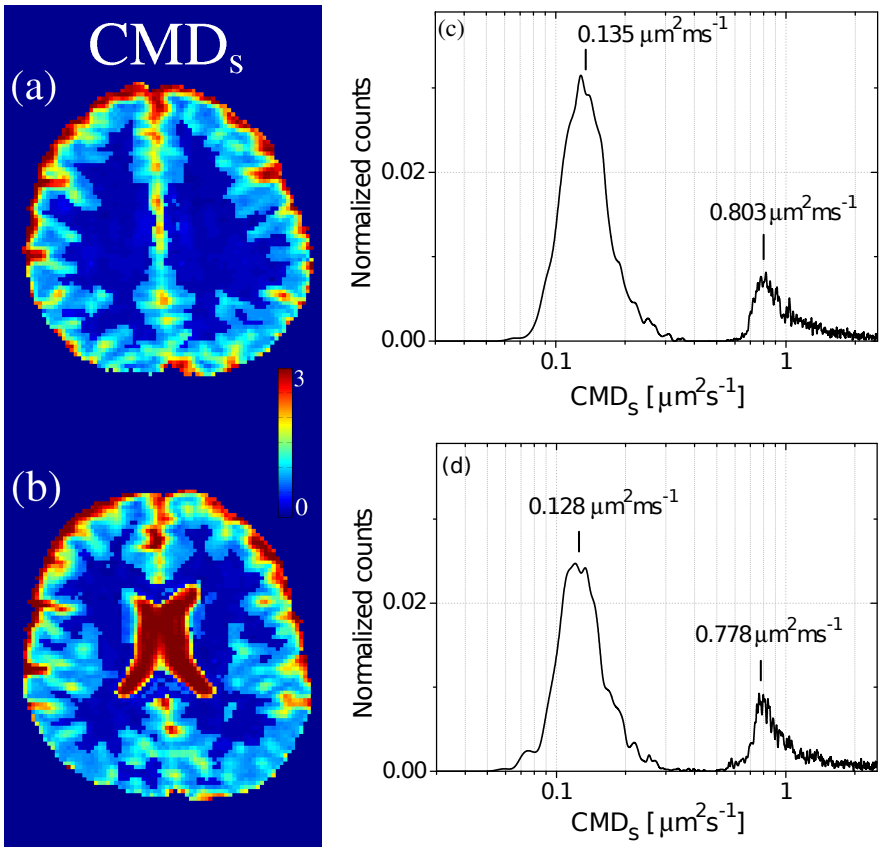


Figure 5.14: *Maps of* CMD_s *(a,b) and the corresponding histograms (c,d) of the entire first (a,c) and second (b,d) slice.*

histogram of MD_s. The histogram of the second slice in Figure 5.14(d) is very similar to that of the first slice.

5.4 Discussions

In this study, combined DKI and BEDTA in the extended range of *b*-values is proposed as a practical framework of measuring non-Gaussian water diffusion in the human brain. Both DKI and BEDTA permit one to overcome the limitations of the simple Gaussian model and to obtain enhanced information on water diffusion and tissue microstructure in comparison to the routinely used DTI protocols. DKI was introduced recently [36, 163] as the simplest, model-free method of assessing non-Gaussian diffusion. Since then, it has been shown to provide a more sub-

stantial characterization of neuronal tissue [37, 164, 165] than the DTI. Despite that, their number of studies based on the DKI remains rather low and more experimental data are required. Our results demonstrate a strong GM-WM contrast produced by the DKI. Histogram analysis revealed specific double-peaked curves which were satisfactorily approximated by a sum of two Gaussian components. The components were attributed to non-WM and WM based on their correlation with the FA. Due to the rather moderate overlap of the two components, DKI can be suggested as a complementary tool of tissue differentiation. The corresponding peak values of the averaged histograms at 0.73 and 1.08 were in a good agreement with the mean values of 0.74 and 1.09 reported earlier for GM and WM [163], respectively. As shown earlier [165], the average values of MK are sensitive to the developmental changes in various WM and GM structures. One can also expect that other quantitative parameters characterising diffusion kurtosis, such as the standard deviations δ_i evaluated in this work, might provide complementary information in assessing the changes of the tissue microstructure.

In comparison to DTI, DKI allows one to extend the range of the b-values by a factor of about two to three. Full signal attenuation is, however, not achieved in this range. Therefore, a serious disadvantage of the DKI is that it is applicable only in the limited range of the diffusion weightings (typically, below 3.0 ms μm^{-2}) making it incapable of capturing more detailed information related to smaller molecular displacements. This limitation is a principal one and cannot be circumvented by any further hardware or pulse sequence improvements. In this context, biexponential tensor analysis can be considered as the next extension in assessing the non-Gaussian behaviour of water diffusion in brain tissue. In contrast to DKI, BEDTA uses the whole available range of the diffusion weightings. On up-todate medical human scanners, the latter is restricted by the hardware and safety limitations rather than by a complete signal attenuation itself. It is noteworthy that nearly one third of the initial signal still remains available in some WM regions and in some gradient directions even at $b = 7.0$ ms μm^{-2}. As shown in this study, the biexponential analysis of the attenuations measured at such high b-values allows one to discriminate up to 8–10 times smaller ap-

parent diffusivities than the mono-exponential fits. According to the Einstein relation (Equation 2.27), the characteristic molecular displacements probed during the same observation time are approximately three times smaller. That is, more detailed information on the microstructure on the subvoxel level can potentially be resolved.

Our results should be compared with the reported results from other groups. In this work, BEDTA was performed on the voxel-by-voxel basis. An orientation independence of the parameter f_f was elaborated. This is in contrast to most of the earlier published works [22, 30, 34, 35] in which the biexponential model was applied for selected attenuation curves from selected regions-of-interest. Besides, usually all three free parameters, D_f, D_s and f_f, were independently fitted to the individual attenuation curves without any orientation constraints. However, whereas this is justified with respect to ADCs, an underlying orientation dependence of the parameter f_f contradicts with any physical model assuming an existence of two (non-exchanging) water pools irrespective of their origin. Only more complex models may potentially give rise to an "apparent" dependence of f_f on the orientation (for example, if the orientational dependence of the exchange rates [24] was additionally included in the Kärger model [41]. In such models, however, the apparent dependence of f_f on the orientation would not be arbitrary. In absence of any specific model, using an arbitrary fitting of f_f is not clearly justified and may unfavourably influence the fitting procedure of the other two free parameters.

To the best of our knowledge, voxel-based biexponential tensor analysis of the human brain tissue was performed before in two studies only [31,32]. In the first work, by Clark et al. [31], very simple procedure of fitting two mono-exponential functions independently to each of two points in the low and high ranges of b-values was employed. The whole diapason of b-values was restricted to 3.5 ms $\mu\mathrm{m}^{-2}$. In the second work, by Maier et al. [32], the data points were acquired in a broader range of $b \leq 5.0$ ms $\mu\mathrm{m}^{-2}$ but the biexponential fitting procedure using the orientation constraints on the parameter f_f was step-like. First, the values of f_f were evaluated from the composite attenuation curve and then used as a fixed parameter in separate fits of the fast and slow diffusion tensors to the experimental curves. In this work, we have shown for the first

time that BEDTA is applicable when using the voxel-based approach and setting the relative component sizes as orientation-independent shared parameters. It is thus demonstrated that a physical model assuming an existence of two (non-exchanging) water pools in the human WM can, in principle, be elaborated in agreement with the *in vivo* experimental data. A voxel-based approach allowed us to evaluate and analyse the histograms of the valuable quantitative metrics such as MD_f, MD_s, MD_f/MD_s, f_f, FA_m, FA_f, FA_s, MK, and CMD_s related to the entire slices or specific voxel subsets ($FA_m \leq 0.25$ and $FA_m > 0.25$). In addition, a comprehensive statistical analysis based on the averaged data of the group of 14 subjects was performed. The range of the diffusion weighting factors was extended further to 7.0 ms μm^{-2} and the measurements were carried out at a higher magnetic field strength (3T versus 1.5T in [32]) improving the image quality.

Several maps were evaluated on the basis of combined DKI and BEDTA studies. The map parameters include MD_f, MD_s, f_f, CMD_s, FA_f/CFA_f, FA_s/CFA_s, ACPhi, α_M, $\alpha_\parallel$ and $\alpha_\perp$. The MD_s/CMD_s maps were shown to exhibit better contrast between GM and WM than the conventional ADC maps. It is worth noting that MD_m tends to be rather insensitive to the two tissue types. The mean values related to GM and WM are very close to each other and the anatomical contrast of the directionally averaged ADC maps is typically low. This is despite essential differences in the GM-WM cellular architecture. At the same time, MD_s tends to be about 2–3 times smaller in WM than in GM. Therefore, one can expect an enhanced sensitivity of MD_s/CMD_s to the changes of the tissue microstructure in comparison to the conventional ADC. Besides, the features of the CMD_s histogram (whose low-value component refers predominantly to WM) can be expected to be indicative of changes in pathological cellular conditions such as cell swelling or membrane disruptions.

It is hypothesised here that the FA_s and CFA_s maps could hold promise as novel biomarkers. These maps exhibit considerably higher values than the conventional FA_m maps and visualise more structural details in WM regions. In particular, this was demonstrated, for instance, at the levels of frontal gyrus, anterior cingulate and cuneus. Our

results thus demonstrate that FA_s maps have the potential of essentially improving WM mapping and of revealing otherwise hidden microstructure. The higher value of FA_s maps was previously observed by Maier et al. [32] a few years ago. We believe that this is an important feature as one can expect FA_s to be a more sensitive parameter when monitoring any developmental, degenerative or pathological changes in the WM microstructure which are usually assessed via conventional anisotropy indices. This kind of investigations is currently in progress in our laboratory. In this work, our findings were substantiated quantitatively by the analysis of the corresponding histogram averaged over a large group of 14 subjects: indeed, a significant part of the FA_s histogram was shifted towards significantly higher values in comparison to that of FA_m as clearly demonstrated by Figure 5.10(b).

The colour-coded directional maps of the fast and slow tensors in the human brain, Figures 5.7 and 5.8, were computed for the first time. They show that, in most of WM, the major eigenvectors of the fast and slow tensors tend to be strongly correlated with each other and with the orientations of the mono-exponential tensor. The reasons for the discrepancies observed in a few marked regions (circles in the middle rows of Figures 5.7 and 5.8) are not quite clear and clarification thereof requires further work. As demonstrated in χ^2-maps in Figures 5.3(c) and 5.3(d), fit errors were not enhanced in the highlighted regions and can thus be ruled out as a source of the potential artefact. One viable explanation could be that these regions comprise multiple fibre tracts for which the biexponential model tends to be inadequate and may cause various discrepancies in evaluation of the free parameters.

On a quantitative basis, the correlation of the orientations of the fast and slow tensors was accessed by means of ACPhi maps, see Figure 5.11. The latter demonstrate a high degree of co-alignment in WM regions in contrast to a rather random co-alignment in GM. Potentially, information contained in the CFA_s and ACPhi maps can be utilised for development of valuable complementary, or even new, fibre-tracking tools.

With respect to voxel-based BEDTA, it is important to keep in mind that biexponential fitting is not adequate for curves which exhibit only minor deviations from the mono-exponential function. Due to noise,

however, such deviations always exist. In addition, biexponential fitting tends to lack reliability if the fitted exponentials are not sufficiently differentiated from each other. As shown by our average histograms in Figure 5.6(b), it is worth noting that the values of f_{f} related to non-WM voxels ($\mathrm{FA_m} \leq 0.25$) are distributed in a very broad range. That is, the biexponential fits do not provide a common specific feature for this type of tissue in contrast to our finding in WM ($\mathrm{FA_m} > 0.25$) in which the average histogram shows a well defined peak. Due to these reasons, in our opinion a justification of biexponential decomposition regarding GM remains questionable and requires a separate analysis. A smooth change of the curvature and rather moderate deviations from the exponential function suggest that a continuous distribution of the diffusivities might be a more appropriate model for the quantification of diffusion in GM than BEDTA. However, this type of the analysis was deemed to be beyond the scope of this study; future work will focus on this issue. Regardless, in order to avoid inadequate fitting, in this work BEDTA was restricted only to the regions with sufficiently strong deviations from Gaussian behaviour, i.e. predominantly to WM. A new option for diffusion mapping was suggested based on the combined analysis of the diffusion response with models based on Equations 3.13, 3.16 and 3.24. In the composite maps, voxels showing weak deviations from Gaussian diffusion were quantified by their mean ADCs whereas BEDTA was applied in the remaining voxels. A differentiation of the "weak" and "strong" deviations was made with the help of MK providing a direct unbiased measure of the non-exponentiality.

New map parameters α_{M}, $\alpha_{\parallel}$ and $\alpha_{\perp}$ were proposed as complementary characteristics of the deviations from non-Gaussian diffusion. These parameters evaluated in the frame of BEDTA were shown to produce a contrast related to the underlying fibre structure. Interestingly, whereas WM regions appear rather uniform in the $\mathrm{MD_s}$ maps, the alpha maps reveal differences in different fibre tracts such as internal capsule and ACPhi maps corpus callosum. Thus, more detailed investigations might lead to a better understanding of the relationship between the diffusion mechanisms and the underlying cellular organisation (neuron packing density, cell size, myelination, etc.). In comparison to kurtosis maps, the

α_{M}, $\alpha_{\parallel}$ and $\alpha_{\perp}$ maps produce a weaker GM-WM contrast but exhibit more structural details. As these are new parameters, their potential use remains to be investigated in future work.

The biophysical cause of deviations from patterns of Gaussian diffusion in the brain tissue remains poorly understood. The BEDTA performed in this works implies that at least two water pools exist for which the MSD during the observation time appear different as a result of complex interplay of factors which may include restrictions by cell membranes, permeability, distribution of the axon radii, the density of their packing, exchange with "bound" water, etc. Generally, a discrimination of the specific factors affecting diffusion remains a challenging task which requires further intensive studies involving both an extended range of the b-values and time dependent-diffusion experiments.

The main disadvantages of biexponential tensor analysis are related to the low SNR at high b-values leading to prolonged acquisition times, high sensitivity to bulk motions, and the problems of the numerical minimization algorithms. Despite these drawbacks, BEDTA remains, in our opinion, a model of choice when enhanced information on water diffusion is to be accessed by extending the range of diffusion weightings. BEDTA should logically be combined with DKI as the latter can be easily evaluated from the same experimental curves, and no additional measurements are required. If diffusion weightings are to be restricted to a moderate range of b-values, DKI alone, as the simplest extension of conventional DTI, promises to become a robust and efficient tool in neurological studies and routine clinical applications [95]. In general, our results acquired from healthy volunteers allow us to conclude that a combined DKI and BEDTA framework permits one to significantly enhance information deduced from DW images; based on these results, novel biomarkers are proposed. The full power of the proposed scalar metrics, however, has to be verified in future dedicated studies related to the assessment of tumours, infarcted regions, traumatic injuries, Alzheimer's decease, and cognitive impairments, to name only a few.

5.4.1 Limitations of the study

DW MRI is prone to the effects of bulk motion especially in the range of high b-values. In this study, special motion correction techniques such as cardiac gating or CSF suppression were not applied. Their efficiency in terms of gaining better image quality and reducing the number of acquisitions should be examined in future in order to facilitate clinical applications in acceptable acquisition times. Another limitation concerns the restrictions on the maximal b-values which could not be extended beyond 7.0 ms μm^{-2} due to the safety and hardware limitations set by the manufacturer. Consequently, in some highly ordered WM regions the attenuation of the slow diffusion component even at the highest b-values was insufficient for a reliable determination of the corresponding slope. This problem was ameliorated by setting a low boundary constraint in the biexponential fits. Fortunately, the subset of voxels for which a given constraint was encountered happened to constitute only a small fraction of the total number of voxels in the slice and therefore was uncritical for the analysis performed here.

5.5 Conclusions

Voxel-based, combined DKI and biexponential tensor analysis offers a novel and valuable framework of studying non-Gaussian water diffusion in human brain tissue *in vivo*. Both DKI and BEDTA overcome the limitations of conventional DTI related to the Gaussian assumption and permit one to substantially improve tissue characterisation. DKI represents the simplest extension to DTI but is limited to a range of b-values exceeding the conventional ones by only a factor of two to three. BEDTA, in contrast, can be performed in the full accessible range of diffusion weightings. However, it requires that a sufficient signal attenuation of the slow diffusion component is achieved. In this work, a reasonable attenuation of the slow component was achieved in the majority of the voxels by measurements in a fairly extended range of b-values (up to 7.0 ms μm^{-2}). On the other hand, as an empirical quantification tool, BEDTA is appropriate only in tissue regions in which the deviations from the Gaussian function are sufficiently strong. The identification of such

regions was based on a quantitative assessment of the non-exponentiality of the signal attenuation curve using excess kurtosis as a direct, unbiased criterion. Novel parameter maps were constructed and discussed in the context of their potential perspectives for neurological applications.

An increased GM-WM contrast was demonstrated in the maps of MD_s with respect to conventional metrics. The colour-coded directional maps related to BEDTA were constructed for the first time. The maps of FA_s/CFA_s were shown to substantially improve WM mapping and to visualise more structural details in comparison to the maps of FA_m/CFA_m and FA_f/CFA_f. It was demonstrated that the histogram of FA_s exhibits an additional peak at higher values. This feature tends to be retained also in the average histogram of 14 subjects. It is suggested that FA_s/CFA_s could exhibit an enhanced sensitivity to pathological change due to its considerably larger values in many WM structures and more favourable histograms in comparison to those of FA_m/CFA_m. The colour-coded directional maps demonstrate an overall strong correlation of the major eigenvectors of the fast and slow diffusion tensors. The origin of a few anomalous regions in which the fast-slow tensor orientations were heterogeneously split remains unclear. It is assumed to be due to the superposition of the multiple fibres which cannot be adequately described by BEDTA. Quantitatively, the correlation between the fast-slow tensor orientations was assessed via the ACPhi maps. The latter emphasised the large degree of co-alignment in WM in contrast to the randomly distributed orientations in the non-WM regions. New alpha-maps based on BEDTA were introduced as a complementary tool characterising the degree of deviations from the Gaussian model. In conclusion, we believe that a multi-parameter approach based on combined DKI and BEDTA has the potential to constitute efficient novel biomarkers of developmental and pathological changes in brain WM and could find valuable applications in neurosciences and in clinical practice.

Chapter 6

On the optimal *b*-value range in DKI

Parts of the work presented in this chapter have been published in:
E. Farrher, F. Grinberg, and N.J. Shah. "Optimal b-Value Range in Diffusion Kurtosis Imaging", Proc. Intl. Soc. Mag. Reson. Med., 20, p. 3560, 2012.

6.1 Introduction

A remarkable success in the assessment of non-Gaussian water diffusion was achieved by DKI [36, 95]. It has been shown to be sensitive to the axonal water fraction in WM [166] and was successfully exploited in the assessment of neurological diseases [91,167–169], traumatic brain injuries [170], normal brain maturation [164, 165, 171], and in the estimation of the fibre orientation distribution function [172].

DKI is a straightforward extension of the DTI model in the cumulant expansion of the DW signal attenuation up to second order in the b-value [34,36,95]. The water displacement is characterized by the ADC, D_{app} (ideally the same as in DTI), and the deviation from the Gaussian diffusion behaviour is quantified by the ADK (K_{app}). At least three b-values are required to evaluate K_{app} in a single gradient direction and for the evaluation of the 4^{th}-rank symmetric kurtosis tensor, D_{app} and K_{app} must be evaluated in at least 15 gradient encoding directions [37, 163]. Complementing the conventional DTI parameters, DKI provides addi-

tional rotationally invariants such as the mean kurtosis, transversal and longitudinal kurtosis, and kurtosis anisotropy, which are proposed as promising biomarkers for tissue characterization [37, 164, 166, 173]. Application of the DKI model in the analysis of the DW signal attenuation has demonstrated to reduce the dependence of the DTI metrics on the range of b-values [174], although the dependence of K_{app} has not still been assessed.

Although DKI enables one to analyse the DW signal in the extended range of b-values, several aspects need to be taken into account when choosing the b-value range. Due to the fact that DKI is based on a truncated cumulant expansion, the diffusion metrics, i.e. D_{app} and K_{app} may, in principle, depend on the b-value range. The optimal b-value range is restricted both, on the side of low as well as on the side of high diffusion weightings. On the one hand, DKI must be analysed in a sufficiently large b-value range in order to allow the DW signal to reach a large enough deviation from the Gaussian diffusion behaviour. On the other hand, the b-value range cannot be extended towards arbitrarily large values since applicability of DKI is limited with respect to the maximum allowed b-value, b_{max}, determined by $b_{\mathrm{max}} = 3/\left(D_{\mathrm{app}} K_{\mathrm{app}}\right)$ [36, 95]. For $b > b_{\mathrm{max}}$, this model predicts a non-physical increase of the DW signal and cannot be applied to describe experimental points. Typically, the largest b-values used in human brain DKI studies reported in the literature include 1.8 ms μm^{-2} [171], 2.0 ms μm^{-2} [95, 166, 175], 2.5 ms μm^{-2} [25, 34, 163, 167, 172], 2.8 ms μm^{-2} [176] and 4.0 ms μm^{-2} [30, 177].

While a quantitative estimation of DKI parameters is influenced by a selected range of b-values, a few works have been carried out on the optimisation of the experimental parameters [99,171,178]. Previously, an optimisation scheme for the DW settings was published by D.H. Poot et al. [99], where the Cramér-Rao lower bound of a given DKI parameter of interest is minimized in order to have the optimal DW acquisition scheme (gradient directions and b-values). However, their optimisation was based on an a priori knowledge of the distribution of DKI model parameters in the brain which was evaluated using the conventional approach and the maximum b-value was restricted to 2.8 ms μm^{-2}. One of the instructive

results was to show that, in some cases, increasing the maximum b-value might increase the accuracy of the estimated DKI metrics. In other work, by S.L. Hu et al. [178], the positive definiteness of the kurtosis tensor was analysed both theoretically and numerically. However, within the context of optimisation, the positive definiteness is an insufficient condition as it only guarantees that the DW signal will not become larger than the non-DW signal, but does not prevent the DW signal being an increasing function for increasing b-values.

As DKI applications are becoming more and more prevalent in research and clinical practice, there is an increasing necessity for understanding the influence of the experimental settings on the fitted metrics. Therefore, one of the major aims of this work is to provide a comprehensive investigation of the dependence of DKI metrics on the experimental range of b-values for various gradient directions and for various tissue types. Based on this analysis, we propose a simple voxel-by-voxel optimisation scheme which allows the DW signal to have a sufficiently large deviation from the Gaussian diffusion behaviour, on the one hand, but restricts the range of b-values below $b_{\max}$, thereby excluding a physically meaningless application of the DKI model.

6.2 Theory

In this section, a brief description of the formulae utilised in the analysis is carried out. For a more comprehensive understanding of the underlying theory, the reader is referred to Chapter 3, Section 3.5.

The cumulant expansion of the DW signal $S(b)$ around $b = 0$ up to second order, which is in fact a Taylor expansion of the natural logarithm, $\ln S(b)$, is expressed as:

$$\ln S(b) = \ln S(0) - bD_{\text{app}} + \frac{1}{6}b^2 D_{\text{app}}^2 K_{\text{app}} + \vartheta\left(b^3\right), \tag{6.1}$$

where D_{app} and K_{app} are the so-called ADC and ADK, respectively, and $S_0 \equiv S(b=0)$ [36]. The theoretical minimal kurtosis value is -2, while for Gaussian diffusion it equals zero [95]. In the context of DTI, the second and higher order terms Equation 6.1 are neglected so that the signal takes the form

$$\ln S(b) \approx \ln S(0) - bD_{\text{app}}. \tag{6.2}$$

This truncation is valid provided that $\left|(bD_{\text{app}})^2 K_{\text{app}}/6\right| \ll 1$, and therefore the optimal range of b-values for DTI will depend on the sample considered. If the chosen range is too small, then the signal attenuation will be insufficient for a reliable estimation of the slope (i.e. D_{app}) as a consequence of the influence of the background noise. On the other hand, if the range of b-values is too large, systematic errors will bias the measured D_{app} due to deviations from the Gaussian behaviour of the DW signal [83, 95, 174]. In DKI, the DW signal is obtained by neglecting the third and higher order terms in the cumulant expansion

$$\ln S(b) \approx \ln S(0) - bD_{\text{app}} + \frac{1}{6}b^2 D_{\text{app}}^2 K_{\text{app}}. \tag{6.3}$$

The optimal range of b-values for kurtosis measurement is subject to even more constraints. On the one hand, it must be sufficiently extended in order to enable a significant deviation from the mono-exponential behaviour, which is important for a reliable estimation of K_{app}. On the other hand, the approximation remains valid provided that $|\vartheta(b^3)| \ll 1$. Furthermore, given that $S(b)$ is a monotonically decreasing function of b [36], the valid range of b-values is constrained by an upper boundary, i.e. $b \leq b_{\max}$, where $b_{\max}$ denotes the position of the minimum of Equation 6.3 which is determined by solving the equation $\partial S(b)/\partial b = 0$ [95] and is given by the following expression

$$b_{\max} = \frac{3}{D_{\text{app}} K_{\text{app}}}. \tag{6.4}$$

For $b > b_{\max}$, $S(b)$ will be an increasing function of b, and any fitting of Equation 6.3 in this range will be physically meaningless.

6.3 Methods

6.3.1 DW MRI experiments

In vivo DW MRI experiments were carried out with a whole-body 3T Siemens MAGNETOM Tim-Trio scanner (Siemens Medical Systems, Er-

langen, Germany) using a body coil for RF transmit and a gradient system providing a maximal gradient strength of 40 mT/m. The TRSE EPI pulse sequence was used with the following protocol parameters: repetition-time, T_R = 1300 ms; echo-time, T_E = 109 ms; voxel-size, 2×2×2 mm^3; receive bandwidth, BW = 1446 Hz/pixel; matrix-size, 128×128. Diffusion attenuations were measured for a set of 26 b-values in the range 0-5.0 ms μm^{-2} with an increasing step of 0.2 ms μm^{-2}. Due to acquisition time constraints, the number of diffusion gradient directions was set to 6. Three subjects were measured with different number of averages and slices, in order to assess the robustness of the approach. The subjects have provided a written, informed consent. The numbers of slices/averages were: subject 1, 2/6; subject 2, 6/16; subject 3, 8/16. All slices were taken parallel to the anterior-posterior-commissures (AC-PC) line. Experiments for subjects 1 and 2 were acquired with a 32-channel phased array coil and for subject 3, the data were acquired with a 12-channel phased array coil.

6.3.2 Data processing

All the non-DW images from experiments 1 and 2 for each subject were coregistered using the FLIRT method with the affine 12-parameter model available in FSL [179–181] and the estimated motion parameters were applied to the corresponding sets of DW images. Spatial smoothing with a Gaussian convolution kernel was applied to the DW images (standard deviation of 0.65). The bias in the DW images due to background noise was reduced using the PI method [123,124], while the ML estimator was used to evaluate the standard deviation of the background noise [120,122] (See Chapter 3, Section 3.10).

Non-linear fitting of Equation 6.3 to the normalized and noise bias-corrected experimental data, $S_{\mathbf{e}}(b)$, was done by minimizing the objective function

$$f_n = \sum_{i=1}^{n} S_e(b_i)^2 \left[\ln S(b_i) - \ln S_{\mathrm{e}}(b_i)\right]^2, \tag{6.5}$$

where $n = 3 \ldots 26$, denotes the subscript of the largest b-value considered in the fitting, hereafter called b_n. In order to avoid non-physical fits and

numerical problems in the evaluation of Equation 6.4, the following constraints were applied: $10^{-2} \leq D_{\text{app}} \leq 3.0$ μm^2 ms^{-1} and $10^{-3} \leq K_{\text{app}}$. In practice, the lower constraint in K_{app} was encountered only in a few voxels in the CSF, where the theoretical kurtosis value is zero. In this work, we will skip the discussion on CSF voxels since the expected behaviour is largely exponential and any observed deviations might reflect the influence of noise and/or physiological motion [34]. Due to the fact that Equation 6.3 is a truncated Taylor expansion of the logarithm of the DW signal around $b = 0$, its precision with respect to the underlying DW signal is b-value dependent. To account for this, the objective function f_n includes a weighting factor given by a monotonically decreasing function of b, $S_{\text{e}}(b)^2$. All diffusion experimental data were processed using in-house Matlab scripts (Matlab, The MathWorks, Natick, MA, USA).

Minimization of Equation 6.5 was performed for 21 ranges of b-values $[0, \ldots, b_n]$ on a voxel-by-voxel basis using the Nelder-Mead algorithm. The value of b_n was increased in steps of 0.2 ms μm^{-2} from 1.0 ms μm^{-2} (range 1) up to 5.0 ms μm^{-2} (range 21). The dependence of the parameters D_{app} and K_{app} on b_n was assessed for each gradient direction individually. The mean parameters $\langle D_{\text{app}} \rangle$ and $\langle K_{\text{app}} \rangle$ were evaluated as the average of D_{app} and K_{app} over the gradient directions. Hereafter, the notation $\langle \ldots \rangle$ refers to the average of the corresponding parameter over gradient directions. Unless specified otherwise, all results are shown for subject 1.

In order to show the dependence on b_n of a given parameter, the histograms of D_{app}, $\langle D_{\text{app}} \rangle$, K_{app}, $\langle K_{\text{app}} \rangle$, b_{max} and $\langle b_{\text{max}} \rangle$ were evaluated for all values of b_n individually and put consecutively one next to each other in order to build the surfaces showing such dependence. The number of bins in each of the conventional histograms, i.e. fixed value of b_n, was set to 70. Afterwards, the built surfaces were smoothed by applying a bilinear interpolation function.

6.4 Results

6.4.1 Dependence of D_{app} and K_{app} on b_n

Figure 6.1(a) shows the DW signal attenuations from a ROI selected in WM (6 adjacent voxels in the corpus callosum) for two gradient directions. The angles between these directions with respect to the preferential fibre orientations were $\theta_1 = (85\pm2)^\circ$ (circles) and $\theta_2 = (27\pm3)^\circ$ (squares).

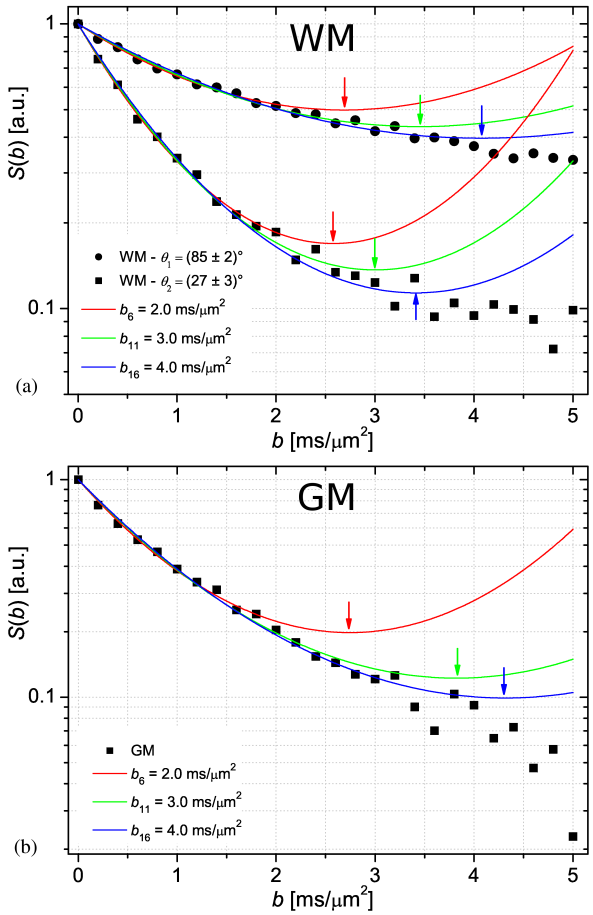


Figure 6.1: *DW signal attenuation for two gradient directions selected in a ROI in the WM (a) and a single gradient direction in GM (b). The corresponding ROIs are shown by the cyan arrows in Figure 6.4. Solid lines denote the fits of Equation 6.3 for three ranges of b-values: 0 - 2.0* ms μm^{-2} *(red), 0 - 3.0* ms μm^{-2} *(green), 0 - 4.0* ms μm^{-2} *(blue). The minimum of each fitted function is shown by the corresponding arrow.*

The fibre orientation was determined by the eigenvector associated to the largest eigenvalue of the conventional diffusion tensor. Figure 6.1(b) depicts the signal attenuation from the ROI (6 adjacent voxels) selected in GM. The attenuation curve is shown for one gradient direction since the directional dependence was negligible. The position of the ROIs is shown by the cyan arrows in Figure 6.4. In Figures 6.1(a) and 6.1(b), the fits of Equation 6.3 for three different ranges of b-values are shown by the solid curves: $b_6 = 2.0$ ms μm^{-2} (red), $b_{11} = 3.0$ ms μm^{-2} (green) and $b_{16} = 4.0$ ms μm^{-2} (blue). For each fitted curve, the positions of the minima at $b_{\max}$ are shown by the arrows in the corresponding colour. Table 6.1 shows the values of $b_{\max}$ for each fitting range. Three features of these fittings should be emphasized: i) $b_{\max}$ is an increasing function of b_n; ii) $(b_{\max} - b_n) \to 0$ for increasing b_n; iii) in WM $b_{\max}$ depends on the gradient direction within the same fitting range, i.e. the larger the angle between the gradient and main fibre direction, the larger $b_{\max}$ (Figure 6.1(a)).

	$b_{\max}$ [ms μm^{-2}]		
b_n [ms μm^{-2}]	WM, $\theta_1 \approx 85°$	WM, $\theta_2 \approx 27°$	GM
2.0	2.69 ± 0.04	2.60 ± 0.10	2.75 ± 0.08
3.0	3.45 ± 0.02	3.01 ± 0.08	3.82 ± 0.06
4.0	4.07 ± 0.02	3.41 ± 0.07	4.32 ± 0.04

Table 6.1: *The values of $b_{\max}$ for the three fitting ranges shown in Figures 6.1(a) and 6.1(b), for WM (2 directions) and GM (1 direction). θ_1 and θ_2 are the angles between the given gradient direction and the eigenvector of the conventional diffusion tensor associated to the largest eigenvalue.*

Figures 6.2(a) - 6.2(d) demonstrate the dependence of D_{app} (a,b) and K_{app} (c,d) on b_n for WM (a,c) and GM (b,d), evaluated from the DW signal attenuations in Figures 6.1(a) and 6.1(b). They demonstrate that the fitting parameters D_{app} and K_{app} as well as their standard deviations decrease with increasing b_n in both WM and GM. In WM, D_{app} decreases by approximately (25 ± 3) % and (15 ± 1) % for $\theta_1 = 85°$ (red) and $\theta_2 = 27°$ (black), respectively, in the range of b_n, from $b_{11} = 1.0$ ms μm^{-2} to $b_{26} = 5.0$ ms μm^{-2}. In GM, the observed decrease in D_{app} is about (22 ± 1) %. A significantly stronger dependence was observed for K_{app}.

In WM, the decrease in K_{app} is about (51 ± 5) % and (38 ± 4) % for the red and black curves, respectively. The decrease in GM is about (59 ± 2) %.

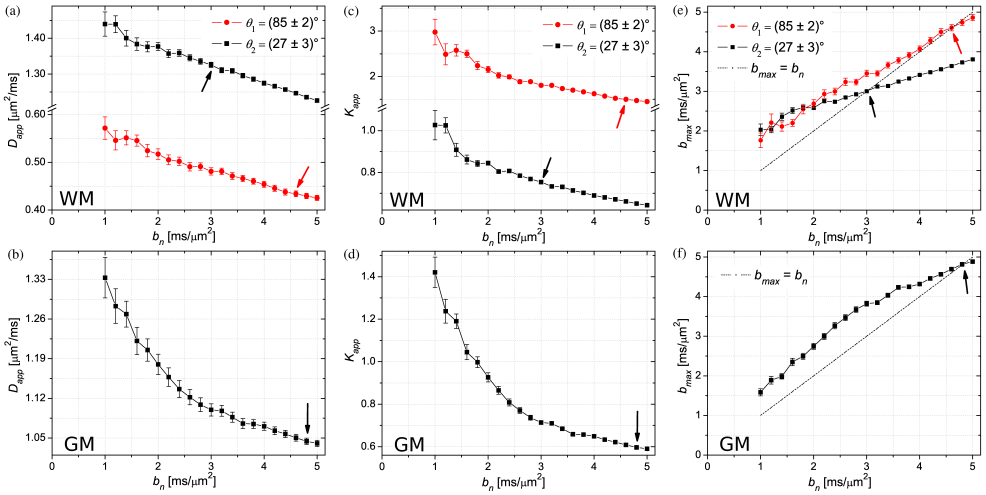


Figure 6.2: *Fitted values of* D_{app} *(a,b) and* K_{app} *(c,d) and the evaluated* b_{max} *(e,f), as a function of* b_n *for WM (a,c,e) and GM (b,d,f). The error bars correspond to the values of the standard deviations* σ_{D} *(a,b) and* σ_{K} *(c,d), assessed in the fitting, and the corresponding error propagation using* σ_{D} *and* σ_{K} *(e,f).*

Figures 6.2(e) and 6.2(f) show how the values of b_{max} evaluated from the fitted values D_{app} and K_{app} depend on b_n. One can see that in the range of low b_n, $b_{\text{max}}(b_n) > b_n$. As already indicated above, $[b_{\text{max}}(b_n) - b_n] \to 0$ with increasing b_n, so that $b_{\text{max}}(b_n) = b_n$ (i.e. there is a fitting b-value range for which the value of b_n equals the evaluated b_{max}) at a certain value of b_n (see crossing of the curves $b_{\text{max}}(b_n)$ with the dashed lines representing the function $h(b_n) = b_n$). Further increase of b_n results in $b_{\text{max}}(b_n) < b_n$, leading to the physically unjustified increase of the kurtosis function (Equation 6.3) in the fitting range. In the following sections, we will denote this critical value of b_{max} for which $b_{\text{max}}(b_n) = b_n$ as b^*_{max}. It represents the superior boundary for the validity of the kurtosis approach, Equation 6.3. In Figures 6.2(a) - 6.2(f), the values of b^*_{max} are shown by arrows. An important observation here is that b^*_{max} (and thus the validity range) strongly depends on: a) the tissue type (GM or WM), and b) on the gradient orientation in WM (compare, for example,

the value of $b^*_{\max}$ equal to ~ 3.0 ms μm^{-2} for $\theta_1 = 27°$ and ~ 4.6 ms μm^{-2} for $\theta_2 = 85°$).

Figures 6.3(a) - 6.3(i) show the dependence of the histograms of D_{app} (a), $\langle D_{\text{app}} \rangle$ (b), K_{app} (d), $\langle K_{\text{app}} \rangle$ (e), $b_{\max}$ (g), and $\langle b_{\max} \rangle$ (h) on b_n, evaluated over 4 slices in subject 1, and the average of the histograms of $\langle D_{\text{app}} \rangle$, $\langle K_{\text{app}} \rangle$ and $\langle b_{\max} \rangle$ over the three subjects (c,f,i). One can observe that the peak of D_{app} and $\langle D_{\text{app}} \rangle$ show a similar behaviour when b_n increases. Moreover D_{app} decreases by ~ 7 % for the whole range of b_n while the decrease in $\langle D_{\text{app}} \rangle$ and its average over the three volunteers is ~ 8 %.

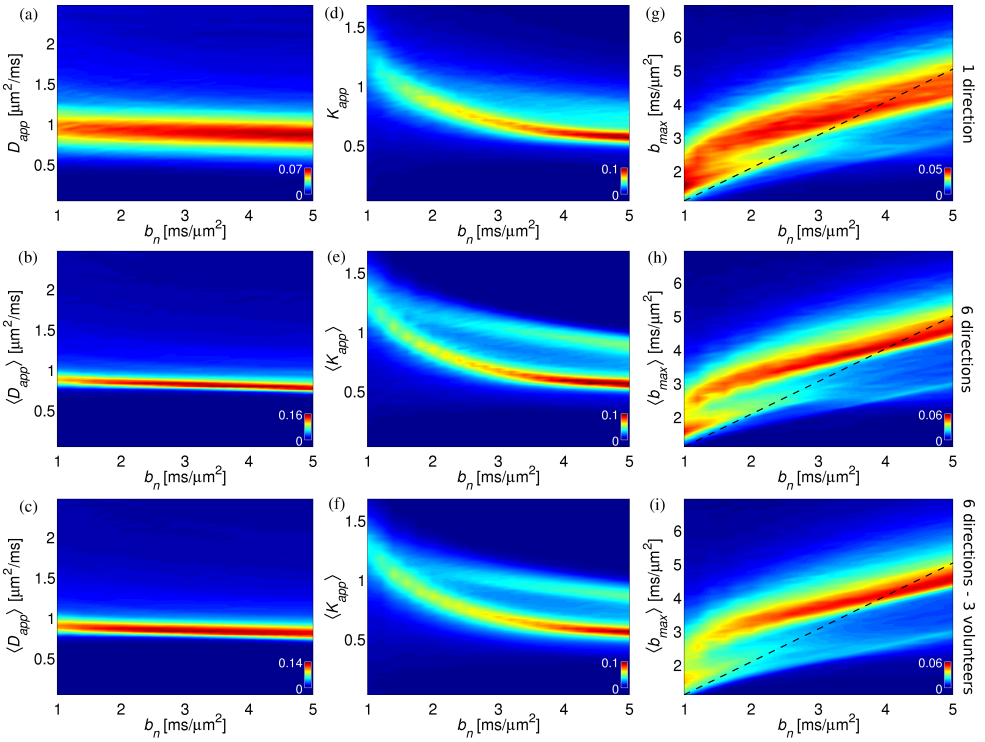


Figure 6.3: *Dependence of the histograms of* D_{app} *(a),* K_{app} *(d),* $b_{\max}$ *(g),* $\langle D_{\text{app}} \rangle$ *(b),* $\langle K_{\text{app}} \rangle$ *(e)* $\langle b_{\max} \rangle$ *(h) on* b_n *evaluated for subject 1, and the histograms of* $\langle D_{\text{app}} \rangle$, $\langle K_{\text{app}} \rangle$ *and* $\langle b_{\max} \rangle$ *averaged over the three subjects (c,f,i). Each individual histogram (*b_n *fixed) was built by dividing the corresponding range in 70 bins. The colour of each histogram refers to the number of normalized counts. The dashed black lines in Figures (g) - (i) denote the function* $h(b_n) = b_n$.

b_n [ms μm^{-2}]	2.0	2.4	2.8	3.2	3.6	4.0
1 dir [%]	9.3	15.0	20.2	24.8	32.8	43.3
6 dirs [%]	8.0	13.6	19.3	25.1	32.2	41.7

Table 6.2: *Percentage of voxels where the condition $b_n < b_{\max}$ is violated, for the fitting ranges shown in Figure 6.4, for a single gradient direction (first row) and for 6 gradient directions (second row), for a single slice.*

The dependence of the diffusional kurtosis on b_n is stronger than in the case of diffusivities. The peak value in the histogram of K_{app} shows a decrease of ~ 55 % in the whole range of b_n. Interestingly the peak shown in the histogram of $\langle K_{\text{app}} \rangle$ splits into two peaks for $b_n > 1.8$ ms μm^{-2}. In the case of the average of $\langle K_{\text{app}} \rangle$ over volunteers, the split occurs for $b_n > 2.2$ ms μm^{-2}. These two peaks are attributed to WM (upper peak) and GM (lower peak). Similar to Figures 6.2(e) and 6.2(f), the dashed black lines in Figures 6.3(g) - 6.3(i) denote the function $h(b_n) = b_n$. It should be noted that for a fixed value of b_n, the sum of the counts in the part of the histogram below the dashed line corresponds to the fraction of voxels in which the condition $b_n < b_{\max}$ is violated. At low values of b_n, the condition $b_n < b_{\max}$ remains valid for almost all the voxels (most of the counts remain above the dashed line).

Figure 6.4 shows the maps D_{app}, $\langle D_{\text{app}} \rangle$, K_{app} and $\langle K_{\text{app}} \rangle$ for six fitting ranges with the following fixed values of b_n: $b_6 = 2.0$ ms μm^{-2}, $b_8 = 2.4$ ms μm^{-2}, $b_{10} = 2.8$ ms μm^{-2}, $b_{12} = 3.2$ ms μm^{-2}, $b_{14} = 3.6$ ms μm^{-2} and $b_{16} = 4.0$ ms μm^{-2}. The maps D_{app} and $\langle D_{\text{app}} \rangle$ show a slight dependence on b_n. On the other hand, one can observe that for small values of b_n the maps of K_{app} and $\langle K_{\text{app}} \rangle$ are noisier in general, and contain more artefacts such as the black spots shown in the corpus callosum (zoomed illustrations will be shown below). With increasing b_n, the artefacts in kurtosis maps tend to reduce. However, while improving kurtosis evaluation in some voxels, increasing b_n leads to an increase of the fraction of voxels in which the condition $b_n < b_{\max}$ is violated. This is demonstrated in Table 6.2 which shows the fraction of such voxels both for a single gradient direction (first row) and for all 6 gradient directions (second row).

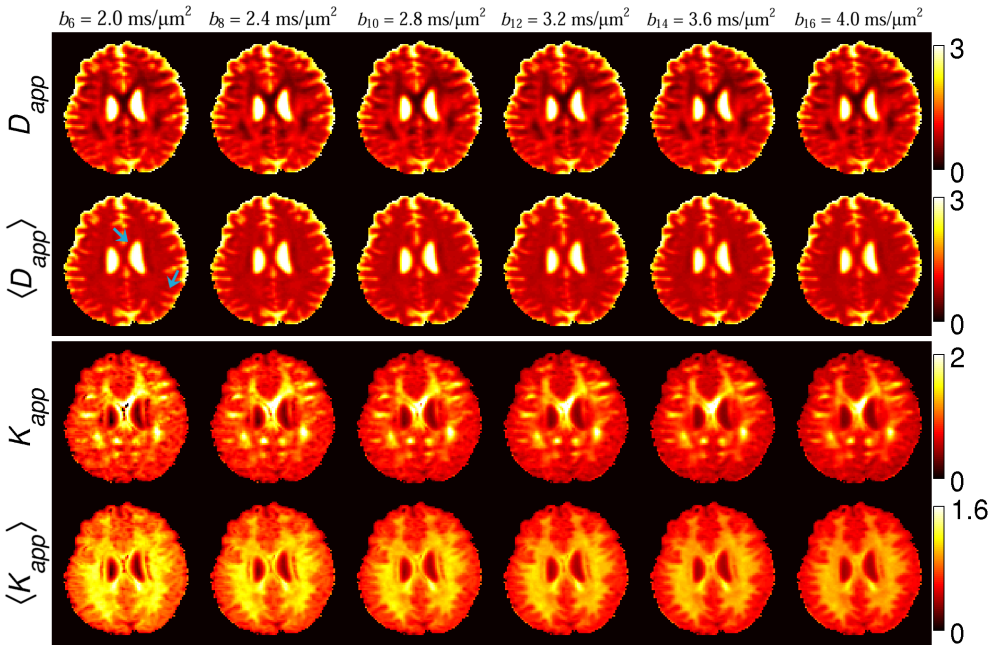


Figure 6.4: *The maps of* D_{app}, $\langle D_{\text{app}} \rangle$, K_{app} *and* $\langle K_{\text{app}} \rangle$ *for six fitting b-value ranges with the following values of* b_n*:* $b_6 = 2.0$ ms μm^{-2}, $b_8 = 2.4$ ms μm^{-2}, $b_{10} = 2.8$ ms μm^{-2}, $b_{12} = 3.2$ ms μm^{-2}, $b_{14} = 3.6$ ms μm^{-2} *and* $b_{16} = 4.0$ ms μm^{-2} *(from left to right). Cyan arrows show the position of the ROIs discussed in Figures 1 and 2.*

6.4.2 Maps of b^*_{max}

The results presented so far show that, in the range of b_n considered here, b_{max} is an increasing function of b_n with a slope approximately less than one (Figures 6.3(g) - 6.3(i)) ensuring the existence of a value b^*_{max} such that $b_{\text{max}}\,(b^*_{\text{max}}) \approx b_n$ (we use the symbol "$\approx$" here since we have a discrete set of values of b_n). A simple algorithm was proposed in order to evaluate the maps of b^*_{max} on a voxel- and direction-based manner (shown in Appendix 6.7).

The maps of b^*_{max} for two selected gradient directions evaluated with the help of the former algorithm are shown in Figures 6.5(a) and 6.5(b). Figure 6.5(c) shows the directionally averaged map of b^*_{max}, $\langle b^*_{\text{max}} \rangle$. Clearly, the maps of b^*_{max} significantly change for different gradient directions in WM regions (compare Figures 6.5(a) and 6.5(b)). In GM, the values of b^*_{max} tend to be larger than in WM and rather homogeneous. Interest-

ingly, voxels affected by PVE, that is, "blue stripes" along the contour line of GM and the ventricles, show rather small values, $b^*_{\max} \approx (2.4 \pm 0.7)$ ms μm^{-2}.

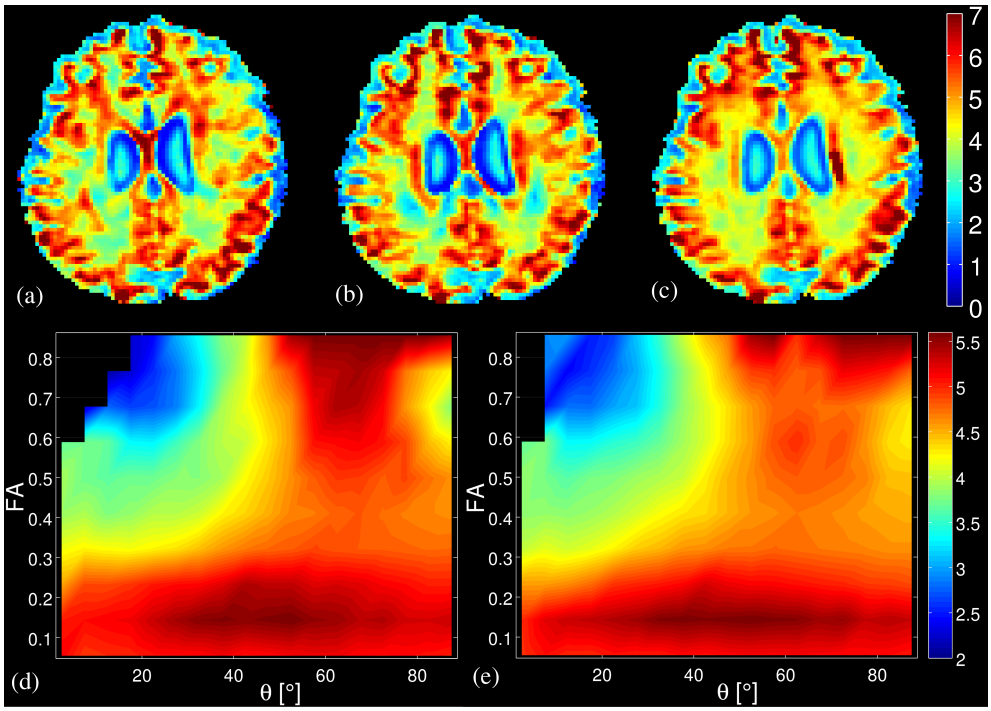


Figure 6.5: *The maps of $b^*_{\max}$ for two selected gradient directions (a,b) and its average over six gradients directions, $\langle b^*_{\max} \rangle$ (c). The correlation of $b^*_{\max}$ with FA and the angle between the gradient direction and the eigenvector of the diffusion tensor linked to the main eigenvalue, θ, for subject 1 (d) and the average of the map over the three subjects (e). The size of each bin in the maps is 5° in the θ-dimension and 0.09 in the FA-dimension.*

The correlation of $b^*_{\max}$ with the FA of the tissue and the angle (θ) between the gradient direction and the major eigenvector of the diffusion tensor (i.e. linked to the largest eigenvalue) is shown by the map in Figure 6.5(d). The average of that surface over the three subjects is shown in Figure 6.5(e). In the construction of the correlation surfaces, the aim was to demonstrate the differences between GM and WM tissues. Due to this reason, the CSF and PVE-affected voxels where omitted using a binary mask. The represented surfaces clearly demonstrate that $b^*_{\max}$ is orientationally independent in the GM regions, i.e. $FA < 0.25$, and has an average value of $\sim (5.2 \pm 0.1)$ ms μm^{-2}. It can be also observed

that the higher FA, the stronger is the dependence of $b^*_{\max}$ on θ. For the largest values of FA, $b^*_{\max}$ changes from $\sim$ 1.5 ms μm^{-2} at $\theta \approx 0°$ up to $\sim$ 5.1 ms μm^{-2} at $\theta \approx 90°$. The same features are observed in the averaged surface shown in Figure 6.5(e).

6.4.3 An optimized voxel-based evaluation of K_{app}

A voxel-based optimisation of the b-value fitting range is proposed in this section, based on the gradient-direction dependent maps of $b^*_{\max}$. In each voxel and for each gradient direction, we set the value of b_n to $\beta \times b^*_{\max}$, where β is empirically taken as 0.7. Thus, two facts can be ensured: i) $b_n < b^*_{\max}$ and no meaningless fitting of Equation 6.3 is carried out, and ii) b_n provides a sufficient extended range for each individual curve, $S(b)$, to develop a large enough deviation from the mono-exponential behaviour.

In Figures 6.6(a) - 6.6(d) we compare the maps of K_{app} and $\langle K_{\text{app}} \rangle$ evaluated within the conventional approach using a fixed fitting range for all measured DW signal attenuations (Figures 6.6(a) and 6.6(b)) with the maps using the optimized voxel-based approach (Figures 6.6(c) and 6.6(d)). The maps in Figures 6.6(a) and 6.6(b) are shown for two values of b_n: $b_6 = 2.0$ ms μm^{-2} (left) and $b_8 = 2.4$ ms μm^{-2} (right). Zoomed regions delineated by the cyan rectangle are shown below each image. The black arrows indicate those voxels where a drop out of the diffusional kurtosis is observed under the conventional approach of a fixed b-value range. These artefacts are more pronounced for b_6 than for b_8. In the optimized approach (Figures 6.6(c) and 6.6(d)), these artefacts are practically eliminated and the corpus callosum presents with a rather homogeneous appearance (black arrows). As another example of this feature, a more homogeneous appearance of the anterior thalamic radiation is also observed in the optimized approach compared to the conventional one (shown by the black ovals). Another significant feature of this approach is the appearance of a more clearly defined contour line between GM and WM compared to the conventional approach, as shown by the green arrows. Finally, the optimized approach shows an increase of kurtosis values in the contour line between GM and CSF as shown by the cyan arrows.

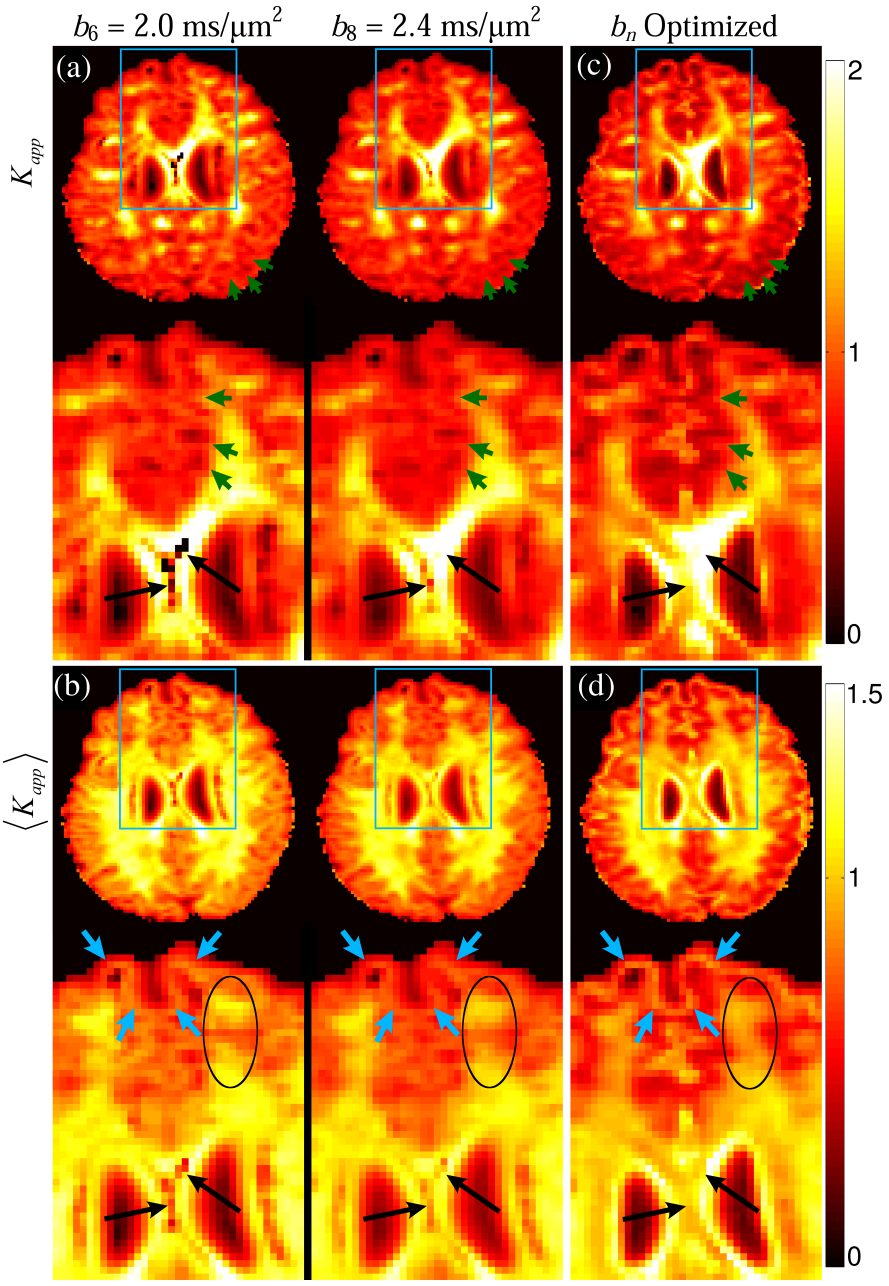


Figure 6.6: *Maps of* K_{app} *and* $\langle K_{\mathrm{app}} \rangle$ *evaluated within the conventional approach using two fixed fitting ranges for all DW signal attenuations (a,b):* $b_6 = 2.0$ ms μm^{-2} *(left) and* $b_8 = 2.4$ ms μm^{-2} *(right), and the optimized voxel- and direction-based fitting range (c,d). Zoomed regions delineated by the cyan rectangle are shown below each image. The black arrows indicate the voxels where a drop out of the diffusional kurtosis is observed. Cyan arrows shown the voxels affected by PVE where the diffusional kurtosis is enhanced.*

6.4.4 Clinically relevant approach

In this section we consider the optimisation approach under clinically relevant conditions, i.e. with a reduced number of measured b-values. We apply the former approach to a data subset of 5 b-values: (0, 1.0, 2.0, 3.0, 4.0) ms μm^{-2}. Figures 6.7(a) - 6.7(d) provide a comparison of kurtosis maps using the fixed fitting ranges (a, b): [0, 1.0, 2.0] ms μm^{-2} (left) and [0, 1.0, 3.0] ms μm^{-2} (right) and the optimized approach (c, d). As can be observed, the maps of both K_{app} (a) and $\langle K_{\text{app}} \rangle$ (b) evaluated using the fixed ranges exhibit artefacts in the corpus callosum similar to those demonstrated with the full data sets in Figures 6.6(a) and 6.6(b): see drop outs in the highlighted area (cyan rectangle). These drop outs are essentially ameliorated in the optimized maps (Figures 6.7(c) and 6.7(d)).

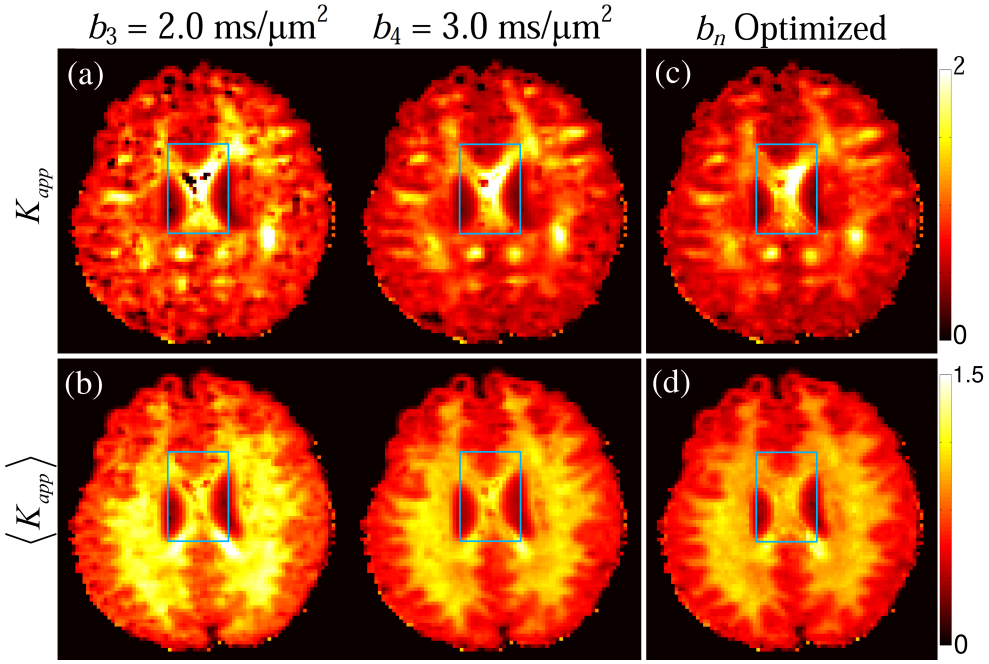


Figure 6.7: *Maps of K_{app} (a,c) and $\langle K_{\text{app}} \rangle$ (b,d) evaluated using the fixed fitting ranges (a,b): [0,1.0, 2.0]* ms μm^{-2} *(left) and [0, 1.0, 3.0]* ms μm^{-2} *(right) and the optimized approach (c,d). Areas delineated by cyan lines show the voxels where the evaluated diffusional kurtosis suffers a drop out.*

6.5 Discussion

The magnitude of deviations from the Gaussian model is tissue specific and provides useful information on the complexity of the diffusion processes and the tissue microstructure. DKI represents the simplest model-free approach for quantifying these deviations that can be applied under clinical conditions. However, being a rather novel approach, no consensus currently exists on the optimal b-value range. In this work, we performed for the first time a detailed characterization of the dependence of the DKI metrics on the b-value range (0 - 5.0 ms μm^{-2}) with incremental steps of 0.2 ms μm^{-2} (Figures 6.2, 6.3 and 6.4). We have shown that using Equation 6.3 to fit the DW signal, the metrics D_{app} and K_{app} (and therefore b_{max}) show a dependence on the largest b-value utilized in the fitting. First, it was demonstrated that the water diffusivity is a slightly decreasing function of the largest b-value used in the fitting process (Figures 6.3(a) - 6.3(c)) in the whole brain. On average, the observed decrease of D_{app} was rather small, $\sim 7-8$ %. However, some voxels located predominantly in the corpus callosum, exhibited relatively higher variation of D_{app} ($\sim 15-25$ %) as demonstrated in Figures 6.2(a) and 6.2(b). In this regard, an analysis of the behaviour of D_{app} has been discussed by Veraart et al. [174] using an approach of histograms for different anatomical regions, although within a smaller and less dense range of b-values (up to $b = 2.8$ ms μm^{-2}). Their main conclusion was that DKI provides more stable estimations of D_{app} (and diffusion tensor derived metrics) than DTI. On the other hand, our results show that, in contrast to the behaviour of D_{app}, K_{app} strongly depends on the b-value range (Figures 6.3(d) - 6.3(f)).

DKI evaluation using the fixed range of b-values reveals two typical problems. The first problem arises if the fitting range is too small (i.e. approximately $b_n \sim< 2.2$ ms μm^{-2}), in which case the deviations of $S(b)$ from the Gaussian behaviour in many voxels/directions are insufficient for a reliable quantification (i.e. the second order term in the cumulant expansion, $(bD_{\text{app}})^2 K_{\text{app}}/6$, is comparable to the noise level). Consequently, the estimation of K_{app} will be subject to high errors, leading to the drop outs in K_{app} and $\langle K_{\text{app}} \rangle$ observed at the corpus callosum in some cases (Figures 6.4(c), 6.4(d), 6.6(a) and 6.6(b)). These drop

outs of the diffusional kurtosis are improved by increasing b_n as shown in Figures 6.4(c) and 6.4(d). However, increasing b_n leads us to the second problem which while improving the fitting conditions in one part of the voxels/directions, it significantly increases the fraction of voxels/directions in which the condition $b_n < b_{\max}$ is violated (Table 6.2).

The observed linear increase of $b_{\max}(b_n)$ with a slope whose global behaviour is less than one (as shown in Figures 6.3(g) - 6.3(i)) allowed as to define a superior boundary for the maximum physically permitted b-value in DKI, $b^*_{\max}$, as the value of b_n for which $b_{\max}(b_n) = b_n$. A simple algorithm has been proposed to estimate $b^*_{\max}$. Here, it is worth mentioning that the smaller the incremental steps of b_n, the larger is the accuracy in the evaluation of $b^*_{\max}$. Besides, the b-value range must be large enough to ensure that $b^*_{\max}$ will be encountered. Our results have demonstrated that $b^*_{\max}$ is both tissue dependent (GM & WM), and directionally dependent in WM. The maps of $b^*_{\max}$ (Figure 6.5(c)) show that the average value $b^*_{\max}$ is ~ 5.2 ms μm^{-2}, ~ 4.3 ms μm^{-2} and ~ 2.4 ms μm^{-2} for GM, WM and PVE-voxels (blue stripes around GM in Figures 6.5(a) - 6.5(c)), respectively.

In the context of the above numbers, it is useful to compare our results on $b_{\max}$ with the radius of convergence of a power series discussed by V. Kiselev et al. [34]. According to their study, the range of applicability of a cumulant expansion, e.g. Equation 6.3, depends on its convergence radius, b_c, for which the series converges only if $b < b_c$ [182]. In Reference [34], the parameter b_c was calculated analytically for the special case of the biexponential model. Their experiments exhibited a value of $b_c \sim 3.8$ ms μm^{-2}, ~ 2.4 ms μm^{-2} and ~ 1.3 ms μm^{-2} for GM, WM (directionally averaged) and PVE-voxels, respectively. Interestingly, similar to the behaviour of b_c, the average of $\langle b^*_{\max} \rangle$ show large values in GM (~ 5.2 ms μm^{-2}), intermediate values in WM (~ 4.3 ms μm^{-2}) and rather small values in PVE-affected voxels (~ 2.4 ms μm^{-2}).

Based on the estimated maps of $b^*_{\max}$, we have proposed a simple, voxel- and direction-based scheme, for the optimisation of the range of b-values for DKI based on the application of Equation 6.3 to describe the DW signal. As a compromise of the previously discussed points, the fits of Equation 6.3 were carried out up to the value of $b_n \approx 0.7 \times b^*_{\max}$

(given our discrete set of b-values). Thus, for every voxel and gradient direction, the condition $b_n < b_{\max}$ is ensured. On the other hand, as depicted in Figures 6.6(c) and 6.6(d), the optimized range eliminates the drop outs of K_{app} and $\langle K_{\text{app}} \rangle$.

Voxels affected by PVE exhibited an increase in kurtosis values (cyan arrows in Figures 6.6(c) and 6.6(d)) compared to results obtained with the conventional approach (cyan arrows in Figures 6.6(b) and 6.6(d)). These high kurtosis values arise due to a superposition of two signals from compartments with different diffusivities (CSF and tissue) in the same voxel (provided that each of the contributions is not negligible). Since the attenuation of the CSF signal is much faster (fast diffusion) than that of the tissue, the composite DW signal attenuation happens to be highly non-Gaussian. The deviations from the Gaussian diffusion behaviour is especially pronounced in the range of low b-values due to the high diffusivity of CSF (typically in the range of $b \sim< 1.0$ ms μm^{-2} according to our results). In our optimized approach, the signal in the PVE voxels was fitted up to approximately $b_4 \approx 1.6$ ms μm^{-2} which is the b-value range where the DW signal is highly non-Gaussian. However, when the conventional approach of fixed b-value ($b >\sim 2.0$ ms μm^{-2}) is used, this characteristic is smoothed out.

Regarding clinically relevant experimental conditions, that is, in which the number of b-values is limited (5 in our experiments), our results have clearly demonstrated that the optimized approach can eliminate drop outs and underestimations of the diffusional kurtosis parameters (as shown in Figure 6.7). With respect to the enhancement of kurtosis values in the voxels affected by PVE, it is worth mentioning that this effect appears only if sufficient experimental points are acquired in the range of b-values 0-1.0 ms μm^{-2}. In the clinically relevant optimisation approach, however, this range is not sampled with a sufficiently small step of b-values and therefore the enhancement of the PVE-affected voxels cannot be observed. However, it is clear that a voxel- and direction-based optimisation of the fitting b-value range under the clinically relevant conditions improves the kurtosis estimation of the human brain tissue.

6.6 Conclusions

In this Chapter, we have carried out a detailed evaluation of the dependence of DKI metrics on the range of b-values used in the fitting process. It was demonstrated that, while the evaluated ADC of water molecules is slightly dependent on the b-value range, the corresponding diffusional kurtosis values change dramatically. Based on this analysis, we have proposed an experimental approach to estimate the maximum b-value allowed in DKI for each DW signal attenuation curve individually. This value was demonstrated to be tissue-dependent (WM - GM) and it was found to be strongly dependent on the gradient direction in WM.

We proposed a simple optimisation approach for the fitting b-value range to allow the DW signal to reach a sufficiently large deviation from the mono-exponential behaviour, on the one hand, and to fulfil the requirements imposed for the validity of the DKI analysis, on the other hand. This approach has been shown to significantly improve the diffusional kurtosis evaluation, especially in those regions where a deviation from the Gaussian behaviour of the DW signal is not sufficiently strong (i.e., the range of b-values is not sufficiently large), and is troublesome in the evaluation of DKI metrics. Finally, the feasibility of the optimized approach under clinically relevant conditions has been examined and discussed.

6.7 Appendix 6.A. Algorithm for the assessment of $b^*_{\max}$

Here we describe the algorithm to estimate the value of $b^*_{\max}$ for each gradient direction on a voxel-by-voxel basis by step-wise incrementing b_n and evaluating $b_{\max}$ from the fitted values of D_{app} and K_{app}, up to the largest b_n that fulfilled the condition $b_n < b_{\max}$. A schematic representation of the algorithm is shown in Figure 6.8. It includes the following steps:

1. Minimization of the objective function f_n (Equation 6.5) starting at a relatively low value of b_n (in this work the starting value was 1.0 ms μm^{-2}).

2. Evaluate $b_{\max}(b_n)$ from the fitted values of D_{app} and K_{app}.

3. If $b_{\max}(b_n) > b_n$ the index n is incremented to $n+1$ and the algorithm starts from step 1; if $b_{\max}(b_n) < b_n$, then $b^*_{\max} \equiv b_{\max}(b_{n-1})$; if $b_{\max}(b_n) = b_n$, then $b^*_{\max} = b_n$.

4. If the largest experimental b-value is reached and still $b_{\max}(b_n) > b_n$, then it is assumed that $b^*_{\max} = b_{\max}(b_n)$.

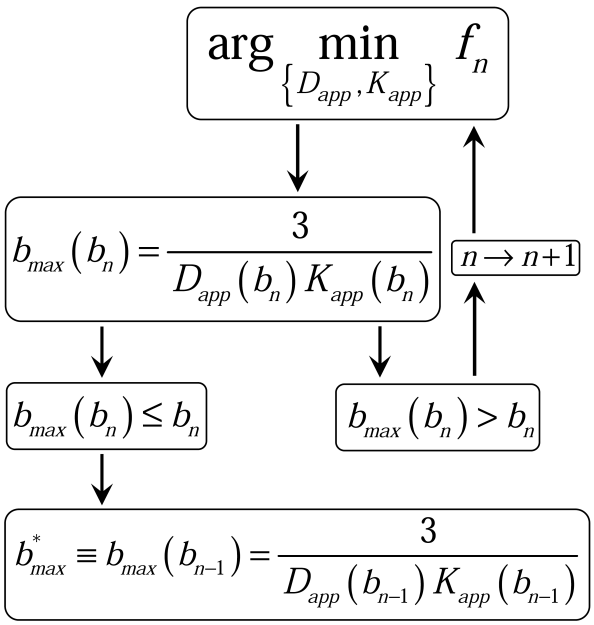


Figure 6.8: *A schematic representation of the algorithm for the evaluation of* $b^*_{\max}$.

Chapter 7

DKI and statistical approach in stroke animal models

Parts of the work presented in this chapter have been published in:
F. Grinberg, L. Ciobanu, E. Farrher, and N.J. Shah. "Diffusion kurtosis imaging and log-normal distribution function imaging enhance the visualisation of lesions in animal stroke models", NMR in Biomedicine, Vol. 25, Nr. 11, p. 1295–1304, 2012.

7.1 Introduction

DW MRI has been established as a major tool for the early detection of stroke and the characterisation of tissue affected thereafter [183–187]. Ischaemic lesions manifest themselves within the first 30 minutes after the onset of stroke via a hyperintense signal in DW images or strongly reduced ADCs. This is different from other conventional MRI modalities which exhibit changes hours later [184,188], often in correlation with the development of vasogenic oedema. The biophysical mechanisms which cause a decrease in ADC are not yet fully understood [185]. The most frequent interpretation refers to an inter-compartmental water shift, giving rise to cell swelling (cytotoxic oedema) as a result of a failure of the sodium/potassium pump. In this case, more water tends to experience restrictions in the ICS, thereby reducing the ADC. An accompanying increased tortuosity of the ECS also contributes to a reduction in ADC. Many parameters, such as intra- and extracellular ADCs, intracellular

water volume fraction, membrane permeability and bound water, come into play [189–192]. Other interpretations include an enhanced intracellular viscosity as a result of breakdown of subcellular organelles and microstructural disorganisation [193,194], reduction in intracellular ADC caused by alterations in molecular interactions and cytoplasmic streaming [195], and neurite beading (focal enlargements followed by constrictions) in response to ischaemic conditions [196].

Although DKI is still at an early stage of development, promising results in terms of better tissue characterisation have been reported [37, 95, 166, 170, 173, 197]. At the same time, the practical utility of DKI for various diagnostic and/or monitoring purposes remains to be proven. Recently, preliminary results of the application of DKI to stroke assessment in humans [167] have demonstrated that this method provides strongly enhanced contrast between ischaemic and contralateral normal-appearing WM tissue. The relative changes occurring in kurtosis metrics were significantly larger than those in conventional scalar DTI parameters. These changes were especially pronounced for axial kurtosis.

Another approach for the treatment of non-mono-exponential attenuation curves is the *statistical approach* (described in Chapter 3, Section 3.4), using a log-normal distribution function for the continuous distribution of diffusivities [92], which has found a broad application in various scientific disciplines [93]. In particular, it has been successfully applied to describe the heterogeneity of diffusion processes in complex polymer solutions [94], but thus far has been rarely evoked for the quantification of water diffusion in brain tissue [198].

In this chapter, we report an *in vivo* case study of the ischaemic middle cerebral artery occlusion model [199] of stroke in rats with the help of two methods that allow us to quantify the deviations from the Gaussian model of diffusion, i.e. DKI and log-normal distribution function imaging (LNDFI). Previously, applications of DKI to stroke in animals have been reported as conference abstracts [200–204], including our own preliminary investigation [202] and one of the studies [200] that represents a retrospective analysis of old data [205]. LNDFI studies of stroke have not been reported in the literature. Investigations of the animal models of ischaemic stroke in conjunction with the development of new diagnos-

tic methods and potential biomarkers are very important, as they can be performed under less restrictive conditions than in human patients. In addition, they allow the risks for human patients to be reduced when the performance of various medication schemes is assessed in correlation with the efficiency of the new biomarkers.

We investigate the implications of stroke on GM tissue in rat brain using diffusion analysis in the extended range of diffusion weightings. It was of particular interest to investigate whether the changes in kurtosis in the GM lesions were of the same magnitude as reported for kurtosis in oriented human WM tissue affected by ischaemic stroke [167]. Another goal was to examine the applicability of the diffusion metrics based on LNDFI in the assessment of stroke in GM tissue.

7.2 Materials and methods

7.2.1 Animals

All experiments complied with French legislation and guidelines for animal research. The animal protocol used was approved by the *Comité d'Ethique en Expérimentation Animale Commissariat à l'Energie Atomique et aux énergies alternatives Direction des Sciences du Vivant Ile de France* (CETEA CEA DSV IdF). For the stroke experiments, transient middle cerebral artery occlusion was induced [199] in three animals (300 g, Sprague-Dawley male rats). The rats underwent a 90-min transient occlusion and were imaged 24 h after reperfusion. The animals were anaesthetised with isoflurane (2%) administered in a mixture of air-oxygen through a nose cone and maintained at constant temperature (37 °C) using a feedback-controlled air heating system (MR compatible small animal heating system; Small Animal Instruments, Inc. (SAII), Stony Brook, NY, USA). The DW acquisitions were respiration triggered.

7.2.2 MRI experiments

All MRI experiments were performed on a 7T system (Bruker BioSpin, Ettlingen, Germany) equipped with magnetic field gradients with a maximum strength of 760 mT/m and using a homebuilt RF surface coil (diam-

eter, 2.5 cm). Diffusion attenuations for DKI and LNDFI were measured with typical DTI protocols, but with additional b-values. Four-segment DW SE EPI images were acquired with the following acquisition parameters: TR/TE = 3000/30 ms; FoV, 3×3 cm^2; matrix size, 128×128; voxel in-plane size, $0.234 \times 0.234 \times 1$ mm^3; number of slices, 4; slice gap, 0.2 mm; diffusion gradient duration δ, 5 ms; number of excitations, 4. The inter-pulse spacing between the diffusion gradient pulses was 17 ms. We used 20 gradient directions (the specification of the vector units is omitted as this investigation is focused mainly on the orientationally averaged parameters) and five b values for all animals: 0, 0.5, 1.0, 2.5, 3.5 ms μm^{-2}. For animal 1, two further b-values, at 5.0 and 6.0 ms μm^{-2}, were added to the measurement protocol in order to check the influence of the larger b-value range on the fits. Rapid acquisition with refocused echoes (RARE) T_2-weighted images were acquired to localise the lesions (TR = 5530 ms; effective TE = 76 ms; field of view, 3×3 cm^2; matrix size, 128×128; slice thickness, 1 mm; number of excitations, 2).

7.2.3 Models and data analysis

The bias in the DW images caused by the background noise was corrected using the PI method [123, 124] (See Chapter 3, Section 3.10). Computation of parameter maps was performed with the help of in-house Matlab scripts (Matlab, The MathWorks, Natick, MA, USA).

In this work, we used the mono-exponential, kurtosis and log-normal distribution function to fit the normalised signal intensities $S(b)$ on a voxel-by-voxel basis with the help of the non-linear Nelder-Mead algorithm. Conventional diffusion tensors were evaluated according to Equations 3.1 and 3.3 for the range of b-values between 0 and 1.0 ms μm^{-2}. The upper boundary constraint (3.0 ms μm^{-2}) was set with regard to the diffusivity of free water at 37°C. The maps were constructed for the following parameters: MD (Equation 3.8), FA (Equation 3.11) and colour-coded FA (CFA) directional maps (Equation 3.12).

Ischaemic lesions studied in this work were located only in the GM where diffusion tends to be macroscopically isotropic. As a result, the observed dependence of the DW signal attenuations on the orientation of the applied diffusion gradients in these regions was rather weak. There-

fore, we accessed kurtosis via the mean values only (in other words, the metrics of kurtosis anisotropy, such as the axial or radial kurtoses, were not evaluated separately). Moreover, in order to increase the SNR ratio (especially important at high b-values) and to facilitate the fitting procedure, we applied the fits of Equation 3.24 to the mean curves averaged over the 20 gradient directions. Therefore, in the following, the notation of the fitted parameters D_{app} and K_{app} in Equation 3.24 is replaced by D_{K} and MK, respectively. The fits were limited to the range of $b \leq 3.5$ ms μm^{-2} in all animals. For typical D_{K} and MK values observed in our experiments, this range did not exceed the value of $b_{\text{max}} = 3/(D_{\text{K}}MK)$, which denotes the value of the minima in Equation 3.24; b_{max} restricts the range of applicability of DKI (discussed in Chapter 6) depending on the values of the product of D_{K} and MK. The maps were evaluated for D_{K} and MK.

In frame of the statistical approach (See Chapter 3, Section 3.4), the signal attenuation is described by means of the distribution function of diffusivities, $p(D)$, according to Equation 3.15. In this work, we assumed that $p(D)$ can be approximated by a log-normal distribution function (Equation 3.19). LNDFI requires a minimum of three b-values and, in terms of the minimal measurement time, is equivalent to DKI, which also requires a minimum of three b-values. The choice of b-values is a matter of optimisation, taking into account the SNR. In this part, the fits of Equations 3.15 and 3.19 were applied to the mean curves averaged over the 20 gradient directions for $b \leq 3.5$ ms μm^{-2} in all animals. This is the same range as used for DKI. In addition, in animal 1, the curves were fitted over the full range of b-values available, i.e. $b \leq 6.0$ ms μm^{-2}. The maps were constructed for both of the free parameters, D_{LD} and σ.

7.3 Results

7.3.1 DW signal attenuation

Figure 7.1 shows typical diffusion attenuation curves for two representative voxels located in the affected and non-affected areas of the brain (voxel locations are indicated by arrows in Figure 7.2(a)). The signal

amplitudes were averaged over all gradient directions; the bars indicate the standard deviations from the mean values. The cyan curves in Figure 7.1(a) represent fits according to Equation 3.24 (kurtosis), and all other curves are fits of Equation 3.15 assuming a log-normal distribution (Equation 3.19). Log-normal fits in the range of $b \leq 6.0$ ms μm^{-2} are shown in black, and fits in the range of $b \leq 3.0$ ms μm^{-2} are shown in magenta. Clearly, the initial slope of the curve in the ischaemic region is strongly decreased (reduced MD) in comparison with that in the contralateral region. The degree of non-Gaussianity is larger in the ischaemic region than in the healthy region. Figure 7.1(b) shows the maps of χ^2 for all three fits. All maps demonstrate a satisfactory homogeneity across most parts of the images shown.

7.3.2 Maps and histograms

Figures 7.2 show the anatomical RARE images (a) and the maps of MD (b), FA (c), CFA (d), D_{K} (e), MK (f), D_{LD} (g) and σ (h) for animal 1. An extended ischaemic lesion can be clearly identified on the left of all images/maps, excluding FA (c) and CFA (d). In the latter, the differences between the affected and healthy regions are ambiguous. MD, D_{K} and D_{LD} are decreased in the ischaemic region, as expected, but both MK and σ are strongly enhanced.

Figures 7.3 shows the histograms of MD (a), FA (b), D_{K} (c), MK (d), D_{LD} (e) and σ (f) for the affected (left) and unaffected (right) hemispheres of one individual slice (i.e. the third slice from the left in Figure 7.2). The histograms of FA in the healthy and ischaemic hemispheres are essentially overlapped. In contrast, the histograms of MD, D_{K} and D_{LD} reveal substantial parts that are shifted towards significantly smaller values, whereas the histograms of MK and σ exhibit shifts towards significantly higher values.

7.3.3 Analysis over regions-of-interest

We evaluated the average values of different metrics in two ROIs located in the ischaemic lesions, and compared them with the corresponding values in the healthy counterparts. The first ROI was placed in the cerebral

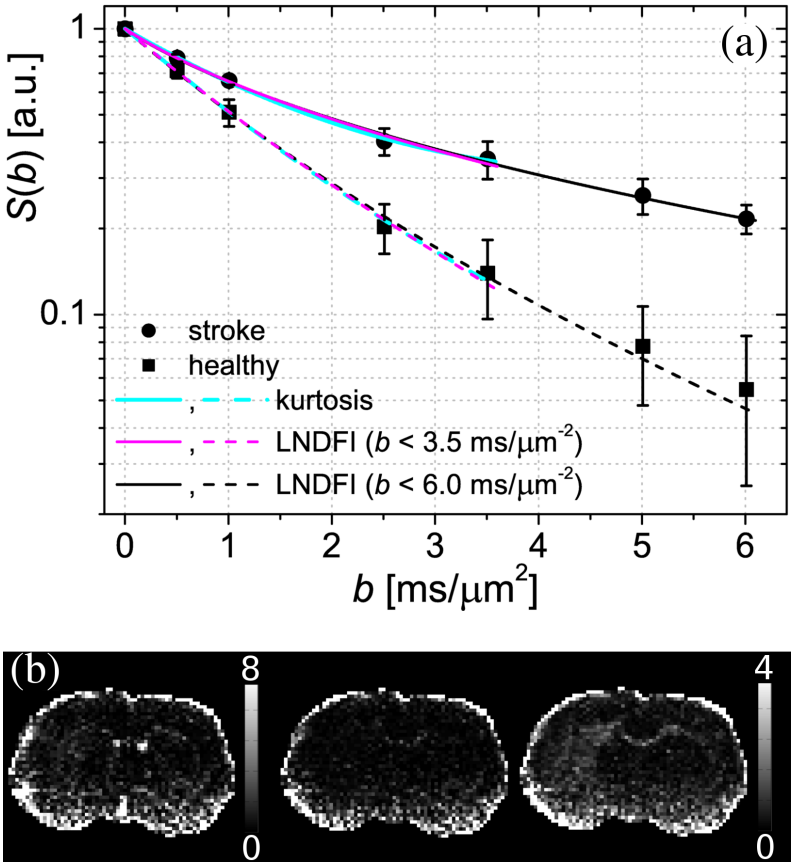


Figure 7.1: *(a) Diffusion attenuation curves in two representative voxels located in the affected and healthy tissue (animal 1) as shown in Figure 7.2. The signal amplitudes were averaged over 20 gradient directions; the bars indicate the standard deviations. Cyan curves represent fits of Equation 3.24 to the experimental points (DKI). Black and magenta curves represent the fits of Equations 3.15 and 3.19 to the experimental points (LNDFI) in the range of* $b \leq 6.0$ ms μm^{-2} *and* $b \leq 3.5$ ms μm^{-2}*, respectively. DKI fitting parameters were as follows:* $D_K = 0.7$ μm^2 ms^{-1} *and* $MK = 0.43$ *for healthy tissue and* $D_K = 0.48$ μm^2 ms^{-1} *and* $MK = 1.32$ *for affected tissue. LNDFI fitting parameters were as follows:* $b \leq 6.0$ ms μm^{-2}*:* $D_{LD} = 0.65$ μm^2 ms^{-1} *and* $\sigma = 0.5$ *for healthy tissue and* $D_{LD} = 0.34$ μm^2 ms^{-1} *and* $\sigma = 1.02$ *for affected tissue;* $b \leq 3.5$ μm^2 ms^{-1}*:* $D_{LD} = 0.65$ μm^2 ms^{-1} *and* $\sigma = 0.43$ *for healthy tissue and* $D_{LD} = 0.34$ μm^2 ms^{-1} *and* $\sigma = 0.99$ *for affected tissue. (b) Maps of* χ^2 *for all three fits: DKI (left); LNDFI,* $b \leq 3.5$ ms μm^{-2} *(middle); LNDFI,* $b \leq 6.0$ ms μm^{-2} *(right). The left and right scale bars refer to DKI and LNDFI, respectively. The indicated numbers should be multiplied by* 10^{-4}*.*

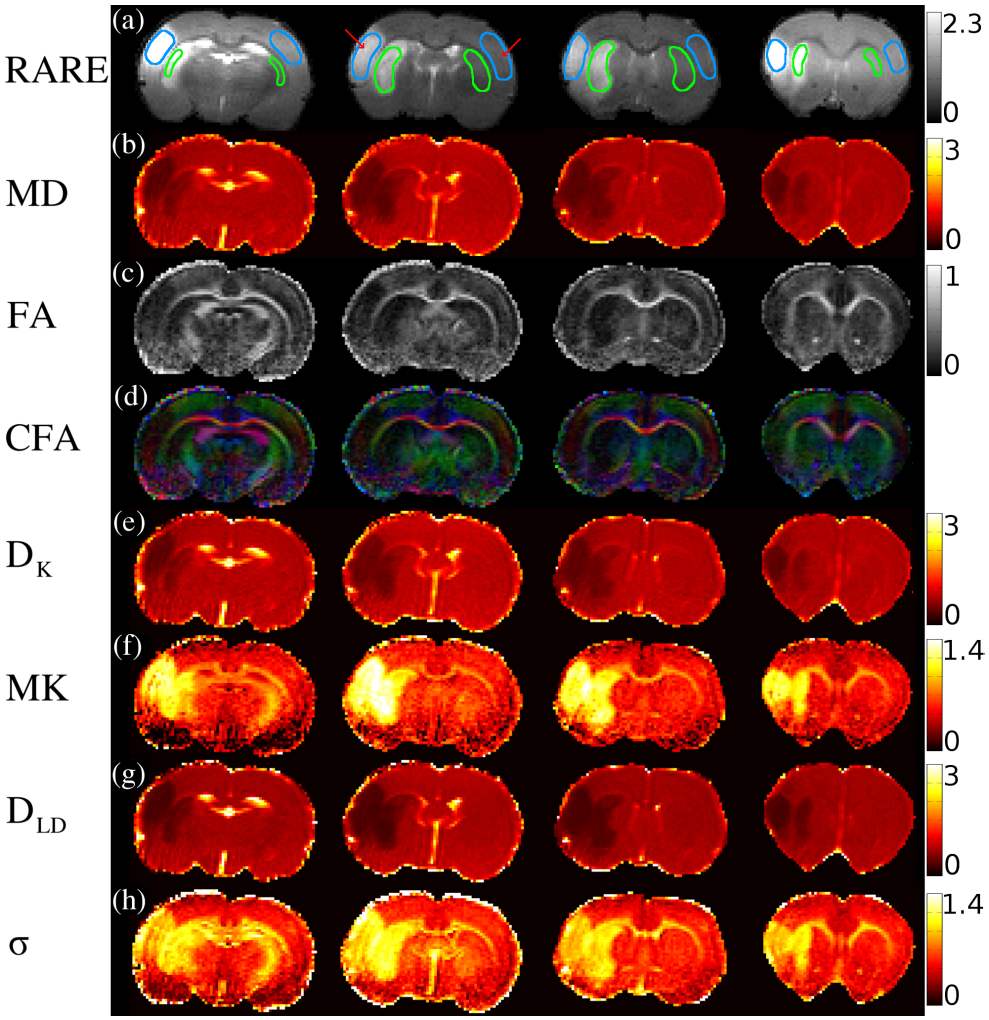


Figure 7.2: *(a) Anatomical rapid acquisition with refocused echoes (RARE) images and maps of MD (b), FA (c), colour-coded FA (CFA) (d), apparent diffusivity (D_K) (e), apparent kurtosis (MK) (f), peak diffusivity (D_{LD}) (g) and σ (h) of animal 1. The ROIs used to average the measured parameters are shown in RARE images (a) in cyan and green.*

cortex (CT) and the second ROI in the caudate putamen (CPu) (see Figure 7.2(a)). Two equivalent ROIs were placed on the contralateral side. The average values of various metrics quantifying the apparent diffusivities (MD, D_K and D_{LD}) and the deviations from the Gaussian model (MK and σ), as well as their relative changes in the affected/healthy regions, are summarised in Table 7.1 (all parameters refer to animal 1).

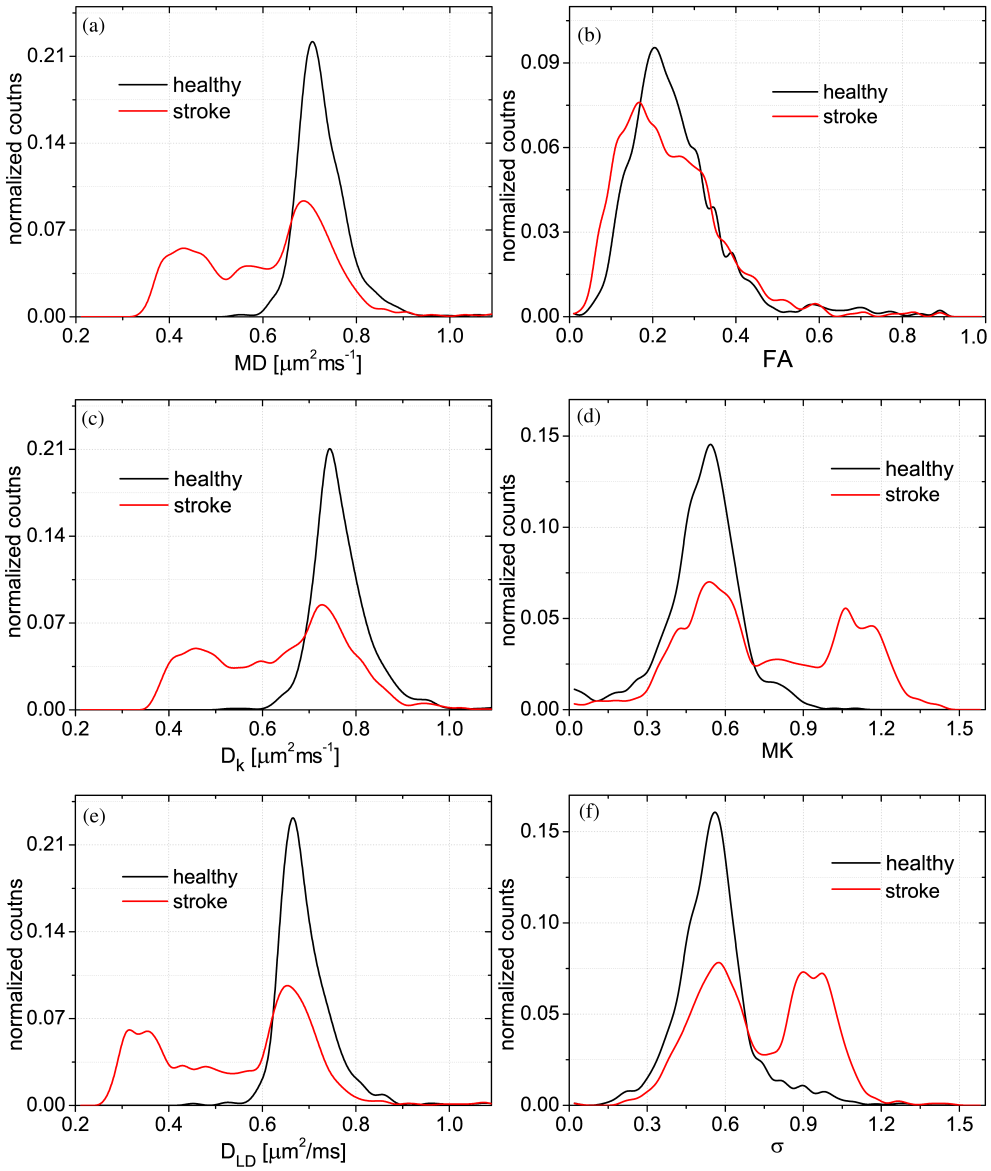


Figure 7.3: *Histograms of MD (a), FA (b), apparent diffusivity (D_{K}) (c), apparent kurtosis (MK) (d), peak diffusivity (D_{LD}) (e) and σ (f) for the affected (left) and healthy (right) hemispheres of one individual slice (animal 1).*

The relative changes were calculated, in per cent, as the ratio of the difference between the average values of a given parameter in the ischaemic and healthy ROIs with respect to the average value in the healthy ROI. Table 7.1 shows that the largest changes were observed for MK and σ.

Similar ischaemic lesions of slightly varying spatial extension were

	CT			CPu		
	healthy	affected	rel. change [%]	healthy	affected	rel. change [%]
MD	0.73 ± 0.08	0.43 ± 0.07	-42	0.72 ± 0.03	0.49 ± 0.05	-32
D_{K} [μm^2 ms^{-1}]	0.77 ± 0.09	0.46 ± 0.08	-40	0.76 ± 0.02	0.52 ± 0.05	-32
K	0.50 ± 0.09	1.15 ± 0.10	133	0.57 ± 0.09	1.12 ± 0.10	97
D_{LD} [μm^2 ms^{-1}]	0.70 ± 0.08	0.34 ± 0.06	-51	0.68 ± 0.03	0.39 ± 0.04	-42
σ	0.53 ± 0.08	0.96 ± 0.09	79	0.60 ± 0.08	1.02 ± 0.07	70

Table 7.1: *Values of the map parameters MD, D_{K}, MK, D_{LD} and σ averaged over the indicated ROIs in each slice and over four slices in animal 1. The ROIs are shown in Figures 7.2(a)*

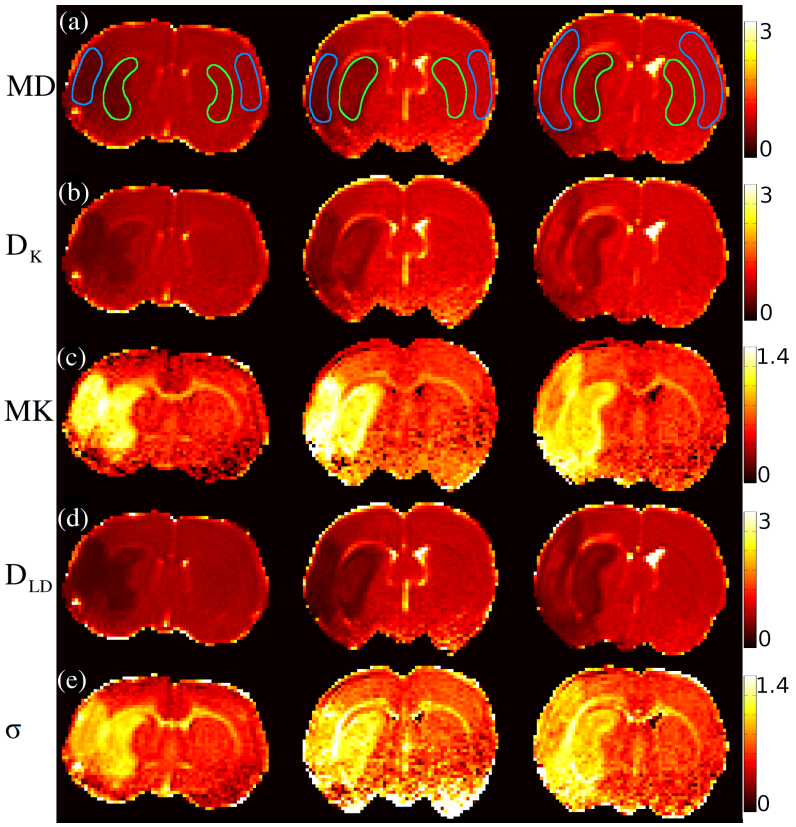


Figure 7.4: *Maps of MD (a), apparent diffusivity (D_{K}) (b), apparent kurtosis (MK) (c), peak diffusivity (D_{LD}) (d) and σ (e) for one selected slice best representing the ischaemic lesion in each of three animals. The ROIs used for averaging the measured parameters are shown in MD maps (a) in cyan and green.*

observed in all three animals studied. Figure 7.4 shows the maps of MD (a), D_{K} (b), MK (c), D_{LD} (d) and σ (e) for one selected slice in each of the animals (best representing the ischaemic lesion). Again, the largest contrast was produced by MK and σ maps in all lesions. The *t-test* performed for the healthy versus affected ROIs showed that the changes in all the above parameters (MD, D_{K}, MK, D_{LD} and σ) were significant ($p < 0.001$). Figure 7.5 summarises the relative changes in MD, D_{K}, MK, D_{LD} and σ averaged over four slices in animal 1 (a) and over all 12 slices in the three animals (b).

The data represented in Table 7.1 and Figure 7.5 show that the observed values of MD decreased by 42% (CT) and 32% (CPu) in animal

1; the average decreases over all slices/animals were in the same range: 38% (CT) and 31% (CPu). The relative decreases in D_{K} were 40% (CT) and 32% (CPu) in animal 1, and 37% (CT) and 30% (CPu) when averaged over all slices/animals. In ischaemic lesions, MK increased by 133% (CT) and 97% (CPu) in animal 1, whereas the average changes over all slices/animals were about 114% (CT) and 90% (CPu). The relative decreases in D_{LD} were 51% (CT) and 42% (CPu) in animal 1, and 46% (CT) and 36% (CPu) when averaged over all slices/animals. The relative increases in σ were 79% (CT) and 70% (CPu) in animal 1, and 65% (CT) and 61% (CPu) when averaged over all slices/animals.

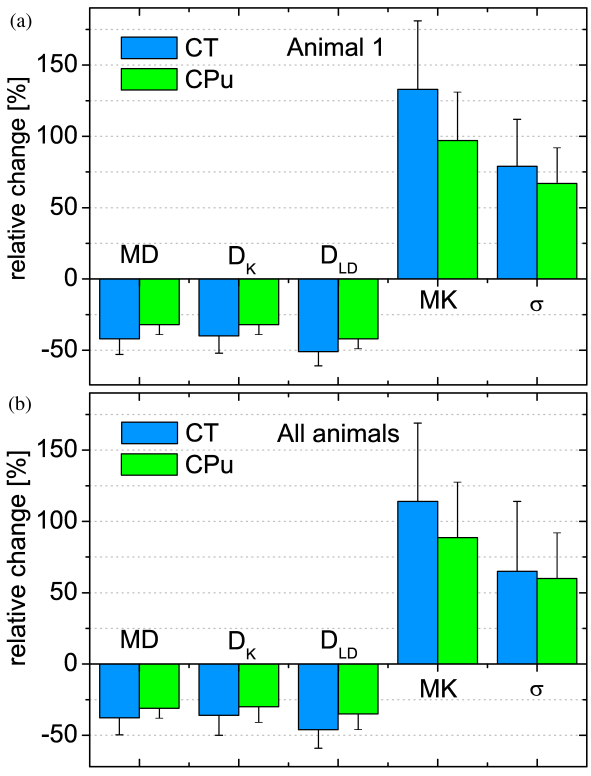


Figure 7.5: *Relative changes in per cent of the values of MD, D_{K}, MK, D_{LD} and σ, averaged over all slices in animal 1 (a) and over all three animals (b); error bars indicate the standard deviations. CPu, caudate putamen; CT, cerebral cortex.*

7.4 Discussion

In this chapter, we have demonstrated that the quantitative metrics of the deviations from the Gaussian diffusion model (MK, σ) are subject to significantly larger changes in the ischaemic lesions in the subacute phase than are the parameters quantifying the apparent diffusivity itself (MD, D_{K}, D_{LD}). The relative changes in MD were in the same range as reported in the literature: about 30-40% [184]. The largest relative change caused by stroke was observed for MK (on average, 90-114%), exceeding that of MD by as much as approximately a factor of three. The observed increase in σ (61-65%) was significantly larger, by a factor of 1.5-2, than the change in MD and D_{LD} (36-46%).

Our results are substantiated by the analysis of the histograms for the representative animal 1 (Figure 7.3), illustrating a significant shift in various diffusion metrics in the affected versus healthy brain hemispheres. The relative changes in D_{K} (-37%) and MD were similar to each other. The parameter D_{LD} showed a higher sensitivity to ischaemic change than did MD (for example, in CT: -46% for D_{LD} versus -38% for MD averaged over all slices/animals; Figure 7.5).

In this context, we should recall that D_{LD} represents the peak value of the distribution, which, for asymmetric functions, such as the log-normal distribution, does not coincide with the mean. The parameter D_{K} represents the initial slope of the attenuation and, when ADCs are distributed, coincides with the mean of the distribution (irrespective of its form) (see Equation 3.16). The evaluation of MD, in turn, is based on the low range of diffusion weightings in which the attenuation is assumed to be mono-exponential. Therefore, in practice, within the accuracy of the Gaussian assumption, MD should be close to D_{K}, and this is in agreement with our observations. It should, however, be kept in mind that deviations from the Gaussian approximation may introduce biased errors in the estimates of the diffusion metrics: the stronger the diffusion weighting, the larger the error. In the literature, this feature is sometimes addressed as a b-value dependence of the DTI parameters [83] (as discussed in Chapter 6), although other error sources can contribute to an apparent dependence of the evaluated parameters on b [206]. For this reason, DKI was suggested to be a more accurate method for the estimation of the mean ADC in

comparison with DTI [174].

The significant difference between our results and kurtosis data in humans [167] is related to diffusion anisotropy. The lesions investigated in Reference [167] were located predominantly in WM. Therefore, tissue anisotropy played an essential role in that study. For example, a large increase after stroke was observed for axial kurtosis (more than by a factor of two), whereas the change in radial kurtosis was much smaller. In other words, the dominating contribution to the observed large change in MK was from the axial component. The interpretation of these findings was given by the authors in the context of changes in the intra-axonal diffusivity and increasing heterogeneity in the axial direction (for instance, as a result of bead-like swellings, or caused by other factors, such as cytoskeletal breakdown or the accumulation of unfolded proteins). In our work, in contrast, the lesions were localised in GM tissue with characteristically rather low diffusion anisotropy (FA values were about 0.2, typical for GM, in the ROIs located in healthy tissue). However, it is remarkable that, in spite of the low FA, the magnitude of the mean kurtosis changes in GM lesions in the rat brain observed in this work (90–114% on average) is comparable with the magnitude of the changes (also of the order of 100%) reported in Reference [167] for WM lesions in the human brain. It is worth noting that experimental data published in the literature are not uniform, even with respect to conventional DTI. For example, a dedicated DTI study of 12 stroke patients [207] revealed two distinct levels of diffusion reduction in the affected regions, with a more severe average reduction of MD in WM (46%) than in GM (31%). Other authors were unable to observe any significant differences between WM and GM diffusion properties in stroke [192]. Referring to kurtosis work on animals, very few data are available in the literature for a comparison with our results [201, 203, 204]. DKI was applied to visualise ischaemic lesions located in cortical GM in mice [201] and in two GM ROIs in rats [203,204]. Observed increases in MK of about 75% [201] and 100% [203] at 24 h after reperfusion were in satisfactory agreement with our results ($\sim$ 100% on average). An interesting observation was noted in Reference [203], showing that MK increases with time from the hyperacute (first 1.5 h) to the acute phase, whereas the ADC tends to renormalise at 24–48 h

after stroke. It was concluded that MK, which characterises the changing heterogeneity of the tissue, may offer a valuable tool for the staging of ischaemic brain injury. In humans, kurtosis data for GM lesions, published as a conference abstract [208], demonstrated only a small (6%) increase in kurtosis for the shortest observation time and, surprisingly, even a decrease ($\sim$ 40%) for longer diffusion times in spite of a significant decrease in MD.

This work is a case study and is thus preliminary in nature. Given that only very few data have been published on DKI of stroke, much more experimental work and statistical analysis are required in order to better understand the complex chain of events in stroke. As already mentioned above, we observed a huge change in MK in GM lesions (animals), which was of the same magnitude as that reported for WM lesions in humans [167]. The resolution of whether tissue infarction in WM and GM is governed by similar or different cellular mechanisms is important for a better understanding of the histo-pathological changes in both tissue types during stroke. Such changes, reducing water ADC during stroke, have not yet been fully elucidated [185,195]. Most frequently, the biophysical mechanisms are attributed to the consequences of cytotoxic cellular swelling, increasing the effective influence of restrictions on water diffusion. Our observation supports an assumption that the dominating underlying mechanisms in GM and WM are likely to be of a similar nature. In particular, this would be consistent with the model of cytotoxic oedema which affects cells in both GM and WM. Potential contributions to ADC reduction include the change in extra- and intracellular volume fractions, with more water subjected to intracellular restrictions by cell membranes and organelles, an increased tortuosity of the ECS, an increased intracellular viscosity as a result of microtubule dissociation and changes in the membrane-bound water fraction [3,183,185]. In contrast, the hypothesis of bead-like swelling, increasing diffusion heterogeneity in the axial direction [167], and the corresponding axial kurtosis, at first glance, seems to be more specific for ordered WM tissue rather than for GM. However, it is worth mentioning that, together with isotropic substructures (neurons, glial cells), GM contains a significant fraction of anisotropic microstructures (neuronal dendrites and axons) whose ori-

entations in typical voxels (linear size of about 200 mm) appear to be strongly distributed. In general, these structures may give rise to similar effects to those of ordered axons in WM, as they tend to restrict diffusion in directions perpendicular to the main symmetry axes. Diffusion attenuation in such systems (modelled as an array of subunits with cylindrical anisotropy and distributed orientations [209]) exhibits strong deviations from a Gaussian behaviour, as demonstrated previously for various materials [209–212]. A similar approach was adapted by Jespersen et al. [27] to model brain tissue microstructure.

In general, theoretical models and approaches proposed to describe the patterns of non-Gaussian diffusion behaviour in brain tissue (for details, see the recent reviews [65, 74]) can be differentiated by their methodology. Some of these models attempt to approximate the governing features of complex tissue architecture in terms of simple geometric schemes [26, 40], such as a set of oriented cylinders used to approximate axonal formations in WM. The others represent more empirical approaches [36, 39] that allow one to describe the attenuation of the MRI signal using a set of phenomenological parameters. In this context, LNDFI is based on the same underlying biophysical background as the statistical model suggested by D. Yablonskiy et al. [39]. The statistical model accounts for the enormous complexity of various restrictions and hindrances imposed by cellular membranes, sub- and super-cellular microstructures on the propagation of water molecules in the biological tissue via the distribution of ADCs (Equation 3.15). It describes the DW signal as an integral of signals from a large number of spin packets, each characterized by its individual ADC. These spin packets are assumed to originate from different positions in a voxel and to explore somewhat different local environments (restrictions, hindrances) during the diffusion time. It is worth noting that the individual spin packets are not necessarily identified with separate physical compartments in the tissue, but can originate from the same compartment. This was demonstrated, for example, by Monte Carlo simulations [136] and phantom studies [131, 135] for radial diffusion in the interstitial space of the oriented cylindrical objects (one single compartment). It was shown that even such a simple system may give rise to non-Gaussian signal attenuations in a certain

range of diffusion times.

The measured function $p(D)$ does not necessarily represent the distribution of intrinsic water diffusivities [213], unless the measurements were performed at very short diffusion times (so short that the diffusion lengths are much smaller than the typical length scales associated with restrictions). In practice, such short diffusion times can hardly be achieved using the standard techniques exploited in our work. (For the same reasons, it is worth noting that the ADCs measured in the low b-value range of conventional DTI do not reflect the intrinsic diffusivities of water molecules as governed by the temperature and local viscosity of the surrounding media.) The characteristic displacements evaluated as $\sqrt{2D_{\mathrm{LD}}t_{\mathrm{d}}}$ during the observation time ($\sim$ 15 ms) in our work were about 4-5 μm, comparable with the length scale of the cellular structures. Moreover, as the linear voxel size is much larger (> 200 μm), the measured $p(D)$ can also be modulated, quite generally, by structural heterogeneities on the scale essentially exceeding the diffusion length (but still below the voxel size). However, given that changes caused by stroke are usually attributed to changes on the cellular level, these large-scale heterogeneities are not likely to play a significant role in our study.

Reconstruction of the distribution $p(D)$ from the experimental data according to Equation 3.15 (inverse Laplace transform) represents a well-known, ill-conditioned mathematical problem leading to unstable computational solutions [214]. An alternative procedure implies the assumption of an explicit form of $p(D)$ and fitting it to the experimental values. It is worth mentioning that, in general, one can find a multitude of different distribution functions providing satisfactory fits to the experimental points. In the absence of any theories explicitly predicting a specific form of the distribution, the choice of the distribution function for fitting purposes is usually dictated by mere empirical reasons. For instance, in the original statistical model by D. Yablonskiy et al. [39], the authors made use of a truncated normal distribution. In this work, for reasons of convenience, we exploit the log-normal distribution function. We checked the hypothesis that LNDFI, as an empirical approach, can be useful for the quantification of diffusion changes in stroke. Our results have demonstrated that the log-normal distribution function provides a good descrip-

tion of the experimental data, and that both free parameters, D_{LD} and σ exhibit an enhanced sensitivity to ischaemic lesions. The main advantage of the log-normal distribution is that it is a positive definite function, and therefore does not require an artificial truncation of the negative values. Although the truncated normal distribution might represent a reasonable approximation for rather narrow distributions [39], it might become problematic for broader ones for which the final form of the truncated distribution would strongly deviate from the original bell-shaped function. These limitations do not apply with the log-normal distribution. At the same time, in the limit of narrow distributions, a log-normal distribution can be satisfactorily approximated by the original normal distribution.

Another interesting, although preliminary, observation is that some of the ischaemic lesions exhibit an inhomogeneous appearance in both the maps of apparent diffusivity (MD, D_{K}, D_{LD}) and in the "heterogeneity" maps (MK, σ): for instance, the dark rims around the lesions in the MD, D_{K} and D_{LD} maps correlate with the enhanced kurtosis and σ values (see Figure 7.4, second and third rows from the left). Future work should show whether this inhomogeneity is correlated with the degree of tissue damage caused by infarction.

Thus, DKI and LNDFI have been demonstrated to be useful tools for the characterisation of tissue affected by stroke. The strong sensitivity of these methods to changes observed in GM tissue makes them especially promising for the assessment of pathological changes localised in GM. This is because, as a result of low anisotropy, some important DTI metrics, such as FA, are not informative regarding GM tissue. More investigations are required in order to elucidate the further potential and practical use of these methods.

7.5 Conclusions

In this chapter, we applied two non-Gaussian approaches, DKI and LNDFI, to quantify the diffusion changes caused by the consequences of the ischaemic middle cerebral artery occlusion model of stroke in three animals. A substantial enhancement of the visualisation contrast of lesions was observed in the MK and σ maps. On average, the relative changes in MK

were significantly larger, by approximately a factor of three, than those of the apparent diffusivity itself. The degree of these changes was consistent with the preliminary data [167] reported in the literature for ischaemic lesions located in WM of humans. Our findings support an assumption that similar cellular mechanisms may be responsible for diffusion-related contrast in GM and WM lesions. Significantly enhanced lesion contrast was also observed in σ maps in comparison with MD and D_{LD} maps. Thus, both DKI and LNDFI have demonstrated that the metrics of the non-Gaussian diffusion behaviour tend to be very sensitive biomarkers of ischaemia, and have a potential to significantly improve the characterisation of pathological brain tissue affected by stroke.

Chapter 8

Conclusions and outlook

This work is concerned with analysis of the DW MRI signal in biological tissue at very high diffusion weightings (b-values) in comparison to those used in conventional methods. A summary of various theoretical approaches proposed in the literature for this analysis was presented.

An artificial anisotropic fibre phantom for diffusion MRI applications was developed. In this novel design, several regions with different configurations of interwoven fibres were integrated in a single phantom. In particular, one of the regions is composed of nearly parallel fibres with a spatial gradient of the fibre volume fraction. This feature allowed us to characterize the water diffusivity in an extended range of volume fibre fractions within the same measurement and under the same physical conditions. The phantom has been also used for the comparison of two post-processing techniques related to high angular resolution diffusion imaging experiments, namely, the *constrained spherical deconvolution* and the *q-ball* imaging techniques. Both methods were shown to recognize the presence of single- and multi-modal diffusion profiles for different values of signal-to-noise ratio. In future investigations, it is proposed to integrate various properties of multi-fibre populations, such as continuous angular distribution of crossing fibres. Furthermore, using other materials with different structure would allow one to assess additional factors that affect the diffusion processes in biological tissues.

The analysis of the non-Gaussian DW MRI signal attenuation in the extended range of b-values in the human brain has been performed using a combined DKI and BEDTA approach. These models were shown to

provide better characterization of the brain tissue microstructure than conventional low b-value approaches. New parameters were proposed to quantify the deviations of the DW MRI signal from the mono-exponential function. The potential of these parameters as novel biomarkers of the tissue pathology has been discussed.

Regarding the experimental protocols, a detailed evaluation of the dependence of the DKI metrics on the fitting range of b-values was carried out. Based on this analysis, a simple voxel- and direction-based optimisation algorithm for the range of b-values was developed. The proposed optimisation was shown to improve the DKI fittings, which reduced the amount of artefacts in most of the ordered areas of the brain (such as corpus callosum, for example).

In the last part of this work, DKI and LNDFI were used to quantify the deviations from the Gaussian diffusion profile in animal stroke models. Diffusion metrics of both DKI and LNDFI were shown to greatly enhance the contrast between the ischaemic lesions and the contralateral healthy tissue, compared to DTI. We have discussed the potential effects of various biophysical processes caused by stroke on the DKI and LNDFI metrics.

Summarising, all non-Gaussian models considered in this work were shown to provide valuable quantitative information regarding the tissue microstructure and condition, and are therefore considered to be promising biomarkers for tissue pathology and ageing. The results obtained here contribute to a better understanding of tissue microstructure and provide clearer quantitative relationships between the evaluated diffusion metrics and the underlying diffusion mechanisms.

Acknowledgements

I would like to express my most sincere gratitude to my supervisor, Prof. Dr. N. Jon Shah, for giving me the opportunity of conducting my research in the exciting field of MRI at the Medical Imaging Physics Group at the Institute of Neuroscience and Medicine - 4 at Forschungszentrum Jülich. Prof. Shah provided a most stimulating research environment and was always present to discuss new ideas.

I am also truly indebted to my supervisor, Dr. Farida Grinberg. Her extensive scientific knowledge and excellent advice have been of vital importance to the success of this work, as well as for my personal scientific development. I thoroughly enjoyed our many brainstorming sessions and discussions about new ideas. Moreover, I want to thank Dr. Grinberg for proofreading and greatly improving my manuscripts as well as this dissertation.

My thanks also go to Dr. Ivan I. Maximov who has been always present for exciting discussions and helpful advice. His knowledge of physics and mathematics were of great help. I also want to thank Dr. Maximov for providing me many superbly helpful programming tricks and for proofreading and improving this thesis.

I want to thank Dr. Michael Poole, Dr. Marcus Ullisch, Dr. Vincent Gras, Dr. Desmond Tse and Mr. Jorge Arrubla for proofreading parts of this dissertation. Their comments and suggestions have greatly improved it. Moreover, I would like to thank Dr. Wieland Worthoff and Mr. Johannes Lindemeyer for translating to German the abstract of this thesis.

I am very much indebted to my colleagues with whom I have had the pleasure of having worked alongside and discussed my research with, especially Mr. Johannes Lindemeyer, Mr. Jorge Arrubla, Mr. Zaheer Ab-

bas, Mr. Étienne Besançon, Dr. Marcus Ullisch, Dr. Wieland Worthoff, Dr. Vincent Gras, Dr. Desmond Tse, Dr. Michael Poole, Ms. Elodie André, Mr. Juan Carlos Galindo, Dr. Daniel Pflugfelder, Mr. Rüdiger Stirnberg, Mr. Fabian Keil, Mr. Daniel Brenner, Mr. Daniel Fiege, Dr. Miriam Kubach, Mr. Jesús-Erasmo Batta and all the Medical Imaging Physics Group, at the Forschungszentrum Jülich.

Finally, I could have never finished this work were it not for the unconditional love and support of all my friends and family. This work is dedicated to my parents, my grandparents and my brothers. They are and always will be the very best of role models.

List of Figures

2.1 Zeeman splitting for a spin $^1/_2$ in a magnetic field 8
2.2 Evolution of the magnetisation during the RF pulse . . . 10
2.3 Free Induction Decay (FID) 12
2.4 Spin-echo pulse sequence diagram 13
2.5 Stimulated-echo pulse sequence diagram 14
2.6 Schematic representation of the slice selection 17
2.7 Spin-echo with echo planar imaging (EPI) readout 19
2.8 Representation of the restricted diffusion process 21
2.9 Schematic representation of the central nervous system . 23
2.10 Pulsed field gradient spin-echo sequence diagram 25
2.11 Diffusion-weighted stimulated-echo sequence diagram . . 29
2.12 Twice-refocused spin-echo bipolar diffusion-weighted sequence diagram 29

3.1 DW MRI signal and the ADC approach 33
3.2 Tensor ellipsoid representation 36
3.3 DTI scalar rotationally invariants 39
3.4 Statistical approach using Gaussian-like and log-normal distribution functions 44
3.5 Diffusion propagators with different kurtosis and the corresponding DW MRI signals 47
3.6 DTI and DKI invariants for an axial slice 50

4.1 Micrograph of a bundle of Dyneema® fibres 64
4.2 Acrylic platform for the fibre phantom 65
4.3 Photograph of the fibre phantom 66

4.4 Fibre density and conventional DTI maps for the fibre phantom 71
4.5 DW MRI signal in the parallel-area of the fibre phantom 72
4.6 DKI metrics vs. observation time and fibre density . . . 73
4.7 CSD and QBI in the cross-area in the fibre phantom . . 75
4.8 CSD in the parallel-area with gradient of fibre density in the fibre phantom 76
4.9 QBI in the parallel-area with gradient of fibre density in the fibre phantom 77
4.10 Streamline CSD-based fibre tractography of the fibre phantom 78

5.1 Map reconstruction workflow for BEDTA 86
5.2 DW MRI images in the extended range of b-values . . . 91
5.3 DW MRI signal for two selected voxels in GM and WM and the χ^2 error maps 93
5.4 Maps of BEDTA metrics 94
5.5 Histograms of diffusivities in BEDTA 95
5.6 Histograms of the fast diffusing water fraction in BEDTA 96
5.7 FA and colour-FA maps from BEDTA (slice 1) 98
5.8 FA and colour-FA maps from BEDTA (slice 2) 99
5.9 FA maps from BEDTA for 14 volunteers 100
5.10 Histograms of FA from BEDTA 101
5.11 Maps of ACPhi from BEDTA 102
5.12 Maps of MK and the corresponding histograms 103
5.13 *alpha*-maps from BEDTA 104
5.14 Maps of $\mathrm{CMD_s}$ from BEDTA 106

6.1 DW MRI signal attenuation and DKI fits for different ranges of b-values 121
6.2 Dependence of D_{app} and K_{app} on the fitting b-value range 123
6.3 Histograms showing the dependence of DKI metrics on the b-value 124
6.4 Maps of DKI metrics showing their dependence on the b-value 126
6.5 Maps of b^*_{max} and the correlation with FA and θ 127

6.6 Optimized DKI metrics 129
6.7 Optimized DKI metrics under clinical conditions 130
6.8 Algorithm for the evaluation of $b^*_{\max}$ 135

7.1 DW MRI signal attenuation in the stroke animal model . 143
7.2 Maps of the DTI, DKI and LNDFI metrics for the stroke animal model 144
7.3 Histograms of the DTI, DKI and LNDFI metrics for the stroke animal model 145
7.4 Maps of the DTI, DKI and LNDFI metrics for the three stroke animal models 147
7.5 Relative difference between the affected and healthy tissues for the DTI, DKI and LNDFI metrics 148

Acronyms

ADC apparent diffusion coefficient

ADK apparent diffusion kurtosis

BEDTA biexponential diffusion tensor analysis

CNS central nervous system

CPu caudate putamen

CSD constrained spherical deconvolution

CSF cerebrospinal fluid

CT cerebral cortex

DKI diffusion kurtosis imaging

DTI diffusion tensor imaging

DW diffusion-weighted

ECS extracellular space

EMF electromotive force

EPI echo planar imaging

FA fractional anisotropy

FD fibre density

FID free induction decay

FOD fibre orientation distribution

GM grey matter

HARDI high angular resolution diffusion imaging

ICS intracellular space

LNDFI log-normal distribution function imaging

MD mean diffusivity

ML maximum likelihood

MRI magnetic resonance imaging

MSD mean square displacement

NMR nuclear magnetic resonance

ODF orientation density function

PFG pulsed field gradient

PI power images

PVE partial volume effect

QBI q-ball imaging

RA relative anisotropy

RF radio-frequency

ROI region-of-interest

SD spherical deconvolution

SE spin-echo

SEMC spin-echo multi-contrast

SGP short gradient pulse

SNR signal-to-noise ratio

STE stimulated-echo

TRSE twice-refocused spin-echo

WM white matter

Bibliography

[1] H. Johansen-Berg and T. E. Behrens, eds., *Diffusion MRI. From Quantitative Measurement to In vivo Neuroanatomy*. Elsevier, London, Burlington, San Diego., 2009.

[2] C. Beaulieu, "The basis of anisotropic water diffusion in the nervous system - a technical review," *NMR Biomed*, vol. 15, no. 7-8, pp. 435–455, 2002.

[3] D. Le Bihan, "The 'wet mind': water and functional neuroimaging," *Phys Med Biol*, vol. 52, pp. R57–R90, Apr 2007.

[4] P. J. Basser and D. K. Jones, "Diffusion-tensor mri: theory, experimental design and data analysis - a technical review," *NMR Biomed*, vol. 15, no. 7-8, pp. 456–467, 2002.

[5] D. Le Bihan, J. F. Mangin, C. Poupon, C. A. Clark, S. Pappata, N. Molko, and H. Chabriat, "Diffusion tensor imaging: concepts and applications," *J Magn Reson Imaging*, vol. 13, pp. 534–546, Apr 2001.

[6] P. Skudlarski, K. Jagannathan, V. D. Calhoun, M. Hampson, B. A. Skudlarska, and G. Pearlson, "Measuring brain connectivity: diffusion tensor imaging validates resting state temporal correlations," *Neuroimage*, vol. 43, pp. 554–561, Nov 2008.

[7] Y. Assaf, "Can we use diffusion mri as a bio-marker of neurodegenerative processes?," *Bioessays*, vol. 30, pp. 1235–1245, Nov 2008.

[8] O. Ciccarelli, M. Catani, H. Johansen-Berg, C. Clark, and A. Thompson, "Diffusion-based tractography in neurological dis-

orders: concepts, applications, and future developments," *Lancet Neurol*, vol. 7, pp. 715–727, Aug 2008.

[9] Y.-W. Shin, J. S. Kwon, T. H. Ha, H.-J. Park, D. J. Kim, S. B. Hong, W.-J. Moon, J. M. Lee, I. Y. Kim, S. I. Kim, and E. C. Chung, "Increased water diffusivity in the frontal and temporal cortices of schizophrenic patients," *Neuroimage*, vol. 30, pp. 1285–1291, May 2006.

[10] O. Mayzel-Oreg, Y. Assaf, A. Gigi, D. Ben-Bashat, R. Verchovsky, M. Mordohovitch, M. Graif, T. Hendler, A. Korczyn, and Y. Cohen, "High b-value diffusion imaging of dementia: application to vascular dementia and alzheimer disease," *J Neurol Sci*, vol. 257, pp. 105–113, Jun 2007.

[11] P. Mukherjee and R. C. McKinstry, "Diffusion tensor imaging and tractography of human brain development," *Neuroimaging Clin N Am*, vol. 16, pp. 19–43, vii, Feb 2006.

[12] T. Paus, D. L. Collins, A. C. Evans, G. Leonard, B. Pike, and A. Zijdenbos, "Maturation of white matter in the human brain: a review of magnetic resonance studies," *Brain Res Bull*, vol. 54, pp. 255–266, Feb 2001.

[13] M. Moseley, "Diffusion tensor imaging and aging - a review," *NMR Biomed*, vol. 15, no. 7-8, pp. 553–560, 2002.

[14] S. Michielse, N. Coupland, R. Camicioli, R. Carter, P. Seres, J. Sabino, and N. Malykhin, "Selective effects of aging on brain white matter microstructure: a diffusion tensor imaging tractography study," *Neuroimage*, vol. 52, pp. 1190–1201, Oct 2010.

[15] T. R. Barrick, R. A. Charlton, C. A. Clark, and H. S. Markus, "White matter structural decline in normal ageing: a prospective longitudinal study using tract-based spatial statistics," *Neuroimage*, vol. 51, pp. 565–577, Jun 2010.

[16] D. S. Tuch, T. G. Reese, M. R. Wiegell, N. Makris, J. W. Belliveau, and V. J. Wedeen, "High angular resolution diffusion imag-

ing reveals intravoxel white matter fiber heterogeneity," *Magn Reson Med*, vol. 48, pp. 577–582, Oct 2002.

[17] D. S. Tuch, "Q-ball imaging," *Magn Reson Med*, vol. 52, pp. 1358–1372, Dec 2004.

[18] J.-D. Tournier, F. Calamante, D. G. Gadian, and A. Connelly, "Direct estimation of the fiber orientation density function from diffusion-weighted mri data using spherical deconvolution," *Neuroimage*, vol. 23, pp. 1176–1185, Nov 2004.

[19] E. Ozarslan, T. M. Shepherd, B. C. Vemuri, S. J. Blackband, and T. H. Mareci, "Resolution of complex tissue microarchitecture using the diffusion orientation transform (dot)," *Neuroimage*, vol. 31, pp. 1086–1103, Jul 2006.

[20] M. Descoteaux, E. Angelino, S. Fitzgibbons, and R. Deriche, "Regularized, fast, and robust analytical q-ball imaging," *Magn Reson Med*, vol. 58, pp. 497–510, Sep 2007.

[21] D. Le Bihan, S.-i. Urayama, T. Aso, T. Hanakawa, and H. Fukuyama, "Direct and fast detection of neuronal activation in the human brain with diffusion mri," *Proc Natl Acad Sci U S A*, vol. 103, pp. 8263–8268, May 2006.

[22] R. V. Mulkern, S. J. Haker, and S. E. Maier, "On high b diffusion imaging in the human brain: ruminations and experimental insights," *Magn Reson Imaging*, vol. 27, pp. 1151–1162, Oct 2009.

[23] Y. Cohen and Y. Assaf, "High b-value q-space analyzed diffusion-weighted mrs and mri in neuronal tissues - a technical review," *NMR Biomed*, vol. 15, no. 7-8, pp. 516–542, 2002.

[24] C. A. Clark and D. Le Bihan, "Water diffusion compartmentation and anisotropy at high b values in the human brain," *Magn Reson Med*, vol. 44, pp. 852–859, Dec 2000.

[25] F. Grinberg, E. Farrher, J. Kaffanke, A.-M. Oros-Peusquens, and N. J. Shah, "Non-gaussian diffusion in human brain tissue at high

b-factors as examined by a combined diffusion kurtosis and biexponential diffusion tensor analysis," *Neuroimage*, vol. 57, pp. 1087–1102, Aug 2011.

[26] Y. Assaf and P. J. Basser, "Composite hindered and restricted model of diffusion (charmed) mr imaging of the human brain," *Neuroimage*, vol. 27, pp. 48–58, Aug 2005.

[27] S. N. Jespersen, C. D. Kroenke, L. Østergaard, J. J. H. Ackerman, and D. A. Yablonskiy, "Modeling dendrite density from magnetic resonance diffusion measurements," *Neuroimage*, vol. 34, pp. 1473–1486, Feb 2007.

[28] O. P. Posnansky and N. J. Shah, "On the problem of diffusivity in heterogeneous biological materials with random structure," *J Biol Phys*, vol. 34, pp. 551–567, Dec 2008.

[29] M. Descoteaux, R. Deriche, D. L. Bihan, J.-F. Mangin, and C. Poupon, "Diffusion propagator imaging: using laplace's equation and multiple shell acquisitions to reconstruct the diffusion propagator," *Inf Process Med Imaging*, vol. 21, pp. 1–13, 2009.

[30] L. Minati, D. Aquino, S. Rampoldi, S. Papa, M. Grisoli, M. G. Bruzzone, and E. Maccagnano, "Biexponential and diffusional kurtosis imaging, and generalised diffusion-tensor imaging (gdti) with rank-4 tensors: a study in a group of healthy subjects," *MAGMA*, vol. 20, pp. 241–253, Dec 2007.

[31] C. A. Clark, M. Hedehus, and M. E. Moseley, "In vivo mapping of the fast and slow diffusion tensors in human brain.," *Magn Reson Med*, vol. 47, pp. 623–628, Apr 2002.

[32] S. E. Maier, S. Vajapeyam, H. Mamata, C.-F. Westin, F. A. Jolesz, and R. V. Mulkern, "Biexponential diffusion tensor analysis of human brain diffusion data," *Magn Reson Med*, vol. 51, pp. 321–330, Feb 2004.

[33] S. E. Maier and R. V. Mulkern, "Biexponential analysis of diffusion-related signal decay in normal human cortical and deep gray matter," *Magn Reson Imaging*, vol. 26, pp. 897–904, Sep 2008.

[34] V. G. Kiselev and K. A. Il'yasov, "Is the "biexponential diffusion" biexponential?," *Magn Reson Med*, vol. 57, pp. 464–469, Mar 2007.

[35] R. V. Mulkern, S. Vajapeyam, R. L. Robertson, P. A. Caruso, M. J. Rivkin, and S. E. Maier, "Biexponential apparent diffusion coefficient parametrization in adult vs newborn brain," *Magn Reson Imaging*, vol. 19, pp. 659–668, Jun 2001.

[36] J. H. Jensen, J. A. Helpern, A. Ramani, H. Lu, and K. Kaczynski, "Diffusional kurtosis imaging: the quantification of non-gaussian water diffusion by means of magnetic resonance imaging," *Magn Reson Med*, vol. 53, pp. 1432–1440, Jun 2005.

[37] E. S. Hui, M. M. Cheung, L. Qi, and E. X. Wu, "Towards better mr characterization of neural tissues using directional diffusion kurtosis analysis," *Neuroimage*, vol. 42, pp. 122–134, Aug 2008.

[38] K. M. Bennett, K. M. Schmainda, R. T. Bennett, D. B. Rowe, H. Lu, and J. S. Hyde, "Characterization of continuously distributed cortical water diffusion rates with a stretched-exponential model," *Magn Reson Med*, vol. 50, pp. 727–734, Oct 2003.

[39] D. A. Yablonskiy, G. L. Bretthorst, and J. J. H. Ackerman, "Statistical model for diffusion attenuated mr signal," *Magn Reson Med*, vol. 50, pp. 664–669, Oct 2003.

[40] P. N. Sen and P. J. Basser, "Modeling diffusion in white matter in the brain: a composite porous medium," *Magn Reson Imaging*, vol. 23, pp. 215–220, Feb 2005.

[41] J. Kärger, H. Pfeifer, and W. Heink, "Principles and applications of self-diffusion measurements by nuclear magnetic resonance," *Advances in Magnetic Resonance In Advances in Magnetic Resonance*, vol. 12, pp. 1–89, 1988.

[42] I. I. Rabi, J. R. Zacharias, S. Millman, and P. Kusch, "A new method of measuring nuclear magnetic moment," *Phys. Rev.*, vol. 53, pp. 318–318, Feb 1938.

[43] E. M. Purcell, H. C. Torrey, and R. V. Pound, "Resonance absorption by nuclear magnetic moments in a solid," *Phys. Rev.*, vol. 69, pp. 37–38, Jan 1946.

[44] F. Bloch, "Nuclear induction," *Phys. Rev.*, vol. 70, pp. 460–474, Oct 1946.

[45] F. Bloch, W. W. Hansen, and M. Packard, "The nuclear induction experiment," *Phys. Rev.*, vol. 70, pp. 474–485, Oct 1946.

[46] P. C. Lauterbur, "Image formation by induced local interactions - examples employing nuclear magnetic-resonance," *Nature*, vol. 242, no. 5394, pp. 190–191, 1973.

[47] P. Mansfield, "Multi-planar image formation using nmr spin echoes," *Journal of Physics C: Solid State Physics*, vol. 10, no. 3, p. L55, 1977.

[48] E. L. Hahn, "Spin echoes," *Phys. Rev.*, vol. 80, pp. 580–594, Nov 1950.

[49] H. Y. Carr and E. M. Purcell, "Effects of diffusion on free precession in nuclear magnetic resonance experiments," *Phys. Rev.*, vol. 94, pp. 630–638, May 1954.

[50] H. C. Torrey, "Bloch equations with diffusion terms," *Phys. Rev.*, vol. 104, pp. 563–565, Nov 1956.

[51] D. G. Taylor and M. C. Bushell, "The spatial mapping of translational diffusion coefficients by the nmr imaging technique," *Physics in Medicine and Biology*, vol. 30, no. 4, p. 345, 1985.

[52] D. Le Bihan and E. Breton, "Imagerie de Diffusion In Vivo par Résonance Magnétique Nucléaire.," *CR Académie des Sciences de Paris*, vol. 301, pp. 1109–1112, 1985.

[53] D. Le Bihan, E. Breton, D. Lallemand, P. Grenier, E. Cabanis, and M. Laval-Jeantet, "Mr imaging of intravoxel incoherent motions: application to diffusion and perfusion in neurologic disorders," *Radiology*, vol. 161, no. 2, pp. 401–407, 1986.

[54] A. Abragam, *Principles of Nuclear Magnetism*. The International Series of Monographs on Physics, Oxford University Press, USA, 1961.

[55] P. T. Callaghan, *Principles of Nuclear Magnetic Resonance Microscopy*. Oxford Science Publications, Clarendon Press, 1993.

[56] D. Nishimura, *Principles of magnetic resonance imaging*. Stanford University, 1996.

[57] I. Ardelean and R. Kimmich, "Principles and unconventional aspects of nmr diffusometry," vol. 49, pp. 45 – 115, 2003.

[58] D. K. Jones, *Diffusion MRI: Theory, Methods, and Applications*. OUP USA, 2011.

[59] N. Bloembergen, E. M. Purcell, and R. V. Pound, "Relaxation effects in nuclear magnetic resonance absorption," *Phys. Rev.*, vol. 73, pp. 679–712, Apr 1948.

[60] J. Tanner, "Use of the stimulated echo in nmr diffusion studies," *Journal of Chemical Physics*, vol. 52, pp. 2523–2526, 1970.

[61] E. Haacke, R. Brown, M. Thompson, and R. Venkatesan, *Magnetic Resonance Imaging: Physical Principles and Sequence Design*. Wiley, 1999.

[62] T. G. Reese, O. Heid, R. M. Weisskoff, and V. J. Wedeen, "Reduction of eddy-current-induced distortion in diffusion mri using a twice-refocused spin echo," *Magn Reson Med*, vol. 49, pp. 177–182, Jan 2003.

[63] N. Bodammer, J. Kaufmann, M. Kanowski, and C. Tempelmann, "Eddy current correction in diffusion-weighted imaging using pairs of images acquired with opposite diffusion gradient polarity," *Magn Reson Med*, vol. 51, pp. 188–193, Jan 2004.

[64] T.-K. Truong, N. kuei Chen, and A. W. Song, "Dynamic correction of artifacts due to susceptibility effects and time-varying eddy currents in diffusion tensor imaging," *Neuroimage*, vol. 57, pp. 1343–1347, Aug 2011.

[65] L. Minati and W. P. Weglarz, "Physical foundations, models, and methods of diffusion magnetic resonance imaging of the brain: A review," *Concepts in Magnetic Resonance Part A*, vol. 30A, no. 5, pp. 278–307, 2007.

[66] W. S. Price, "Pulsed-field gradient nuclear magnetic resonance as a tool for studying translational diffusion: Part 1. basic theory," *Concepts in Magnetic Resonance*, vol. 9, no. 5, pp. 299–336, 1997.

[67] P. N. Sen, "Time-dependent diffusion coefficient as a probe of geometry," *Concepts in Magnetic Resonance Part A*, vol. 23A, no. 1, pp. 1–21, 2004.

[68] P. P. Mitra, P. N. Sen, and L. M. Schwartz, "Short-time behavior of the diffusion coefficient as a geometrical probe of porous media," *Phys. Rev. B*, vol. 47, pp. 8565–8574, Apr 1993.

[69] A. Leemans, B. Jeurissen, J. Sijbers, and D. K. Jones, "Exploredti: a graphical toolbox for processing, analyzing, and visualizing diffusion mr data," in *Proceedings 17th Scientific Meeting, International Society for Magnetic Resonance in Medicine, Honolulu*, vol. 17, (Honolulu, USA), p. 3537, 2009.

[70] R. Snell, *Clinical Neuroanatomy*. Clinical Neuroanatomy, Wolters Kluwer Health/Lippincott Williams & Wilkins, 2010.

[71] A. Leemans, *Modeling and Processing of Diffusion Tensor Magnetic Resonance Images for Improved Analysis of Brain Connectivity*. Phd thesis, University of Antwerp, Antwerp, 2006.

[72] C. Nicholson and E. Syková, "Extracellular space structure revealed by diffusion analysis," *Trends Neurosci*, vol. 21, pp. 207–215, May 1998.

[73] E. O. Stejskal and J. E. Tanner, "Spin diffusion measurements: Spin echoes in the presence of a time-dependent field gradient," *The Journal of Chemical Physics*, vol. 42, no. 1, pp. 288–292, 1965.

[74] D. A. Yablonskiy and A. L. Sukstanskii, "Theoretical models of the diffusion weighted mr signal," *NMR Biomed*, vol. 23, pp. 661–681, Aug 2010.

[75] T. Niendorf, R. M. Dijkhuizen, D. G. Norris, M. van Lookeren Campagne, and K. Nicolay, "Biexponential diffusion attenuation in various states of brain tissue: implications for diffusion-weighted imaging," *Magn Reson Med*, vol. 36, pp. 847–857, Dec 1996.

[76] G. J. Stanisz, A. Szafer, G. A. Wright, and R. M. Henkelman, "An analytical model of restricted diffusion in bovine optic nerve," *Magn Reson Med*, vol. 37, pp. 103–111, Jan 1997.

[77] Y. Assaf and Y. Cohen, "Non-mono-exponential attenuation of water and n-acetyl aspartate signals due to diffusion in brain tissue," *J Magn Reson*, vol. 131, pp. 69–85, Mar 1998.

[78] P. J. Basser, J. Mattiello, and D. Le Bihan, "Estimation of the effective self-diffusion tensor from the nmr spin echo," *J Magn Reson B*, vol. 103, pp. 247–254, Mar 1994.

[79] P. J. Basser, J. Mattiello, and D. Le Bihan, "Mr diffusion tensor spectroscopy and imaging," *Biophys J*, vol. 66, pp. 259–267, Jan 1994.

[80] P. J. Basser and C. Pierpaoli, "Microstructural and physiological features of tissues elucidated by quantitative-diffusion-tensor mri," *J Magn Reson B*, vol. 111, pp. 209–219, Jun 1996.

[81] L.-C. Chang, D. K. Jones, and C. Pierpaoli, "Restore: robust estimation of tensors by outlier rejection," *Magn Reson Med*, vol. 53, pp. 1088–1095, May 2005.

[82] I. I. Maximov, F. Grinberg, and N. J. Shah, "Robust tensor estimation in diffusion tensor imaging," *J Magn Reson*, vol. 213, pp. 136–144, Dec 2011.

[83] E. S. Hui, M. M. Cheung, K. C. Chan, and E. X. Wu, "B-value dependence of dti quantitation and sensitivity in detecting neural tissue changes," *Neuroimage*, vol. 49, pp. 2366–2374, Feb 2010.

[84] P. J. Basser, S. Pajevic, C. Pierpaoli, J. Duda, and A. Aldroubi, "In vivo fiber tractography using dt-mri data," *Magn Reson Med*, vol. 44, pp. 625–632, Oct 2000.

[85] C. Pierpaoli and P. J. Basser, "Toward a quantitative assessment of diffusion anisotropy," *Magn Reson Med*, vol. 36, pp. 893–906, Dec 1996.

[86] P. J. Basser, "Inferring microstructural features and the physiological state of tissues from diffusion-weighted images," *NMR Biomed*, vol. 8, no. 7-8, pp. 333–344, 1995.

[87] K. M. Hasan, A. L. Alexander, and P. A. Narayana, "Does fractional anisotropy have better noise immunity characteristics than relative anisotropy in diffusion tensor mri? an analytical approach," *Magn Reson Med*, vol. 51, pp. 413–417, Feb 2004.

[88] S. Pajevic and C. Pierpaoli, "Color schemes to represent the orientation of anisotropic tissues from diffusion tensor data: application to white matter fiber tract mapping in the human brain," *Magn Reson Med*, vol. 42, pp. 526–540, Sep 1999.

[89] L. Minati, T. Banasik, J. Brzezinski, M. L. Mandelli, A. Bizzi, M. G. Bruzzone, M. Konopka, and A. Jasinski, "Elevating tensor rank increases anisotropy in brain areas associated with intra-voxel orientational heterogeneity (ivoh): a generalised dti (gdti) study," *NMR Biomed*, vol. 21, pp. 2–14, Jan 2008.

[90] R. V. Mulkern, H. Gudbjartsson, C. F. Westin, H. P. Zengingonul, W. Gartner, C. R. Guttmann, R. L. Robertson, W. Kyriakos, R. Schwartz, D. Holtzman, F. A. Jolesz, and S. E. Maier, "Multi-component apparent diffusion coefficients in human brain," *NMR Biomed*, vol. 12, pp. 51–62, Feb 1999.

[91] F. Grinberg, L. Ciobanu, E. Farrher, and N. J. Shah, "Diffusion kurtosis imaging and log-normal distribution function imaging enhance the visualisation of lesions in animal stroke models," *NMR Biomed*, vol. 25, pp. 1295–1304, Nov 2012.

[92] E. Crow and K. Shimizu, *Lognormal Distributions: Theory and Applications*. Statistics: A Series of Textbooks and Monogrphs, Marcel Dekker, 1988.

[93] E. Limpert, W. A. Stahel, and M. Abbt, "Log-normal distributions across the sciences: Keys and clues," *Bioscience*, vol. 51, no. 5, pp. 341–352, 2001-01-01 00:00:00.0.

[94] T. Zhao, H. W. Beckham, H. L. Ricks, and U. H. F. Bunz, "Self-diffusion of poly(p-phenyleneethynylene)s in dilute solution determined by pulsed-field-gradient nmr," *Polymer*, vol. 46, no. 13, pp. 4839 – 4844, 2005.

[95] J. H. Jensen and J. A. Helpern, "Mri quantification of non-gaussian water diffusion by kurtosis analysis," *NMR Biomed*, vol. 23, pp. 698–710, Aug 2010.

[96] K. P. Balanda and H. L. Macgillivray, "Kurtosis: A critical review," *American Statistician*, vol. 42, pp. 111–119, 1988.

[97] L. Qi, Y. Wang, and E. X. Wu, "D-eigenvalues of diffusion kurtosis tensors," *J. Comput. Appl. Math.*, vol. 221, pp. 150–157, Nov. 2008.

[98] L. Qi, D. Han, and E. X. Wu, "Principal invariants and inherent parameters of diffusion kurtosis tensors," *Journal of Mathematical Analysis and Applications*, vol. 349, pp. 165–180, 2009.

[99] D. H. J. Poot, A. J. den Dekker, E. Achten, M. Verhoye, and J. Sijbers, "Optimal experimental design for diffusion kurtosis imaging," *IEEE Trans Med Imaging*, vol. 29, pp. 819–829, Mar 2010.

[100] L. R. Frank, "Characterization of anisotropy in high angular resolution diffusion-weighted mri," *Magn Reson Med*, vol. 47, pp. 1083–1099, Jun 2002.

[101] E. Ozarslan and T. H. Mareci, "Generalized diffusion tensor imaging and analytical relationships between diffusion tensor imaging and high angular resolution diffusion imaging," *Magn Reson Med*, vol. 50, pp. 955–965, Nov 2003.

[102] A. W. Anderson, "Measurement of fiber orientation distributions using high angular resolution diffusion imaging," *Magn Reson Med*, vol. 54, pp. 1194–1206, Nov 2005.

[103] D. K. Jones, M. A. Horsfield, and A. Simmons, "Optimal strategies for measuring diffusion in anisotropic systems by magnetic resonance imaging," *Magn Reson Med*, vol. 42, pp. 515–525, Sep 1999.

[104] R. Stirnberg, T. Stöcker, and N. J. Shah, "A new and versatile gradient encoding scheme for dti: a direct comparison with the jones scheme," in *Proceedings 17th Scientific Meeting, International Society for Magnetic Resonance in Medicine, Stockholm*, 2009.

[105] J.-D. Tournier, F. Calamante, and A. Connelly, "Robust determination of the fibre orientation distribution in diffusion mri: non-negativity constrained super-resolved spherical deconvolution," *Neuroimage*, vol. 35, pp. 1459–1472, May 2007.

[106] M. Descoteaux, R. Deriche, D. L. Bihan, J.-F. Mangin, and C. Poupon, "Multiple q-shell diffusion propagator imaging," *Med Image Anal*, vol. 15, pp. 603–621, Aug 2011.

[107] D. S. Tuch, T. G. Reese, M. R. Wiegell, and V. J. Wedeen, "Diffusion mri of complex neural architecture," *Neuron*, vol. 40, pp. 885–895, Dec 2003.

[108] E. J. Canales-Rodríguez, L. Melie-García, and Y. Iturria-Medina, "Mathematical description of q-space in spherical coordinates: exact q-ball imaging," *Magn Reson Med*, vol. 61, pp. 1350–1367, Jun 2009.

[109] B. Horwitz, "The elusive concept of brain connectivity," *Neuroimage*, vol. 19, pp. 466–470, Jun 2003.

[110] S. Mori, B. J. Crain, V. P. Chacko, and P. C. van Zijl, "Three-dimensional tracking of axonal projections in the brain by magnetic resonance imaging," *Ann Neurol*, vol. 45, pp. 265–269, Feb 1999.

[111] D. K. Jones, A. Simmons, S. C. Williams, and M. A. Horsfield, "Non-invasive assessment of axonal fiber connectivity in the human brain via diffusion tensor mri," *Magn Reson Med*, vol. 42, pp. 37–41, Jul 1999.

[112] M. Lazar, "Mapping brain anatomical connectivity using white matter tractography," *NMR in Biomedicine*, vol. 23, no. 7, pp. 821–835, 2010.

[113] H. Johansen-Berg and M. F. Rushworth, "Using diffusion imaging to study human connectional anatomy," *Annual Review of Neuroscience*, vol. 32, no. 1, pp. 75–94, 2009. PMID: 19400718.

[114] B. Jeurissen, A. Leemans, D. K. Jones, J.-D. Tournier, and J. Sijbers, "Probabilistic fiber tracking using the residual bootstrap with constrained spherical deconvolution," *Hum Brain Mapp*, vol. 32, pp. 461–479, Mar 2011.

[115] S. Rice, *Mathematical Analysis of Random Noise*. Bell telephone system technical publications, American Telephone and Telegraph Company.

[116] A. Kristoffersen, "Optimal estimation of the diffusion coefficient from non-averaged and averaged noisy magnitude data," *J Magn Reson*, vol. 187, pp. 293–305, Aug 2007.

[117] R. M. Henkelman, "Measurement of signal intensities in the presence of noise in mr images," *Med Phys*, vol. 12, no. 2, pp. 232–233, 1985.

[118] H. Gudbjartsson and S. Patz, "The rician distribution of noisy mri data," *Magn Reson Med*, vol. 34, pp. 910–914, Dec 1995.

[119] C. D. Constantinides, E. Atalar, and E. R. McVeigh, "Signal-to-noise measurements in magnitude images from nmr phased arrays," *Magn Reson Med*, vol. 38, pp. 852–857, Nov 1997.

[120] J. Sijbers and A. J. den Dekker, "Maximum likelihood estimation of signal amplitude and noise variance from mr data," *Magn Reson Med*, vol. 51, pp. 586–594, Mar 2004.

[121] M. E. Brummer, R. M. Mersereau, R. L. Eisner, and R. J. Lewine, "Automatic detection of brain contours in mri data sets," *IEEE Trans Med Imaging*, vol. 12, no. 2, pp. 153–166, 1993.

[122] I. I. Maximov, E. Farrher, F. Grinberg, and N. J. Shah, "Spatially variable rician noise in magnetic resonance imaging," *Med Image Anal*, vol. 16, pp. 536–548, Feb 2012.

[123] A. J. Miller and P. M. Joseph, "The use of power images to perform quantitative analysis on low snr mr images," *Magn Reson Imaging*, vol. 11, no. 7, pp. 1051–1056, 1993.

[124] G. McGibney and M. R. Smith, "An unbiased signal-to-noise ratio measure for magnetic resonance images," *Med Phys*, vol. 20, no. 4, pp. 1077–1078, 1993.

[125] B. A. Landman, P.-L. Bazin, and J. L. Prince, "Estimation and application of spatially variable noise fields in diffusion tensor imaging," *Magn Reson Imaging*, vol. 27, pp. 741–751, Jul 2009.

[126] B. A. Landman, P.-L. Bazin, S. A. Smith, and J. L. Prince, "Robust estimation of spatially variable noise fields," *Magn Reson Med*, vol. 62, pp. 500–509, Aug 2009.

[127] C. Reischauer, P. Staempfli, T. Jaermann, and P. Boesiger, "Construction of a temperature-controlled diffusion phantom for quality control of diffusion measurements," *J Magn Reson Imaging*, vol. 29, pp. 692–698, Mar 2009.

[128] C. Poupon, B. Rieul, I. Kezele, M. Perrin, F. Poupon, and J.-F. Mangin, "New diffusion phantoms dedicated to the study and validation of high-angular-resolution diffusion imaging (hardi) models," *Magn Reson Med*, vol. 60, pp. 1276–1283, Dec 2008.

[129] A. Moussavi-Biugui, B. Stieltjes, K. Fritzsche, W. Semmler, and F. B. Laun, "Novel spherical phantoms for q-ball imaging under in vivo conditions," *Magn Reson Med*, vol. 65, pp. 190–194, Jan 2011.

[130] M. Perrin, C. Poupon, B. Rieul, P. Leroux, A. Constantinesco, J.-F. Mangin, and D. Le Bihan, "Validation of q-ball imaging with

a diffusion fibre-crossing phantom on a clinical scanner," *Philos Trans R Soc Lond B Biol Sci*, vol. 360, pp. 881–891, May 2005.

[131] E. Fieremans, Y. D. Deene, S. Delputte, M. S. Ozdemir, Y. D'Asseler, J. Vlassenbroeck, K. Deblaere, E. Achten, and I. Lemahieu, "Simulation and experimental verification of the diffusion in an anisotropic fiber phantom," *J Magn Reson*, vol. 190, pp. 189–199, Feb 2008.

[132] L. Walker, M. Curry, A. Nayak, N. Lange, C. Pierpaoli, , and the Brain Development Cooperative Group, "A framework for the analysis of phantom data in multicenter diffusion tensor imaging studies," *Human Brain Mapping*, pp. n/a–n/a, 2012.

[133] S. J. Teipel, S. Reuter, B. Stieltjes, J. Acosta-Cabronero, U. Ernemann, A. Fellgiebel, M. Filippi, G. Frisoni, F. Hentschel, F. Jessen, S. Klöppel, T. Meindl, P. J. W. Pouwels, K.-H. Hauenstein, and H. Hampel, "Multicenter stability of diffusion tensor imaging measures: a european clinical and physical phantom study," *Psychiatry Res*, vol. 194, pp. 363–371, Dec 2011.

[134] T. Zhu, R. H., X. Qiu, M. Taylor, Y. Tso, C. Yiannoutsos, B. Navia, S. Mori, S. Ekholm, G. Schifitto, and J. Zhong, "Quantification of accuracy and precision of multi-center dti measurements: a diffusion phantom and human brain study," *Neuroimage*, vol. 56, pp. 1398–1411, Jun 2011.

[135] E. Farrher, J. Kaffanke, A. A. Celik, T. Stöcker, F. Grinberg, and N. J. Shah, "Novel multisection design of anisotropic diffusion phantoms," *Magn Reson Imaging*, vol. 30, pp. 518–526, May 2012.

[136] F. Grinberg, E. Farrher, A.-M. Oros-Peusquens, and N. J. Shah, "Random walks in model brain tissue," *AIP Conf Proc*, vol. 1330, pp. 31–34, 2011.

[137] S. Boujraf, R. Luypaert, H. Eisendrath, and M. Osteaux, "Echo planar magnetic resonance imaging of anisotropic diffusion in asparagus stems," *MAGMA*, vol. 13, pp. 82–90, Oct 2001.

[138] J. Lätt, M. Nilsson, A. Rydhög, R. Wirestam, F. Ståhlberg, and S. Brockstedt, "Effects of restricted diffusion in a biological phantom: a q-space diffusion mri study of asparagus stems at a 3t clinical scanner," *MAGMA*, vol. 20, pp. 213–222, Oct 2007.

[139] E. E. Sigmund and Y.-Q. Song, "Multiple echo diffusion tensor acquisition technique," *Magn Reson Imaging*, vol. 24, pp. 7–18, Jan 2006.

[140] J. D. Trudeau, W. T. Dixon, and J. Hawkins, "The effect of inhomogeneous sample susceptibility on measured diffusion anisotropy using nmr imaging," *J Magn Reson B*, vol. 108, pp. 22–30, Jul 1995.

[141] M. Neeman, J. P. Freyer, and L. O. Sillerud, "A simple method for obtaining cross-term-free images for diffusion anisotropy studies in nmr microimaging," *Magn Reson Med*, vol. 21, pp. 138–143, Sep 1991.

[142] T. A. Sibgatullin, F. J. Vergeldt, E. Gerkema, and H. V. As, "Quantitative permeability imaging of plant tissues," *Eur Biophys J*, vol. 39, pp. 699–710, Mar 2010.

[143] E. Fieremans, *Validation methods for diffusion weighted magnetic resonance imaging in brain white matter*. PhD thesis, Ghent University, 2008.

[144] J. S. W. Campbell, K. Siddiqi, V. V. Rymar, A. F. Sadikot, and G. B. Pike, "Flow-based fiber tracking with diffusion tensor and q-ball data: validation and comparison to principal diffusion direction techniques," *Neuroimage*, vol. 27, pp. 725–736, Oct 2005.

[145] S. Madi, K. M. Hasan, and P. A. Narayana, "Diffusion tensor imaging of in vivo and excised rat spinal cord at 7 t with an icosahedral encoding scheme," *Magn Reson Med*, vol. 53, pp. 118–125, Jan 2005.

[146] F. N. Golabchi, D. H. Brooks, W. S. Hoge, U. D. Girolami, and S. E. Maier, "Pixel-based comparison of spinal cord mr diffu-

sion anisotropy with axon packing parameters," *Magn Reson Med*, vol. 63, pp. 1510–1519, Jun 2010.

[147] H. H. Ong, A. C. Wright, S. L. Wehrli, A. Souza, E. D. Schwartz, S. N. Hwang, and F. W. Wehrli, "Indirect measurement of regional axon diameter in excised mouse spinal cord with q-space imaging: simulation and experimental studies," *Neuroimage*, vol. 40, pp. 1619–1632, May 2008.

[148] C.-P. Lin, V. J. Wedeen, J.-H. Chen, C. Yao, and W.-Y. I. Tseng, "Validation of diffusion spectrum magnetic resonance imaging with manganese-enhanced rat optic tracts and ex vivo phantoms," *Neuroimage*, vol. 19, pp. 482–495, Jul 2003.

[149] N. Yanasak and J. Allison, "Use of capillaries in the construction of an mri phantom for the assessment of diffusion tensor imaging: demonstration of performance," *Magn Reson Imaging*, vol. 24, pp. 1349–1361, Dec 2006.

[150] S. H. Han, Y. K. Song, F. H. Cho, S. Ryu, G. Cho, Y.-Q. Song, and H. Cho, "Magnetic field anisotropy based mr tractography," *J Magn Reson*, vol. 212, pp. 386–393, Oct 2011.

[151] B. Siow, I. Drobnjak, A. Chatterjee, M. F. Lythgoe, and D. C. Alexander, "Estimation of pore size in a microstructure phantom using the optimised gradient waveform diffusion weighted nmr sequence," *J Magn Reson*, vol. 214, pp. 51–60, Jan 2012.

[152] E. A. H. von dem Hagen and R. M. Henkelman, "Orientational diffusion reflects fiber structure within a voxel," *Magn Reson Med*, vol. 48, pp. 454–459, Sep 2002.

[153] F. B. Laun, S. Huff, and B. Stieltjes, "On the effects of dephasing due to local gradients in diffusion tensor imaging experiments: relevance for diffusion tensor imaging fiber phantoms," *Magn Reson Imaging*, vol. 27, pp. 541–548, May 2009.

[154] R. Lorenz, M. E. Bellemann, J. Hennig, and K. A. Il'yasov, "Anisotropic phantoms for quantitative diffusion tensor imag-

ing and fiber-tracking validation," *Applied Magnetic Resonance*, vol. 33, pp. 419–429, 2008. 10.1007/s00723-008-0087-7.

[155] M. Watanabe, S. Aoki, Y. Masutani, O. Abe, N. Hayashi, T. Masumoto, H. Mori, H. Kabasawa, and K. Ohtomo, "Flexible ex vivo phantoms for validation of diffusion tensor tractography on a clinical scanner," *Radiat Med*, vol. 24, pp. 605–609, Nov 2006.

[156] P. Pullens, A. Roebroeck, and R. Goebel, "Ground truth hardware phantoms for validation of diffusion-weighted mri applications," *J Magn Reson Imaging*, vol. 32, pp. 482–488, Aug 2010.

[157] M. Holz, S. R. Heil, and A. Sacco, "Temperature-dependent self-diffusion coefficients of water and six selected molecular liquids for calibration in accurate 1h nmr pfg measurements," *Phys. Chem. Chem. Phys.*, vol. 2, pp. 4740–4742, 2000.

[158] V. G. Kiselev, "Effect of magnetic field gradients induced by microvasculature on nmr measurements of molecular self-diffusion in biological tissues," *J Magn Reson*, vol. 170, pp. 228–235, Oct 2004.

[159] J. Lindemeyer, A.-M. Oros-Peusquens, E. Farrher, F. Grinberg, , and N. J. Shah, "Orientation and microstructure effects on susceptibility reconstruction: a diffusion phantom study," in *Proceedings 19th Scientific Meeting, International Society for Magnetic Resonance in Medicine, Montréal*, p. 4516, 2011.

[160] E. Fieremans, Y. D. Deene, S. Delputte, M. S. Ozdemir, E. Achten, and I. Lemahieu, "The design of anisotropic diffusion phantoms for the validation of diffusion weighted magnetic resonance imaging," *Phys Med Biol*, vol. 53, pp. 5405–5419, Oct 2008.

[161] J. Ashburner and K. J. Friston, "Unified segmentation," *Neuroimage*, vol. 26, pp. 839–851, Jul 2005.

[162] T. Liu, H. Li, K. Wong, A. Tarokh, L. Guo, and S. T. C. Wong, "Brain tissue segmentation based on dti data," *Neuroimage*, vol. 38, pp. 114–123, Oct 2007.

[163] H. Lu, J. H. Jensen, A. Ramani, and J. A. Helpern, "Three-dimensional characterization of non-gaussian water diffusion in humans using diffusion kurtosis imaging," *NMR Biomed*, vol. 19, pp. 236–247, Apr 2006.

[164] M. M. Cheung, E. S. Hui, K. C. Chan, J. A. Helpern, L. Qi, and E. X. Wu, "Does diffusion kurtosis imaging lead to better neural tissue characterization? a rodent brain maturation study," *Neuroimage*, vol. 45, pp. 386–392, Apr 2009.

[165] M. F. Falangola, J. H. Jensen, J. S. Babb, C. Hu, F. X. Castellanos, A. D. Martino, S. H. Ferris, and J. A. Helpern, "Age-related non-gaussian diffusion patterns in the prefrontal brain," *J Magn Reson Imaging*, vol. 28, pp. 1345–1350, Dec 2008.

[166] E. Fieremans, J. H. Jensen, and J. A. Helpern, "White matter characterization with diffusional kurtosis imaging," *Neuroimage*, vol. 58, pp. 177–188, Sep 2011.

[167] J. H. Jensen, M. F. Falangola, C. Hu, A. Tabesh, O. Rapalino, C. Lo, and J. A. Helpern, "Preliminary observations of increased diffusional kurtosis in human brain following recent cerebral infarction," *NMR Biomed*, vol. 24, pp. 452–457, Jun 2011.

[168] E. S. Hui, E. Fieremans, J. H. Jensen, A. Tabesh, W. Feng, L. Bonilha, M. V. Spampinato, R. Adams, and J. A. Helpern, "Stroke assessment with diffusional kurtosis imaging," *Stroke*, Aug 2012.

[169] E. S. Hui, F. Du, S. Huang, Q. Shen, and T. Q. Duong, "Spatiotemporal dynamics of diffusional kurtosis, mean diffusivity and perfusion changes in experimental stroke," *Brain Res*, vol. 1451, pp. 100–109, Apr 2012.

[170] J. Zhuo, S. Xu, J. L. Proctor, R. J. Mullins, J. Z. Simon, G. Fiskum, and R. P. Gullapalli, "Diffusion kurtosis as an in vivo imaging marker for reactive astrogliosis in traumatic brain injury," *Neuroimage*, vol. 59, pp. 467–477, Jan 2012.

[171] M. Kudzinava, D. Poot, A. Plaisier, and J. Sijbers, "Optimized workflow for diffusion kurtosis imaging of newborns," in *Biomedical Imaging: From Nano to Macro, 2011 IEEE International Symposium on*, pp. 922 –926, 30 2011-april 2 2011.

[172] M. Lazar, J. H. Jensen, L. Xuan, and J. A. Helpern, "Estimation of the orientation distribution function from diffusional kurtosis imaging," *Magnetic Resonance in Medicine*, vol. 60, no. 4, pp. 774–781, 2008.

[173] E. X. Wu and M. M. Cheung, "Mr diffusion kurtosis imaging for neural tissue characterization," *NMR Biomed*, vol. 23, pp. 836–848, Aug 2010.

[174] J. Veraart, D. H. J. Poot, W. V. Hecke, I. Blockx, A. V. der Linden, M. Verhoye, and J. Sijbers, "More accurate estimation of diffusion tensor parameters using diffusion kurtosis imaging," *Magn Reson Med*, vol. 65, pp. 138–145, Jan 2011.

[175] A. Tabesh, J. H. Jensen, B. A. Ardekani, and J. A. Helpern, "Estimation of tensors and tensor-derived measures in diffusional kurtosis imaging," *Magn Reson Med*, vol. 65, pp. 823–836, Mar 2011.

[176] J. Veraart, W. V. Hecke, and J. Sijbers, "Constrained maximum likelihood estimation of the diffusion kurtosis tensor using a rician noise model," *Magn Reson Med*, vol. 66, pp. 678–686, Sep 2011.

[177] L. Minati, "Rapid generation of biexponential and diffusional kurtosis maps using multi-layer perceptrons: a preliminary experience," *MAGMA*, vol. 21, pp. 299–305, Jul 2008.

[178] S. Hu, Z.-H. Huang, H.-Y. Ni, and L. Qi, "Positive definiteness of diffusion kurtosis imaging," *Inverse Problems and Imaging*, vol. 6, no. 1, pp. 57–75, 2012.

[179] S. M. Smith, M. Jenkinson, M. W. Woolrich, C. F. Beckmann, T. E. J. Behrens, H. Johansen-Berg, P. R. Bannister, M. D. Luca, I. Drobnjak, D. E. Flitney, R. K. Niazy, J. Saunders, J. Vickers,

Y. Zhang, N. D. Stefano, J. M. Brady, and P. M. Matthews, "Advances in functional and structural mr image analysis and implementation as fsl," *Neuroimage*, vol. 23 Suppl 1, pp. S208–S219, 2004.

[180] M. W. Woolrich, S. Jbabdi, B. Patenaude, M. Chappell, S. Makni, T. Behrens, C. Beckmann, M. Jenkinson, and S. M. Smith, "Bayesian analysis of neuroimaging data in fsl," *Neuroimage*, vol. 45, pp. S173–S186, Mar 2009.

[181] M. Jenkinson and S. Smith, "A global optimisation method for robust affine registration of brain images," *Med Image Anal*, vol. 5, pp. 143–156, Jun 2001.

[182] A. F. Frøhlich, L. Ostergaard, and V. G. Kiselev, "Effect of impermeable boundaries on diffusion-attenuated mr signal," *J Magn Reson*, vol. 179, pp. 223–233, Apr 2006.

[183] M. E. Moseley, Y. Cohen, J. Mintorovitch, L. Chileuitt, H. Shimizu, J. Kucharczyk, M. F. Wendland, and P. R. Weinstein, "Early detection of regional cerebral ischemia in cats: comparison of diffusion- and t2-weighted mri and spectroscopy," *Magn Reson Med*, vol. 14, pp. 330–346, May 1990.

[184] C. H. Sotak, "The role of diffusion tensor imaging in the evaluation of ischemic brain injury - a review," *NMR Biomed*, vol. 15, no. 7-8, pp. 561–569, 2002.

[185] P. W. Schaefer, W. A. Copen, M. H. Lev, and R. G. Gonzalez, "Diffusion-weighted imaging in acute stroke," *Magn Reson Imaging Clin N Am*, vol. 14, pp. 141–168, May 2006.

[186] R. Weber, P. Ramos-Cabrer, and M. Hoehn, "Present status of magnetic resonance imaging and spectroscopy in animal stroke models," *J Cereb Blood Flow Metab*, vol. 26, pp. 591–604, May 2006.

[187] S. P. Kloska, M. Wintermark, T. Engelhorn, and J. B. Fiebach, "Acute stroke magnetic resonance imaging: current status and future perspective," *Neuroradiology*, vol. 52, pp. 189–201, Mar 2010.

[188] M. Hoehn-Berlage, "Diffusion-weighted nmr imaging: application to experimental focal cerebral ischemia," *NMR Biomed*, vol. 8, no. 7-8, pp. 345–358, 1995.

[189] A. Gass, T. Niendorf, and J. G. Hirsch, "Acute and chronic changes of the apparent diffusion coefficient in neurological disorders–biophysical mechanisms and possible underlying histopathology," *J Neurol Sci*, vol. 186 Suppl 1, pp. S15–S23, May 2001.

[190] P. Vestergaard-Poulsen, B. Hansen, L. Ostergaard, and R. Jakobsen, "Microstructural changes in ischemic cortical gray matter predicted by a model of diffusion-weighted mri," *J Magn Reson Imaging*, vol. 26, pp. 529–540, Sep 2007.

[191] A. Szafer, J. Zhong, and J. C. Gore, "Theoretical model for water diffusion in tissues," *Magn Reson Med*, vol. 33, pp. 697–712, May 1995.

[192] P. van Gelderen, M. H. de Vleeschouwer, D. DesPres, J. Pekar, P. C. van Zijl, and C. T. Moonen, "Water diffusion and acute stroke," *Magn Reson Med*, vol. 31, pp. 154–163, Feb 1994.

[193] C. van Pul, W. Jennekens, K. Nicolay, K. Kopinga, and P. F. F. Wijn, "Ischemia-induced adc changes are larger than osmotically-induced adc changes in a neonatal rat hippocampus model," *Magn Reson Med*, vol. 53, pp. 348–355, Feb 2005.

[194] M. Wick, Y. Nagatomo, F. Prielmeier, and J. Frahm, "Alteration of intracellular metabolite diffusion in rat brain in vivo during ischemia and reperfusion," *Stroke*, vol. 26, pp. 1930–3; discussion 1934, Oct 1995.

[195] R. M. Dijkhuizen, R. A. de Graaf, K. A. Tulleken, and K. Nicolay, "Changes in the diffusion of water and intracellular metabolites after excitotoxic injury and global ischemia in neonatal rat brain," *J Cereb Blood Flow Metab*, vol. 19, pp. 341–349, Mar 1999.

[196] M. D. Budde and J. A. Frank, "Neurite beading is sufficient to decrease the apparent diffusion coefficient after ischemic stroke," *Proc Natl Acad Sci U S A*, vol. 107, pp. 14472–14477, Aug 2010.

[197] I. Blockx, G. D. Groof, M. Verhoye, J. V. Audekerke, K. Raber, D. Poot, J. Sijbers, A. P. Osmand, S. V. Hörsten, and A. V. der Linden, "Microstructural changes observed with dki in a transgenic huntington rat model: evidence for abnormal neurodevelopment," *Neuroimage*, vol. 59, pp. 957–967, Jan 2012.

[198] I. Ronen, S. Moeller, K. Ugurbil, and D.-S. Kim, "Analysis of the distribution of diffusion coefficients in cat brain at 9.4 t using the inverse laplace transformation," *Magn Reson Imaging*, vol. 24, pp. 61–68, Jan 2006.

[199] L. Belayev, O. F. Alonso, R. Busto, W. Zhao, and M. D. Ginsberg, "Middle cerebral artery occlusion in the rat by intraluminal suture. neurological and pathological evaluation of an improved model," *Stroke*, vol. 27, pp. 1616–22; discussion 1623, Sep 1996.

[200] J. H. Jensen and J. A. Helpern, "Quantifying non-gaussian water diffusion by means of pulsed-field-gradient mri," in *Proceedings 11th Scientific Meeting, International Society for Magnetic Resonance in Medicine, Toronto, Canada.*, p. 2154, 2003.

[201] A. Lemke, S. Grudzenski, J. Döpfert, F. Laun, T. Kuder, M. Fatar, and L. Schad., "In vivo kurtosis imaging in murine cerebral ischemia," in *Proceedings 19th Scientific Meeting, International Society for Magnetic Resonance in Medicine, Montréal*, p. 2156, 2011.

[202] F. Grinberg, E. Farrher, L. Ciobanu, F. Geffroy, and N. J. Shah, "Stroke analysis by means of kurtosis diffusion imaging in in vivo animal studies," in *Proceedings 19th Scientific Meeting, International Society for Magnetic Resonance in Medicine, Montréal*, p. 1989, 2011.

[203] E. S. Hui, F. Du, Q. Shen, S. Huang, and T. Q. Duong., "Diffusion kurtosis is sensitive to hyperacute cerebral ischemia and increases with ischemic progression without renormalization," in *Proceedings 19th Scientific Meeting, International Society for Magnetic Resonance in Medicine, Montréal*, p. 4071, 2011.

[204] E. S. Hui, F. Du, Q. Shen, S. Huang, and T. Q. Duong., "Can diffusion kurtosis imaging provide better ischemic lesion delineation?," in *Proceedings 19th Scientific Meeting, International Society for Magnetic Resonance in Medicine, Montréal*, p. 3958, 2011.

[205] J. Pfeuffer, S. W. Provencher, and R. Gruetter, "Water diffusion in rat brain in vivo as detected at very large b values is multicompartmental," *MAGMA*, vol. 8, pp. 98–108, May 1999.

[206] D. K. Jones and P. J. Basser, ""squashing peanuts and smashing pumpkins": how noise distorts diffusion-weighted mr data," *Magn Reson Med*, vol. 52, pp. 979–993, Nov 2004.

[207] P. Mukherjee, M. M. Bahn, R. C. McKinstry, J. S. Shimony, T. S. Cull, E. Akbudak, A. Z. Snyder, and T. E. Conturo, "Differences between gray matter and white matter water diffusion in stroke: diffusion-tensor mr imaging in 12 patients," *Radiology*, vol. 215, pp. 211–220, Apr 2000.

[208] J. Lätt, D. van Westen, M. Nilsson, R. Wirestam, F. Ståhlberg, S. Holtås, and S. Brockstedt, "Diffusion time dependent kurtosis maps visualize ischemic lesions in stroke patients.," in *Proceedings 17th Scientific Meeting, International Society for Magnetic Resonance in Medicine, Honolulu.*, p. 40, 2009.

[209] P. T. Callaghan, K. W. Jolley, and J. Lelievre, "Diffusion of water in the endosperm tissue of wheat grains as studied by pulsed field gradient nuclear magnetic resonance," *Biophys J*, vol. 28, pp. 133–141, Oct 1979.

[210] P. T. Callaghan and O. Soderman, "Examination of the lamellar phase of aerosol ot/water using pulsed field gradient nuclear magnetic resonance," *The Journal of Physical Chemistry*, vol. 87, no. 10, pp. 1737–1744, 1983.

[211] K. Ulrich, P. Galvosas, J. Kärger, and F. Grinberg, "Effects of self-assembly on diffusion mechanisms of triblock copolymers in aqueous solution," *Phys Rev Lett*, vol. 102, p. 037801, Jan 2009.

[212] K. Ulrich, P. Galvosas, J. Kärger, F. Grinberg, J. Vernimmen, V. Meynen, and P. Cool, "Self-assembly and diffusion of block copolymer templates in sba-15 nanochannels," *J Phys Chem B*, vol. 114, pp. 4223–4229, Apr 2010.

[213] D. S. Novikov and V. G. Kiselev, "Effective medium theory of a diffusion-weighted signal," *NMR Biomed*, vol. 23, pp. 682–697, Aug 2010.

[214] P. Callaghan, *Translational Dynamics and Magnetic Resonance: Principles of Pulsed Gradient Spin Echo NMR*. OUP Oxford, 2011.